2016

Risk, Resilience, and Sustainability-Informed Assessment and Management of Aging Structural Systems

You Dong
Lehigh University

Risk, Resilience, and Sustainability-Informed Assessment and Management of Aging Structural Systems

by

You Dong

Presented to the Graduate and Research Committee
of Lehigh University
in Candidacy for the Degree of
Doctor of Philosophy

in

Structural Engineering

Lehigh University

May 2016

Approved and recommended for acceptance as a dissertation in partial fulfillment of the requirements for the degree of Doctor of Philosophy

_____

Date

_____

Dr. Dan M. Frangopol
Dissertation Advisor
Professor of Civil and
Environmental Engineering
Lehigh University

_____

Approved Date

Committee Members:

_____

Dr. John L. Wilson
Committee Chairperson
Professor of Civil and
Environmental Engineering
Lehigh University

_____

Dr. Ben T. Yen
Member
Emeritus Professor of Civil and
Environmental Engineering
Lehigh University

_____

Dr. Paolo Bocchini
Member
Assistant Professor of Civil and
Environmental Engineering
Lehigh University

_____

Dr. Liang Cheng
Member
Associate Professor of Computer
Science and Engineering
Lehigh University

ACKNOWLEDGMENTS

Foremost, I would like to express my gratitude to my advisor, Prof. Dan M. Frangopol for his time, patience, assistance, contribution, and continuous support throughout my Ph.D. program at Lehigh University. Prof. Frangopol is more than just a professor, he is a teacher, a mentor, an inspiration, and a friend. I believe without doubt that this work would not be completed without Prof. Frangopol's guidance. As a result, I was able to co-author with Prof. Frangopol 15 papers published in reputable peer-reviewed archival journals, and 16 conference papers, including several keynotes. Additionally, I was awarded the P.C. Rossin Fellowship of Lehigh University in 2014 and the International Civil Engineering Risk and Reliability Association (CERRA) Student Recognition Award in 2015.

Besides my advisor, I offer my sincere thanks to Prof. John L. Wilson, who serves as the Chairperson of this committee, Prof. Ben T. Yen, Assistant Prof. Paolo Bocchini, and Associate Prof. Liang Cheng, for their insightful comments and valuable suggestions on my work.

I gratefully acknowledge the support of (a) the National Science Foundation (NSF) through grants CMS-0639428 and CMMI-1537926, (b) the Commonwealth of Pennsylvania, Department of Community and Economic Development, through the Pennsylvania Infrastructure Technology Alliance (PITA) through several contracts, (c) the U.S. Federal Highway Administration (FHWA) Cooperative Agreement Award

DTFH61-07-H-00040, (d) the U.S. Office of Naval Research (ONR) Awards N00014-08-1-0188 and N00014- 12-1-0023, and (e) the National Aeronautics and Space Administration (NASA) Award NNX10AJ20G. My research advisor, Prof. Frangopol, served as the Principal Investigator in all these grants and contracts.

I would also like to sincerely thank the former and current students of Prof. Frangopol's research team including: (a) Dr. Duygu Saydam, Dr. Mohamed Soliman, and Ph.D. Candidate Samantha Sabatino for their cooperation, constructive comments, inspirational discussions, and helpful suggestions and (b) Alberto Decò and Benjin Zhu, former Ph.D. students, current Ph.D. Candidate Alysson Mondoro, and former M.Sc. student Jie Liu, for their warm friendship and support, and for creating a cordial working environment. Also, I would like to thank Peter Bryan, the IT Manager of ATLSS, for always providing technological support and software solutions for the computations needed in this study.

Finally and most importantly, I am very grateful for the unconditional support of my family in China, which made this work possible. I thank you all: mom, dad, and my sister. Nothing would be meaningful without you.

TABLE OF CONTENTS

LIST OF TABLES

LIST OF FIGURES

ABSTRACT

During their service life, structural systems (e.g., civil and marine structures) may be subjected to aggressive deteriorations such as corrosion and fatigue and/or extreme events such as floods, collisions, earthquakes, and fires. These deteriorations may start from the day the structures enter in service and, if not effectively managed, can cause a significant reduction in structural functionality and safety. Maintaining performance and functionality of structural systems under these adverse effects is gaining increased attention. This highlights the necessity of effective assessment and management of civil and marine structures in a life-cycle context.

The main objective of this study is to develop a risk, sustainability and resilience-informed approach for the life-cycle management of structural systems with emphasis on highway bridges, bridge networks, buildings, interdependent structural systems, and ship structures. Risk - based performance indicators combining the probability of structural failure with the consequences associated with a particular failure event are investigated in this study. Furthermore, a wide range of performance measures is covered under "sustainability" to reflect three aspects: economic, social, and environmental. Sustainability is described as "meeting the needs of present without altering the needs of future generations" (Adams 2006). Sustainability can serve as a useful tool in decision making and risk mitigation associated with civil and marine structures. In addition to risk and sustainability, resilience is another indicator that accounts for structural functionality and recovery patterns after extreme events. Presidential Policy Directive (PPD 2013)

defines resilience as "a structure's ability to prepare for and adapt to changing conditions while simultaneously being able to withstand and recover rapidly from functionality disruptions". Overall, risk, sustainability, and resilience assessment considering aging and multi-hazard effects are of vital importance to ensure structural safety and functionality of structural systems during their service life.

Risk is assessed for highway bridges under the effects of climate change and multiple hazards, including aging effects, flood-induced scour, and earthquake, whereas the adverse effects associated with aging and earthquake are investigated for bridge networks. The sustainability of highway bridges and bridge networks is assessed considering social, economic, and environmental metrics. The seismic resilience of highway bridges under mainshock (MS) only and mainshock-aftershock (MSAS) sequences is investigated to account for structural performance and recovery patterns under extreme events. Additionally, the seismic performance of buildings and interdependent healthcare - bridge network systems is investigated considering correlation effects and uncertainties. Furthermore, a probabilistic methodology to establish optimum pre-earthquake retrofit plans of bridge networks based on risk and sustainability is developed.

For ship structures, a decision support system considering structural deteriorations (i.e., corrosion and fatigue) and extreme events (e.g., collision) is established. Specifically, the probabilistic ship collision risk and sustainability are investigated incorporating the attitude of a decision maker. A novel approach is developed to evaluate the time-variant risk of ship structures under corrosion and fatigue during the investigated

time interval. Furthermore, a multi-objective optimization problem, which accounts for structural deteriorations and various uncertainties, is formulated to determine optimum inspection planning that reduces the extent of adverse consequence associated with ship failure while simultaneously minimizing the expected total maintenance cost. Additionally, a probabilistic approach for reliability and risk updating of both inspected and uninspected fatigue-sensitive details at both component and system levels is developed considering uncertainties and correlation effects.

Overall, this study provides methodologies for the risk, sustainability, and resilience-informed assessment and management of structural systems under structural deteriorations and extreme events in a life-cycle context. Based on the inspection information, the reliability and risk could be updated for the near real-time decision making of deteriorating structures. The proposed probabilistic frameworks are illustrated on highway bridges, bridge networks, buildings, interdependent structural systems, and ship structures. The proposed methodology can be used to assist decision making regarding risk mitigation activities and, ultimately, improve the sustainability of structural systems in a life-cycle context.

CHAPTER 1

INTRODUCTION

1.1. OVERVIEW AND BACKGROUND

Both civil and marine structural systems play an essential role in the sustained economic growth and social development of most countries. During their service life, these systems are exposed to gradual deteriorations (e.g., corrosion, fatigue) and/or sudden hazards (e.g., collision, earthquakes, and floods), which can hamper their performance and functionality. The American Society of Civil Engineers (ASCE) reported, within the 2013 Report Card for America's Infrastructure, 3.6 trillion USD was needed to improve the condition of American infrastructure systems (ASCE 2013). Similarly, the failure of marine structures under deteriorations (e.g., corrosion, weather condition, grounding, fire/explosion, and collision) could bring devastating consequences to the economy and society. These aspects highlight the need to implement optimal management strategies to maintain performance of deteriorating structural systems above acceptable levels while attempting to satisfy budgetary constraints. In an attempt to address this issue, risk and sustainability-informed methods are gaining increasing attention in design, assessment, maintenance, and management of deteriorating systems in a life-cycle context (Frangopol 2011).

In order to properly facilitate the life-cycle management framework of civil and marine structures, a probabilistic performance assessment approach that has the capability to consider the probability of structural failure, vulnerability of the

deteriorating systems, and consequences of structural failure to the economy, society, and environment, should be established. As there are uncertainties associated with structural capacity, load, and modeling, a probabilistic approach is needed for the performance assessment considering different performance indicators. Structural reliability, as a measure of probability of a structure survival given a limit state, has been used within civil and marine structures. Nowadays, risk and sustainability-informed assessment approach is gaining increased attention. A risk-based performance indicator can provide a means of combing the probability of components or systems failures with the consequences of this event (Ellingwood 2005; Frangopol 2011). Since failures associated with structural systems could result in significant economic and social impacts, risk-based methodologies are more appropriate for structural system assessment than the reliability. Methodologies incorporating risk within the life-cycle management of civil and marine structures are presented in this study.

Sustainability, defined as the meeting of the needs of present without altering the needs of future generations (Adams 2006), can cover a wide range of performance measures and serve as a useful tool in risk-mitigation and decision making associated with structural systems. Sustainability could also denote as the "Triple Bottom Line" satisfying three objectives: economic, social, and environmental (Elkington 2004). Sustainability, covering economic, social, and environmental metrics, should be incorporated within the life-cycle assessment and management of deteriorating structural systems.

Various modules associated with assessment of structural systems, analyses of system and component performance interaction, optimization of management activities (e.g., inspection, monitoring, and maintenance), and updating the life-cycle performance based on information from structural health monitoring and/or inspection should be integrated to achieve a comprehensive management framework. Accordingly, based on the structural performance assessment, the following step of life-cycle management would be the optimization of life-cycle management activities. There could be multiple goals associated with the life-cycle management of civil and marine structures, including maximizing the life-cycle structural performance and simultaneously minimizing the total life-cycle cost of the interventions required to keep the system in its functional status, among others.

Another essential task within the life-cycle management is decision making. In general, decision making process may be divided into five separate stages: the pre-analysis, problem set-up, uncertainty quantification, utility assignment, and optimization (Jiménez *et al.* 2003). Furthermore, the decision making process should combine information regarding the structural performance from structural health monitoring and/or inspection to update the intervention plans. The inspection information of one particular detail can be used to update structural performance of other uninspected details considering correlation effects. Overall, it is of vital importance to incorporate decision making and updating in the life-cycle management of civil and marine structures.

1.1.1. Life-cycle management of civil infrastructure systems

Maintaining performance of civil infrastructure systems at desired levels in a life-cycle context has been an important research area (Ang and De Leon 1997; Frangopol 2011; Frangopol and Soliman 2016). Civil infrastructure systems are subjected to abnormal events such as earthquakes and floods throughout their lifetime. The capacity of civil structures to resist hazard effects is reduced in time by the effects of aging and deterioration.

The majority of the past studies on loss assessment of civil structures under extreme events focus on single hazard without considering the aging and multi-hazard effects (Stein *et al.* 1999; Vu and Stewart 2000; Ang and De Leon 2005; Ghosh and Padgett 2010; Simon *et al.* 2010; Akiyama *et al.* 2011). Effects of any other hazard (e.g., flood-induced scour) can increase the seismic vulnerability of a structure. Additionally, most previous studies of bridge seismic risk assessment have focused on the effects of a mainshock while neglecting the aftershocks (Shinozuka *et al.* 2005; Decò and Frangopol 2013). However, aftershocks may produce disastrous economic and societal consequences compared to a mainshock event (Yeo and Cornell 2009); therefore, the effects of aftershocks should be incorporated within the probabilistic multi-hazard risk assessment of highway bridges.

Quantifying the three metrics of sustainability of structural systems under hazard effects at a system level considering time effects is a challenging task and needed to be addressed in a comprehensive manner. Studies concerning performance of bridge networks have been investigated (Kiremidjian *et al.* 2007; Shiraki *et al.* 2007; Bocchini

and Frangopol 2011, 2012), whereas the sustainability of highway bridge networks have not been investigated by these studies. Risk and sustainability assessment of bridge networks under hazard effects needs to be further developed.

As buildings consume significant amount of natural resources and account for a paramount portion of greenhouse emission, research on sustainability performance of buildings is needed. Although building rating systems, such as LEED (2008), evaluate the greenness of new and existing building systems, the ratings do not measure building hazard performance, which can impact building sustainability performance as well. A methodology to evaluate the seismic sustainability of buildings is needed to meet current performance requirements. As strong earthquakes can destroy infrastructure systems and cause injuries and/or fatalities, it is also important to investigate seismic performance of interdependent healthcare - bridge network systems to guarantee immediate medical treatment after earthquakes. There are several studies focusing the seismic damage assessment of hospitals (Myrtle *et al.* 2005; Yavari *et al.* 2010; Achour *et al.* 2011; Cimellaro *et al.* 2011). However, the damage conditions associated with bridge networks have not been incorporated within the healthcare system performance assessment process and the correlation effects have also not been addressed in previous studies.

In addition to risk and sustainability, resilience is another indicator that accounts for structural functionality and recovery patterns after hazard occurrence. The 2015 Global Presidential Policy Directive (PPD 2013) defines resilience as "a structure's ability to prepare for and adapt to changing conditions while simultaneously being able to withstand and recover rapidly from functionality disruptions". An analytical model has

been widely implemented for resilience quantification of civil infrastructure systems after an extreme event (Bruneau *et al.* 2003; Çăgnan *et al.* 2006; Cimellaro *et al.* 2010; Bocchini and Frangopol 2012; Decò *et al.* 2013). However, there are no explicit studies that incorporate sustainability within the life-cycle management of structural systems to form a comprehensive framework incorporating uncertainties. This study aims to address this aspect.

Nowadays, climate change has become one of the big issuers around the world. The United States Global Change Research Program (USGCRP 2008) reported that the average precipitation has increased 5% during a 50 years interval and the frequency of hazards has increased as well as they have become more intense. There is a need for an investigation of bridge performance under the impact of climate change. The effects associated with continuing change in intensities and probabilities of extreme events are aimed to be investigated in this study.

Another important aspect associated with life-cycle management of civil infrastructures is optimal maintenance actions under tight budget and performance constraints. Multi-objective optimization techniques play an important role to allocate limited resources in an efficient way to balance the cost and performance (Frangopol 1999; Frangopol 2011). There exists a significant need for the effective retrofit strategies of highway bridge networks to improve structural seismic performance using cost-benefit analysis and multi-criteria optimization techniques.

1.1.2. Life-cycle management of ship structures

As ship collision can have devastating impacts on the economy, society, and environment, it is of vital importance to evaluate collision risk in order to plan preventive actions and be sufficiently prepared for possible oil spills and other adverse consequences. A predominant part of past studies regarding ship collision focused on determining the probability of collision (Fujii and Tanake 1971; Macduff 1974; Montewka *et al.* 2010). Very little research has been carried out that properly integrated the probability of ship collision with the consequences associated with collision into a comprehensive risk assessment (Otto *et al.* 2002; Altiok *et al.* 2012). The probabilistic risk and sustainability associated with ship collision is a relatively new research area and is needed to be addressed.

In addition to the extreme events (e.g., ship collision), ship structures could also be subjected to structural deteriorations and be used beyond their intended design life. Consequently, it is crucial to evaluate the risk associated with marine structures subjected to inclement weather and sea conditions when developing a decision management system for ship routing. In general, the most significant structural deteriorations associated with ship structures are corrosion and fatigue (Guedes Soares and Garbatov 1999; Kwon and Frangopol 2012). Therefore, it is essential to mitigate the adverse consequences associated with structural failure under corrosion and fatigue. Although the reliability of ship structures considering flexural failure has been studied (Paik *et al.* 1998; Paik and Frieze 2001; Akpan *et al.* 2002; Okasha *et al.* 2011; Decò *et al.* 2012; Saydam and Frangopol 2013), fatigue failure has not yet to be comprehensively examined in a ship

routing (Guedes Soares *et al.* 2003; Kwon and Frangopol 2012). There has been a lack of research that focuses on risk-based performance assessment of ship structures under corrosion and fatigue. The importance of risk as a performance indicator is emphasized in this study. Additionally, there is very limited research regarding risk-informed life-cycle maintenance optimization of ship structures under corrosion and fatigue.

The structural details associated with a given structural system are correlated due to common parameters associated with materials, design, fabrication, loading, and operational conditions. Based on the correlations, the inspection information of one particular detail can be used to update deterioration performance of others uninspected details. While previous studies have emphasized on reliability-based decision making process considering updating (Ayala-Uraga and Moan 2002; Moan and Song 2000; Chen *et al.* 2011; Huang *et al.* 2013; Maljaars and Vrouwenvelder 2014), research is needed to transfer the information associated with a given inspection event to risk assessment of other details at system level to aid the decision making process.

1.2. OBJECTIVES

The objectives of this study are:

1. Develop an approach for assessing performance of highway bridges and bridge networks under multiple hazards considering economic, social, environmental metrics, and climate change.
2. Propose an approach for performance-based seismic assessment of conventional and base-isolated buildings incorporating resilience and environmental impacts.

3. Develop a probabilistic approach for performance assessment of interdependent healthcare – bridge network systems under seismic hazard considering uncertainty and correlation effects.
4. Develop a probabilistic approach to schedule optimal retrofit and maintenance activities of bridge networks under seismic hazard in a life-cycle context.
5. Propose a probabilistic approach for ship collision risk and sustainability assessment incorporating the attitude of a decision maker.
6. Develop a decision support system of ship routing considering multiple performance criteria: repair loss, fatigue damage, travel time, and CO_2 emission.
7. Propose an approach for risk-informed life-cycle optimal inspection plans of aging ship structures under corrosion and fatigue.
8. Develop an approach for integrating inspection information into life-cycle risk assessment and updating of fatigue-sensitive structures at both component and system levels.

1.3. SUMMARY OF THE APPROACH

The overall purpose of this study is to develop a life-cycle management and decision making framework of structural systems under time-dependent structural deteriorations and extreme events. Figure 1.1 shows the proposed schematic framework composed of following 5 modules: identification of deterioration scenarios (i.e., module 1), structural vulnerability analyses (i.e., module 2), structural performance assessment and prediction (i.e., module 3), risk and sustainability-informed management and decision making (i.e., module 4), and integration of updating into decision making (i.e., module 5). In this

study, the application of the life-cycle management and decision making framework is applied to single bridges, buildings, bridge networks, interdependent structural systems, and ship structures.

The framework starts with the identification of deterioration scenarios (i.e., module 1) that affect the component and system performances. The time-dependent structural deteriorations and extreme events are considered in this study. Specifically, corrosion, fatigue, ship collision, flood, and earthquake are emphasized. This study takes the uncertainties associated with both the probabilities of occurrence and intensities of these deteriorations into account. Additionally, the climate change associated with increase in hazard intensity and frequency is considered in this module. In module 2, the structural vulnerability of structural systems under the deterioration scenarios that are identified in Module 1 is investigated. As there are uncertainties associated with structural capacity and load effect, the probability-based concepts are incorporated within the evaluation process. Limit state functions covering different failure modes are identified and the corresponding probabilities of failure associated with these functions are computed using reliability analysis. The advanced performance evaluation techniques, such as nonlinear finite element analysis, hydrodynamic analysis, and first/second orders reliability analyses are employed within this study to investigate the structural performance.

Module 3 is associated with the structural performance assessment and prediction. Risk, resilience, and sustainability are considered as performance indicators as shown in Figure 1.1. The structural prediction is related to the deterioration mechanisms and extreme events, such as aging, corrosion, and earthquakes. Adverse consequences

associated with economic, social, and environmental metrics are investigated to cover a comprehensive evaluation process. Resilience, accounting for structural functionality and recovery patterns after hazard occurrence, is another performance indicator investigated herein. Furthermore, the effects of climate change on the life-cycle performance are also considered in the performance assessment and prediction module. The uncertainties associated with deterioration scenarios, structural vulnerability, and consequence evaluation are incorporated within this module.

The following module, Module 4, within the life-cycle management framework is risk and sustainability-informed optimization and decision making process. In this module, multiple goals are considered simultaneously in the optimization process to seek the optimal management strategy. For example, the objective could be minimization of the total life-cycle maintenance cost considering inspection and repair costs, and maximization of structural performance level considering sustainability and resilience. Genetic algorithms are adopted to obtain the optimal solutions providing information concerning the optimal sequence and timing of structural inspection and repair planning. In this study, decision making associated with risk and sustainability-informed optimal pre-earthquake seismic retrofit plan of bridge networks and optimal ship maintenance strategies under corrosion and fatigue is investigated.

Finally, the last module is integration of updating into decision making process. The inspection information is adopted to improve the assessment and prediction of structural performance using Bayesian techniques. Approaches for updating inspected and uninspected details at component and system levels are developed. Subsequently, updated

maintenance plans could be obtained to yield more accurate prediction and management module. The integration of updating within the management and decision making framework can reduce the uncertainties associated with the prediction process. Overall, the proposed methodology can be used in assisting decision making regarding maintenance activities to improve the performance of structural systems in a life-cycle context.

The entire study is developed by using self-developed, commercial and freeware programs, including (a) MATLAB (The MathWorks 2014) codes for managing the necessary calculation and connecting other software, (b) Finite Element (FE) software for the structural performance analyses, such as SAP2000 (CSI 2009) and OpenSees (OpenSees 2011), (c) the reliability programs RELSYS (Estes and Frangopol 1998) for component and system reliability analyses, and (d) the program PDSTRIP (2006) which is a hydrodynamic software for seakeeping analysis.

1.4. OUTLINE

This study is divided into two parts. Part I focuses on civil infrastructure systems, including highway bridges, buildings, bridge networks, and interdependent structural systems. Part II emphasizes aging ship structures. Part I develops a probabilistic approach for life-cycle assessment and management of civil infrastructure systems under structural deteriorations and extreme events considering risk, sustainability, and resilience. Part II proposes a framework for risk-informed life-cycle assessment, maintenance, and updating of ship structures under collision, corrosion, and fatigue. Specifically, the study is organized as follows:

- **Chapter 1** serves as introduction.

Part I – Life-Cycle Assessment and Management of Civil Infrastructure Systems Incorporating Risk, Resilience, and Sustainability

- **Chapter 2** presents a framework for assessing time-variant sustainability of bridges subjected to multiple hazards incorporation structural deterioration. The approach accounts for the effects of flood-induced scour on seismic vulnerability. Sustainability is quantified in terms of social, environmental, and economic metrics. The effects of corrosion on reinforcement bars and concrete cover spalling are accounted for. The seismic fragility curves at different points in time are obtained through non-linear finite element analyses. The variation of sustainability metrics is presented.
- **Chapter 3** proposes an approach for probabilistic seismic performance assessment of highway bridges subjected to mainshock and aftershocks. The seismic ground motion intensity, seismic vulnerability, and consequences evaluation under mainshock and aftershock sequences are considered along with their associated uncertainties. The probabilistic recovery functions associated with different damage states are integrated within the proposed functionality and resilience assessment procedure. The probabilistic direct loss, indirect loss, and resilience of bridges under mainshock only and both mainshock and aftershock are investigated.
- **Chapter 4** presents a novel approach for probabilistic time-dependent multi-hazard life-cycle loss assessment considering climate change. Life-cycle loss and resilience of highway bridges under time-dependent hazards are investigated. The uncertainties

associated with hazard intensity and frequency, structural vulnerability, and consequence are incorporated within the framework. The hazards of earthquake and flood are investigated herein. Both the lateral and vertical failures of bridge under flood are investigated. Additionally, the life-cycle losses with and without aging effects and climate change are computed.

- **Chapter 5** proposes a methodology to evaluate the seismic sustainability and resilience of both conventional and base-isolated steel buildings. The proposed approach is used to explore the difference between the performance associated with these buildings by considering the three pillars of sustainability: economic, social, and environmental, and resilience, aiming to cover a comprehensive performance-based assessment context. The uncertainties associated with performance and consequence evaluation of structural and non-structural components are incorporated within this study.
- **Chapter 6** presents a framework for the time-variant seismic risk and sustainability assessment of highway bridge networks. The methodology considers the probability of occurrence of a set of seismic scenarios that reflect the seismic activity of the region. The sustainability and risk depend on the damage states of both the links and the bridges within the network. The time-variation of sustainability metrics of a highway bridge network under seismic hazard is identified.
- **Chapter 7** proposes a methodology for the healthcare - bridge network systems performance analysis considering spatial seismic hazard, vulnerability of bridges and links in the network, and damage condition of a hospital at component and system

levels. The system level performance is evaluated considering travel and waiting time based on the damage conditions of the components. The effects of correlation among the seismic intensities at different locations are investigated. Additionally, the correlations associated with damage indices of the investigated structures are also incorporated within the probabilistic assessment process. The conditional seismic performance of the hospital given the damage conditions of the bridge network and the effect of bridge retrofit actions are investigated.

- **Chapter 8** develops a probabilistic methodology to establish optimum pre-earthquake retrofit plans of bridge networks based on sustainability. A multi-criteria optimization problem is formulated to find the optimum timing of retrofit actions for bridges within a network. The sustainability of a bridge network and total retrofit cost are considered as conflicting criteria. The effects of the time horizon on the Pareto optimal solutions are also investigated.
- **Chapter 9** proposes an approach for the optimal bridge network retrofit planning based on cost-benefit evaluation and multi-attribute utility theory. The total benefit of a retrofit plan is quantified in terms of the reduction in the seismic loss during a given time interval using multi-attribute utility theory. Moreover, retrofit actions associated with varying improvement levels are considered.

Part II – Risk-Informed Life-Cycle Assessment, Maintenance, and Updating of Aging Ship Structures under Collision, Corrosion, and Fatigue

- **Chapter 10** proposes an approach to assess risk and sustainability of ship collision. The probability of ship collision is computed by taking into account traffic data and

operational conditions. Economic, social, and environmental metrics are evaluated and social and environmental metrics are converted into an economic metric considering their associated monetary values. Epistemic and aleatory uncertainties associated with damage conditions of ships and consequences are considered. Risk attitudes are incorporated within risk analysis by utilizing utility functions.

- **Chapter 11** develops a generalized decision making framework performing a variety of tasks, including, but not limited to quantifying the flexural and fatigue performance of ship structures and employing multi-attribute utility theory to evaluate ship mission performance. A structural reliability approach is utilized to compute the probability of failure considering the uncertainty in structural capacity and load effects. Expected repair cost, cumulative fatigue damage, total travel time, and carbon dioxide emissions associated with a ship routing are considered within the decision making process.
- **Chapter 12** develops a probabilistic approach to provide optimum inspection and repair plans for ship structures considering corrosion and fatigue. Risk is assessed by considering the losses associated with structural failure. A multi-objective optimization problem, which accounts for structural deterioration scenarios and various uncertainties, is formulated to find the optimum inspection and repair planning of aging ship structures. The life-cycle risk associated with flexural failure and expected total inspection and maintenance costs are considered as conflicting criteria.

- **Chapter 13** presents a framework for fatigue risk assessment and updating using inspection information. A quantitative risk assessment model using rating functions is utilized to identify inspection priority among multiple fatigue-sensitive details. Bayesian techniques are adopted for reliability and risk updating of both inspected and uninspected fatigue-sensitive details at component and system levels. Correlation of fatigue damage among different critical details is considered and incorporated within risk assessment and updating process.
- **Chapter 14** provides the conclusions drawn from this study and the suggestions for future work.

1.5. CONTRIBUTIONS

The main contributions of this study are: (i) proposing a novel assessment approach of structural systems subjected to structural deteriorations and extreme events incorporating risk, (ii) proposing a performance assessment methodology at a system level considering uncertainties and correlation effects, and (iii) developing a comprehensive management and decision making framework using cost-benefit analysis and multi-attribute utility theory.

The detailed contributions of this study are listed as:

1. Proposing a comprehensive assessment approach of deteriorating highway bridges under multiple hazards (e.g., earthquake, flood, and aging effects) considering risk. The uncertainties associated with hazard scenarios, structural vulnerability, and consequence are incorporated within the assessment procedure.

2. Developing a performance-based assessment approach of highway bridges under mianshock and aftershock sequences. The functionality, risk, and resilience with and without considering aftershocks are computed.
3. Proposing a comprehensive methodology for the probabilistic time-dependent multi-hazard life-cycle loss of highway bridges under flood and earthquake. The effects of climate change and time-dependent hazard model on the life-cycle loss are investigated.
4. Proposing a novel performance-based seismic assessment approach for buildings. The environmental impacts and resilience are investigated and compared between the conventional and base-isolated buildings.
5. Proposing a novel assessment approach of bridge networks and interdependent healthcare – bridge network systems considering the correlations and uncertainties involved in the evaluation process. The correlations associated with hazard intensities and damage indices among investigated structural components are considered.
6. Proposing an integrated approach for optimizing the timing and types of retrofit actions during the service life of a bridge network considering sustainability. The ultimate aim of this framework is to reduce the extent of earthquake damage to society, economy, and environment, while simultaneously minimizing the total retrofit costs of a bridge network.

7. Developing a probabilistic approach for ship collision risk and sustainability assessment considering economic, social, and environmental metrics. Risk attitudes are incorporated within risk analysis by utilizing utility function.
8. Developing a generalized decision making framework to quantify the flexural and fatigue performance of ship structures and employ multi-attribute utility theory to evaluate ship mission performance using Multi-Attribute Utility theory.
9. Proposing a risk-informed probabilistic approach to provide optimum inspection and repair plans for ship structures subjected to corrosion and fatigue. A multi-objective optimization problem, which accounts for structural deterioration scenarios and various uncertainties, is formulated to find the optimum inspection and repair planning of deteriorating ship structures.
10. Proposing an approach for system level risk assessment and updating using inspection information to reduce uncertainty. A quantitative risk assessment model using rating functions is proposed to identify inspection priority among multiple fatigue-sensitive details considering the correlation among critical details.

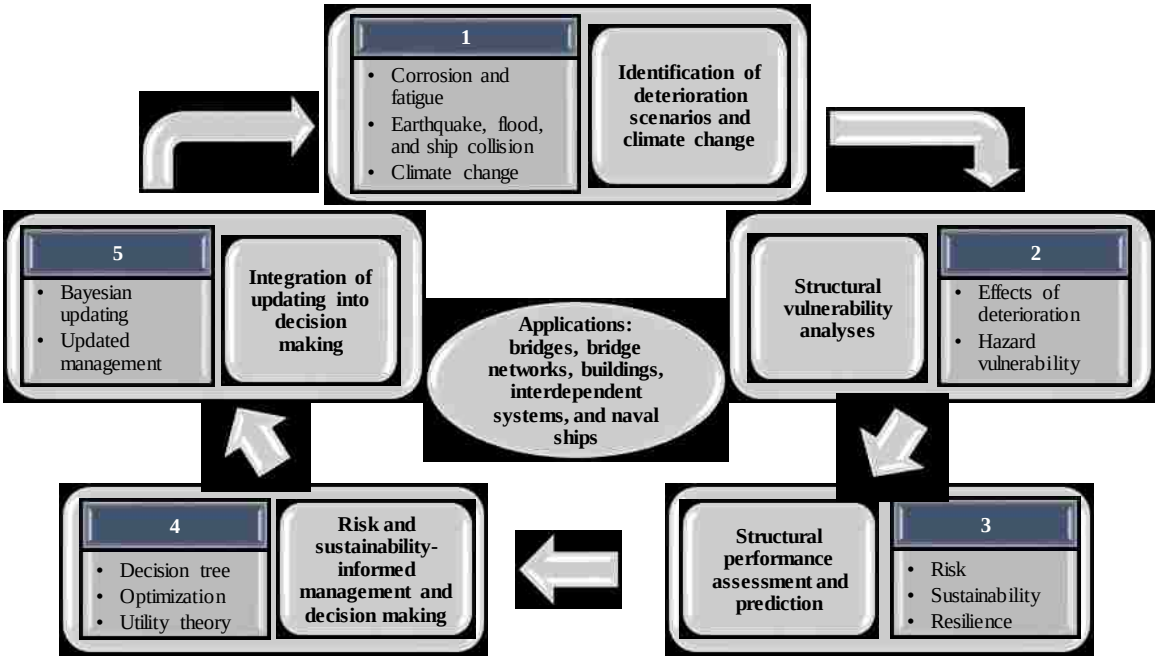

Figure 1.1 Framework for life-cycle management and decision making

PART I

LIFE-CYCLE ASSESSMENT AND MANAGEMENT OF CIVIL INFRASTRUCTURE SYSTEMS INCORPORATING RISK, RESILIENCE, AND SUSTAINABILITY

CHAPTER 2

TIME-VARIANT SUSTAINABILITY ASSESSMENT OF BRIDGES SUBJECTED TO MULTIPLE HAZARDS

2.1. INTRODUCTION

Civil infrastructure plays a vital role in the economy of a country. Structures are often subjected to abnormal events such as earthquakes and fires throughout their lifetime. The capacity of structural systems to resist these hazards is reduced in time by the effects of aging and deterioration. Maintaining structural safety at desired levels in a life-cycle context has been an area of interest for many researchers (Ang and De Leon 1997; Frangopol 2011). A wide range of performance measures is covered by "sustainability" to reflect these aspects. There is the need for well established methods for quantifying the metrics of sustainability. In general, sustainability can be defined as the "development that meets the needs of the present generations without compromising the ability of future generations to meet their own needs" (Adams 2006). Sustainability has been quantified in terms of social, environmental, and economic metrics in recent studies (Spencer *et al.* 2012). In fact, these metrics are measures of the costs and losses associated with different hazards. However, quantifying the three metrics of sustainability associated with different hazards at system level considering the time effects is a challenging task.

The majority of the past studies on loss assessment of structures focus on single hazard without considering the time-variant effects (Stein *et al.* 1999; Ang and De Leon 2005). However, the effects of any other hazard, such as flood-induced scour, can

increase the vulnerability of a structure associated with seismic hazard. For instance, the flood-induced scour can cause loss of lateral support at bridge foundations and thus amplify the effect of seismic hazard (Banerjee and Prasad 2012). There is the need for a framework for accurate seismic loss assessment of bridges considering also the effects of other hazards.

Concrete bridges are subjected to harsh environmental conditions through their lifetime. Corrosion in reinforced concrete (RC) members is initiated when chloride ions penetrate the concrete cover and react with the reinforcing steel. The corrosion induced deterioration can affect the seismic response of bridges and reveal a significant increase in seismic vulnerability over time (Ghosh and Padgett 2010; Akiyama *et al.* 2011). Corrosion causes tensile stresses in concrete, which leads to concrete spalling (Vu and Stewart 2000). Simon *et al.* (2010) showed that the spalling of concrete cover has impacts on the seismic vulnerability of bridges.

In this chapter, a framework for assessing the time-variant sustainability of bridges under seismic hazard considering the effects of deterioration is presented. The approach accounts for the effects of flood-induced scour on seismic fragility. Sustainability is quantified in terms of its social, environmental, and economic metrics. These include the expected downtime and number of fatalities, expected energy waste and carbon dioxide emissions, and the expected loss. However, the effects of other hazards can be incorporated in the framework. The seismic fragility curves are obtained based on non-linear finite element analysis of the structure. The assessment of costs and losses associated with seismic hazard is based on a set of damage states which are mutually

exclusive and collectively exhaustive. The proposed approach is illustrated on a single-bent RC bridge. The effects of flood-induced scour on both seismic fragility and sustainability are also investigated. This chapter is based on a published paper Dong *et al.* (2013).

2.2. METHODOLOGY OF ASSESSING SUSTAINABILITY

The first step of the methodology for assessing sustainability consists of identifying vulnerable components of the structure to seismic hazard. A flow chart summarizing the methodology is presented in Figure 2.1. An FE model able to capture the non-linear behavior of these components is used to assess the fragility. The set of ground motions to be used in the fragility analysis should be identified. The seismic fragility curves can be obtained by performing demand-capacity evaluation through non-linear time history analyses (THA) of the FE model under the selected ground motion intensity. For a desired intensity of earthquake, the probabilities of a structure being in various damage states following the earthquake can be determined using the fragility curves. In order to include the effects of other hazards on seismic fragility, the procedure described should be repeated by updating the FE model. In this way, the effects of any other hazards can be accounted for. For instance, the level of springs used to model the interaction between the pile and the soil should be updated to account for the effects of flood-induced scour. Each damage state may have different outcomes. For instance, the downtime for a bridge in severe damage state is much longer than that of the same bridge in slight damage state. The social outcomes (downtime and fatalities), the environmental outcomes (energy waste and carbon dioxide emissions), and the economic outcomes (costs) associated with

each damage state should be evaluated. Then, the expected metrics of sustainability associated with each damage state can be quantified by multiplying these outcomes by the probability of each damage state. The total value of a metric is the sum over all damage states as the damage states form a set of mutually exclusive and collectively exhaustive events. To clarify this issue, the quantification of total loss based on the damage state is illustrated in Figure 2.2. In order to include the time effects (i.e., the effects of deterioration), the described procedure should be repeated for each time instant, including updating the FE model.

2.3. MODELING TIME EFFECTS

2.3.1. Bridge deterioration modeling

The performance of highway bridges under environmental stressors degrades with time. The seismic performance of bridges may be highly influenced by the structural deterioration. In this section, brief information on the corrosion and spalling models for RC structures and the use of finite element (FE) method for performance assessment of bridges is presented.

Corrosion of reinforcing steel initiates with the ingression of chloride ions from the concrete surface through the concrete cover to the reinforcing steel. The effective cross-sectional area of the reinforcing bar decreases and this causes additional tensile stresses in the concrete. A corrosion model uniform along the length and the depth of the bar is used in the illustrative example for the clarity of presentation. The effects of localized pitting corrosion are not accounted for. The rate of corrosion is considered constant after the corrosion initiation. Uncertainty in the corrosion rate is included. This model had

been used in a number of previous studies (Vu and Stewart 2000; Simon *et al.* 2010). The time-variant cross section area of the reinforcement bar subjected to corrosion can be expressed as (Thoft-Christensen *et al.* 1997)

$$A(t) = \begin{cases} D_i^2 \dfrac{\pi}{4} & for \quad t \le T_i \\ [D(t)]^2 \dfrac{\pi}{4} & for \quad T_i < t < T_i + D_i / r_{coor} \\ 0 & for \quad t \ge T_i + D_i / r_{coor} \end{cases} \tag{2.1}$$

where D_i is the initial diameter of steel reinforcement; r_{corr} is the corrosion rate; and $D(t)$ is reinforcement diameter at the $(t - T_i)$ years, which can be represented as

$$D(t) = D_i - r_{corr}(t - T_i) \tag{2.2}$$

where T_i is time to corrosion initiation.

The corrosion rate can be represented in terms of the water-cement ratio and the concrete cover as (Vu and Stewart 2000)

$$r_{corr} = \frac{0.438(1 - w/c)^{-1.64}}{C}(mm/year) \tag{2.3}$$

The water-cement ratio is expressed using the Bolomey's formula:

$$w/c = \frac{27}{f_{cy}^{'} + 13.5} \tag{2.4}$$

where $f_{cy}^{'}$ is the concrete compressive strength in MPa; *w/c* is the water-cement ratio; and *C* is the concrete cover (*mm*).

2.3.2. Spalling of concrete cover

Simon *et al.* (2010) showed that spalling of the concrete cover of the bridge column has significant influence on the seismic fragility of the bridge. The occurrence of the spalling

of the concrete cover is induced by the tensile stress in the concrete due to the corrosion of the reinforcing bar. According to Val and Stewart (2003) the spalling of concrete cover occurs at approximately $10T_{cr1}$ from the corrosion initiation for uniform corrosion rates. The time-dependent probability of spalling can be calculated as

$$P_{sp}(t) = P(T_i + T_{cr} \le t) = P(T_i + 10T_{cr1} \le t) \tag{2.5}$$

where T_{cr1} is the time from corrosion initiation to corrosion cracking (Maaddawy and Soudki 2007).

2.3.3. Finite element model

A three-dimensional (3-D) finite element model can be established using the SAP 2000 (Computers and Structures Inc. 2010) which includes special types of elements, such as elements with fiber sections, for modeling the desired components of the bridge, which are expected to deform in the non-linear range. The interaction between the pile and the soil can be modeled using springs. According to Ghosh and Padgett (2010), effect the corrosion of the superstructure on the seismic performance of the bridge can be neglected. The deterioration of the reinforcement and spalling of the concrete cover in the column should be updated in the finite-element model at each time step in order to account for the time effects in the fragility analysis. The time-dependent increase in concrete strength due to the continuous hydration can be accounted by updating the resistance model at each time step.

2.4. SEISMIC FRAGILITY ANALYSIS

The seismic vulnerability of bridges, commonly expressed in the form of fragility curves, is a key component for the seismic loss assessment. Due to the fact that the structural performance deteriorates with time, the fragility curves should be updated during the lifetime of the structure.

2.4.1. Generating seismic fragility curves

In this chapter, the fragility curves are based on the non-linear THA. These curves can be used to predict the conditional probability of the seismic demand exceeding the seismic capacity at different damage states under certain ground motion intensity parameter. Due to the effects of aging and deterioration on the seismic vulnerability, the fragility curves should be updated during the lifetime. The FE analysis is used to obtain the maximum displacement under a ground motion record. Based on the fragility curves and consequences of various damage states, it is possible to evaluate the loss for a certain damage state given a seismic event. Shome *et al.* (1998) stated that a particular number of ground motions is sufficient for the accuracy of fragility analyses under certain criteria associated with different faults. Kim and Shinozuka (2004) showed that the seismic vulnerability of only the columns of a bridge is adequate for seismic fragility analysis. Aviram *et al.* (2008) presented a collection of recommendations for the seismic vulnerability analysis of highway bridges using finite element software. Five different damage states of the seismic damage for a bridge are defined based on the ductility demand of the columns. The damage states and the corresponding ductility demands and downtime associated with the damage states are presented in Table 2.1.

The probability that seismic demand exceeds the capacity for a given *PGA* is

$$p_f = P(\frac{C_S}{D_S} \le 1 | PGA) \tag{2.6}$$

where C_S is the bridge seismic capacity and D_S is the seismic demand. The demand can be based on the displacement ductility of the column. Choe *et al.* (2008) showed that the deformation failure model dominates the vulnerability analysis, so the shear failure model is not considered here. The displacement of the column in longitudinal and transversal directions can be obtained based on FE analysis. The displacement ductility can be computed using the displacement of the column at the top point. The ductility of the column is the ratio of the peak displacement of the top of the column to the displacement at the same location when the first yield of the reinforcement occurs. The probabilistic characteristics of the demand can be represented by a lognormal distribution (Cornell *et al.* 2002)

$$D_S = \ln(S_d, \beta_d) \tag{2.7}$$

where S_d and β_d are the median value and the standard deviation of the demand of displacement ductility, respectively.

The reduced rebar cross-sectional area and concrete cover spalling can make the structure more vulnerable to the seismic hazard. Harvat (2009) studied the effect of corrosion and concrete cover spalling without considering the time-variant deterioration effects. The time-variation of the fragility curve parameters due to corrosion and concrete cover spalling can be expressed as a function of time. Using curve fitting techniques, a quadratic model of the parameters with respect to fragility curve can be obtained. The

time-variant median value of seismic demand can be obtained from the regression analysis (Hwang *et al.* 2001)

$$\ln(S_d(t)) = a(t) + b(t) \cdot \ln(PGA) \tag{2.8}$$

where $a(t)$ and $b(t)$ are the time-variant regression coefficients. The time-variant fragility curves for specific ground acceleration can be expressed as (Hwang *et al.* 2001)

$$P\left[DS \geq DS_i \middle| PGA\right](t) = \Phi\left[\frac{-\ln(S_c(t)/S_d(t))}{[(\beta_c(t))^2 + (\beta_d(t))^2]^{0.5}}\right] \tag{2.9}$$

where DS_i is a damage state of the bridge; $\beta_d(t)$ and $\beta_c(t)$ are the lognormal standard deviations of the demand and capacity, respectively; and $\Phi(.)$ is the standard normal cumulative distribution function.

2.4.2. Effects of flood-induced scour

Flood-induced scour can reduce lateral support of a bridge at foundation and has a major effect on the seismic vulnerability of a bridge. The local scour can induce the erosion of the soil around the column and reduce the capacity of the foundation. Although the joint probability of occurrence of multiple hazards is small, past experience shows that successive occurrences of extreme events happen. Hence, it is required to consider the effects of flood-induced scour in the seismic loss assessment, especially for the bridges located at the seismically flood-prone zone. The depth of the flood-induced scour can be determined based on the HEC-18 guide (Richardson and Davis 2001). The effect of the flood-induced scour in the FE model can be accounted for by eliminating the springs in the region affected by scour. Banerjee and Prasad (2012) stated that the effects of flood-induced scour do not worsen significantly beyond 3 m of scour depth.

2.5. TIME-VARIANT SUSTAINABILITY ANALYSIS

The topic of sustainability in structures has become an important research area. Sustainability can be quantified in terms of social, environmental, and economic metrics. In this section, evaluation of the consequences associated with various seismic damage states is presented.

2.5.1. Social metrics

Following an extreme event, a bridge can be closed for traffic resulting in detour and downtime in the transportation network. In this chapter, the expected downtime and the expected number of fatalities are considered as the social metrics of sustainability. The expected downtime for a bridge due to hazards effects can be expressed as (Padgett *et al.* 2009)

$$DT(t) = \sum_{i=1}^{4} P_{DS_i|PGA}(t) \cdot d_i \tag{2.10}$$

where i indicates the damage state; $P_{DSi|PGA}(t)$ is the conditional probability of the structure being in damage state i after an earthquake with certain PGA at a given year t; d_i is the downtime associated with the damage state i.

The estimated expected average number of fatalities following a seismic hazard occurred at a certain time can be expressed as

$$FA(t) = \sum_{i=1}^{4} P_{DS_i|PGA}(t) \cdot FT_i \tag{2.11}$$

where FT_i is average number of fatalities associated with the damage state i. A statistical analysis is required to evaluate the number of fatalities after a hazard.

2.5.2. *Environmental metrics*

The total embodied energy within a structure depends on the material and geometry of the structure. The carbon dioxide is the primary greenhouse gas emitted through human activities. The energy waste and carbon dioxide emissions due to downtime are other factors contributing to environmental metric, as follows

$$EN(t) = \sum_{i=1}^{4} P_{DS_i|PGA}(t) \cdot ADTD_i \cdot D_l \cdot d_i \cdot \left[Enp_{car} \cdot (1 - \frac{T}{100}) + Enp_{Truck} \cdot \frac{T}{100} \right] \quad (2.12)$$

where Enp_{car} *and* Enp_{Truck} are the environmental metric per unit distance for cars and trucks, respectively (e.g., carbon dioxide kg/km); D_l is the length of the detour (km); *ADTD* is the average daily detour traffic; d_i is the duration of the detour (days); and T represents the average daily truck traffic ratio. The expected energy waste and carbon dioxide emissions due to the repair associated with each damage state are taken as a fraction of the value for the entire structure based on the damage ratio for respective damage state. The energy waste is measured in terms of MJ/m^3 and the carbon dioxide emission is measured in terms of kg/m^3.

2.5.3. *Economic metrics*

The economic consequences are evaluated in terms of monetary values. The forecast of future value must consider the dependency of future monetary losses on the present value of consequences. Starting from the year of construction, the value of consequences for each specific year t can be calculated as follows

$$PV = FV(t) \frac{1}{(1+r)^t} \quad (2.13)$$

where $FV(t)$ is the future monetary value referred to year t; PV is the present monetary value; and r represents the annual discount rate of money.

The repair cost associated with a certain damage state can be considered proportional to the rebuilding cost of the bridge (Mander 1999; Stein *et al.* 1999) and expressed as

$$C_{REP,i} = RCR_i \cdot c_{REB} \cdot W \cdot L \tag{2.14}$$

where RCR_i is the modified repair cost ratio for a bridge at damage state i; c_{REB} is the rebuilding cost per square meter (USD/m^2); W is the bridge width (m); and L represents the bridge length (m).

In the case of bridge closure, the users are forced to follow the detour. The running costs associated with a certain damage state can be expressed as (Stein *et al.* 1999)

$$C_{Run,i} = \left[c_{Run,car}(1 - \frac{T}{100}) + c_{Run,truck} \frac{T}{100} \right] D_l ADTD_i \cdot d_i \tag{2.15}$$

where $c_{Run,car}$ and $c_{Run,truck}$ are the average costs for running cars and trucks per unit length (USD/km), respectively. $ADTD$ is related to the functionality level of a bridge under given seismic hazard.

The monetary value of the time loss for users and goods traveling through the detour at a given damage state can be expressed as (Stein *et al.* 1999)

$$C_{TL,i} = \left[c_{AW} o_{car}(1 - \frac{T}{100}) + (c_{ATC} o_{truck} + c_{goods}) \frac{T}{100} \right] \cdot \left[\frac{D_l \cdot ADTD_i \cdot d_i}{S} + ADTE(\frac{l}{S_d} - \frac{l}{S_0}) \right] \tag{2.16}$$

where c_{AW} is the average wage per hour (USD/h); c_{ATC} is the average total compensation per hour (USD/h); c_{goods} is the time value of the goods transported in a cargo (USD/h); $ADTE$ is the average daily traffic remaining on the damaged link; o_{car} and o_{truck} are the average vehicle occupancies for cars and trucks, respectively; S_0 and S_D represents the

average speed on the intact link and damaged link (km/h), respectively; and *S* represents the average detour speed (km/h).

The life loss cost depends on the number of casualties associated with a certain damage state and can be expressed as (Rackwitz 2002)

$$C_{SL,i} = FT_i \cdot ICAFB \tag{2.17}$$

where *ICAFB* is implied cost of averting a fatality for bridge engineering.

The total economic loss, which is the sum of costs weighted with the probability of having this cost, consists of repair loss, running loss of the detouring vehicles, time loss due to the unavailability of the highway segment and life loss. The total economic loss can be expressed as

$$L_{ENC}(t) = \sum_{i=1}^{4} P_{DS_i|PGA}(t) \cdot (C_{REP,i} + C_{Run,i} + C_{TL,i} + C_{SL,i}) \tag{2.18}$$

where the expected losses associated with different damage states are summed over the number of damage states.

2.6. ILLUSTRATIVE EXAMPLE

The presented framework for quantifying the metrics of sustainability is applied to a bridge (Mackie and Stojadinovic 2001) designed based on Caltrans' Bridge Design Specification and Seismic Design Criteria (Caltrans 2006). The bridge is a typical single bent and two-span RC bridge as shown in Figure 2.3(a). The bridge has two lanes of traffic in each direction. In this case study, it is assumed that the bridge was built 30 years ago and the service life is 75 years. As shown in Figure 2.3 (b), an FE model is built as described previously. The seismic fragility curves of the bridge are obtained also

accounting for the effects of scour and deterioration. In this chapter, the expected metrics of sustainability are quantified based on the various seismic damage states, which are mutually exclusive and collectively exhaustive, after a certain level of ground excitation.

2.6.1. Time-variant fragility analysis

A 3-*D* finite-element model of the bridge is built using SAP2000 (Computers and Structures Inc. 2010). The top regions of the columns, where plastic hinges occur under seismic loads, are modeled using fiber elements capturing the non-linear behavior. The seismic performance of the bridge is evaluated based on 20 ground motions assuming columns as vulnerable members. The objective of this chapter is to propose a framework for sustainability assessment of bridges under seismic hazard and more ground motions should be used for better accuracy. The ground motion records used in the illustrative example are obtained based on Coyote Lake (1979), Park Field (1966), Livermore (1980), Morgan Hill (1984), Loma Prieta (1989), Kobe (1995), Tottori (2000), and Erzincan (1992) earthquakes (Aviram *et al.* 2008). Non-linear THAs were performed using the ground accelerations scaled with a uniform scale factor of 2.0 to guarantee the development of response in nonlinear range within the bridge columns. The confined concrete model proposed by Mander (1998) is used to capture the material behavior of concrete columns. Geometric nonlinearity was also considered in the analyses. The superstructure is assumed to remain in the elastic range under seismic loading. Nonlinear springs are used to represent the interaction between soil and the piles along the length of the pile.

The uniform corrosion model is used in this example; however, any corrosion model can be incorporated in the framework. The effects of deterioration in time are accounted in the FE model based on Eqs. (2.1) to (2.4). The corrosion parameters that were used in the FE model are generated based on Latin Hypercube Sampling (McKay *et al.*1979), with 10,000 samples, using the values of probabilistic parameters given in Table 2.2. The mean value of the cross-sectional area of the reinforcing steel is used in the FE model. The effects of spalling are accounted in the FE model by removing the concrete cover along the length of the column (Simon *et al.* 2010). The probability of spalling is evaluated using Eq. (2.5). The probability of cover spalling through the lifetime is presented in Figure 2.4. This figure indicates that the probability of the concrete cover spalling increases significantly through the end of lifetime. For instance, the probability of concrete cover spalling is about 69% at 60 years. In order to consider the expected effects of spalling, the column top displacement values weighted with the probability of spalling are used.

In this chapter, the procedure used to develop the probabilistic demand models are based on the relationship between the maximum lateral drift from non-linear THA and *PGA* of earthquakes. The time-variant fragility curves are computed based on the seismic displacement demand obtained from FE analyses and Eqs. (2.8) and (2.9). Figure 2.5 and Figure 2.6 present the seismic fragility curves for various time instants with and without the effects of flood-induced scour, respectively. In these figures, each curve represents the probability of exceeding a damage state with respect to *PGA*. In these figures, the increasing probability of damage states with time is due to the effects of corrosion of the

longitudinal reinforcement of the columns and the spalling of concrete cover. In Figure 2.5, the conditional probability of exceeding moderate damage state under $PGA = 0.5g$ is about 0.37 initially; however this value reaches 0.48 at t = 40 years. The seismic vulnerability of the bridge is affected significantly by the flood-induced scour. The depth of flood-induced scour is treated as deterministic in the illustrative example. The effect of flood-induced scour on the seismic vulnerability is investigated during the lifetime of the bridge as shown in Figure 2.6.

2.6.2. Metrics of sustainability

As indicated previously, the time-variant sustainability of the bridge is evaluated in terms of social, environmental, and economic metrics. The social and environmental metrics can be converted into economic metrics if it is possible to evaluate the monetary value of the consequences of these metrics. In this chapter, the social metrics are related to the economic metric by considering also the costs. The energy consumption aspect associated with the environmental metrics is also included within the total economic metric by considering the cost of extra running of vehicles. However, it is challenging to evaluate monetary value of carbon dioxide emissions due to the lack of data and knowledge, and it is out of the scope of this chapter.

The social metrics quantified are expected downtime and expected number of fatalities. They are computed according to Eqs. (2.10) and (2.11), respectively. The downtime values associated with each damage state are given in Table 2.1. In this case study, the mean estimated number of fatalities per collapse due seismic hazard is considered as 4.154 (Dennemann 2009). The time-variation of expected downtime and

expected number of fatalities is illustrated in Figure 2.7 (a) and (b), respectively. The difference between these metrics for the cases with and without scour increases in time. The environmental metrics quantified are expected energy waste and expected carbon dioxide emissions and computed according to Eq. (2.12). The values of the variables used in Eq. (2.12) are presented in Table 2.3. The time-variation of expected energy waste and expected carbon dioxide emissions is illustrated in Figure 2.7 (c) and (d), respectively. Similarly, the difference between these metrics for the cases with and without scour increases in time.

The consequences associated with damage states are computed according to Eqs. (2.14) to (2.17). The values of the variables used in these equations are presented in Table 2.3. An annual discount ratio r = 2% is used in the calculations. The expected value of total losses, as the economic metric of sustainability, is computed according to Eq. (2.18). The total economic loss associated with a damage state is the sum of consequences weighted with the probability of having this consequence. The probability of being in a certain damage state following an earthquake is computed as the difference between the fragility curves (cumulative probability of exceeding certain damage state) of consecutive damage states.

The time-variation of the expected value of total loss for five different *PGA* levels, $PGA = 0.2g$, $PGA = 0.4g$, $PGA = 0.6g$, $PGA = 0.8g$ and $PGA = 1.0g$, for the cases with and without flood-induced scour is presented in Figure 2.8. In these figures, the time-variant values on the each curve indicate the expected loss given that an earthquake with a certain *PGA* occurred at a time instant. The expected loss reaches the maximum value

at the end of the investigated time span as no rehabilitation and retrofit actions are applied. The expected losses associated with higher *PGA* levels are higher and the differences increase dramatically in time. The expected losses associated with higher *PGA* levels are higher and the differences increase dramatically in time. For instance in Figure 2.8 (a), at t = 50 years, the expected loss is $\$5.28\times10^6$ for the $PGA = 0.4g$ and is $\$1.78\times10^7$ for $PGA = 0.8g$. It is worthy to note that this illustration is made for a scenario where the bridge suffers the effects of flood-induced scour occurred prior to the earthquake.

In order to illustrate the variation in the loss, uncertainty in the parameters regarding consequences are incorporated in the methodology. The probabilistic parameters used for the random variables associated with the consequences are presented Table 2.3. Figure 2.9 (a) and (b) represent the variation of the economic losses at t = 40 years and at the end of investigated horizon (t = 75 years). The coefficient of variation of the economic loss increases with time due to the increased uncertainties.

The expected loss highly depends on the outage duration (d_i) after a hazard as the consequences of outage are very large. To illustrate the effect of the outage duration (d_i) associated with various damage states, the loss analysis described is performed for different values of d_i. The comparison of expected economic loss for $0.5d_i$, d_i, and $1.5d_i$ is provided in Figure 2.10. The difference between the curves increases significantly with time.

The proposed framework (i.e., information on time-variant sustainability metrics) can be used as an intuitive tool for decision making. Furthermore, based on the

framework presented in this chapter, the selection of design alternatives, and the type and schedule of maintenance actions can be formulated as a multi-criteria optimization problem in a life-cycle context (Frangopl 2011) to help decision making.

2.7. CONCLUSIONS

This chapter presents a framework for assessing the time-variant sustainability of seismically vulnerable bridges under multiple hazards considering the effects of deterioration and aging. Sustainability is quantified in terms of its social, environmental, and economic metrics.

The following conclusions are drawn:

- Quantifying sustainability in terms of social, environmental, and economic metrics provides insight understanding of present and future risk associated with the failure of a structure following scenario hazards.
- The severity of seismic hazard has significant impacts on the metrics of sustainability. Therefore, the bridges in seismically active zones need additional attention in order to satisfy acceptable sustainability levels.
- As the deterioration can induce severe reduction in structural capacity, the sustainability of bridges located in regions prone to high-corrosion can be an issue compared to the bridges located in low-corrosion regions. Furthermore, the time elapsed since the bridge was built has an impact on the metrics of sustainability as the effects of the deterioration are increasing with time.

- In quantification of the sustainability metrics, the assumptions play a crucial importance on the accuracy of the results, especially in evaluating the consequences (i.e., monetary values). One important measure is the downtime of a bridge following an earthquake.

Table 2.1 Damage states and corresponding ductility demands and downtime

Damage State	Ductility Demand	Downtime
1. No Damage	[< 1] [a]	
2. Slight Damage	[1, 2.90] [a]	7 days [b]
3. Moderate	[2.90, 4.60] [a]	30 days [b]
4. Major Damage	[4.60, 5.0] [a]	120 days [b]
5. Complete	[> 5.0] [a]	400 days [b]

[a]: based on Banerjee and Prasad 2012; [b]: based on Padgett *et al.* 2009.

Table 2.2 Parameters of the random variables associated with corrosion of RC column.

Random variables	Mean	COV	Distribution
C_0 (surface *Cl* concentration)	3.78 kg/m^3 [a]	0.5	Lognormal
C_r (threshold *Cl* concentration)	1.4 kg/m^3 [a]	0.2	Normal
Diffusion coefficient	$3.5 \cdot 10^{-8}$ cm^2/s [a]	0.07	Normal
Cover depth	42 mm [b]	0.2	Lognormal
Reinforcement nominal yield	448 MPa [b]	0.15	Lognormal
Concrete compressive	34.5 MPa [b]	0.15	Lognormal

[a]: Vu (2003); [b]: Mackie and Stojadinovic (2001)

Table 2.3 Parameters of the random variables associated with the consequences.

Random variables	Mean	COV	Distribution type
ADT	Varies [a]	DNA	DNA
ADTT/ADT ratio	0.12 [a]	0.2	LN
Average compensation (truck drivers)	26.97 USD/h [a]	0.15	LN
Average detour speed	50 km/h [a]	0.15	LN
Average vehicle occupancies for cars	1.5 [a]	0.15	LN
Average wage (car drivers)	22.82 USD/h [a]	0.15	LN
Average vehicle occupancies for trucks	1.05 [a]	0.15	LN
Length of detour	2.9 km [a]	DNA	DNA
Rebuilding costs	1292 USD/m^2 [a]	0.2	LN
Running costs for cars	0.08 USD/km [a]	0.2	LN
Running costs for trucks	0.375 USD/km [a]	0.2	LN
Time value of a cargo	4 USD/h [a]	0.2	LN
Energy waste of cars	3.8 MJ/km [b]	0.2	LN
Energy waste of trucks	7.8 MJ/km [b]	0.2	LN
Cars carbon dioxide emissions	0.22 kg/km [b]	0.2	LN
Trucks carbon dioxide emissions	0.56 kg/km [b]	0.2	LN
Concrete embodied energy	2762 MJ/m^3 [c]	0.2	LN
Steel embodied energy	245757 MJ/m^3 [c]	0.2	LN
Concrete embodied carbon dioxide emissions	376 kg/m^3 [c]	0.2	LN
Steel embodied carbon dioxide emissions	9749 kg/m^3 [c]	0.2	LN

LN=lognormal distribution; COV=coefficient of variation; DNA=do not apply;
[a]: Decò A, Frangopol (2011); [b]: Gallivan *et al.* (2010); [c]: Tapia *et al.* (2011)

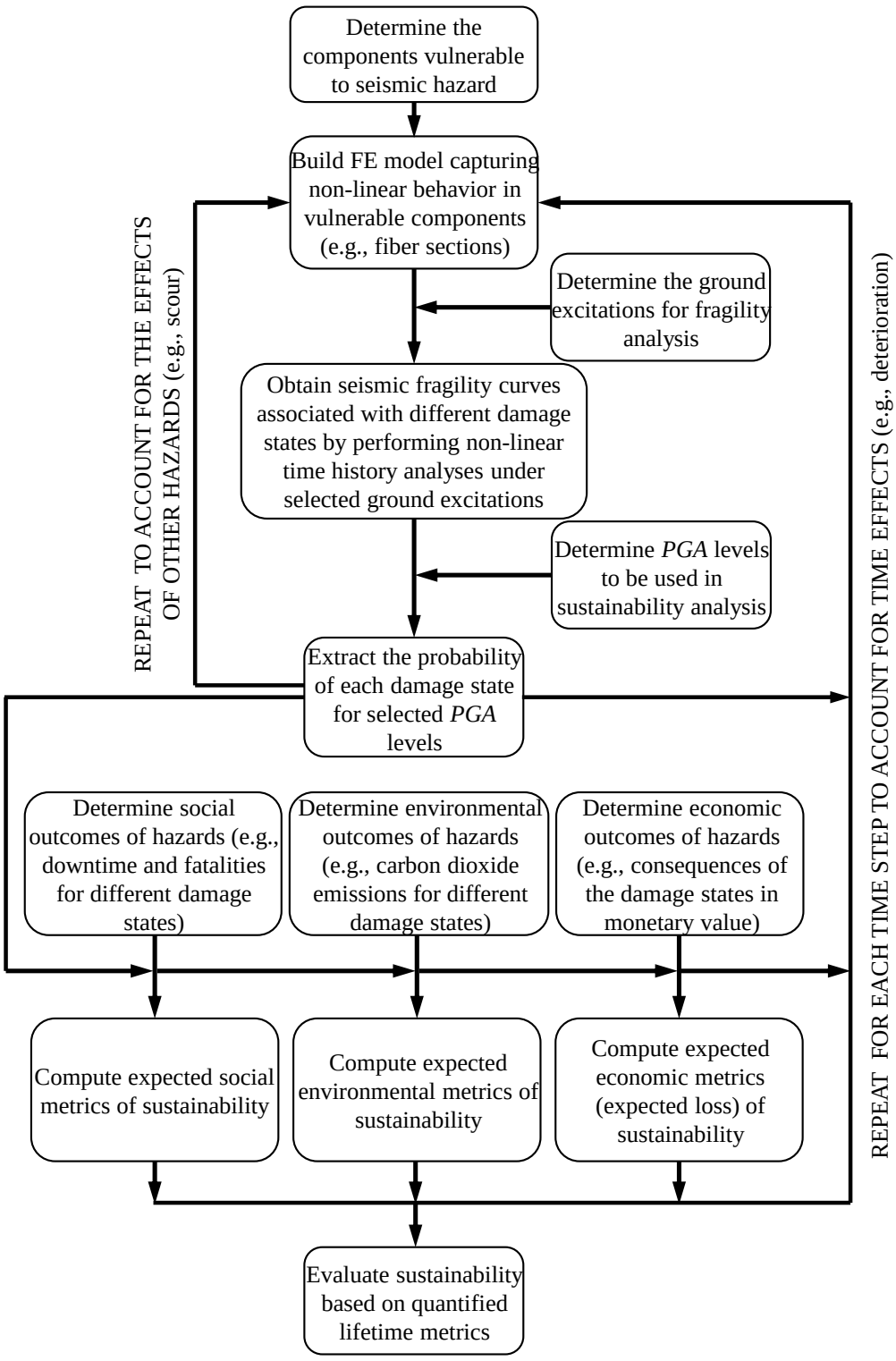

Figure 2.1 The methodology of assessing time-variant sustainability

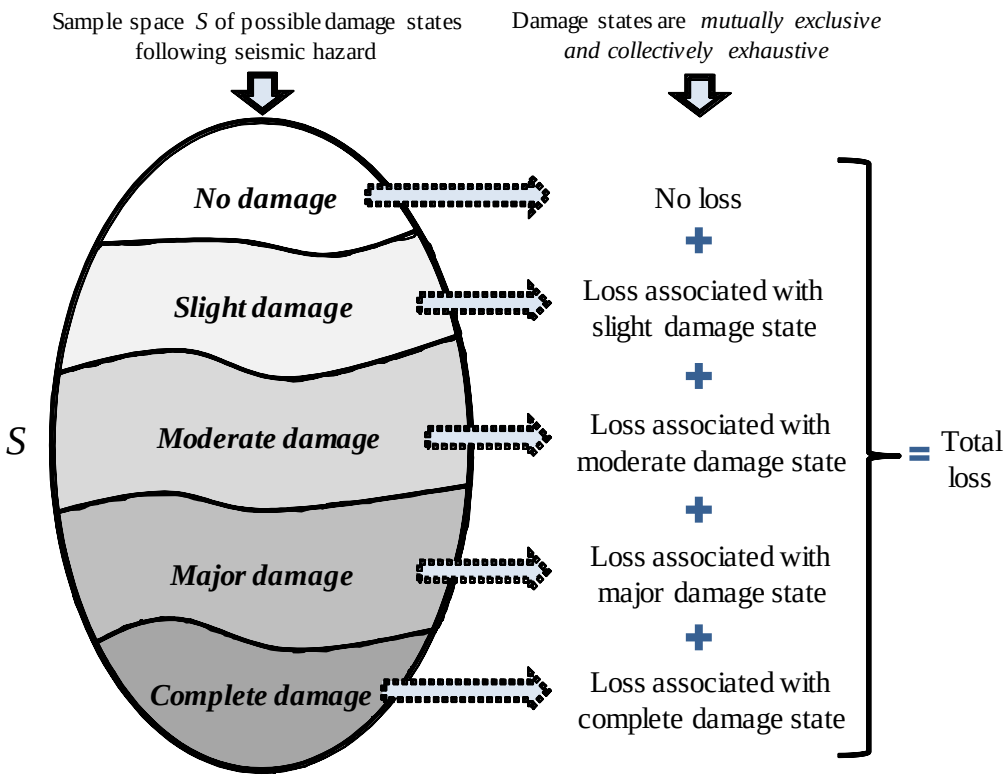

Figure 2.2 Quantification of metrics based on damage states

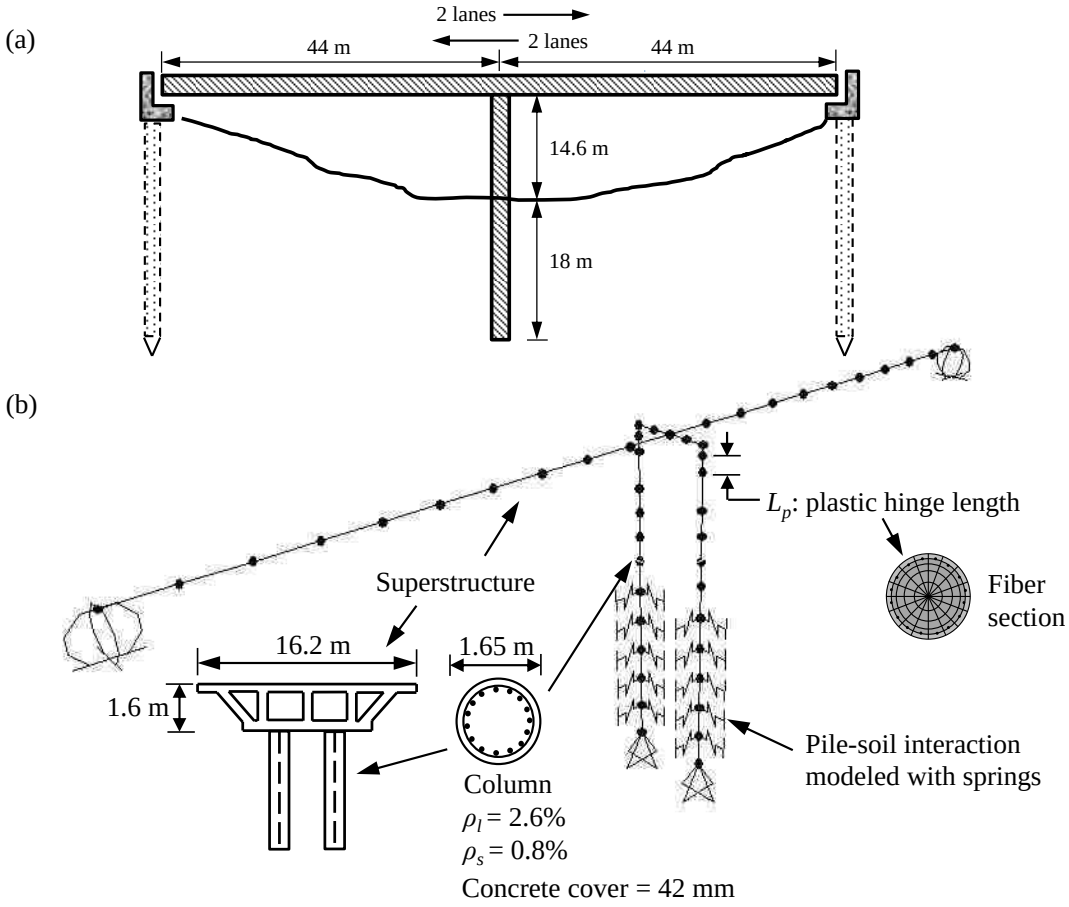

Figure 2.3 (a) Elevation view of the bridge (not to scale) in case study and (b) the three-dimensional finite element model of the bridge.

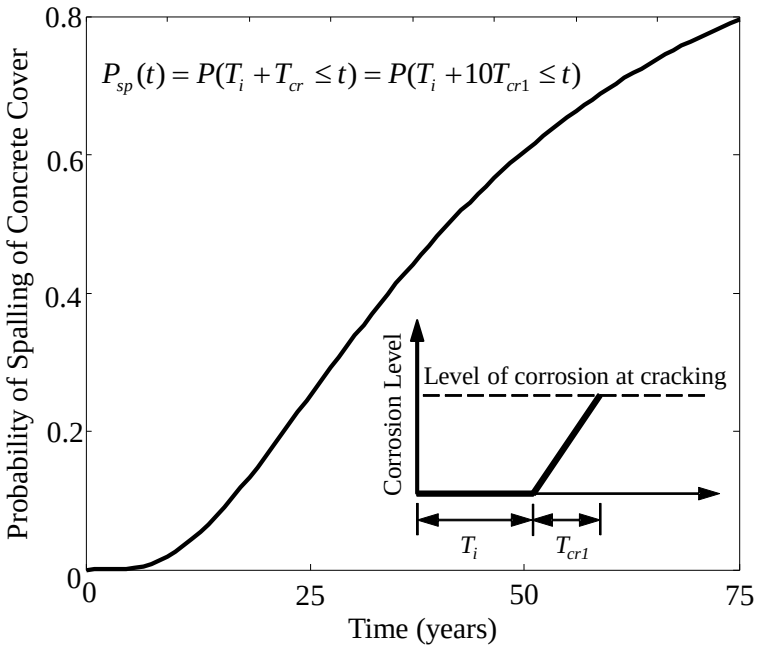

Figure 2.4 Time-variant probability of concrete cover spalling

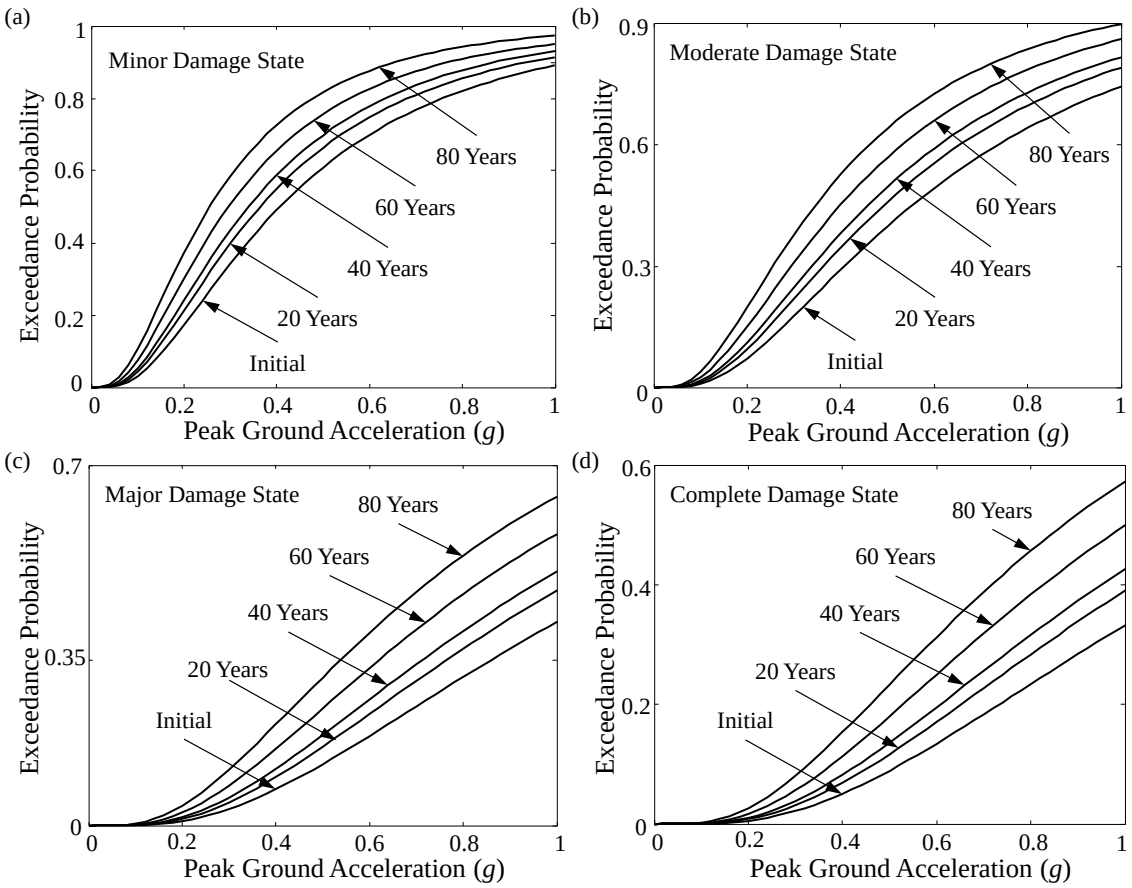

Figure 2.5 Seismic fragility curves of the bridge without flood-induced scour for (a) minor damage state, (b) moderate damage state, (c) major damage state, and (d) complete damage state.

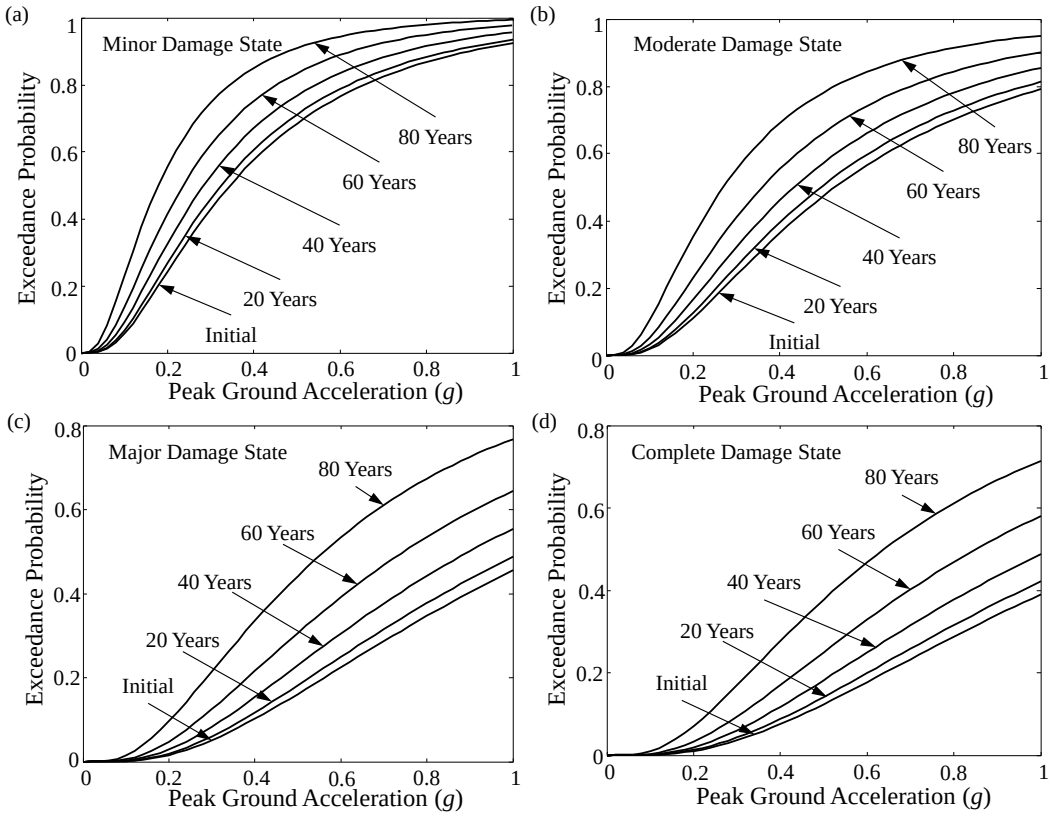

Figure 2.6 Seismic fragility curves of the bridge with flood-induced scour for (a) minor damage state, (b) moderate damage state, (c) major damage state, and (d) complete damage state.

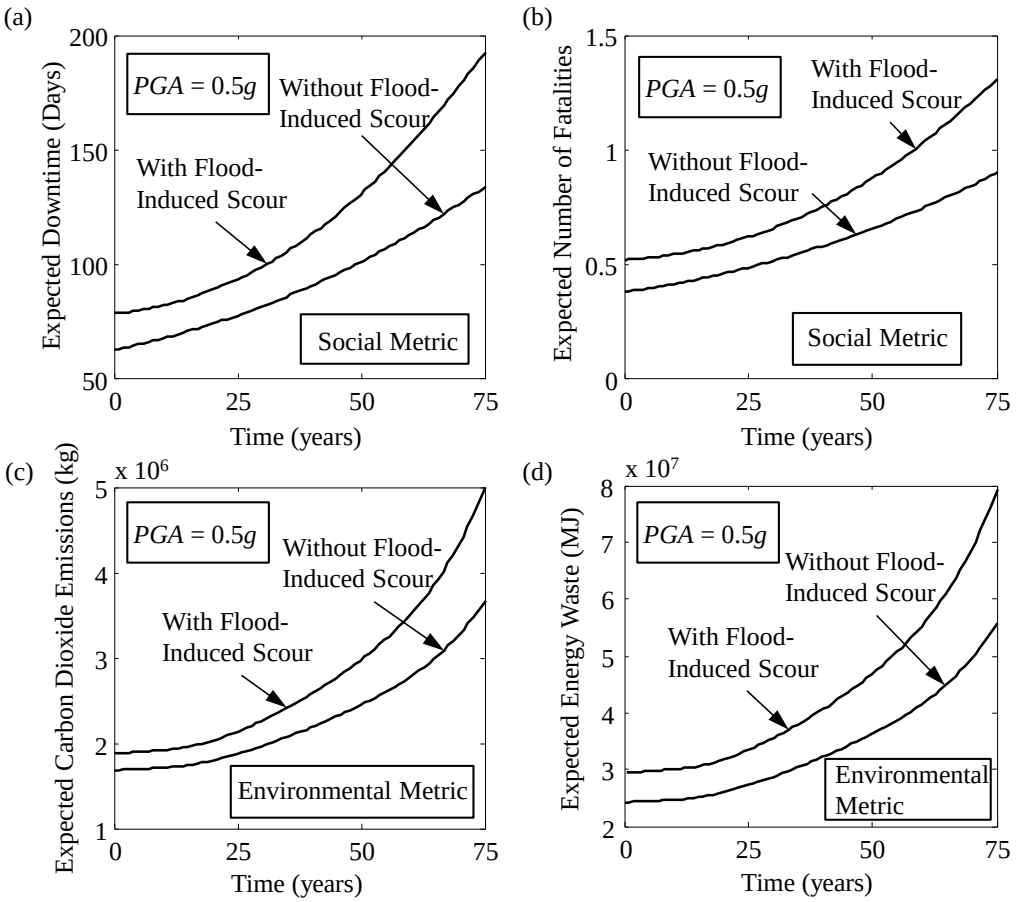

Figure 2.7 Time-variant of expected value of (a) downtime, (b) number of fatalities, (c) carbon dioxide emissions, and (d) energy waste, associated with PGA = 0.5g for the cases with and without scour.

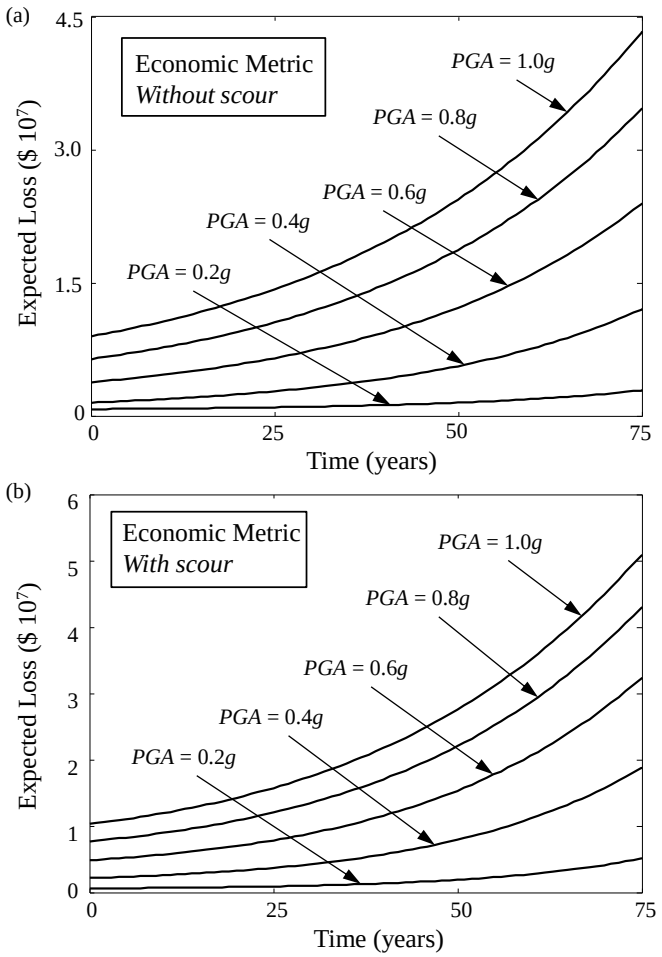

Figure 2.8 Time-variant expected value of total loss associated with different PGAs (a) without flood-induced scour and (b) with flood-induced scour

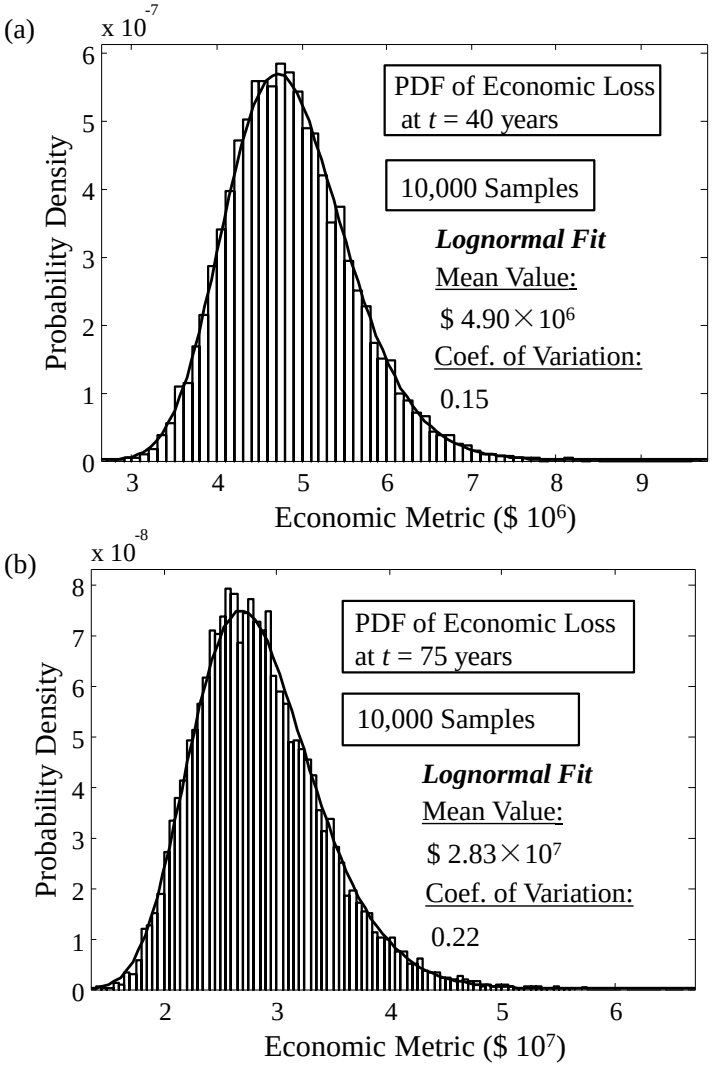

Figure 2.9 Probability density function of (a) economic loss at t = 40 years and (b) economic loss at t = 75 years.

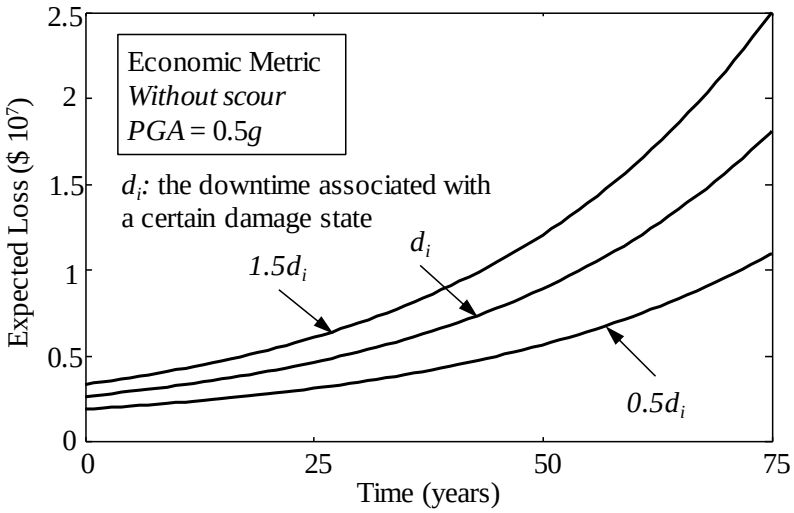

Figure 2.10 Effect of the downtime on expected economic loss without flood-induced scour associated with PGA = 0.5g

CHAPTER 3

RISK AND RESILIENCE ASSESSMENT OF BRIDGE UNDER MAINSHOCK AND AFTERSHOCK SEQUENCES INCORPORATING UNCERTAINTIES

3.1. INTRODUCTION

Mainshocks are typically followed by a few aftershocks. Usually, these aftershocks occur close in time to the mainshock. Therefore, repair or retrofit activities are often not possible to be applied within this time interval; this, in turn, may increase the risk associated with already damaged structures. Consequently, it is necessary to evaluate structural performance after a mainshock and during aftershocks in order to aid emergency management procedures and repair/retrofit decision processes. This chapter presents a generalized framework that includes the consideration of seismic ground motion hazard, seismic vulnerability associated with the bridge ability to resist aftershock hazard, and consequences evaluation under MSAS sequences.

Most previous studies associated with bridge seismic risk assessment have focused on the effects of a mainshock while neglecting aftershocks (Shinozuka *et al* 2005; Decò and Frangopol 2013; Zhu and Frangopol 2013). However, aftershocks may produce disastrous economic and societal consequences compared to a mainshock event (Yeo and Cornell 2009); therefore, the effects of aftershocks should be incorporated within the approach for probabilistic seismic risk assessment of highway bridges. The seismic

performance of a bridge considering aftershocks is related to the seismic intensity of the ground motions and conditional damage state of a structure under mainshock (Ryu *et al.* 2011). This chapter aims to compare the effect of mainshock alone with that associated with the mainshock followed by aftershocks, and to investigate the effects of aftershocks on seismic consequences and functionality associated with damaged bridges.

Various methods may be adopted for seismic demand assessment of structural systems. One method is the three dimensional (3D) nonlinear time-history analysis, which is complex and time consuming (Hatzigeorgiou and Beskos 2009). Another reliable approach is associated with static nonlinear pushover analysis and can also be used to determine seismic demand of structural systems (Chopra and Goel 2002). Simplified force-displacement-based single degree of freedom (SDOF) models representative of complex structural systems can be generated using pushover analysis (Ruiz-Garcia and Miranda 2003; Goda *et al.* 2009). Generally, an idealized inelastic SDOF system can be adopted to evaluate the nonlinear response of a structure whose dynamic behavior is dominated by the fundamental vibration mode (Goda 2012). The approximate method using SDOF may only produce accurate results for specific periods of vibration. To account for aftershock effects, structural systems should be subjected to a series of mainshock and aftershock sequences (Amadio *et al.* 2003; Goda 2012; Li and Ellingwood 2007; Zhai *et al.* 2014). Most of the previous studies regarding aftershock effects were focused on buildings. Overall, there has been limited research regarding bridge seismic performance under MSAS sequences (Ruiz-García *et al.* 2009; Alessandri *et al.* 2013).

Risk-based performance measures combine the probability of system failure with the consequences associated with a particular event (Frangopol 2011). Since failures associated with bridge structures under seismic hazard can have significant impact on the economic, social, and environmental systems, risk-based methodologies are the most appropriate for bridge management under extreme events. An approach to compute the repair cost of bridges under seismic hazard that utilizes repair cost ratios associated with different damage states has been formulated (Mander 1999). Similar methodologies have been adopted in (Shinozuka *et al.* 2005; Werner *et al.* 2006; Decò and Frangopol 2013; Dong *et al*. 2013; Zhu and Frangopol 2013). Research is required to handle risk–based decision making concerning highway bridges while incorporating MSAS seismic sequences.

In addition to risk, resilience is another indicator that accounts for structural functionality and recovery patterns after hazard occurrence. Based on the functionality of a bridge under extreme events, the probability of a bridge experiencing different performance and functionality levels (e.g., one lane closed, all lanes closed) can be obtained. Generally, the criteria regarding the decision-making process to open traffic on bridges can be established on basis of functionality. Federal Highway Administration (FHWA 2010) investigated bridge functionality considering different seismic damage states; the functionality restoration process was modelled by a normal cumulative distribution function. Presidential Policy Directive (PPD 2013) defines resilience as a structure's ability to prepare for and adapt to changing conditions while simultaneously being able to withstand and recover rapidly from functionality disruptions. The

quantification of seismic resilience should be processed through a probabilistic framework because of the considerable amount of uncertainties in the seismic vulnerability and consequence assessments. An analytical model that has been widely implemented for resilience quantification of critical infrastructure systems after an extreme event was proposed by Bruneau *et al.* (2003). This analytical model was previously applied to bridge and transportation networks (Bocchini and Frangopol 2012; Decò *et al.* 2013), healthcare facilities (Cimellaro *et al.* 2010), and power networks (Çăgnan *et al.* 2006). To the best of the authors' knowledge, the effects of aftershocks on structural seismic resilience have not been studied yet. This chapter aims to not only quantify the seismic vulnerability of bridges but also to integrate the resilience performance indicator within a seismic risk assessment process under MSAS sequences through a probabilistic framework.

In this chapter, a framework for the seismic performance assessment of bridges subjected to mainshock and aftershocks is presented. An analytical model of a highway bridge subjected to MSAS seismic sequences, considering damage or collapse is developed. The uncertainties associated with seismic scenarios, seismic vulnerability analysis of bridges, and consequences evaluation under mainshock and aftershocks are incorporated within this framework. Ultimately, the probabilistic risk and resilience of bridges under mainshock and aftershock sequences can provide decision makers with a better understanding of structural performance under seismic hazard and help them implement appropriate risk-informed mitigation strategies. This chapter is based on a published paper Dong and Frangopol 2015c.

3.2. SEISMIC SCENARIOS OF MAINSHOCK AND AFTERSHOCK

The first step in seismic performance assessment of bridges is to identify representative seismic events that characterize region under investigation. A flowchart summarizing the proposed methodology is shown in Figure 3.1. A specific seismic scenario associated with a mainshock should be generated and applied to structural systems. The earthquake early warning system (EEWS) consists of a set of seismic stations that are located in potentially active seismic zones, which can provide real-time data regarding the mainshock magnitude within the first few seconds of an earthquake (Iervolino *et al.* 2006). Based on P-wave signals received by the seismic stations, the seismic magnitude can be obtained. Then, using historical data and real time information, the earthquake magnitude and source-to-site distance can be updated using Bayes' theorem. Based on Bayes' theorem, the probability density function (PDF) associated with the mainshock magnitude and source-to-site distance can be updated considering prior information and likelihood function. More detailed information regarding the Bayes updating process can be found in Iervolino *et al.* (2006). The posterior distribution of the mainshock can be used to achieve a precise prediction of seismic losses, which can ultimately aid the decision making process. In general, the prior probability distribution corresponding to the magnitude of a characteristic earthquake can be defined as a truncated exponential PDF (Cosentino *et al.* 1977). After the updating process, the posterior distribution of the mainshock magnitude can be generated to reduce the seismic uncertainties. Based on Satriano *et al.* (2007), the uncertainties associated with the source-to-site distance are considered to be negligible compared to the uncertainties associated with the magnitude.

Aftershocks happen over a period of time after the occurrence of a mainshock. Based on Omori's law, the frequency of aftershock decreases exponentially with time (Reasenberg and Jone 1989), while Bath's law (Bath 1965) predicts the average magnitude difference (ΔM) between a mainshock and its largest aftershock. Helmstetter and Sornette (2003) stated that this difference is not only controlled by the magnitude of the mainshock but also by aftershock characteristics. Consequently, the difference between the magnitude of the mainshock and largest aftershock should be probabilistic to account for the uncertainties involved. Monte Carlo simulation can be adopted to generate random variables associated with mainshock and aftershock sequences. The level of structural seismic damage greatly depends on the distance between the epicenter of an earthquake and the location of a bridge, in addition to the magnitude associated with mainshock and aftershock intensities. The attenuation relation can be used to predict the ground motion intensity at a certain site under investigation. In this chapter, the median estimation of ground motion intensity (e.g., peak ground acceleration (PGA)) at the location of a bridge is computed according to Campbell and Bozorgnia (2007). The corresponding random locations and magnitude for aftershock seismic events can be generated using a numerical simulation method. The attenuation equation is applied to both mainshock and aftershock to compute the ground motion intensity at the location of a bridge. Detailed information regarding the attenuation equation can be found in Campbell and Bozorgnia (2007).

3.3. SEISMIC PERFORMANCE ASSESSMENT

For a bridge subjected to MSAS sequences, the probability of incremental damage to the already damaged structure can increase. Moreover, there may not be sufficient time available to effectively repair the damaged bridge. Consequently, it is important to assess the seismic performance of mainshock-damaged bridges. Seismic fragility curves are used to predict the conditional probability of a structure exceeding a certain damage state under a given ground motion intensity. Therefore, it is necessary to develop fragility curves associated with bridges under mainshock (MS) only and MSAS sequences.

When both the seismic demand and structural capacity are lognormally distributed, the fragility equation associated with damage state i can be expressed as (Hwang *et al.* 2001)

$$P[C_i - D \le 0 | IM] = \Phi\left(\frac{\ln(\mu_d / \mu_{c,i})}{\sqrt{\beta_d^{\,2} + \beta_{c,i}^{\,2} + \beta_m^{\,2}}}\right) \tag{3.1}$$

where $\Phi(.)$ is the standard normal cumulative distribution function; IM is the ground motion intensity measure (e.g., PGA, spectral acceleration amplitude); μ_d is the median value for the seismic demands which is a function of the ground motion intensity; $\mu_{c,i}$ is the median value associated with seismic capacity corresponding to damage state i; β_d and $\beta_{c,i}$ are the lognormal standard deviation of the demand and capacity, respectively; and β_m is the lognormal standard deviation that represents the modelling uncertainty. The five damage states considered within this chapter are as follows: none (i.e., intact state), slight, moderate, major and complete, denoted as DS_1, DS_2, DS_3, DS_4, and DS_5, respectively. The probability of a bridge being in damage state i can be computed by the

difference between the probabilities of exceedance of damage states *i* and *i*+1, where damage state *i*+1 is more severe than damage state *i*.

Nonlinear dynamic time-history analysis can be performed on either a full, intact multiple- degree-of-freedom (MDOF) model, or an equivalent SDOF model using the selected sets of ground motions. An equivalent SDOF structural model is used in this chapter to evaluate seismic damage of highway bridges subjected to MS only and MSAS sequences. In order to capture the nonlinear characteristics of a bridge, a non-linear static analysis associated with pushover should be performed for the bridge under investigation. In general, a SDOF structural system can be obtained using a nonlinear pushover analysis. The mainshock and aftershock seismic sequences are applied to the SDOF structure to capture the seismic performance (e.g., peak displacement). The peak ductility demand due to both the mainshock and aftershock can then be obtained. Based on Goda (2012), the inelastic responses caused by MSAS sequences are larger than those associated with mainshock only.

The ratio associated with the displacement ductility demand due to MSAS sequences with respect to MS only can be computed to evaluate the relationship between the mainshock and aftershock effects on the seismic demand of a bridge modeled with a SDOF system. The median value of seismic demand of a structure under seismic hazard is (Cornell *et al.* 2002)

$$\mu_d = a \cdot (IM)^b \tag{3.2}$$

where *a* and *b* are regression coefficients associated with seismic demand. Regarding the seismic demand analysis, a 3D FE model was established using SAP2000 2000

(Computers and Structures Inc. 2010). Beam elements are selected to model the superstructure, while elements with fiber sections are employed in modeling the bridge column.

3.4. SEISMIC RISK AND RESILIENCE ASSESSMENT

3.4.1. Economic repair loss

The consequences associated with the damage state of a bridge can be evaluated in terms of monetary value as indicated in Chapter 2. The repair loss associated with a certain damage state can be considered proportional to the rebuilding cost of a bridge.

3.4.2. Functionality

Bridge functionality is quantified within this chapter by mapping the current damage state to a value between 0 and 1.0. A functionality value equal to 1.0 is associated with DS_1, indicating no damage. Conversely, functionality equal to 0 denotes that a structure is categorized as DS_5, completely damaged. The expected functionality can be obtained by multiplying the probability of being in each damage state with the corresponding functionality ratio. Consequently, the functionality of a bridge can be computed as

$$Func = \sum_{i=1}^{5} FR_i \cdot P_{S=DS_i|IM} \tag{3.3}$$

where FR_i is the functionality ratio associated with damage state i and $P_{S=DSi|IM}$ is the conditional probability of a bridge being in damage state i under given ground motion intensity. The functionality associated with different damage states should be probabilistic. The performance levels can be defined based on functionality of the bridge under seismic hazard (Mackie and Stojadinovic 2006). Several scenarios are considered

for illustrative purposes: immediate access, weight restriction, half of lanes are open only, emergency access only, and bridge closed; these functionality categories are mapped to a functionality level between 0 and 1.0 as $Func > 0.9$, $0.6 < Func \leq 0.9$, $0.4 < Func \leq 0.6$, $0.1 < Func \leq 0.4$, and $Func \leq 0.1$, respectively. Regarding the weight restriction case, the traffic flow capacity is 75% of the value associated with the intact bridge. If half of lanes are open, the flow capacity is 50% of the value associated with intact bridge. In emergency, the flow capacity is 25% of the value associated with intact bridge. The decrease in the performance level of the bridge will reduce its traffic capacity.

3.4.3. Indirect loss

Seismic hazard has the potential to cause disastrous consequences to society and the economy. Consequently, the indirect loss associated with seismic hazard may be much larger than the direct loss (i.e., repair loss) for highway bridges. After the functionality of a bridge drops, traffic flow will be redistributed between the route segments containing the bridge. Approximation of travel demand following earthquakes is challenging due to the many socio-economic uncertainties involved (Fan 2003; Shinozuka *et al.* 2005). Based on Chang (2010), (a) if an area does not have damaged facilities, its trip demand will not be affected by an earthquake, and (b) if an area does not offer emergency shelters or hospitals, the traffic demand can remain unchanged.

When a bridge experiences structural damage from an earthquake, its users (i.e., vehicle drivers) are forced to follow detour. The running cost associated with a detour and time loss for users and goods traveling through the detour and damaged link can be computed as based on Stein *et al.* 1999 as indicated in Chapter 2. The total value of

economic loss is the sum over all performance levels as these levels form a set of mutually exclusive and collectively exhaustive events. The investigated time interval starts from the time when the repair/rehabilitation action is applied to the damaged bridge and ends at a given time point. As the functionality of bridge increases with time (e.g., days) due to repair/rehabilitation actions, the daily indirect loss associated with the damaged bridge decreases.

3.4.4. Risk assessment

Risk is defined as the combination of occurrences and consequences of events generated by specific hazards. In general, the risk R associated with a structural system can be expressed as (CIB 2001)

$$R = \int\int \cdots \int \delta(\boldsymbol{X}) \cdot f(\boldsymbol{X}) dx \tag{3.4}$$

where $\delta(\boldsymbol{X})$ represents the consequences and $f(\boldsymbol{X})$ is the joint PDF of the considered random variables $\boldsymbol{X} = (x_1, x_2, \ldots, x_k)$. The solution of this equation is not obvious; therefore, risk can be evaluated by considering an approach that accounts for discrete condition states associated with different bridge damage states as described previously. Consequently, the risk (e.g., seismic loss) of structural systems under hazard effects can be expressed as

$$R = \sum\nolimits_{DS} C_{Cons|DS} \cdot P_{DS|H} \tag{3.5}$$

where DS is the damage state; $C_{Cons|DS}$ (e.g., indirect cost) is the conditional consequence given a damage state (e.g., minor, moderate, major, or complete) and $P_{DS|H}$ is the conditional probability of damage arising from hazard H. The uncertainties associated with seismic scenarios and consequences evaluation are incorporated within this process

for seismic risk assessment. By performing Latin Hypercube sampling (McKay *et al.* 1979), the probabilistic seismic scenarios and consequences can be generated using MATLAB (MathWorks 2013). Subsequently, the statistical parameters associated with the risk can be obtained.

3.4.5. Resilience

Resilience, as a performance indicator, attempts to quantify recovery patterns of engineering systems under hazard effects. The bridge functionality restoration process can be modeled by a normal cumulative distribution function corresponding to each bridge damage state considered (ATC 1999). The recovery functions are highly dependent on their associated damage states. A bridge categorized in a severe damage state may need more time to be restored to its full functionality compared to a bridge slightly damaged. After the occurrence of the seismic event, the bridge functionality without repair or rehabilitation actions can be computed using Eq. (3.3). Subsequently, the recovery actions are applied and the bridge functionality starts to increase with time to a desirable level. Finally, the time-variant bridge functionality under a given recovery scenario is obtained. Consequently, the relevant bridge resilience under the given recovery scenario can be computed. The flowchart to compute the functionality associated with a bridge under a given recovery scenario is shown in Figure 3.2. The most widely adopted approach to quantify the resilience of a structural system is to compute it as (Cimellaro *et al.* 2010; Frangopol and Bocchini 2011)

$$R_{Resi} = \frac{1}{t_h - t_0} \int_{t_0}^{t_h} Q(t)dt \tag{3.6}$$

in which $Q(t)$ is the functionality of the bridge under the recovery function; t_o is the occurrence time of the extreme event; and t_h is the investigated time point. The resilience, as computed by Eq. (3.6), can be illustrated graphically as shown in Figure 3.3 without and with consideration of aftershock effects. As qualitatively shown in this figure, a smaller value of resilience results when the effects associated with aftershocks are incorporated within seismic functionality assessment process.

3.5. ILLUSTRATIVE EXAMPLE

The presented probabilistic framework for seismic risk and resilience assessment of bridges under MSAS is applied to a bridge that was designed on the basis of Caltrans's bridge seismic design criteria (CSDC 2004). The bridge under investigation within this illustrative example is a two-span reinforced concrete bridge with multiple-column bents. The length and width of the bridge are 90 m and 16.5 m, respectively, as shown in Figure 3.4(a). A FE model able to capture the nonlinear behavior of the bridge is established in SAP2000 (Computers and Structures Inc. 2010) to assess its seismic fragility. By performing static nonlinear pushover analysis, an equivalent SDOF system of the bridge can be obtained. The seismic demand of the bridge under MS only and MSAS sequences can be obtained using the equivalent SDOF system. A similar approach has been adopted by Raghunandan and Liel (2013) to evaluate the seismic performance of a building under seismic hazard.

3.5.1. Probabilistic seismic scenarios

Based on historical data and real-time measurements obtained from the earthquake early warning system, the mainshock magnitude can be updated. In general, after the updating

process, the magnitude of mainshock can be modeled as a random variable that follows a lognormal distribution. Based on Satriano *et al.* (2007), uncertainties associated with the source-to-site distance may be considered as negligible with respect to those associated with magnitude. The mainshock earthquake with mean magnitude of 6.9 (Richter scale) is considered herein. Additionally, the earthquake is assumed to occur at a distance of approximately 6 km from the location of the bridge. The detailed information associated with the mainshcok considered in this chapter is shown in Table 3.1.

The parameters associated with the aftershock magnitude and source-to-site distance are treated as random variables herein to account for the uncertainties associated with aftershocks. In this chapter, the magnitude difference (ΔM) between a mainshock and its largest aftershock is considered to follow a triangular PDF with mode equal to 1.2. More information regarding probabilistic mainshock and aftershock scenarios can be found in Table 3.1. Using Monte Carlo simulation, 10,000 samples of the seismic scenarios associated with MSAS can be generated. The PGA is used as the measure of ground motion intensity at the location of the bridge and can be computed based on Campbell and Bozorgnia (2007).

3.5.2. Seismic vulnerability assessment

The FE model of the bridge is established in SAP2000, which can account for the geometric and material nonlinear behaviors. The confined concrete model proposed by Mander *et al.* (1998) is used to capture the material behavior of concrete columns. The beam elements are selected to model the superstructures as elastic model. The columns' plastic hinges are modeled using the fiber hinge in SAP2000 in order to account for

nonlinear behavior. The abutment model consists of a rigid element of finite length (i.e., superstructure width) associated with longitudinal, transverse, and vertical nonlinear responses on both sides. The abutment model was developed based on SDC (2004) and was adopted by Aviram *et al.* (2008). A pinned connection is adopted to model the foundation boundary conditions and rigid soil conditions are assumed. Figure 3.4(b) shows the 3D finite element model and the key components modeled in SAP2000.

The representative SDOF model of the bridge can be generated by performing static nonlinear pushover analysis using SAP2000. Pushover analysis can evaluate the overall strength of a structure under incrementally increased structural loading. The lateral load pushover analysis associated with different directions (i.e., longitudinal, transverse, and an angle with respect to principal directions of the bridge) can be performed on the bridge. Although the transverse direction is emphasized in this chapter as shown in Figure 3.5(a), other directions can also be considered. The elastic period of the bridge associated with the transversal model is 0.783 seconds as obtained through the FE model. The SDOF system is assumed to have the same period as the bridge, 5% damping, 5% post-yield hardening stiffness, and an associated yield displacement that was obtained using nonlinear pushover analysis. In this chapter, seismic ductility demand is defined as the maximum inelastic displacement divided by the yield displacement associated with the bridge structure.

The median values of bridge ductility capacities associated with different damage states are based on Hwang *et al.* (2001) and Prasad (2013), while the seismic demand of the bridge can be obtained using the equivalent SDOF model subjected to a set of ground

motions. The ductility demand, defined as the peak displacement of an inelastic SDOF system normalized by the yield displacement of the system, is computed herein. Goda *et al.* (2009) developed a prediction equation for the peak ductility demand of the SDOF system. This equation is adopted herein to compute the seismic demand of the bridge under seismic scenarios. Using Eq. (3.2), the seismic demand of the bridge under mainshock can be obtained. The regression parameters a and b that are used in this equation are 2.108 and 1.338, respectively. The parameter β_c in Eq. (3.2) is assumed to be 0.25 for all damage states, while the modeling uncertainty parameter β_m is assumed to be 0.2 (Celik and Ellingwood 2010). Consequently, the probability of the bridge exceeding certain damage state can be computed using Eq. (3.1). The fragility curves associated with the bridge subjected to mainshock are shown in Figure 3.5(b). As shown, the seismic vulnerability of the bridge decreases with increases in the ground motion intensity.

The MSAS sequences are applied to the SDOF system to compute the seismic demand of the bridge. The artificial and real aftershock sequences can be used as the input for the seismic ductility demand analysis. The seismic demand of the bridge under MS only and MSAS sequence greatly depends on several factors, such as the mainshock magnitude and total duration of aftershock sequence (Goda 2012). In general, the median value of seismic demand associated with the bridge increases due to MSAS effects. Based on Zhai *et al.* (2014), the effects of aftershocks on the ductility demand can be neglected when the ground motion intensity ratio PGA_{AS}/PGA_{MS} is less than or equal to

0.5. The median value of seismic ductility demand of the bridge under MSAS $\mu_{d,MSAS}$ can be computed as

$$\mu_{d,MSAS} = a \cdot (PGA_{MS})^b \cdot DR_{MSAS} \tag{3.7}$$

$$DR_{MSAS} = \begin{cases} 1 & PGA_{AS} / PGA_{MS} \le 0.5 \\ c \cdot (PGA_{AS} / PGA_{MS}) + d & 0.5 < PGA_{AS} / PGA_{MS} \le 1.5 \end{cases} \tag{3.8}$$

where DR_{MSAS} is the ductility demand ratio that can be computed as peak ductility demand of the bridge under MSAS sequences to ductility demand associated with MS only; PGA_{MS} is the PGA at the location of the bridge associated with mainshock; and PGA_{AS} is the PGA at the location of the bridge associated with the aftershock. A linear relationship between the ratio associated with ground motion intensity measures (PGA_{AS}/PGA_{MS}) and ductility demand ratio (DR_{MSAS}) is assumed. The regression parameters that are used in Eq. (3.7) are c = 0.3 and d = 0.85, respectively. The effects of aftershocks on the standard deviation of seismic demand are not investigated herein. Then, the fragility curves of the bridge under MSAS sequences can be obtained. Figure 3.6 depicts the fragility curves associated with slight, moderate, major and complete damage states of the bridge under MS only and MSAS sequence. As shown, the exclusive consideration of aftershocks can underestimate of the seismic vulnerability. In this figure, the two values associated with PGA_{AS}/PGA_{MS} = 1.0 and 0.8 are adopted for illustrative purposes to investigate the effects of aftershocks on bridge seismic performance.

3.5.3. Probabilistic seismic risk and resilience

In this chapter, the statistical descriptors of the functionality under different damage states are proposed on the basis of literature surveys and engineering judgment (ATC

1999). Table 3.2 summarizes the values of the random variables and parameters adopted for the recovery functions associated with different damage states. The functionality associated with complete damage is 0, while the functionality corresponding to no damage is 1.0. By using Eq. (3.3), the residual functionality of the bridge under MS only and MSAS sequences without the recovery phase is shown in Figure 3.7(a). The expected value of functionality is reduced when the aftershock effects are considered in the computational process. The mean functionality is 0.212 and 0.169 for the cases associated with MS only and MSAS, respectively.

The risk in terms of seismic loss associated with the bridge under seismic hazard can be computed using Eqs. (3.3) to (3.8). The probabilistic repair losses for the bridge including and excluding the effects of aftershock are shown in Figure 3.7(b). As indicated, there is a significant difference between these two cases; the mean value of the repair loss under aftershock effects is much larger than that neglecting these effects. Moreover, the dispersion of the repair loss increases significantly when the aftershocks are considered. The uncertainties related to these aspects should be given special attention, especially at late stages of the investigated time interval. The distribution of the repair loss gives an indication of the dispersion of the collected data and can ultimately aid in the seismic risk mitigation process.

Generally, the occurrence of aftershocks decreases exponentially with time (Reasenberg and Jone 1989). Repair actions are applied to the bridge on the basis that no severe aftershock will increase its seismic damage. The time interval associated with resilience assessment starts from the recovery phase when repair/rehabilitation actions are

applied to the damaged bridge. By performing recovery, the functionality of a bridge can increase to a desirable level. The random variables associated with the recovery scenarios are indicated in Table 3.2. The probabilities of the bridge being in different functionality levels during the investigated time interval are computed and the results are shown in Figure 3.8. As indicated, the probability of the bridge being in a severe functionality level deceases with time, as repair/rehabilitations are applied to the bridge. The sum of the probabilities of being in different functionality levels always equals one; thus, the functionality levels can be defined as a set of mutually exclusive and collectively exhaustive events. As indicated in Figure 3.8, the probability of opening this bridge to traffic after 500 days from the recovery phase is almost 1.0. As shown in Figure 3.8, there is a high probability of one lane being closed within 90 days from the recovery phase, while this probability decreases significantly after this time interval.

The expected time-variant functionality of the bridge is investigated herein and displayed in Figure 3.9(a). As shown in this figure, the aftershock events have great effects on the functionality of the bridge. The difference between the functionality associated with the cases without and with aftershock effects decreases as time goes by. The expected value of the functionality of the bridge can be used for the computation of the resilience. Using Eq. (3.6), the resilience of the bridge can be obtained. Consequently, the resilience of the bridge is 0.810 neglecting aftershock effects; however, this value reduces to 0.778 if aftershock effects are considered. The investigated time interval is 600 days herein and within the time interval the bridge has restored to its full functionality. The resilience from these two cases is different. Given the threshold associated with

resilience, different optimum retrofit and/or maintenance actions can be obtained for these two cases (i.e., without and with aftershocks). The indirect loss associated with the bridge considering partial functionality can be computed using Eqs. (3.5) to (3.6). The parameters that are used in these equations are shown in Table 3.3. The time-variant indirect loss under the investigated time interval is depicted in Figure 3.9(b). The expected daily indirect loss reaches zero at the end of the investigated time interval, as the functionality of the bridge is completely restored. As revealed herein, the expected daily indirect loss for the bridge under probabilistic recovery functions decreases over time. To illustrate the effect of flow capacity associated with weight restriction and emergency cases on seismic loss, the flow capacities corresponding to these two functionality levels are both increased and decreased by 0.1. The comparison of daily indirect losses is provided in Figure 3.9(c). Generally, the risk and resilience are relevant performance indicators and can be used in the pre-event retrofit and post-event rehabilitation optimization of bridge infrastructure

The effects of the uncertainties associated with earthquake scenarios and consequences are also illustrated within the computational process. Figure 3.10(a) shows the profiles of the mean ($\mu = E(Q)$) and mean plus ($\mu + \sigma$) and minus ($\mu - \sigma$) one standard deviation (σ) of the functionality throughout the investigated time horizon. As the results indicate, the bridge functionality under probabilistic hazard scenarios associated with MSAS increases over time. In order to illustrate the variation of the functionality, the PDFs of functionality at t = 10 days, 100 days, 200 days, and 400 days are presented in Figure 3.10(b). As shown, the expected functionality of the bridge increases with time but

does not exceed 1.0. Additionally, the dispersion decreases when bridge functionality approaches full recovery. The relevant results without considering aftershock effects are also investigated herein, as shown in Figure 3.10(c) and (d).

3.6. CONCLUSIONS

This chapter presents a probabilistic framework for seismic risk and resilience assessment of bridges under MSAS sequences. The seismic performances of a highway bridge under MS only and MSAS sequence are computed separately and compared with each other on the basis of fragility curves. The presented approach is illustrated on a highway bridge under seismic hazard.

The following conclusions can be drawn.

1. The effects of aftershocks have an influence on the repair loss and residual functionality of a bridge after a seismic event. The uncertainties associated with repair loss will increase when aftershocks are considered. Consequently, it is of vital importance to consider the effects of aftershocks on bridge seismic performance.
2. Integration of the uncertainties associated with seismic scenarios, modelling, and consequences evaluation in the proposed framework is necessary for a rational risk and resilience assessment of bridges under MSAS. As can be concluded from the results, the resilience and economic loss are affected by uncertainties.
3. The assessment of functionality and probabilities of bridges having different performance levels can aid the decision to open traffic on bridges after extreme events.

4. The presented approach can aid the pre-event decision making process on the basis of proper retrofit strategies to meet the resilience and/or risk performance level that the decision maker can tolerate. Moreover, it can also guide the decision maker to plan post-event repair/rehabilitation activities to reduce economic and social impacts considering MSAS sequences.

Table 3.1 The parameters associated with probabilistic seismic scenarios

Parameter	Mean	COV		Distribution type
Magnitude of mainshock	6.9	0.023		LN
Parameter	**Lower limit**	**Upper limit**	**Mode**	**Distribution type**
ΔM	0	2.4	1.2 [a]	Triangular [b]
Source-to-site distance of aftershocks	2	10	6 [b]	Triangular [b]

[a]: Bath (1965); [b]: assumed.

LN: Log-normal distribution; COV: coefficient of variation

Table 3.2 The parameters associated with bridge restoration functionality in different damage states

Damage state	Mean (days)				COV
	Lower limit	Upper limit	Mode	Distribution type	
Slight	0.2	1	0.6 [a]	Triangular [b]	1 [a]
Moderate	1	5	2.5 [a]	Triangular [b]	1 [a]
Major	30	120	75 [a]	Triangular [b]	0.56 [a]
Complete	120	360	230 [a]	Triangular [b]	0.48 [a]

[a]: ATC (1999); [b]: assumed.
COV: coefficient of variation

Table 3.3 The parameters associated with consequences assessment

Random variables	Mean	COV	Distribution type
ADT	39500 [a]	DNA	DNA
ADTT/ADT ratio	13% [a]	DNA	DNA
Bridge length (m)	88 [a]	DNA	DNA
Bridge width (m)	16.2 [a]	DNA	DNA
Length of link (km)	6 [b]	DNA	DNA
Detour additional distance (km)	2 [b]	DNA	DNA
Vehicle occupancies for cars	1.5 [c]	DNA	DNA
Vehicle occupancies for trucks	1.05 [c]	DNA	DNA
Rebuilding costs	2306 [d]	0.2	LN [e]
Compensation for truck drivers ($/h)	29.87 [c]	0.3	LN [e]
Inventory costs ($/h)	3.81 [c]	0.2	LN [e]
Operating costs for cars ($/km)	0.4 [c]	0.2	LN [e]
Operating costs for trucks ($/km)	0.57 [c]	0.2	LN [e]
Wage for car drivers ($/h)	11.91 [c]	0.3	LN [e]
Detour speed (km/h)	50 [e]	0.2	LN [e]
Link speed (km/h)	80 [e]	0.2	LN [e]

[a]: FHWA (2010); [b]: Google Inc (2011); [c]: AASHTO (2003); [d]: Decò *et al.* (2013); [e]: assumed; LN: Log-normal distribution; COV: coefficient of variation

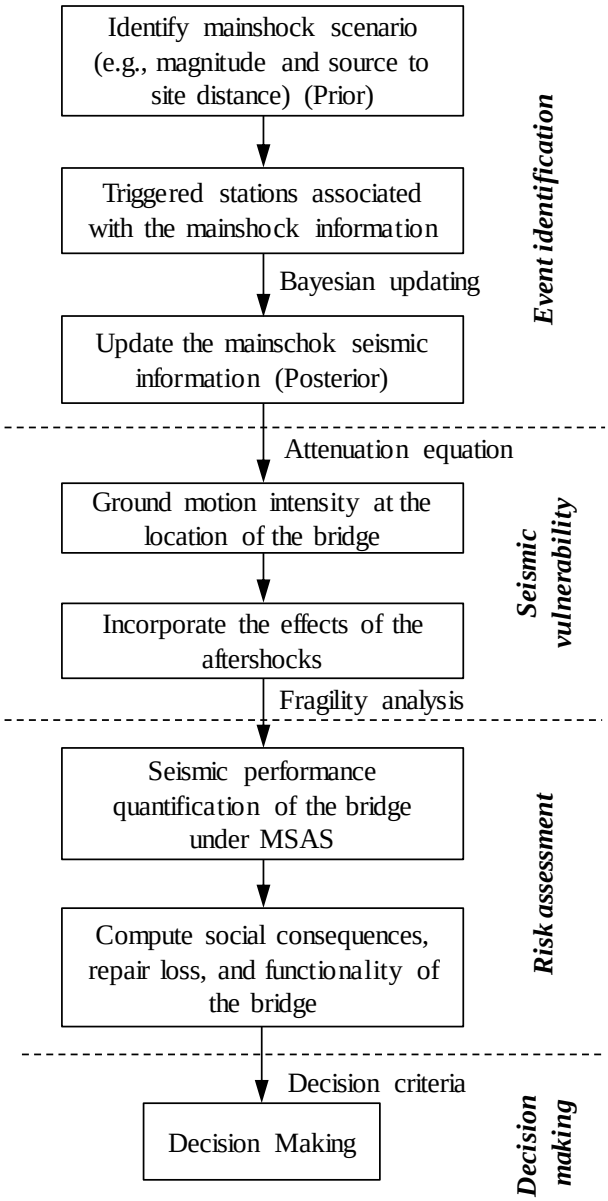

Figure 3.1 Flowchart of the seismic risk-informed decision making

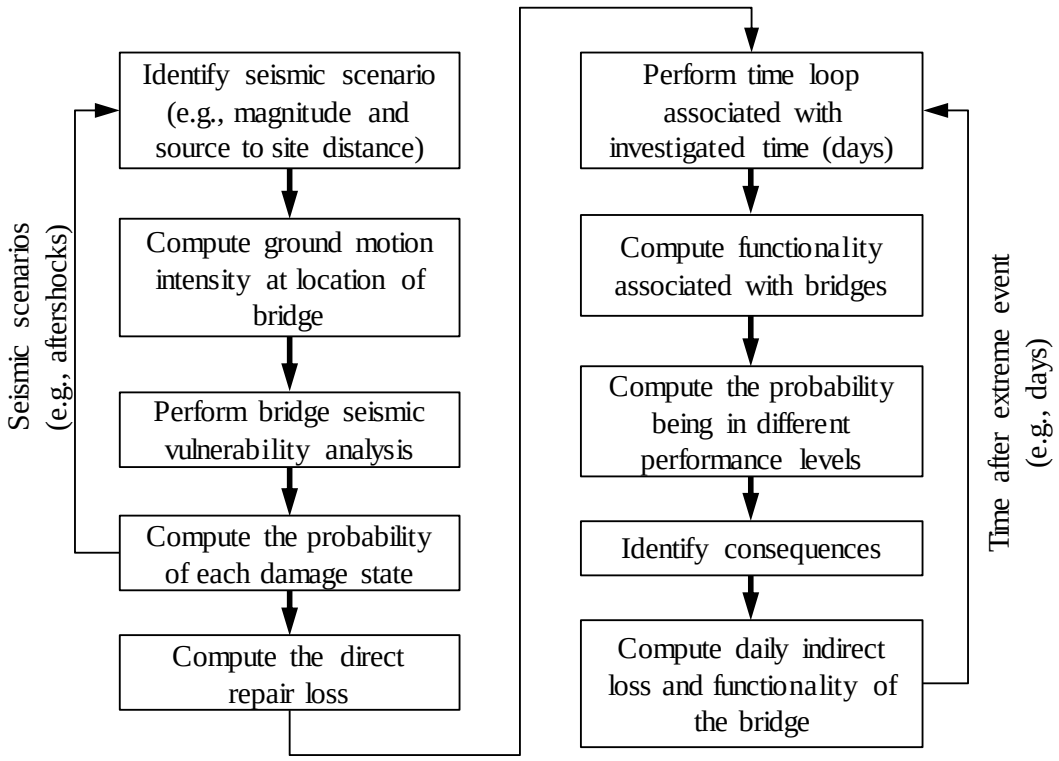

Figure 3.2 Flowchart of time-variant functionality and economic loss assessment under mainshock and aftershock sequences

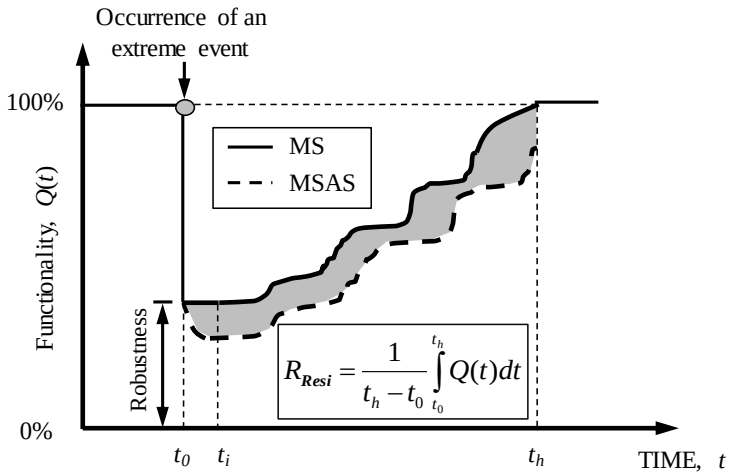

Figure 3.3 Schematic representation of resilience considering uncertainties under mainshock (MS) only and mainshock and aftershock (MSAS)

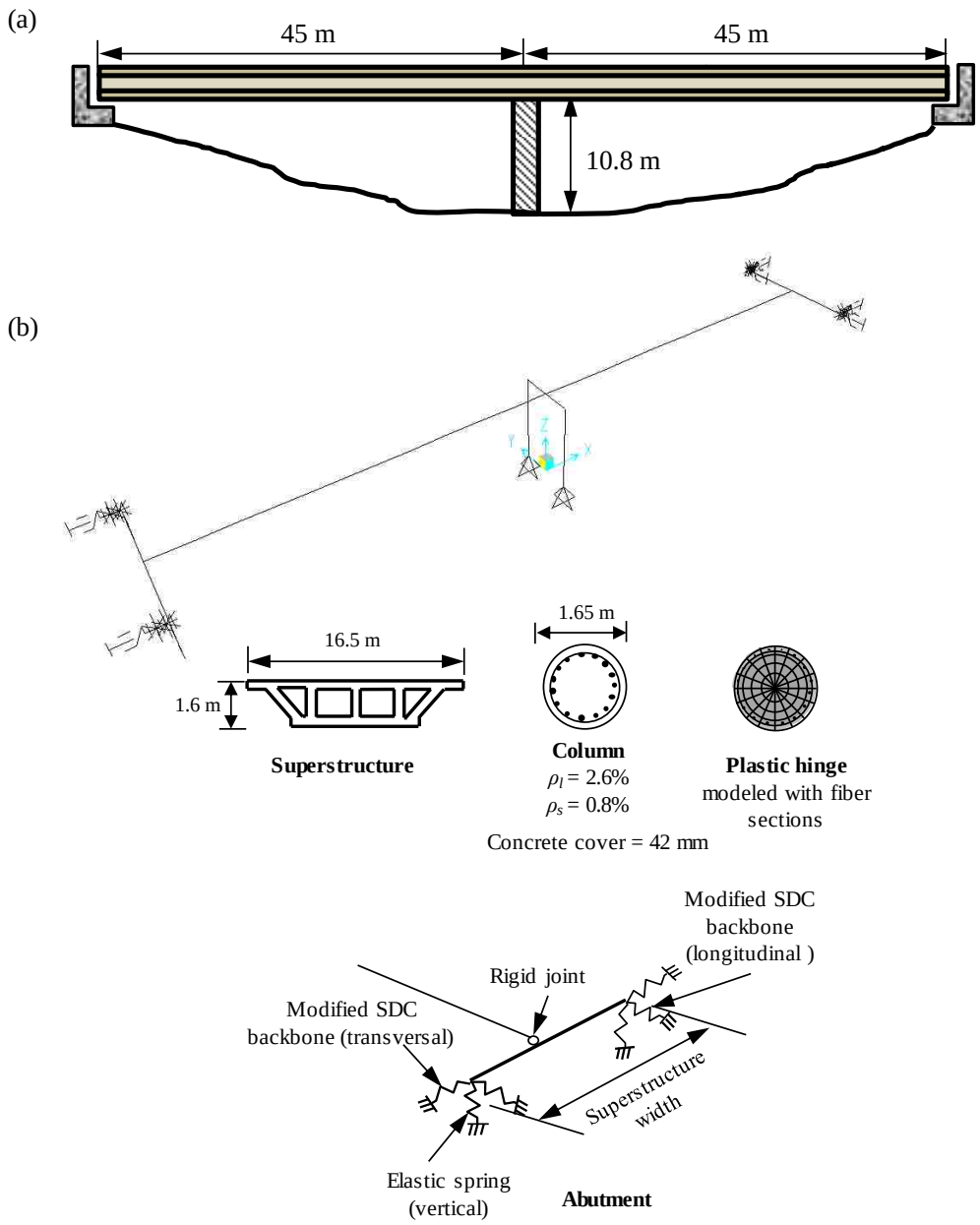

Figure 3.4 (a) Elevation of the bridge under investigation and (b) key components modeled in SAP2000

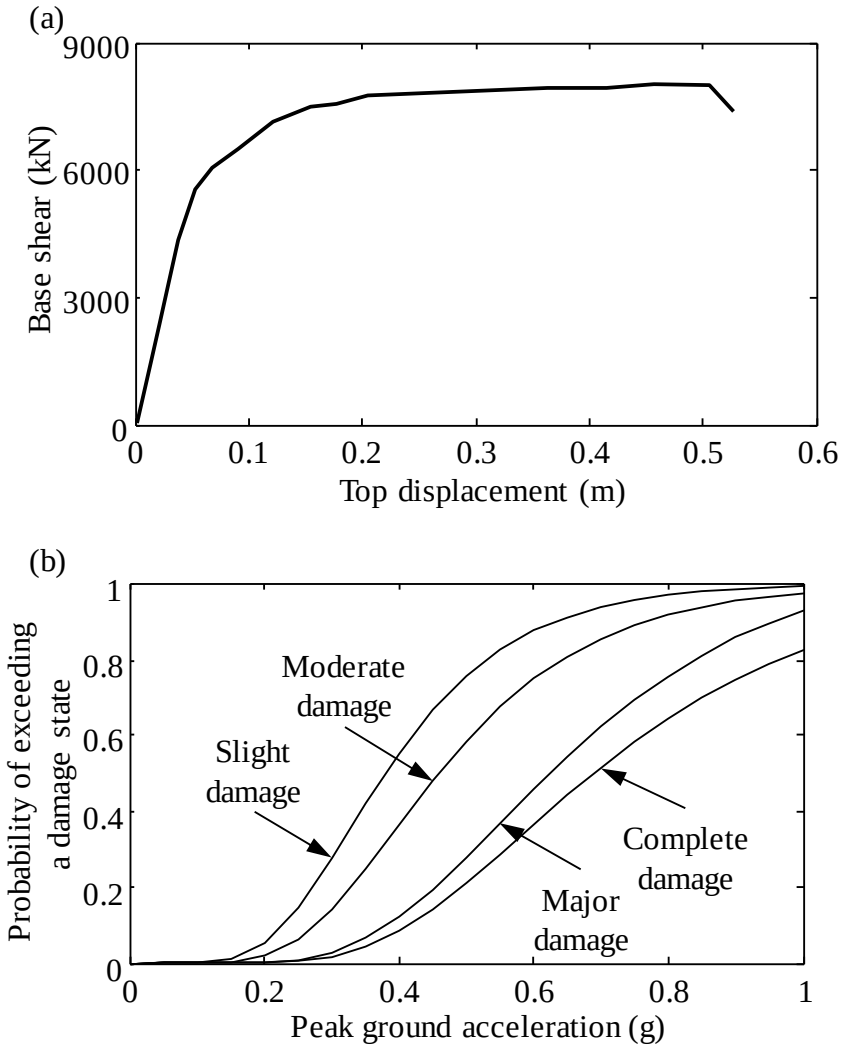

Figure 3.5 (a) Transversal nonlinear pushover analysis and (b) fragility curve associated with the bridge for slight, moderate, major, and complete damage states

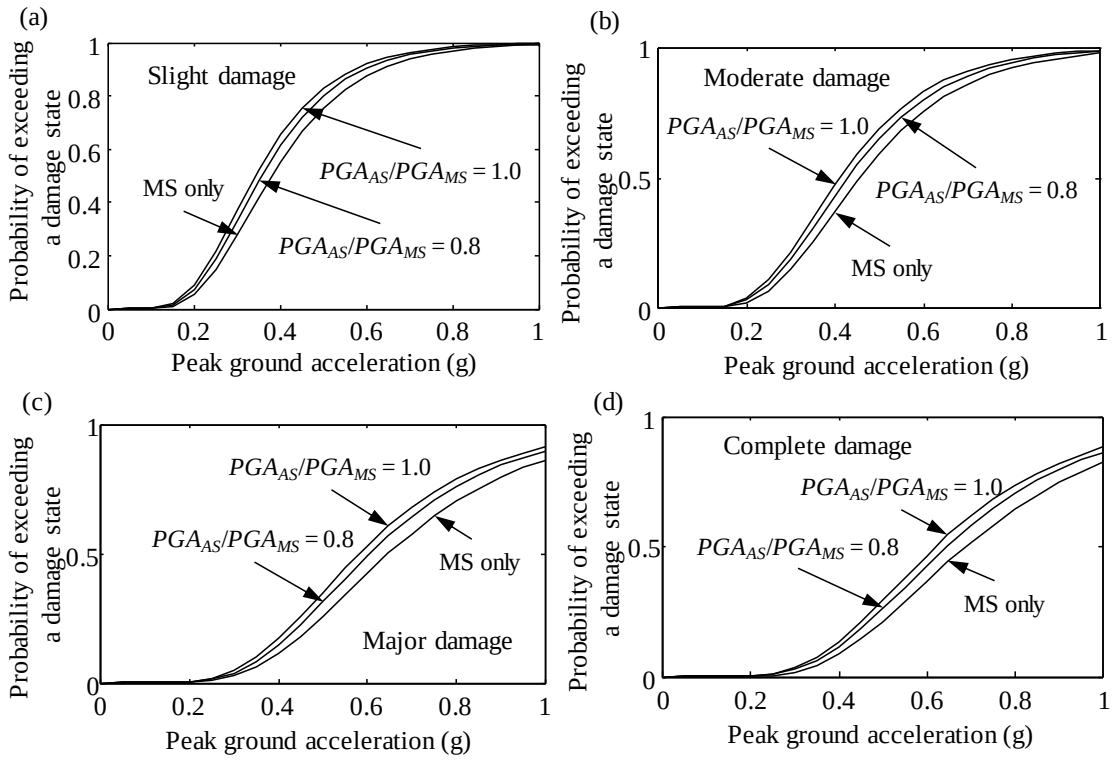

Figure 3.6 Fragility curves associated with (a) slight, (b) moderate, (c) major and (d) complete damage states considering MS only and MSAS

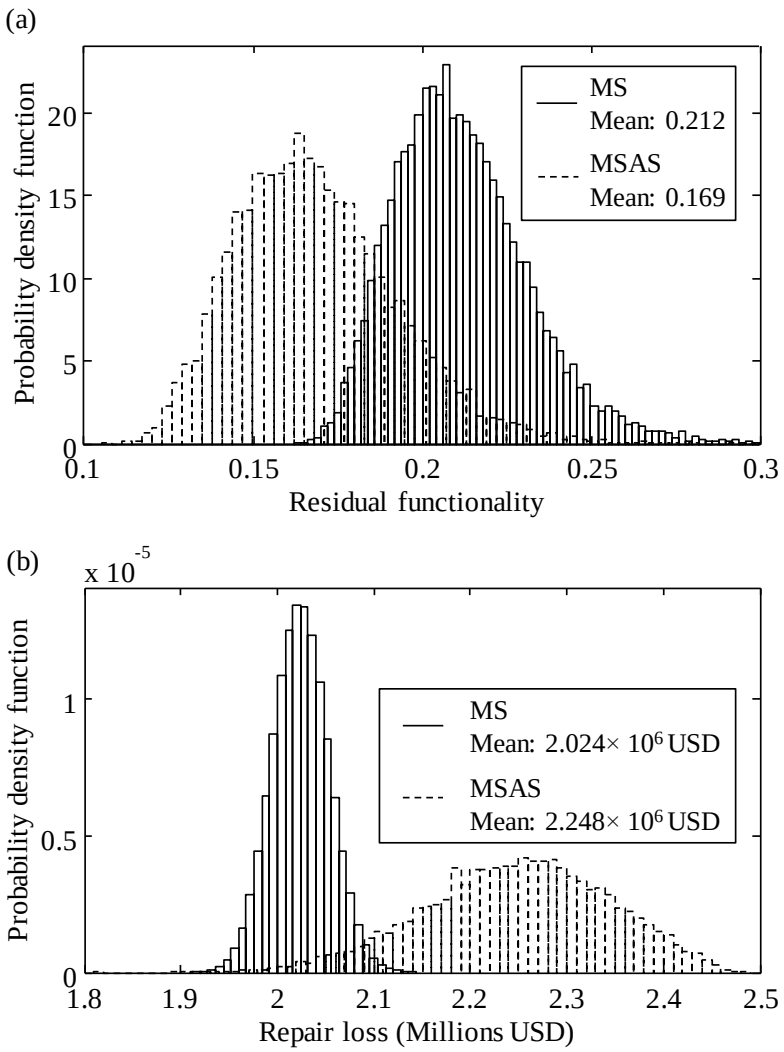

Figure 3.7 (a) Probabilistic residual functionality and (b) direct repair loss with and without considering MS only and MSAS

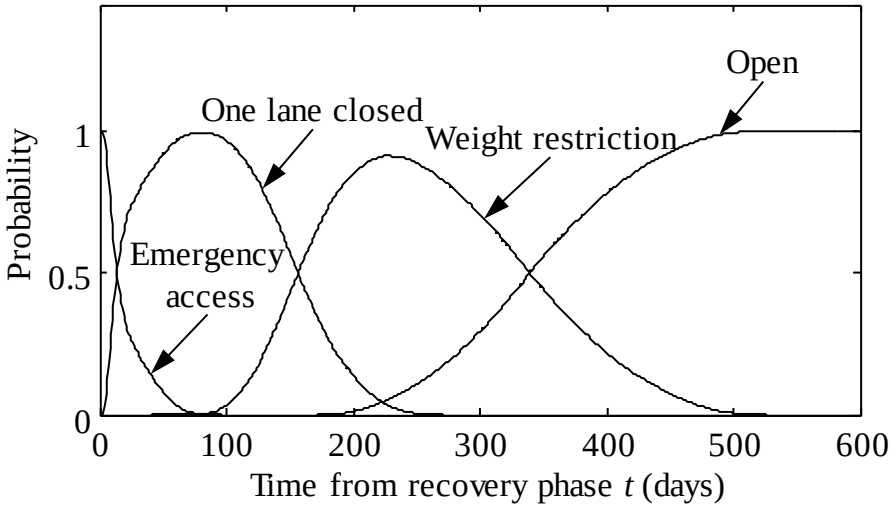

Figure 3.8 Probability of the bridge being in different functionality levels

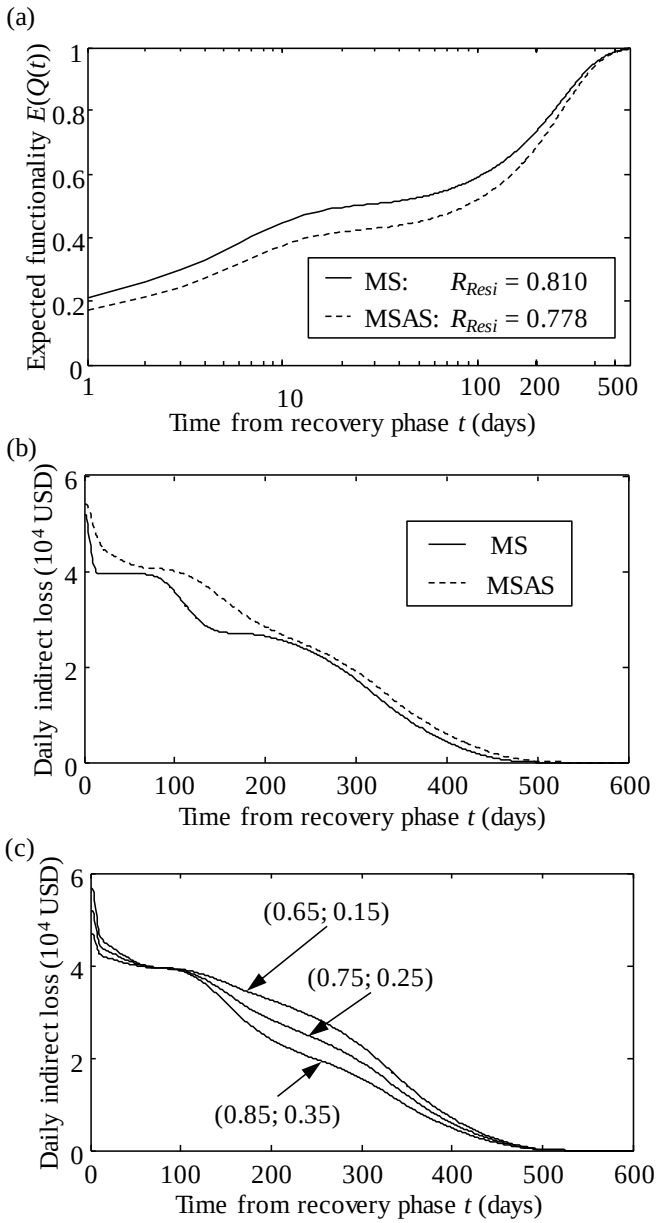

Figure 3.9 (a) Expected functionality of the bridge from the recovery phase considering MS and MSAS; and (b) daily indirect loss with and without considering aftershock effects; and (c) daily indirect loss of the bridge given different flow capacities associated with weight restriction (first number in parentheses) and emergency cases(second number in parentheses) under MSAS

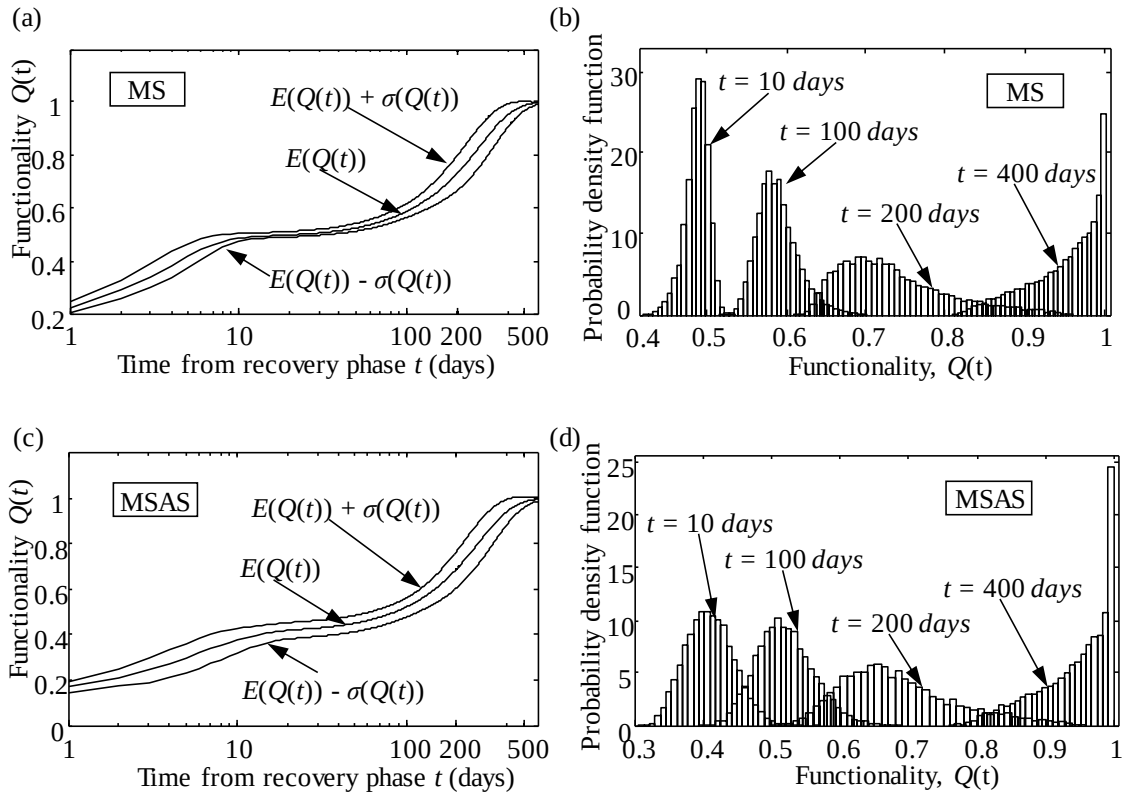

Figure 3.10 (a) Time-variant expected functionality, and mean plus and minus one standard deviation; and (b) PDF of functionality of the bridge at different points in time (days) under MSAS; (c) time-variant expected functionality, and mean plus and minus one standard deviation; and (d) PDF of functionality of the bridge at different points in time (days) under MS

CHAPTER 4

TIME-DEPENDENT MULTI-HAZARD LIFE-CYCLE ASSESSMENT OF BRIDGES CONSIDERING CLIMATE CHANGE

4.1. INTRODUCTION

The United Nations Office for Disaster Risk Reduction reported that in 2011 natural disasters (e.g., earthquakes, floods, and tsunamis) resulted in $366 billion of direct economic losses and 29,782 fatalities worldwide (Ferris and Petz 2011). These staggering statistics highlight the need for effective hazard recovery strategies for communities. Earthquakes are a common natural hazard for the civil infrastructure systems. Seismic loss and risk mitigation of highway bridges are of vital importance. Moreover**,** bridges have suffered exposure of their pier foundations under flood-induced scour, which significantly reduces the foundation bearing capacity and can cause structural damage or even collapse during floods. Scour is one of the main bridge failure causes in the United States accounting for about 58% of all failures (Briaud 2006). Consequently, it is of vital importance to evaluate the performance of bridges under earthquake and flood. This chapter presents a generalized framework for risk mitigation and recovery of highway bridges under multiple hazards incorporating life-cycle hazard loss and resilience.

In the AASHTO LRFD Specifications (2015), the designed extreme hazards are related to the return periods. For example, a design earthquake is set to 475- or 2500-year

return periods for regular and important bridges, respectively. The bridge foundations considering scour are designed for a 100-year flood event. However, the design return period does not account for uncertainties and economic and/or social metrics. Additionally, the time-independent occurrence models have been widely adopted to investigate hazards. Therefore, it is necessary to incorporate the time dependence into hazard loss assessment process. By using a time-dependent model, the probability of earthquake occurrence will increase with the elapsed time since the last large or characteristic earthquake associated with a fault. Furthermore, through their lifetime, bridges are subjected to harsh environmental conditions. Aging and deterioration can affect the performance of bridges by increasing their hazard vulnerability over time (Akiyama *et al.* 2012; Dong *et al.* 2013). Within relevant published literature, only few studies have quantified the annual seismic loss considering time effects (Dong *et al.* 2014; Decò and Frangopol 2013). Furthermore, to the best knowledge of the authors, there is no study that assesses the life-cycle hazard loss of highway bridges considering deterioration and time-dependent hazard.

The significance of resilience and risk-based management of highway bridges has increased in the last few decades. Resilience is an important structural performance indicator that accounts for structural performance and recovery patterns under extreme events (Bruneau *et al.* 2003; Bocchini *et al.* 2014; Dong and Frangopol 2015). Overall, hazard loss and resilience assessment considering aging effects and time-dependent hazard are of vital importance to ensure structural safety and functionality during service

life. In this chapter, the time-variant loss and resilience of highway bridges under earthquake and flood are considered in a life-cycle context.

The United States Global Change Research Program (USGCRP 2008) reported that the average precipitation has increased 5% during a 50 years interval; consequently, the frequency of hazards (e.g., flood) has increased as well as they have become more intense. Generally, climate change and increase in hazard intensity increase the probability of bridge failure due to hazard effects. Understanding how climate change affects the life-cycle performance of bridges can lead to improved preparedness prior to extreme disasters. Consequently, there is a need for an investigation of bridge performance under the impact of climate change. The effects associated with continuing change in intensities and probabilities of extreme events are investigated.

In this chapter, a framework for time-variant hazard loss and resilience assessment of highway bridges under multiple hazards considering time-dependent hazard is presented. Additionally, the life-cycle losses with and without aging effects and climate change are computed. The uncertainties associated with hazard scenarios, structural vulnerability analysis, and consequence evaluation are incorporated within this framework. The work in this chapter in based on Dong and Frangopol (2016c)

4.2. PERFORMANCE UNDER EARTHQUAKE AND FLOOD

4.2.1. Earthquake

The first step in seismic loss assessment is to identify the seismic intensity at the location of the structural system. The next step is to compute the vulnerability of structural systems under seismic hazard. The earthquake rupture could be given a "characteristic"

magnitude-frequency distribution, modeled as a Gaussian distribution using the mean, a standard deviation of 0.12, and a truncation at ± 0.24 magnitude units above and below the mean (USGS 2003). Generally, the mean magnitude associated with earthquake rupture is (Hanks and Bakun 2002)

$$M = \begin{cases} 3.98 + \log_{10}(A_F) & A_F \le 468\ km^2 \\ 3.09 + \frac{4}{3}\log_{10}(A_F) & A_F > 468\ km^2 \end{cases} \quad (4.1)$$

where A_F is the total area of fault segment (km^2) and is

$$A_F = L_F \cdot W_F \cdot R_{sf} \quad (4.2)$$

where L_F is segment length (i.e., the distance between two segmentation points) (km); W_F is fault segment width (km); and R_{sf} is a scaling factor accounting for the role of fault creep in reducing the fault surface area.

A time-dependent hazard model associated with a given fault is characterized by its recurrence-interval probability density function (PDF) (i.e., distribution of times between large earthquakes). In California, time-dependent seismic hazard model could be represented by using a log-normal recurrence interval distribution. The recurrence interval in terms of a log-normal distribution is (Petersen *et al.* 2007)

$$f_T(t) = \frac{1}{\sqrt{2\pi}\varsigma \cdot t} \exp\left(-\left[\ln(t) - \ln(t_m)\right]^2 / (2 \cdot \varsigma_m{}^2)\right) \quad (4.3)$$

$$t_m = 2.8 \cdot 10^{-5} \cdot L_F / V_{sl} \quad (4.4)$$

where t is measured from the time of the last earthquake (year); t_m is the median recurrence interval (year); ζ_m is the standard deviation; and V_{sl} is the slip rate associated with the investigated fault (mm/year). By using the time-dependent hazard model, the conditional time-dependent probability of occurrence P in the time interval (t_e, $t_e + \Delta t$) is given by

$$P(t_e \le T \le t_e + \Delta t | T > t_e) = \frac{P(t_e \le T \le t_e + \Delta t)}{P(t_e \le T \le \infty)} \tag{4.5}$$

where t_e is the elapsed time and ΔT is the time period of interest. The computational process of the conditional probability of occurrence associated with the time-dependent hazard model is qualitatively shown in Figure 4.1(a) for illustrative purpose. An effective Poisson rate, with respect to the time-dependent hazard model can be expressed as

$$\nu_{eff} = -\ln(1-P)/\Delta t \tag{4.6}$$

where P is the conditional time-dependent probability of occurrence as computed using Eq. (4.5).

Fragility curves are commonly used methods to predict structural performance under seismic hazard. Due to time effects, the fragility curves should be evaluated throughout the lifetime of a structure. The time-variant fragility curves can be computed as (Basöz and Mander 1999, Dong *et al.* 2013)

$$P_{S \ge DS_i | IM}(t) = \Phi\left(\frac{\ln(IM) - \ln(m_i(t))}{\beta_i(t)}\right) \tag{4.7}$$

where $\Phi(.)$ is the standard normal cumulative distribution function; IM is the seismic intensity measure (e.g., peak ground acceleration (PGA)); $\beta_i(t)$ is the standard deviation of the damage state i of the structural fragility at time t; and m_i is the median value of ground motion intensity associated with damage state i. The time-variant median and standard deviation of intensity associated with a certain damage state can be expressed as (Dong *et al.* 2013)

$$m_i(t) = m_{i0} \cdot (1 - \gamma_1 \cdot t^{\zeta_1}) \tag{4.8}$$

$$\beta_i(t) = \beta_{i0} \cdot (1 - \gamma_2 \cdot t^{\zeta_2}) \tag{4.9}$$

where m_{io} is median value of the ground motion intensity for damage state i and γ_1 and γ_2 are the aging coefficients. $\zeta = 1$ indicates a linear deterioration, while $\zeta > 1$ denotes a non-linear deterioration. Given the fragility curves at different points in time, the probabilities of the bridge being in different damage states could be computed.

4.2.2. Flood

As bridges are subjected to the exposure of their pier foundations under flood-induced scour, bearing capacities of their foundations could be reduced significantly causing bridge damage or even collapse. Generally, a frequency analysis of annual peak-flow data collected at a stream gage can provide an estimate of the flood magnitude and frequency. The expected annual flow associated with given recurrence interval T can be expressed as (Gotvald *et al.* 2012)

$$Q_T = a_0 \cdot Dra^{b_0} \cdot Apr^{c_0} \cdot Mel^{d_0} \tag{4.10}$$

where Q_T is the annual flow associated with T years recurrence interval (cubic feet per second); Dra is the drainage area (square miles); Mel is the elevation (feet); Apr is the annual precipitation (inches); and a_0, b_0, c_0, and d_0 are regression coefficients. Once the flow discharge is determined, the flow velocity and depth, used in the scour analysis process, can be computed.

Extensive research has been conducted on the prediction of local scour depth and a number of predictive methods have been proposed (Melville 1997; Briaud *et al.* 1999; Richardson and Davis 2001; Briaud *et al.* 2004). The equation proposed by Briaud *et al.* (1999) is employed herein to compute the scour depth as follows

$$\hat{z}_{\max} = 0.18R^{0.635} \tag{4.11}$$

$$z = \frac{t}{\frac{1}{\dot{z}_i} + \frac{t}{\hat{z}_{\max}}} \tag{4.12}$$

where z is the scour depth (mm); t is the time over which a given velocity is applied (hour); $\dot{z}_i$ is the initial rate of scour (mm/h); $\hat{z}_{\max}$ is the maximum depth of scour (mm); R is Reynolds number equal to $V_f D/\upsilon_w$; V_f is the velocity of flow; D is diameter of the pier; and υ_w is the water viscosity (10^{-6} s/m^2 at 20^{o}C).

Given the flood intensity and occurrence probability, the bridge vulnerability under flood should be analyzed considering both vertical and lateral failure modes. The load capacity of a bridge pile is directly related to the interaction between the piles and the surrounding soil. A lack of lateral confinement could result in lateral failure of the pile under flow-induced load and the axial load arising from the weight of the superstructure.

Vertical failure refers to the bridge failure in the vertical direction, which can be caused by inadequate soil support or pile instability. Most of the bridge vertical failures under flood are due to the insufficient soil support. The vertical ultimate resistance is given as (Briaud *et al.* 2014)

$$R_{vu} = 4 f_u L_p D + p_u D^2 - 4 f_u Z \cdot D \tag{4.13}$$

where f_u is ultimate side friction coefficient (kPa); p_u is ultimate point pressure (kPa); A_f is side friction area of the pile (m^2); L_p is embedded length of pile (m); and A_p is tip resistance area (m^2). The performance function g_V can be written as

$$g_V = x_u \cdot d_r \cdot R_{vu} - x_l L_v \tag{4.14}$$

where x_u and x_l are the unbiased value of resistance and load effect, respectively; L_v is the vertical load effect; and d_r is the damage ratio where d_r = 1 denotes total failure.

Similarly, given the lateral capacity and load effect, the performance function g_L associated with lateral failure could also be established.

The flow-induced load is the primarily lateral load that could possibly lead to lateral failure of piles. The high velocity flow can induce large lateral forces on the bridge piles threatening bridge safety. Basically, the pile behavior is dependent on the characteristic length L_T of the pile. Lateral failure of a short rigid pile occurs when the lateral resistance of the soil is exceeded, while the lateral failure of a long flexible pile occurs when the moment at one or more points exceeds the moment resistance. To estimate the performance of bridges during flood, lateral resistance of a bridge with and without flood-induced scour should be identified. For example, the lateral load capacity L_u of the pile in cohesionless soil could be computed using the following equation (Zhang *et al.* 2005)

$$L_u = 0.3(\eta \cdot K_p{}^2 + \xi \cdot K \cdot \tan\delta) \cdot \gamma \cdot a_{dr} \cdot D(2.7a_{dr} - 1.7L_p) \quad (4.15)$$

$$a_{dr} = [-(0.567L_p + 2.7e) + (5.307L_p{}^2 + 7.29e^2 + 10.54 \cdot e \cdot L_p)^{0.5}]/2.1996 \quad (4.16)$$

where e is the eccentricity of loading (m); a_{dr} is depth to the point of rotation (m); K_p is the passive earth pressure coefficient defined as $K_p = \tan^2(45 + \phi'/2)$; ϕ' is the internal friction angle of the soil; η is the shape factor to account for the non-uniform distribution of earth pressure in front of the pile; ξ is the shape factor to account for the non-uniform distribution of lateral shear drag; δ is the interface friction angle between the pile and the soil; and γ_s is the effective unit weight of soil (kN/m^3). The distribution forms for both the frontal soil resistance and side shear resistance are considered in the computational process (Zhang *et al.* 2005). The model proposed by Zhang *et al.* (2005) is used herein to

compute the pile lateral capacity, while other models could also be adopted for the assessment of specific bridge piles (Reese *et al.* 2004; Ko *et al.* 2014).

The flow-induced load as a function of the average flow velocity in terms of the pressure distribution form can be obtained as (AASHTO 2015)

$$p_{avg} = C_D \cdot \frac{\gamma_w \cdot V_w^{\,2}}{2} \tag{4.17}$$

where p_{avg} is average pressure of flowing water (N/m^2); V_w is velocity of water (m/s); γ_w is density of water (kg/m^3); and C_D is drag coefficient and C_D is 1.4, 0.7, and 0.5 for a square, circular, and diamond-shaped piles, respectively. The drag force on a pile bent is the product of the longitudinal pressure times the projected area of the bent. Accordingly, the flow pressure distribution can be transformed into equivalent nodal forces as the applied loads in the analysis.

Considering the lateral and vertical failure, the probability of bridge failure under flood could be expressed as the probability of union of two component failure events as follows:

$$P_f = P[\bigcup_{i=1}^{2} g_i(X) \le 0] \tag{4.18}$$

where g_1 and g_2 refer to performance functions associated with vertical and lateral limit states, respectively.

4.3. CONSEQUENCE EVALUATION AND RESILIENCE

The annual seismic loss of bridges under hazard effects (e.g., earthquake and flood) is presented in this section. Given the limit states of the bridge failure under earthquake and flood, the probability of a bridge being in different damage states including failure could

be computed. Based on the theorem of total probability, the total hazard loss is the sum of consequences weighted with the probability of having these consequences associated with damage states. Therefore, the annual loss given the occurrence of the hazard can be expressed as (Dong *et al.* 2013)

$$L_H(t) = \sum_{DS} C_{Cons|DS}(t) \cdot P_{DS|H}(t) \tag{4.19}$$

where $C_{Cons|DS}(t)$ is the conditional consequence (e.g., economic and social) given a damage state *DS* (e.g., major, complete) at year *t* and $P_{DS|H}(t)$ is the conditional probability of a damage state given a hazard at time *t*. As the aging effects are considered for the hazard vulnerability analysis, the hazard loss is related with time. The total annual hazard loss L_T is the sum of consequences (i.e., repair, time, and operating costs) weighted with the probability of having these consequences associated with damage states and can be computed as (Dong and Frangopol 2015)

$$L_T(t) = L_{REP}(t) + L_{RUN}(t) + L_{TL}(t) \tag{4.20}$$

where L_{REP} is annual repair loss (USD); L_{RUN} is annual operation loss (USD); and L_{TL} is annual time loss (USD). More detailed information regarding these metrics can be found in Chapter 2.

Resilience, as another performance indicator, is defined as the ability of a civil infrastructure system to maintain its functionality and return to normality following an extreme event. The resilience depends on the recovery patterns of structural systems. The repair schedule of highway bridges under extreme events depends on the judgment of the engineers and decision maker. Generally, the functionality of a bridge can be defined as the ability of opening traffic after an extreme event. Different functionality levels should

be considered for emergency response and post-earthquake recovery period. In the emergency response planning, it is of vital importance to identify whether the bridge located on a link is still available to convey the resources to the disaster area. In the post-earthquake recovery phase, the functionality associated with the bridge under hazard event can be defined as closed, limited use, and open which should be determined based on the engineering judgment.

The most widely adopted approach to quantify the resilience of a structural system is to compute it as the integration over time of the functionality under investigation as explained in Chapter 3. The time-variant resilience of bridge considering aging effects given the occurrence of the hazard is illustrated in Figure 4.1(b). As qualitatively shown in this figure given the same investigated time interval (e.g., Δt_1), a relatively smaller value of resilience may result when the extreme event occurs at a later stage of the investigated time. This figure aims to qualitatively show the aging effects on the resilience assessment of a highway bridge under hazard effects. By repeating the resilience assessment procedure at different points in time, the annual resilience of the bridge under the occurrence of hazard could be established.

4.4. LIFE-CYCLE HAZARD LOSS

The life-cycle hazard loss estimation methodologies of civil infrastructure systems traditionally ignore the effects of aging and deterioration during their service life. In general, such assumptions of time-invariant structural resistance are not valid for structures located near sources of environmental degradation. Considering the time

effects on hazard performance of a bridge, the total life-cycle hazard loss during the time interval [0, t_{int}] can be computed as (Yeo and Cornell 2005)

$$LCL_T(t_{\text{int}}) = \sum_{i=1}^{N(t_{\text{int}})} L_T(t_k) \cdot e^{-\gamma t_k} \tag{4.21}$$

where t_{int} is investigated time interval; $N(t_{int})$ is the number of hazard events that occur during the time interval; $L_T(t_k)$ is the expected annual hazard loss at time t_k; and γ is the monetary discount rate. If the aging effects are considered in the structural vulnerability analyses, total annual hazard loss L_T results in a function associated with t_k as indicated in Eq. (4.21). Based on Yeo and Cornell (2005), given the Poisson model, the times t_k have uniform and independent distributions in [0, t_{int}]. Given the $N(t_{int}) = n$, the total expected life-cycle loss could be computed as

$$\begin{aligned} E[LCL(t_{\text{int}}) | N(t_{\text{int}}) = n] &= E\left[\sum_{i=1}^{n} L_T(t_k) \cdot e^{-\gamma t_k}\right] = \sum_{i=1}^{n} E[L_T(t_k) \cdot e^{-\gamma t_k}] \\ &= \sum_{i=1}^{n} \left\{E[L_T(t_k)] \cdot E[e^{-\gamma t_k}] + Cov(L_T(t_k), e^{-\gamma t_k})\right\} \end{aligned} \tag{4.22}$$

$$Cov(L_T(t_k), e^{-\gamma t_k}) = E[(L_T(t_k) - E[L_T(t_k)]) \cdot (e^{-\gamma t_k} - E[e^{-\gamma t_k}])] \tag{4.23}$$

$$E[L_T(t_k)] = \int_0^{t_{\text{int}}} \frac{1}{t_{\text{int}}} L_T(t_k) dt \tag{4.24}$$

$$E[e^{-\gamma t_k}] = \int_0^{t_{\text{int}}} \frac{1}{t_{\text{int}}} e^{-\gamma t_k} dt \tag{4.25}$$

where *Cov* is the covariance between two random variables and *E* is the expected value.

Given the hazard occurrence model and annual hazard loss, the expected total hazard loss during a certain time interval could be obtained using Eqs. (4.21) - (4.25). The hazard occurrence could be assessed using time-dependent or time-independent models. By using Eq. (4.6), an effective Poisson rate associated with the time-dependent hazard could be obtained. The occurrence of earthquake using a homogeneous Poisson process,

which is independent of time, has been investigated (Wen and Kang 2001; Yeo and Cornell 2005). Furthermore, the aging effects are not considered in these studies.

The effects of climate change on the life-cycle hazard loss are also investigated herein. Considering the climate change, the probability of occurrence of the natural hazard is increasing. For example, the precipitation events have increased in frequency during the past 50 years and are expected to further increase in the future; this in turn will increase the flood intensity and occurrence probability. Based on Levinson (2006), the magnitude of the 100-year storm flood would now recur at an interval of 75 years on the basis of data from 1900 to 2005. This effect should be incorporated within the life-cycle hazard loss assessment. Accordingly, the probability of occurrence and hazard intensity would be larger than those associated with previous stages. In order to investigate the climate change effect, two parameters are introduced herein: (a) R_{fre} to represent the possible change in flood occurrence frequency, and (b) R_{int} to represent the increase of hazard intensity.

4.5. ILLUSTRATIVE EXAMPLE

The presented framework is illustrated on a typical two-span concrete box-girder bridges in California. It was designed based on Caltrans Seismic Design Criteria (Mackie and Stojadinovic 2003). The bridge has a single-column bent and Type I integral pile shafts with uniform circular cross section (i.e., D = 1.2 m) and amount of longitudinal reinforcement over the complete column and pile. The pile shaft length is 1.7 times the length of the column above grade. The schematic layout of the bridge with the length L of 36 m and the width W of 8 m, is shown in Figure 4.2.

4.5.1. Structural hazard vulnerability analyses

The probabilistic earthquake scenarios investigated herein are based on the seismic rupture sources in the San Francisco bay area (USGS 2003). The investigated earthquake magnitudes considered are related with the North San Andreas Fault as the bridge is located in this region. The slip rate of the investigated fault is 27 mm/year. The segment length and width of the fault are 191 and 11 km, respectively. By using Eq. (4.1), the expected magnitude *M* associated with the investigated rupture is 7.52. Then by using Monte Carlo simulation, the probabilistic earthquake magnitudes are generated by using the mean, a standard deviation of 0.12, and a truncation at ± 0.24 magnitude units above and below the mean. Subsequently, the ground motion intensity at the location of the bridge could be predicted using an attenuation equation (Campbell and Bozorgnia 2007).

The time-dependent earthquake analysis is adopted herein to investigate the probability of occurrence as indicated in Eqs. (4.3) - (4.5). Given the time-dependent earthquake model, the conditional probability of occurrence in the investigated time interval is computed using Eq. (4.5). Herein, the recurrence interval follows a lognormal distribution as indicated in Eqs. (4.3) and (4.4). Accordingly, the median value associated with this lognormal distribution is 198 years (i.e., $2.8\times10^{-5} \times (191\times10^{6}) / 27$) using Eq. (4.3). The characteristic earthquake considered herein is 1857 Fort Tejon earthquake. As the bridge was built in 1970, the time from this characteristic earthquake t_e is 113 years. Additionally, by using Eq. (6), an effective Poisson rate, with respect to the time-dependent hazard model is computed.

Over time, structural vulnerability increases due to aging effects (Akiyama *et al.* 2012; Dong *et al.* 2013). The investigated time horizon is considered to start from the year when the bridge was built and extends 75 years. The initial values of the fragility parameters are based on Basöz and Mander (1999). The PGA is used as a measure of the ground motion intensity. The parameters of deteriorated fragility curves are assumed to decrease (Decò and Frangopol 2013; Dong *et al.* 2014). The time-variant parameters of the fragility curves can be obtained using Eq. (4.8). The parameters γ_1 and ζ_1 associated with time-variant median are 1.616×10^{-5} and 2.234 to account for the nonlinear deterioration (Dong *et al.* 2014). In order to illustrate the aging effects on fragility curves, the seismic fragility curves for the representative bridge are presented in Figure 4.3(a) for t = 0, 25, 50, and 75 years. Each curve in this figure represents the probability of exceeding a major damage state for a given value of PGA. It is evident from Figure 4.3(a) that the probability of exceeding the major damage state increases with time.

The procedure for predicting bridge performance under flood includes the definition of flood scenario, the simulation of the pile-soil system, and the estimation of flow-induced loads. The vertical and lateral failure of the bridge under flood are computed herein. The three flood scenarios considered are associated with 100, 200, and 500-year.

For the investigated bridge, the annual peak flows of three flood scenarios are computed using Eq. (4.10). The drainage area and annual precipitation associated with the investigated specific area are 110 km^2 and 0.4 m, respectively (Gotvald *et al.* 2012). The values of parameters a_0, b_0, c_0, and d_0 associated with 100-year flood are 48.5, 0.866, 0.556, and 0, respectively (Gotvald *et al.* 2012). The values associated with 200 and 500-

year floods are 61, 0.863, 0.531, 0 and 79.3, 0.86, 0.503, 0, respectively (Gotvald *et al.* 2012). Based on Eq. (4.10), the expected annual discharges and flow velocity corresponding to the three flood scenarios are computed. Given these parameters, the maximum scour depth under the flood scenarios is computed by using Eq. (4.11); the PDFs of the scour depth associated with 100 and 500-year floods are shown in Figure 4.3(b). As indicated, the expected scour depth associated with the 500-year flood is much larger than that of the 100-year flood.

The probabilities of occurrence of the vertical and lateral failure modes are investigated herein. The probability of occurrence associated with vertical failure mode is computed using Eq. (4.14). The ultimate side friction coefficient f_u is 32 kPa and the ultimate point pressure p_u is 360 kPa (Briaud *et al.* 2014). Additionally, the model uncertainty is considered by using the coefficients x_u and x_l, which are assumed lognormally distributed with mean values 1.0 and 1.0, respectively, and the coefficients of variation 0.21 and 0.3, respectively (Briaud *et al.* 2014). The expected vertical load acting on the vertical direction of the bridge is 444.0 kN (Mackie and Stojadinovic 2003). The probability of occurrence of the vertical failure under 100-year flood is 0.0279 by using Monte Carlo simulation.

Similarly, the probability of occurrence of the bridge lateral failure is computed. The soil failure mode dominates the failure modes of the investigated bridge under lateral flood-induced load. Herein, the internal friction angle of the soil is 40° and the effective unit weight of soil γ_s is 17 kN/m^3 (Zhang *et al.* 2005). The shape factors η and ξ associated with the investigated circular pile are 0.8 and 1.0, respectively (Briaud and

Smith 1983). These parameters are selected for this specific bridge. Accordingly, the lateral load capacity is obtained by using Eq. (4.15). More detailed information could be found in Zhang *et al.* (2005). Given the lateral load obtained using Eq. (4.17), the probability of lateral failure under the flood is computed for different flood scenarios. Given the flow intensity Q_T associated with 100-year flood, the probability of lateral failure is 0.087. Finally, for the limit states associated with vertical and lateral failure, the series mode is adopted to compute the bridge system failure under flood as indicated in Eq. (18). Consequently, using the parameters employed in the illustrative example the probability of bridge failure under 100, 200, and 500-year flood are 0.110, 0.242, and 0.4353, respectively. These probabilities act as input for the hazard loss assessment.

4.5.2. Time-dependent hazard loss and resilience assessment

In this section, the hazard loss assessment of bridge under earthquake and flood is presented. The seismic loss is computed firstly. The repair cost ratios associated with slight, moderate, major, and complete damage states are 0.03, 0.08, 0.25, and 1, respectively (Mander 1999). There are uncertainties involved in hazard assessment and consequence evaluation. These uncertainties are considered in the probabilistic hazard loss assessment framework. Given the distribution parameters, these random variables can be generated using MATLAB (MathWorks 2014). By performing numerical simulation, the expected value and dispersion of the hazard loss can be obtained throughout the service life of the bridge. Based on Eqs. (4.19) and (4.20), the annual expected repair loss μ_{rep}, expected loss plus, and minus one standard deviation σ_{rep} are shown in Figure 4.4(a). Under the given seismic scenario, the major and complete

damage states contribute significantly to the total repair loss. The parameters associated with consequence evaluation are indicated in Table 4.1. The expected annual seismic total loss L_T and indirect loss L_{ID} (i.e., $L_{ID} = L_{RUN} + L_{TL}$) under the occurrence of the earthquake are shown in Figure 4.4(b). As indicated, there is a significant difference between the two cases (i.e., with and without considering the indirect loss). The indirect loss contributes significantly to the total seismic loss. Therefore, it is of vital importance to consider the aging effects and indirect consequences within the seismic performance assessment.

The probability of bridge failure under the flood was computed previously. Given $d_r = 0.75$ in Eq. (4.14), the bridge would be in a major damage state; while for $d_r = 1$, the bridge will fail. The damage ratios associated with seismic damage are adopted for the bridge states (e.g., major and complete damage states) under flood. Given the consequences associated with different damage states, the annual loss due to flood is computed. The expected annual loss associated with 100, 200, and 500-year floods is 4.633×10^6, 5.852×10^6, and 7.251×10^6 USD, respectively. As indicated, a significant difference exists among the loss under various flood scenarios. The flood loss associated with occurrence of 500-year flood is about 60% larger than that of the 100-year flood.

The recovery functionality of bridge under hazard is based on ATC (1999), which provides the recovery functionality associated with different damage states of the bridge under hazard effects. Given the investigated time interval and recovery functionality associated with seismic damage, the expected functionality is shown in Figure 4.5(a). As indicated, the functionality is sensitive to changes in the time from recovery and to aging

(i.e., t = 0, 25, 50, and 75 years). The functionality of the bridge increases with the time from recovery and decreases with aging. Subsequently, the resilience of the bridge can be obtained. The expected annual resilience of the bridge under seismic hazard is shown in Figure 4.5(b). As indicated, the expected resilience of the bridge under the occurrence of the earthquake decreases with time due to the aging effects.

The repair scheme associated with seismic damage is also adopted for the bridge states (e.g., major and complete damage states) under flood. Similarly, the resilience under the flood hazard is computed. The time-variant functionality of the investigated bridge under 100, 200, and 500-year floods is shown in Figure 4.6. Then, the corresponding resilience is computed. The resilience of the bridge under 100, 200, and 500-year floods is 0.934, 0.870, and 0.806, respectively. As expected, the 500-year flood is associated with the smallest resilience.

4.5.3. Life-cycle total loss under earthquake and flood

The life-cycle total hazard loss of the bridge under earthquake and flood is computed using Eq. (4.21). The time-dependent hazard model is employed for the earthquake hazard. The effective Poisson rate (see Eq. (4.6)) is used for capturing the time-dependency of the earthquake occurrence. Additionally, since aging effects are considered for the seismic vulnerability, the annual seismic loss depends on time as shown in Figure 4.4(b). Herein, the relationship between annual hazard loss L_{tk} and t_k can be expressed as

$$L_T(t_k) = at_k^{\,2} + bt_k + c \tag{4.26}$$

By using curve fitting techniques embedded in MATLAB (2014), the terms *a*, *b*, and *c* are 294.9, -4846, and 6.644×10^6, respectively. Then by substituting Eq. (4.26) into Eq. (4.22), the expected life-cycle hazard loss given *n* earthquakes is

$$\begin{aligned}
&E[LCL_T(t_{\text{int}}) \mid N(t_{\text{int}}) = n] \\
&= \sum_{k=1}^{n} \{E[L_T(t_k)] \cdot E[e^{-\gamma t_K}] + Cov(L_T(t_k), e^{-\gamma t_K})\} \\
&= \sum_{k=1}^{n} \{E[at_k^{\,2} + bt_k + c] \cdot E[e^{-\gamma t_K}] + Cov(L_T(t_k), e^{-\gamma t_K})\} \\
&= \sum_{k=1}^{n} \{\int_0^{t_{\text{int}}} \frac{(at^2 + bt + c)}{t_{\text{int}}} dt \cdot \int_0^{t_{\text{int}}} \frac{e^{-\gamma t}}{t_{\text{int}}} dt + Cov(L_T(t_k), e^{-\gamma t_K})\} \\
&= \sum_{k=1}^{n} \{\frac{1}{t_{\text{int}}^{\,2}} (\frac{a}{3} t_{\text{int}}^{\,3} + \frac{b}{2} t_{\text{int}}^{\,2} + c t_{\text{int}}) \cdot \frac{1 - e^{-\gamma t_{\text{int}}}}{\gamma} + Cov(L_T(t_k), e^{-\gamma t_K})\} \\
&= \frac{n}{t_{\text{int}}^{\,2}} (\frac{a}{3} t_{\text{int}}^{\,3} + \frac{b}{2} t_{\text{int}}^{\,2} + c t_{\text{int}}) \cdot \frac{1 - e^{-\gamma t_{\text{int}}}}{\gamma} + n \cdot Cov(L_T(t_k), e^{-\gamma t_K})
\end{aligned} \tag{4.27}$$

Since $E[N(t_{int})] = \nu_{eff} \cdot t_{int}$, the expected total life-cycle loss is

$$\begin{aligned}
&E[LCL_T(t_{\text{int}})] \\
&= \frac{E[N(t_{\text{int}})]}{t_{\text{int}}^{\,2}} (\frac{a}{3} t_{\text{int}}^{\,3} + \frac{b}{2} t_{\text{int}}^{\,2} + c t_{\text{int}}) \cdot \frac{1 - e^{-\gamma t_{\text{int}}}}{\gamma} + E[N(t_{\text{int}})] \cdot Cov(L_T(t_k), e^{-\gamma t_k}) \\
&= \nu_{eff} (\frac{a}{3} t_{\text{int}}^{\,2} + \frac{b}{2} t_{\text{int}} + c) \cdot \frac{1 - e^{-\gamma t_{\text{int}}}}{\gamma} + \nu_{eff} t_{\text{int}} \cdot Cov(L_T(t_k), e^{-\gamma t_K})
\end{aligned} \tag{4.28}$$

The covariance between $L_T(t_k)$ and $e^{-\gamma t_k}$ is

$$\begin{aligned}
&Cov(L_T(t_k), e^{-\gamma t_K}) = E[(L_T(t_k) - E(L_{k,T_k})) \cdot (e^{-\gamma t_k} - E(e^{-\gamma t_k}))] \\
&= E[(at_k^{\,2} + bt_k + c - (\frac{a}{3} t_{\text{int}}^{\,2} + \frac{b}{2} t_{\text{int}} + c)) \cdot (e^{-\gamma t_K} - \frac{1 - e^{-\gamma t_{\text{int}}}}{\gamma})] \\
&= \int_0^{t_{\text{int}}} \frac{(at^2 + bt - \frac{a}{3} t_{\text{int}}^{\,2} - \frac{b}{2} t_{\text{int}}) \cdot (e^{-\gamma t} - \frac{1 - e^{-\gamma t_{\text{int}}}}{\gamma})}{t_{\text{int}}} dt \\
&= \frac{b}{t_{\text{int}}} (\frac{1}{\gamma^2} - \frac{\gamma t_{\text{int}} + 1}{\gamma^2 e^{\gamma t_{\text{int}}}}) + \frac{a}{t_{\text{int}}} (\frac{2}{\gamma^3} - \frac{\gamma^2 t_{\text{int}}^{\,2} + 2\gamma t_{\text{int}} + 2}{\gamma^3 e^{\gamma t_{\text{int}}}}) + \frac{b}{2\gamma} (\frac{1}{e^{\gamma t_{\text{int}}}} - 1) + \frac{a t_{\text{int}}}{3\gamma} (\frac{1}{e^{\gamma t_{\text{int}}}} - 1)
\end{aligned} \tag{4.29}$$

By substituting Eq. (4.29) into Eq. (4.28), the expected life-cycle hazard loss is obtained as

$$E[LCL_T(t_{\text{int}})] = \\ = \nu_{eff} \cdot [b(\frac{1}{\gamma^2} - \frac{\gamma t_{\text{int}} + 1}{\gamma^2 e^{\gamma t_{\text{int}}}}) + a(\frac{2}{\gamma^3} - \frac{\gamma^2 t_{\text{int}}{}^2 + 2\gamma t_{\text{int}} + 2}{\gamma^3 e^{\gamma t_{\text{int}}}}) + c \cdot \frac{1 - e^{-\gamma t_{\text{int}}}}{\gamma}] \quad (4.30)$$

Finally, the expected total life-cycle hazard loss is computed using Eq. (4.30). Herein, the total seismic losses associated with four different cases are investigated. These cases are as follows: (a) Case 1 takes into account both time-dependent hazard and aging effects; (b) Case 2 takes into account time-dependent hazard and disregards aging effects; (c) Case 3 assumes time-independent hazard (i.e., Poisson process) and takes into consideration aging effects; and (d) Case 4 assumes time-independent hazard and disregards aging effects. The expected total seismic losses under each of these four cases are shown in Figure 4.7(a). As indicated, the time-dependent hazard can affect the total seismic loss significantly and should be incorporated within the life-cycle loss assessment process. In general, disregarding aging effects can lead to the underestimation of seismic loss. By using the parameters indicated in the illustrative example, the time-dependent hazard model has a stronger effect on the total hazard loss than the aging effects. Considering a time interval of 75 years, the total seismic loss associated with the case considering time-dependent hazard model and aging effects (i.e., Case 1) is about 40% larger than that associated with the case considering the time-independent process and no aging effects (i.e., Case 4).

Additionally, the total expected life-cycle loss depends on the time from last earthquake, discount rate of money, and remaining service life of the deteriorating bridge. The discount rate is assumed to vary in the interval 1 to 4% while the remaining service life of the bridge is assumed to vary from 25 to 100 years. The expected loss under different discount ratios is shown in Figure 4.7(b). An increase in the discount rate tends

to decrease the estimated life-cycle loss, while an increase in remaining service life increases the expected life-cycle loss. The effects of t_e, elapsed time from the last earthquake, are also investigated as indicated in Figure 4.7(c). Both the discount rate and t_e have profound effects on the life-cycle loss and should be well estimated.

The annual flood loss under the occurrence of different flood intensities has been investigated previously. By using Eq. (4.30), the expected life-cycle loss of the bridge under flood could be computed assuming that the occurrence of flood follows a Poisson process. Herein, the terms a and b are assumed 0, and c is 4.633×10^6, 5.852×10^6, and 7.251×10^6 USD for 100, 200, and 500-year floods, respectively. The total loss under different time intervals is shown in Figure 4.8(a). The 100-year flood results in the largest total flood loss. Considering a 75-year interval, the total expected life-cycle flood loss associated with 100-year is found to be about 2.2 times larger than that associated with 500-year flood. Though the annual loss under the occurrence of the 500-year flood is much higher than that associated with100-year flood, the expected total life-cycle flood loss associated with 100-year flood is higher than that associated with 500-year.

As described previously, there is a great amount of uncertainty in predicting how climate change may affect hazard patterns. To assess the impact of the flood intensity and frequency on the total life-cycle loss, the expected life-cycle flood loss is computed considering different scenarios. Two terms are chosen herein to represent a wide range of possible changes in flood frequency and flow intensity: (a) R_{fre} refers to decrease in frequency and is smaller than 1, and (b) R_{int} denotes increase in intensity and is larger than 1. The flood intensity and occurrence interval are computed as $R_{int} \times Q_T$ (flow

intensity) and $R_{fre} \times T$ (occurrence interval). The relevant expected life-cycle flood loss under 100-year flood considering climate change is shown in Figure 4.8(b). The climate change scenarios can be modified as more information becomes available. As indicated, the total life-cycle loss would increase under the investigated climate scenarios. Additionally, the comparison of total hazard loss under earthquake and flood is shown in Figure 4.8(c). As indicated, the expected total life-cycle seismic loss is larger than that associated with 200-year flood and smaller than that with respect to 100-year flood under the investigated time interval.

4.6. CONCLUSIONS

This chapter presents a methodology for the time-variant hazard loss and resilience assessment of highway bridges under earthquake and flood in a life-cycle context considering uncertainties. The effects associated with time-dependent hazard and aging effects are investigated. The methodology is illustrated on a highway bridge located in California.

The following conclusions are obtained:

1. Structural deterioration and time-dependent hazard have effects on resilience and expected total life-cycle loss. In order to provide a more realistic approach, time-dependent hazard model should be adopted in life-cycle loss assessment process.
2. The difference between the life-cycle seismic loss with and without considering aging effects increases as the investigated time interval increases. Moreover, due to aging effects, the resilience of damaged bridges under seismic hazard decreases

significantly with time. Additionally, the expected total loss depends on the indirect consequences.

3. The results of the sensitivity study using the proposed loss model reveal that the changes in total life-cycle loss are sensitive to changes in time from the last earthquake, discount rate of money, and remaining service life. The loss estimates tend to be more sensitive to the parameters associated with the time-dependent hazard model than to the aging effects.
4. Given various hazard occurrence models and discount rates, the total hazard loss associated with earthquake and flood during an investigated time interval is different and the contribution of the hazards changes. The specific risk mitigation strategies associated with the various hazards could be determined.

Table 4.1 Parameters associated with the consequence evaluation

Random variables	Notation	Value	References
Average daily traffic	ADT	19750	FHWA (2015)
Daily truck traffic ratio	T	13%	FHWA (2015)
Length of link (km)	l_l	6	FHWA (2015)
Detour additional distance (km)	D_l	2	FHWA (2015)
Vehicle occupancies for cars	O_{car}	1.5	Stein *et al.* (1999)
Vehicle occupancies for trucks	O_{truck}	1.05	Stein *et al.* (1999)
Rebuilding costs ($/m^2)	c_{reb}	2306	Mander (1999)
Compensation for truck drivers ($/h)	c_{ATC}	29.87	Stein *et al.* (1999)
Operating costs for cars ($/km)	$c_{Run,car}$	0.4	Stein *et al.* (1999)
Operating costs for trucks ($/km)	$c_{Run,truck}$	0.57	Stein *et al.* (1999)
Wage for car drivers ($/h)	c_{AW}	11.91	Stein *et al.* (1999)
Detour speed (km/h)	S	50	Dong and Frangopol (2015)
Link speed (km/h)	S_0	80	Dong and Frangopol (2015)

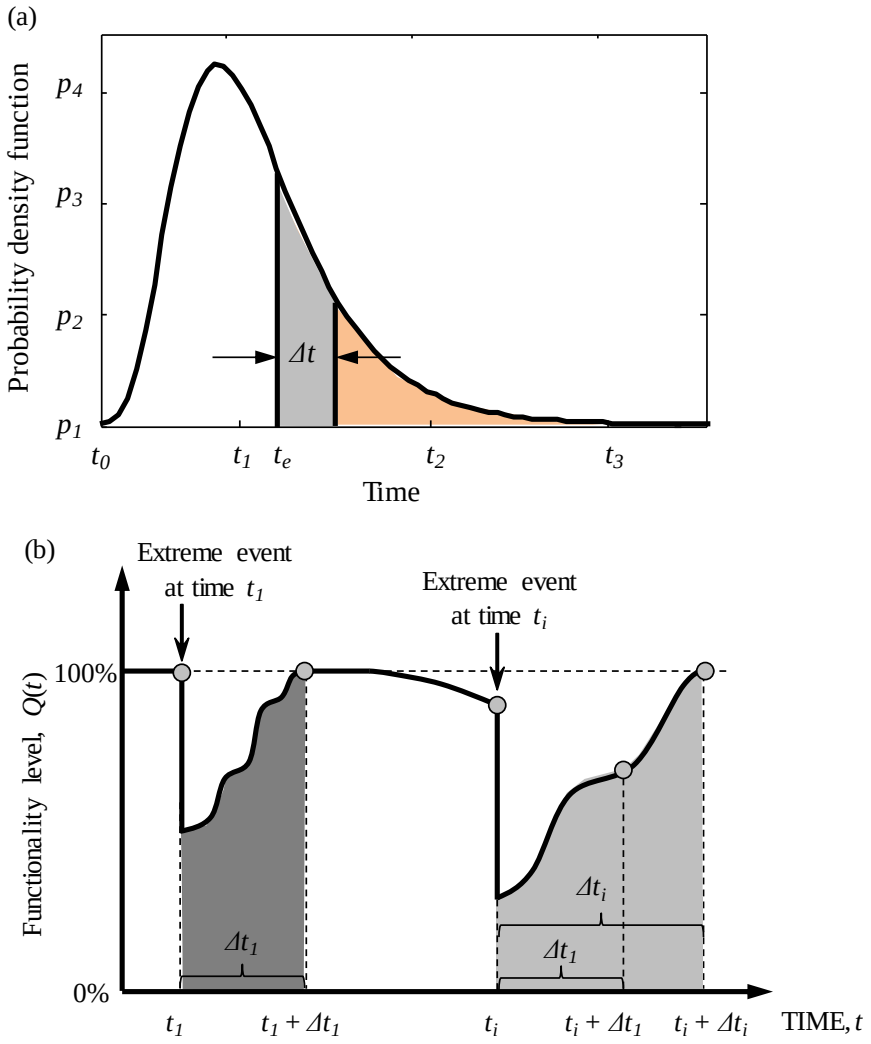

Figure 4.1 (a) Probability density function associated with hazard recurrence interval using time-dependent hazard model and (b) schematic representation of qualitative time-dependent resilience of highway bridges under extreme events in a life-cycle context

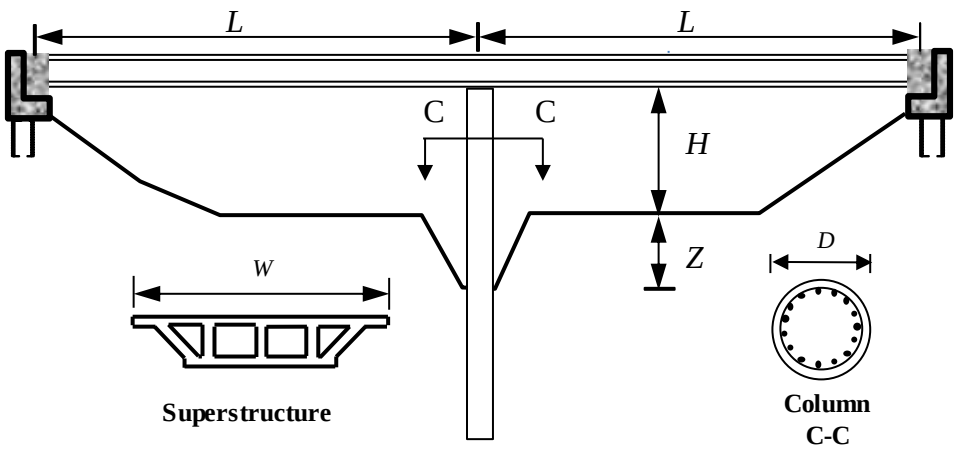

Figure 4.2 Elevation and cross-sectional view for the case study bridge piers (elevation of a typical bridge pier and cross-section)

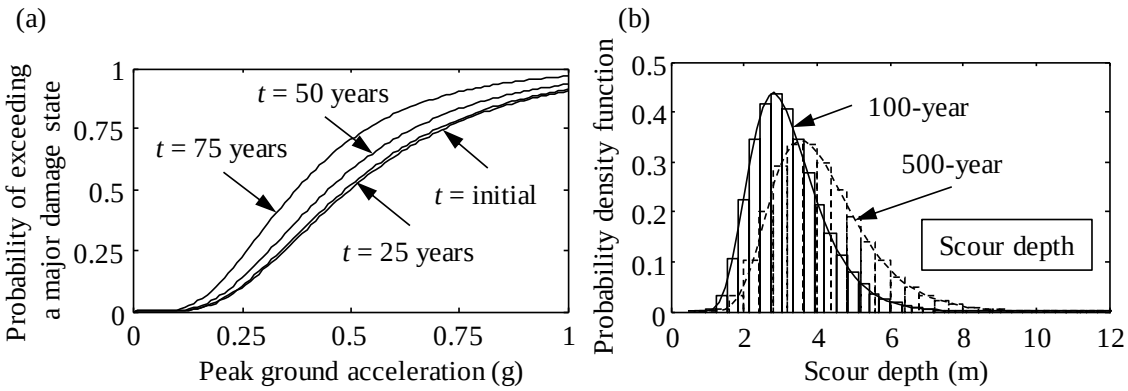

Figure 4.3 (a) Time-dependent fragility curves of the bridge under investigation and (b) probabilistic scour depth under 100 and 500-year floods

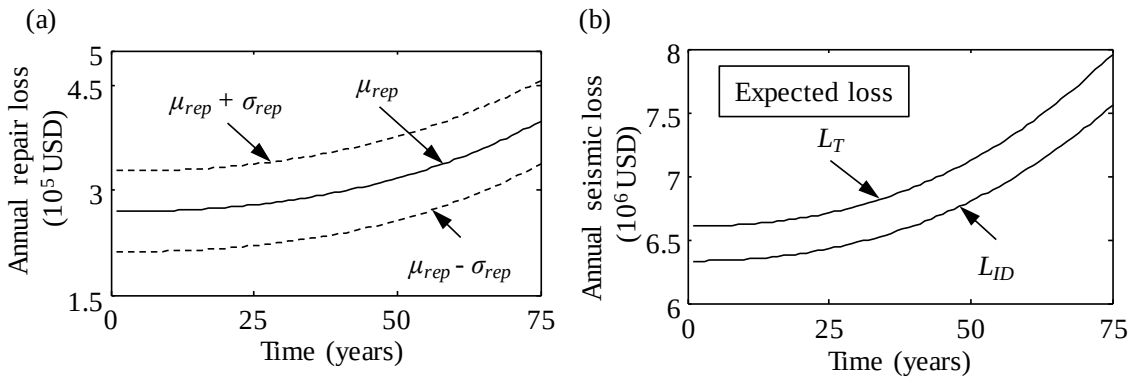

Figure 4.4 (a) Time-dependent seismic expected annual repair loss, and mean plus and minus one standard deviation and (b) expected annual total and indirect seismic loss

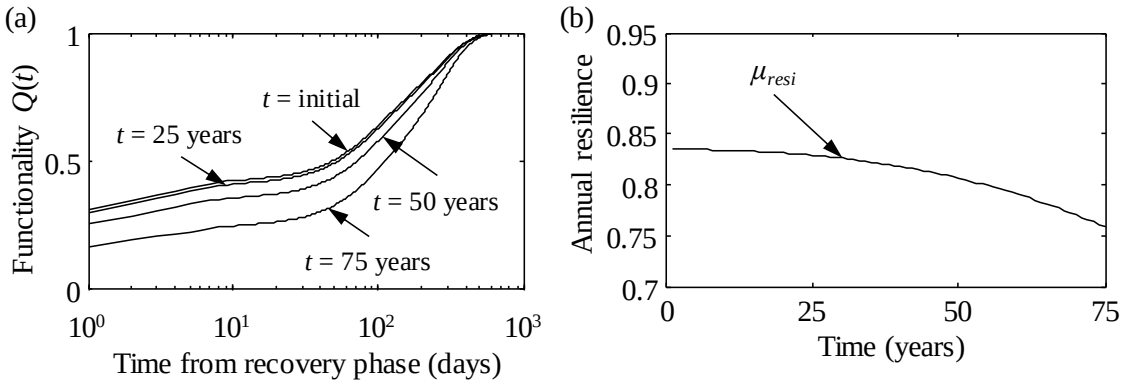

Figure 4.5 (a) Expected functionality of highway bridge under given seismic scenario at t = initial, 25, 50, and 75 years and (b) expected resilience under the occurrence of earthquake

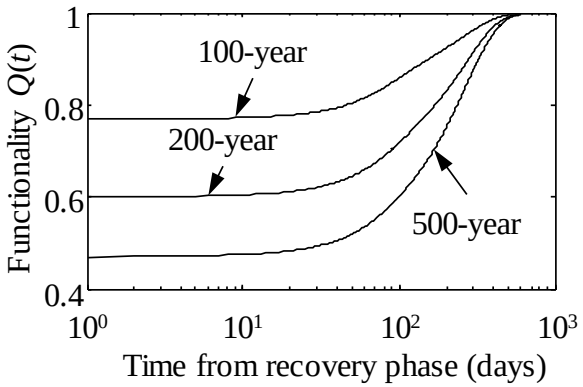

Figure 4.6 Time-variant functionality of the bridge under 100, 200, and 500 years floods

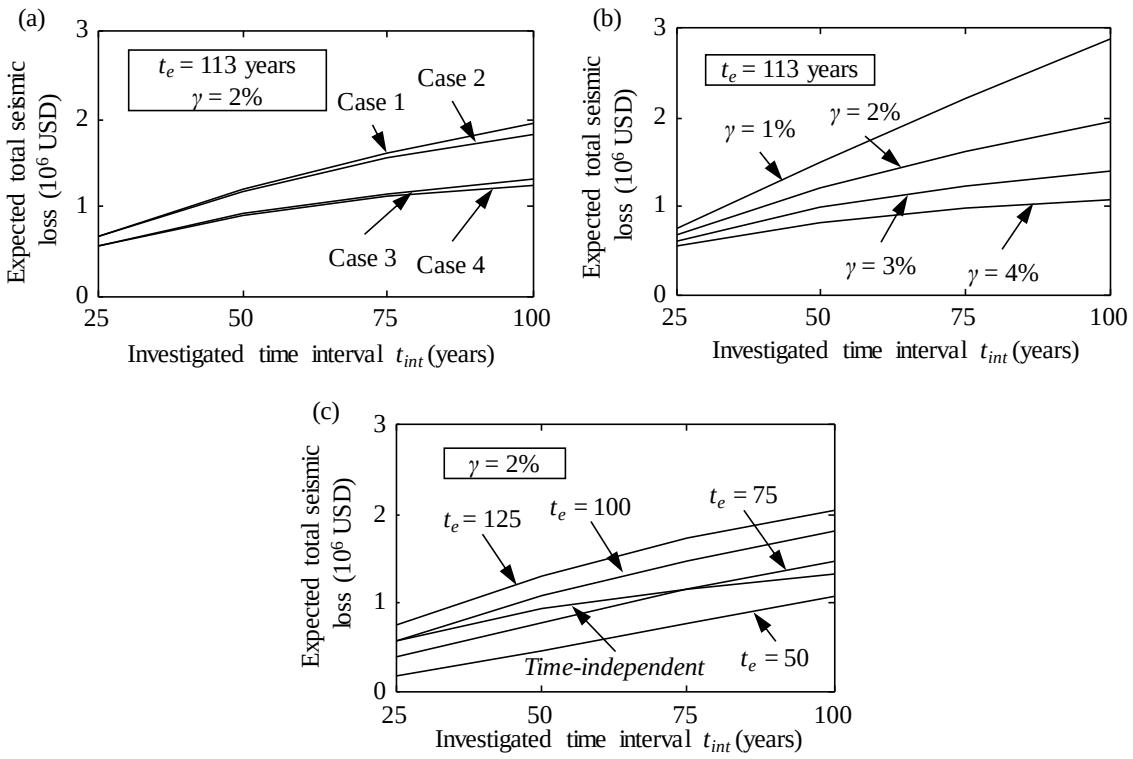

Figure 4.7 (a) Expected life-cycle total seismic loss under different time-intervals considering four different cases, (b) effect of discount rate of money on the expected total seismic loss, and (c) effect of t_e (time from last earthquake) on the total seismic loss

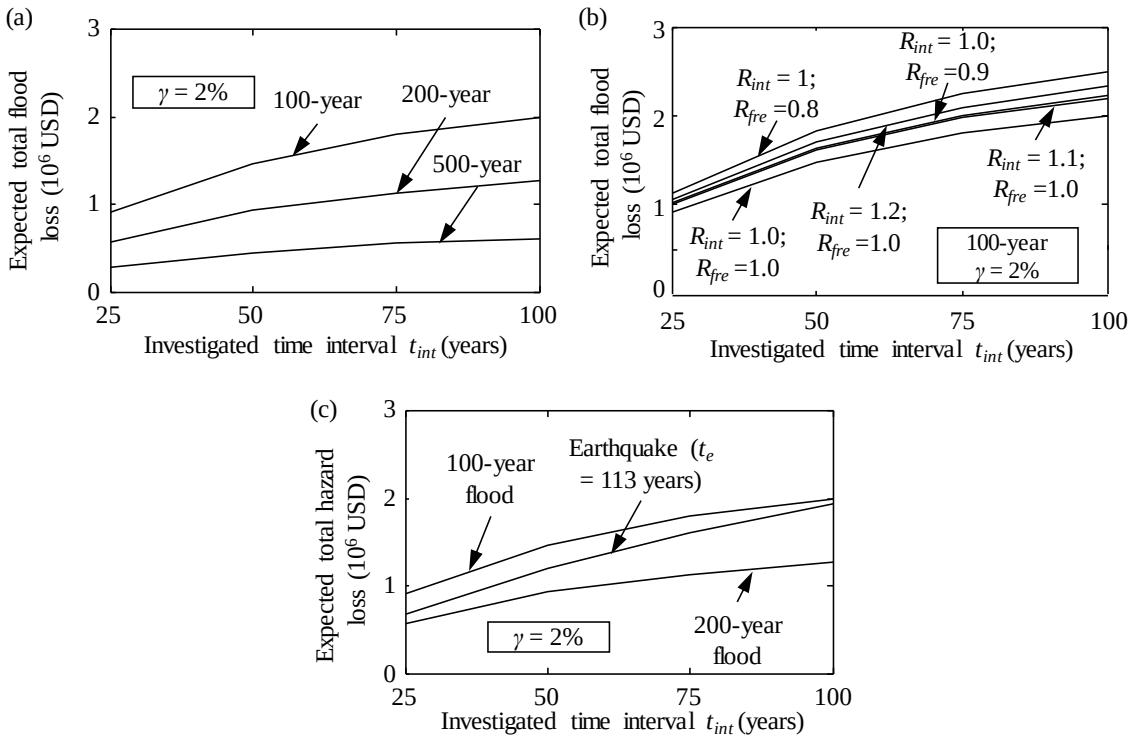

Figure 4.8 (a) Expected total life-cycle loss under different flood scenarios, (b) comparison of expected life-cycle flood loss considering climate change under different hazard intensities and frequencies, and (c) comparison of the expected total life-cycle loss associated with flood and earthquake

CHAPTER 5

SUSTAINABILITY OF HIGHWAY BRIDGE NETWORKS UNDER SEISMIC HAZARD

5.1. INTRODUCTION

Transportation network systems are critical for the economy and the society. After a destructive earthquake, the functionality of highway networks can be significantly affected, leading to disastrous effects on the economy. The 1994 Northridge earthquake caused about 140 roads closures and over 40 billion USD in losses (ABAG 1997). In recent years, the seismic risk assessment of transportation networks has become a popular research area (Shiraki *et al.* 2007; Bocchini and Frangopol 2012). In order to evaluate the seismic risk of transportation networks, it is necessary to develop a methodology that integrates the probabilities of occurrence of seismic events in a region, the vulnerability of the civil infrastructure, and the consequences of the seismic hazard to society, environment and economy. Sustainability can serve as a useful tool in decision making and risk mitigation associated with civil infrastructure systems. Quantifying the seismic loss of transportation networks associated with the three metrics of sustainability at the component and system levels still remains a challenging task.

The three main components of seismic risk analysis are hazard exposure, transportation network configuration, and consequences analysis (Loh *et al.* 2003). Kiremidjian *et al.* (2007) investigated the direct loss from damage to bridge and travel delays under a specific earthquake scenario; Shiraki *et al.* (2007) evaluated the total

bridge network delay due to the seismic hazard based on user-equilibrium analysis; Padgett *et al.* (2010) investigated the seismic risk associated with a bridge network under several deterministic scenarios; Bocchini and Frangopol (2011) presented a novel approach to assess the damage level of bridges in a network using fragility and network flow analysis; Bocchini and Frangopol (2012) investigated the resilience of bridge networks associated with total travel time and distance under seismic hazard. In general, these studies did not account for the uncertainties associated with seismic hazard and the time effects. Decò and Frangopol (2013) presented a framework for the quantitative assessment of time-variant risk of single bridges within a bridge group. Sustainability assessment for single bridges accounting for the effects of flood-induced scour on seismic vulnerability was presented by Dong *et al.* (2013). In this chapter, the time-variant risk and sustainability of highway bridge networks considering earthquake scenarios accounting for the uncertainties associated with seismic hazard and their associated consequences (i.e., environmental, social, and economic) are investigated.

Seismic risk should be treated by considering a large number of earthquakes that can occur in the region. The selected probabilistic seismic scenarios should be able to approximate the regional seismicity associated with the United States Geological Survey (USGS) regional hazard maps. Chang *et al.* (2000) developed a method to identify a set of seismic scenarios to approximate the regional seismic intensity; Vaziri *et al.* (2012) improved this method to estimate long-term earthquake hazards by selecting a small subset of earthquake scenarios to account for possible events; Jayaram and Baker (2010) used importance sampling to simulate a reduced set of seismic scenarios. The intensities

of ground motions at different sites under a seismic scenario should be correlated since they result from the same earthquake. Wang and Takada (2005) computed the correlations of seismic ground motions using dense observation data of earthquakes and determined correlation lengths ranging from 20 to 50 km. Jayaram and Baker (2009) estimated the correlation between spatially distributed spectral accelerations at various spectral periods using data from several past earthquakes. Adachi *et al.* (2009) studied the effects of spatial correlation of seismic intensities on the serviceability of water systems. It is of vital importance to incorporate the correlation of ground motion into sustainability assessment of spatially distributed bridge networks associated with probabilistic seismic scenarios.

A transportation network is defined in terms of its nodes and links. Nodes are locations where highway segments intersect. Links are the highway segments connecting two nodes. The bridges are the vulnerable components in the network and should be paid special attention (Liu and Frangopol 2006). At the component level (i.e., individual bridge), fragility curves are the common tools to define the conditional probability of occurrence of a representative event under certain ground motion intensity. At the system level (i.e., bridge network), performance of the damaged link depends on the number of bridges on the link and the damage states of these bridges. It is important to estimate the damage state of the bridge and its impact on the system performance associated with earthquake scenario. Throughout their lifetime, many bridges are subjected to harsh environmental conditions. Corrosion induced deterioration can affect the seismic performance of bridges by increasing the seismic vulnerability over time (Ghosh and

Padgett 2010; Akiyama *et al.* 2012; Zhu and Frangopol 2013). Consequently, their damage state of the link will worsen through the lifetime. The time-variant seismic risk assessment in a life-cycle context on component and system levels is a relatively new area of research to be explored and will be addressed herein.

In this chapter, a framework for the time-variant seismic sustainability and risk assessment of highway bridge networks is presented. The sustainability of the network is quantified in terms of its social, environmental, and economic metrics. The seismic scenarios consist of the rupture of fault segments nearby the region of interest. The performance of network links is quantified based on individual bridge performance evaluated through fragility analyses. The time-variation of the sustainability metrics and risk due to structural deterioration is identified. The effects of the correlation among the seismic intensities at different locations are also investigated. The approach is illustrated on a transportation network located in Alameda County, California. This chapter is based on a published paper Dong *et al*. (2014a).

5.2. TIME-VARIANT METRICS OF SUSTAINABILITY

The first step of the methodology for assessing sustainability is to identify the characteristics and inventory of the transportation networks that consist of spatially distributed components. A flow chart summarizing the methodology is presented in Figure 5.1. The three metrics of sustainability can be assessed based on probabilistic seismic scenario events (e.g., earthquakes with different magnitudes). A set of seismic scenarios of each active fault in the region should be identified to capture the seismic intensity. For a prescribed earthquake intensity, the probabilities of a structure being in

various damage states following the earthquake can be determined using the fragility curves. All sets of ground motions that capture the seismic activity will be used in the fragility analysis to evaluate damage state of every bridge in the network. Based on the damage state of each bridge, the seismic vulnerability of the link can be assessed. The time-variant seismic vulnerability of the bridges and links is evaluated through their lifetime to capture the time effects due to structural deterioration. This procedure will be repeated for all bridges within the network considering the entire set of earthquake scenarios. The increase in the damage state of the link can reduce the link traffic capacity and speed limit, which results in additional travel time. The amount of traffic volume that exceeds the capacity of the damaged link has to follow the detour. The social metrics (downtime and fatalities), the environmental metrics (energy wastes and carbon dioxide emissions), and the economic metrics (costs) associated with each damage state should be evaluated. Then, the expected metrics of sustainability can be quantified by multiplying these outcomes by the probability of each damage state. In order to include the time effects (e.g., the effects of structural deterioration), the described procedure should be repeated for each time instant considered through the lifetime.

5.3. PROBABILISTIC EARTHQUAKE SCENARIOS

5.3.1. Seismic hazard

Seismic risk assessment should be based on a set of probabilistic earthquake scenarios that will approximately provide the seismic activity of the region under investigation. Each probabilistic seismic scenario is associated with a frequency of occurrence, derived from the fault activity, magnitude, and location. The seismic risk should be considered as

the sum of the risk associated with possible events generated by all fault sources in the region. A set of earthquake rupture events should be selected first based on the region of interest.

In a high seismicity area, the number of seismic scenarios to be used in order to accurately reflect the seismic activity of the region may be very large. It is not practical to consider all of the possible scenario events. The scenarios can be selected to approximate the regional seismic activity using the USGS regional hazard maps. The selection of the specific earthquake scenarios depends on the region of application.

5.3.2. Ground motion intensity and spatial correlation

The level of structural damage depends on the ground motion intensity at the location of the structure. The attenuation relation has been used to predict the ground-motion intensity at a certain site and is usually represented in logarithmic form (Boore *et al.* 1997, Campbell *et al.* 2008). In this chapter, the attenuation relationship proposed by Graizer and Kalkan (2007) is implemented. This attenuation equation, which is for shallow crustal earthquakes, is used as crustal earthquakes dominate in the region of the investigated network (SSA, 2010). The Graizer-Kalkan model provides consistently good approximations not only in the near-fault region but also at farther distances for a wide range of magnitude levels. This approach can be used for earthquakes in other regions and can give accurate predictions against the actual data at a wide range of magnitudes and distances. The attenuation relation is described by the following expression (Graizer and Kalkan 2007)

$$\ln(Y) = \ln[A(M,F)] - 0.5\ln[(1-\frac{R}{R_0})^2 + 4D_0{}^2\frac{R}{R_0}] - 0.5\ln[(1-\sqrt{\frac{R}{R_1}})^2 + 4D_1{}^2\sqrt{\frac{R}{R_1}}] + b_v \ln\frac{VS_{30}}{VA} + \sigma_{\ln Y} \quad (5.1)$$

where Y is the strong-motion parameter of interest; M is the earthquake magnitude; $A(M,F)$ is the magnitude and fault-type scaling function; R is the source-to-site distance; R_0 is the corner distance; R_1 is the distance threshold after which faster attenuation takes place; D_0 is the parameter quantifying the intensity of bump on the attenuation curve; D_1 is the parameter that produces smooth transition to the faster attenuation at distances larger than R_1; F is a parameter characterizing faulting style; VS_{30} is the average shear-wave velocity in upper 30 m; VA and b_v are parameters associated with linear site correction; and σ_{lnY} is the total standard deviation of lnY. The earthquake magnitude M and the average shear-wave velocity VS_{30} in the upper most 30 m are inherently uncertain and, therefore the parameters are considered random. More detailed explanation of terms in Eq. (5.1) can be found in Graizer and Kalkan (2007).

The characteristics of seismic excitations at different sites caused by the same earthquake are correlated. It is demanding to consider the spatial correlation of peak ground motions. Several studies (Bazzurro and Luco 2004, Lee and Kiremidjian 2007) revealed that the PGA for a given seismic scenario at different sites is spatially related and the correlation is higher for closer sites. The seismic performance of the structures with similar characteristics is correlated through the source-to-site distance and soil condition. The spatial relationship of ground motion intensity across the network affects the functionality and seismic loss of the network. Wang and Takada (2005) computed the

correlations using the ground motion time histories records during earthquakes, such as the peak ground accelerations. In this chapter, their approach is adopted to account for correlations.

5.4. SEISMIC VULNERABILITY OF TRANSPORTATION NETWORK

5.4.1. Time-variant seismic fragility curves

Fragility curves define the exceedance probability of a damage state for a given level of peak ground acceleration or ground deformation. Due to the fact that the structural performance deteriorates with time, the fragility curves should be updated through the lifetime of the structure. In this chapter, the time-variant median value of intensity associated with a certain damage state is assumed to vary in time. More detailed information associated with the time-variant fragility curves could be found in Chapter 4.

These conditional probabilities can be mapped to the bridge damage index (*BDI*) value (Shiraki *et al.* 2007) given in Table 5.1. *BDI* can be evaluated by mapping the bridge damage states given the ground acceleration based on realization of a value between 0 and 1. A *BDI* of 1.0 indicates a bridge damage state of collapse. A value of 0 corresponds to no damage state following an earthquake. The expected *BDI* can be obtained by multiplying the probability of being in each damage state with the corresponding damage factor. Accordingly, the time-variant expected *BDI* of a bridge for a certain ground motion intensity is

$$BDI(t) = BDI_1 \cdot P_{DS_1|IM}(t) + BDI_2 \cdot P_{DS_2|IM}(t) + BDI_3 \cdot P_{DS_3|IM}(t) + BDI_4 \cdot P_{DS_4|IM}(t) \quad (5.2)$$

where BDI_i is the bridge damage index for the respective damage state i as presented in Table 5.1.

5.4.2. Damage assessment of link

The transportation network is defined in terms of nodes and links. A link is considered to be a single element connecting the nodes of a network. The bridges are typically the most vulnerable structures in a network and should be paid special attention (Liu and Frangopol 2006). The common assumption that bridges are the only vulnerable elements of the entire network is used herein. Information on seismic vulnerability of roads can be found in Bird and Bommer (2004) and Jibson *et al.* (2004). Following an earthquake, the damaged bridges can be open, closed, or partially open. Consequently, traffic flow in the link can be different and speed limits might be reduced for different damage conditions of the link. As there may be several bridges located on the link, the damage state of each bridge can affect the functionality of the link. The performance of the link after an earthquake can be expressed in terms of link damage index (*LDI*) which depends on the *BDI*s of the bridges on the link. Due to the fact that the seismic vulnerability of the bridge deteriorates with time, *LDI* should also be updated during the investigated time horizon of the transportation networks. *LDI* can be expressed as (Chang *et al.* 2000)

$$LDI(t) = \sqrt{\sum_{j=1}^{n} (BDI_j(t))^2} \tag{5.3}$$

where n is the number of the bridges located in the link; and BDI_j is the expected bridge damage index for bridge j. The level of link traffic flow capacity and flow speed for a damaged link depends on *LDI*. The intact state, slight, moderate, and major damage states represent $LDI \leq 0.5$, $0.5 < LDI \leq 1.0$, $1.0 < LDI \leq 1.5$, and $LDI > 1.5$, respectively (Chang

et al. 2000). In slight damage state, the flow capacity and the flow speed are 100% and 75% of those for the intact link. In moderate damage state, the flow capacity and the flow speed are 75% and 50% of those for the intact link. In major damage state, the flow capacity and the flow speed are 50% and 50% of those for the intact link (Chang *et al.* 2000). The increase in the damage state of the link will reduce the link traffic capacity and speed limit.

5.5. TIME-VARIANT SUSTAINABILITY ASSESSMENT

As stated previously, sustainability is quantified in terms of social, environmental, and economic metrics. These include the expected downtime, expected energy waste and carbon dioxide emissions, and the expected loss. The structure is defined as sustainable if the cost of repair, energy spent on subsequent repair or replacement, and carbon dioxide emissions are less than their target values. The social and environmental metrics can be converted into economic metrics in monetary unit if it is possible to evaluate the monetary value of consequences associated with these two metrics. The earthquake can disrupt traffic flow and affect the emergency responses and recovery operation which may yield higher consequences than the repair or rebuilding of a damaged infrastructure system. In this section, the evaluation of the consequences at both component and system level (e.g., bridge and link levels) associated with the three metrics of sustainability is presented.

5.5.1. Social loss

Following an earthquake, the performance of each component within the bridge network may be affected. For instance, the traffic volume on a link might be reduced. The traffic

might have to follow detours to arrive at the destination. Damage states of links depend on the damage states of the bridges on the link, and the bridge is assumed to be the only vulnerable component in the network. The *social metric* of sustainability is calculated considering the extra travel time and distance experienced by vehicle operators in addition to any fatalities that may occur due to bridge failure. The extra travel time and distance may be representative of the functionality of a bridge network under seismic hazard; large travel times and distances reveal a high reduction of functionality associated with a bridge network (Bocchini and Frangopol 2011).

The extra travel time for the user in a bridge network can be expressed as (Dong *et al.* 2014a)

$$ET(t) = \sum_{j=1}^{n} \sum_{i=1}^{4} P_{LDSj,i|IM,k}(t) d_{ij} [ADE_{ij}(t)(\frac{l_j}{S_{D,j}} - \frac{l_j}{S_{0,j}}) + ADT_{ij}(t)\frac{D_j}{S}] \quad (5.4)$$

where n is the number of links in the transportation network; N is the total number of seismic scenarios under investigation; p_k is the annual probability of occurrence of hazard k; $P_{LDSj,i|IM,k}(t)$ is the conditional probability of the jth link being in damage state i after an earthquake k occurs at time t; d_{ij} is the downtime associated with the ith damage state of the jth link (days); ADT_{ij} is average daily traffic that is detoured at the jth link in damage state i; D_j is length of the detour for the jth link (km); S is the detour speed (km/h); ADE_{ij} is the average daily traffic remaining at the jth link in damage state i; l_j is the length of link j (km); S_0 is the traffic speed on intact link j (km/h); and S_D is the traffic speed on damaged link j (km/h). Similarly, the extra travel distance due to detour can be computed as (Decò and Frangopol 2013)

$$ED(t) = \sum_{j=1}^{n} \sum_{i=1}^{4} P_{LDSj,i|IM,k}(t) d_{ij} ADT_{ij}(t) D_j \tag{5.5}$$

The fatalities following an earthquake are associated with bridge failure as bridges are assumed as the only vulnerable components within the network. A statistical analysis is required to evaluate the number of fatalities within different damage states. The estimated expected average number of fatalities following a seismic hazard occurring at a certain time can be expressed as (based on Padgett *et al.* 2009)

$$FA(t) = \sum_{j=1}^{m} \sum_{i=1}^{4} P_{BDSij|IM}(t) \cdot FT_{ij} \tag{5.6}$$

where $P_{BDSij|IM}(t)$ is the conditional probability of the bridge j being at damage state i after having an earthquake at time t with certain ground motion intensity; FT_{ij} is the average number of fatalities associated with the damage state i of bridge j; and m is the number of the bridges in the transportation network.

5.5.2. Environmental loss

Due to the effects of the traffic detour on the link, additional carbon dioxide emissions are produced and additional energy is consumed. Carbon dioxide is the primary greenhouse gas emitted through human activities and has an important effect on the environment. The energy waste and carbon dioxide emissions due to detour are the main factors that contribute to environmental metric. They are expressed as (based on Stein *et al.* 1999)

$$EN_{DT}(t) = \sum_{j=1}^{n} \sum_{i=1}^{4} P_{LDSij|IM}(t) \cdot ADT_{ij}(t) \cdot D_j \cdot d_{ij} \cdot \left[Enp_{car} \cdot (1 - \frac{T_j}{100}) + Enp_{Truck} \cdot \frac{T_j}{100} \right] \tag{5.7}$$

where Enp_{car} and Enp_{Truck} are the environmental metric per unit distance for cars and trucks, respectively (e.g., carbon dioxide kg/km); and T_j represents the average daily truck traffic ratio (*ADTT*, %) of link *j*.

The total embodied energy within a structure depends on the material and geometry of the structure. The expected energy waste and carbon dioxide emissions due to repair actions associated with each damage state are another source of environmental metric. Based on Padgett *et al.* (2009), the energy wastes associated with different damage states can be taken as a fraction of the entire structure's embodied energy based on the damage ratio. The energy waste is measured in terms of MJ/m^3 and the carbon dioxide emission is measured in terms of kg/m^3. It is computed as

$$EN_{RE}(t) = \sum_{j=1}^{m}\sum_{i=1}^{4} P_{BDSij|IM}(t) \cdot (Enp_{Steel} \cdot V_{j,Steel} + Enp_{Conc} \cdot V_{j,Conc}) \cdot RCR_{ij} \qquad (5.8)$$

where Enp_{Steel} and Enp_{Conc} are the environmental metric per unit volume for steel and concrete, respectively (e.g., carbon dioxide emissions kg/m^3); $V_{j,Steel}$ and $V_{j,Conc}$ are the volume of the steel and concrete of bridge *j*; and RCR_{ij} is the repair cost ratio for a bridge at damage state *i*.

5.5.3. Economic loss

The repair cost of a bridge associated with a certain damage state can be considered proportional to the rebuilding cost of the bridge (Mander 1999, Stein *et al.* 1999). The repair cost of the transportation network sums up the repair cost of all the bridges in the network (based on Stein *et al.* 1999)

$$C_{REP} = \sum_{j=1}^{m}\sum_{i=1}^{4} P_{BDSij|IM}(t) \cdot RCR_{ij} \cdot c_{REB} \cdot W_j \cdot L_j \qquad (5.9)$$

where c_{REB} is the rebuilding cost per square meter (USD/m^2);W_j is the bridge width (m) for bridge j; and L_j represents the bridge j length (m).

In the case of link damage, the users are forced to follow detour. The running costs of a transportation network should sum up the cost of the damage links as follows (based on Stein *et al.* 1999)

$$C_{RUN}(t) = \sum_{j=1}^{n}\sum_{i=1}^{4} P_{LDSij|IM}(t)\left[c_{Run,car}(1-\frac{T_j}{100}) + c_{Run,truck}\frac{T_j}{100}\right] D_j ADT_{ij}(t) d_{ij} \quad (5.10)$$

where $c_{Run,car}$ and $c_{Run,truck}$ are the average costs for running cars and trucks per unit length (USD/km), respectively. The monetary value of the time loss for users and goods traveling through the detour can be expressed as (based on Stein *et al.* 1999)

$$C_{TL}(t) = \sum_{j=1}^{n}\sum_{i=1}^{4} P_{LDSij|IM}(t) d_{ij}\left[c_{AW} O_{car}(1-\frac{T_j}{100}) + (c_{ATC} O_{truck} + c_{goods})\frac{T_j}{100}\right][ADE_{ij}(t)[\frac{l_j}{S_D(t)} - \frac{l_j}{S_0(t)}] + ADT_{ij}(t)\frac{D_j}{S}] \quad (5.11)$$

where c_{AW} is the average wage per hour (USD/h); c_{ATC} is the average total compensation per hour (USD/h); c_{goods} is the time value of the goods transported in a cargo (USD/h); and O_{Car} and O_{Truck} are the average vehicle occupancies for cars and trucks, respectively.

The life loss cost depends on the number of casualties (Rackwitz 2002)

$$C_{SL}(t) = FA(t) \cdot ICAFB \quad (5.12)$$

where *ICAFB* is the implied cost of averting a fatality for bridge engineering

In this research, the carbon dioxide emission is considered as the only source of the pollution damage costs. The cost of carbon dioxide emissions can be transformed into monetary value and can be expressed as (based on Kendall *et al.* 2008).

$$C_{EN}(t) = [EN_{DT}(t) + EN_{RE}(t)] \cdot c_{Env} \quad (5.13)$$

where c_{Env} is the cost value of environmental metric per unit weight (e.g., carbon dioxide USD/kg).

The total economic consequences, $C_T(t)$, of a specific seismic scenario is the sum of repair loss, running loss of the detouring vehicles, time loss due to the unavailability of the highway segment, environmental loss and life loss.

$$C_T(t) = C_{REP}(t) + C_{RUN}(t) + C_{TL}(t) + C_{SL}(t) + C_{EN}(t) \tag{5.14}$$

Seismic risk should consider all the possible earthquakes that can happen in a region. However, it is impractical to take the entire set of earthquakes into consideration as the number of possible earthquake scenarios may be extremely large. The selected probabilistic seismic scenarios should be able to approximate the regional seismicity associated with the USGS regional hazard maps. The total loss is the sum of losses associated with seismic scenarios, which is the sum of costs weighted with the probabilities of having this cost. The total expected loss for all the events is

$$E(L) = \sum_{i=1}^{N} E(C_T | E_i) \cdot P_i \tag{5.15}$$

where $E(C_T|E_i)$ is the expected total loss of scenario event i defined by its magnitude, rupture length, and occurrence location; P_i is the probability occurrence of scenario event i; and N is the total number of events in the region (e.g., selected probabilistic seismic scenarios that approximate the regional seismicity).

5.6. CASE STUDY

The framework presented previously is applied to a transportation network located in the San Francisco Bay Region (SFBR). The region is subjected to major hazards due to the

northwestward motion of the Pacific Plate relative to the North American Plate. Figure 5.3 shows the schematic layout of highways and bridges within the bridge network. The network connects the cities of Emeryville (California) and Millsmont (Oakland, California) through the State 24, 13, and Interstate 580 by a total of 5 nodes and 15 bridges. The time-variant seismic vulnerability of the bridges and links in the transportation network is assessed considering a specific set of seismic scenarios. The *PGA* is used as a measure of earthquake intensity in this chapter. The time-variant seismic losses for the network are based not only on component damage but also on the non-functionality of the transportation network. The time-variant metrics of sustainability are quantified through a time span of 75 years.

5.6.1. Earthquake scenarios

The scenario events can be characterized by uncertainties in magnitude and distance between the rupture and site. The earthquake scenarios are selected based on the seismic rupture sources in the SFBR in Figure 5.4. Kiremidjian *et al.* (2006) demonstrated that the rare earthquakes with large magnitude contribute more to the seismic loss than the frequent earthquakes with smaller magnitude in the SFBR. Annual likelihood of seismic scenarios is accounted for based on USGS data (2003). This information provides the rupture sources with mean magnitude associated with recurrence probabilities as indicated in Figure 5.5. The annual occurrence rate of seismic hazard is used in this illustrative example for the probabilistic sustainability assessment and non-stationary nature of seismic activity is not considered. The model captures the simultaneous rupture of two or more adjacent segments of the fault. Each earthquake scenario corresponds to a

single or simultaneous rupture of the segments in the fault. The process is repeated for all the specific faults located in this region.

The level of expected structural damage relates to the ground motion intensity at the site of the bridge. The attenuation relationship proposed by Graizer and Kalkan (2007) is used in this chapter to predict the ground-motion intensity at a certain site as described in Eq. (5.1). The intensity of ground motions at different sites under a seismic scenario is considered as correlated due to the common source of the seismic scenario. The correlation among the intensities at different locations is modeled as an exponential decay function (Wang and Takada 2005)

$$\rho(h) = \exp(-h/b) \tag{5.16}$$

where h is the distance between two sites and b is the correlation length. The value of b can be estimated based on the statistical analysis of the past earthquake data. It has been demonstrated that this one-parameter exponential decay function can match the data well and can be applied to other cases (Wang and Takada 2005). In this chapter, the value of b is assumed 30 km for all earthquake scenarios. In the illustrative example, the correlation model proposed by Wang and Takada (2005) is used to evaluate the effects of correlation of ground motion on sustainability. Other correlation models (Jayaram and Baker. 2009, Adachi *et al.* 2009) can also be incorporated in the proposed methodology. In this chapter, correlations associated with hazard and bridge type are taken into account. However, other correlations (e.g., correlations associated with the layout of the network) are neglected.

5.6.2. Bridge and bridge network seismic vulnerability

Over time, structural vulnerability increases due to aging and deterioration. The investigated time horizon is considered to start from the year when the last bridge in the network was built (1970) and spans over 75 years. The initial values of the fragility parameters are based on Basöz and Mander (1999) for different bridge types. The types and the construction dates of the bridges within the network are provided in Table 5.2. There are three different types among the 15 bridges in the network according to this classification. The initial seismic fragility curves of these three bridge types are presented in Figure 5.6. The bridge type A, which is a simply supported concrete bridge with multi-column bents, has the highest seismic vulnerability. The bridge type C, which is a single span concrete bridge, has the lowest seismic vulnerability. The parameters of deteriorated fragility curves are assumed based on Decò and Frangopol (2013). A single value of the standard deviation β_i is considered throughout the lifetime in this example. However, if reliable data is provided, the general approach can be implemented using time-variation of β_i. The parameter of the fragility curves is assumed to be 75% of the initial value after 75 years (Decò and Frangopol 2013). In order to illustrate the time effects on fragility curves, the seismic fragility curves for bridge type A are presented for $t = 0$, $t = 35$, and $t = 75$ years in Figure 5.7. Each curve in the figure represents the probability of exceeding a damage state for a given value of *PGA*. In Figure 5.7(c), the conditional probability of exceeding major damage state under $PGA = 0.5g$ is about 0.45 initially (i.e., at $t = 0$); however, this value reaches 0.59 at $t = 75$ years.

The data on links of the network regarding the average daily traffic and detour length are presented in Table 5.3. The functionality of the bridge network defined in terms of link damage is affected by the damage state of bridges located in this network. The damage state of the links related to bridge failure is estimated as time-variant functionality due to aging consideration.

The time-variant probability of link being in a certain damage state is shown in Figure 5.8 associated with an earthquake scenario arising from the Hayward fault (see Figure 5.4). The probability of the link being in a certain damage state is updated during the lifetime. These damage states are mutually exclusive and collectively exhaustive under certain seismic scenario. The conditional probabilities of the link being in no damage, slight, moderate, and major damage state are 0.470, 0.477, 0.053, and 0.0 at t = 50 years under the seismic scenario arising from the Hayward Fault for the non-correlated *PGA*s, respectively. The effect of the correlation among the ground motion intensities at different locations is also illustrated in Figure 5.8. The effects of correlation of ground motion on link damage states are evaluated throughout the investigated time span. This figure indicates that the probability of being in a severe damage state increases with time. By ignoring the correlation, the probabilities of link being in moderate and major damage states are underestimated. For instance, the probability of link 4 that connects nodes 4 and 5 being in moderate damage state at t = 50 years is 0.064 associated with the non-correlated ground motion; while this value reaches 0.11 for the case with correlated ground motion.

5.6.3. Life-cycle sustainability assessment

The three metrics (i.e., social, environmental, and economic) of sustainability of the entire network are evaluated for each earthquake scenario. The social and environmental metrics can be converted into economic metrics if it is possible to evaluate the monetary value of the consequences of these two metrics. In this chapter, the social metrics are converted to the economic metric by considering appropriate monetary value.

In this case study, the mean estimated number of fatalities per collapse due to seismic hazard is considered as 4.154 (Dennemann 2009). The repair time depends on the bridge type and level of damage states of that bridge. The time of repair for each damage state is considered as a uniformly distributed random variable with t_{min} and t_{max} as lower and upper bounds, respectively (Table 5.1). For instance, t_{min} is 60 days and t_{max} is 250 days for the bridge at moderate damage state. Therefore, the time to complete the repair is between these two values. Repair actions have to improve the state of the bridge and the link of the network. The loss assessment should be performed over the time until the bridge in the network is repaired. In this illustrative example, the repair time for the link is assumed to be 50% larger than that for a single bridge. The environmental metrics, computed according to Eqs. (5.7) and (5.8), quantified are expected energy waste and expected carbon dioxide emissions. The values of the variables used in these equations are presented in Table 5.4.

Uncertainty in the parameters regarding consequences is incorporated in the proposed approach to evaluate the uncertainties in the loss. The descriptors of the random variables associated with the consequences are presented in Table 5.4. Latin Hypercube Sampling

(McKay *et al.* 1979) is used to generate the samples of random variables. Figure 5.9 shows the probability density function (PDF) of the losses associated with repair at t = 40 years. The effect of correlation among the seismic intensity at different locations is also illustrated in this figure. The ground motion correlation does not have significant impact on the median value of the loss associated with repair. The median value of loss associated with non-correlated ground motion is slightly higher than that in the case with correlated ground motion. The difference between the cases with and without the correlation is more significant for the losses below 0.78×10^5 USD and above 1.52×10^5 USD.

The contribution of different types of losses to the total expected loss of the network is illustrated in Figure 5.10(a). An annual discount rate of money r = 2% is used in the calculations. The expected value of total losses, as the economic metric of sustainability, is computed according to Eq. (5.15). In Figure 5.10(a), the time-variant curves indicate the expected loss associated with the earthquake scenarios throughout the investigated lifespan of the bridge network. The expected loss reaches the maximum value at the end of the investigated time span as no rehabilitation and retrofit actions are applied within this time period. In this figure, the contributions of different type consequences are evaluated through the investigated time span. The indirect losses such as the time loss and environmental loss yield the largest contribution to the total loss. Figure 5.10(b) shows the profiles of the mean (μ) and mean plus ($\mu + \sigma$) and minus ($\mu - \sigma$) one standard deviation (σ) of the total economic metric through the investigated lifetime. As the results indicate, the values of sustainability indicators as defined in this chapter for a

transportation network under probabilistic hazard scenarios are increasing over time. In order to illustrate the variation of the losses, the probability distributions of the total loss at t = 40 years and t = 75 years are presented in Figure 5.11. As expected, the median value and the dispersion are increasing with time. The expected loss is a relevant performance indicator to be used in the life-cycle maintenance and retrofit optimization of bridge infrastructure.

5.7. CONCLUSIONS

This chapter presents a computational framework for the seismic sustainability and risk of highway bridge networks. The sustainability of the network is quantified in terms of its social, environmental, and economic metrics. The time-variant sustainability metrics and risk due to structural deterioration are identified. The approach is illustrated on a transportation network located in Alameda County, California.

The following conclusions are drawn:

1. Structural deterioration affects both sustainability and risk of highway bridge networks. Sustainability is time-variant not only due to the structural deterioration but also the discount rate of money.
2. It is important to consider the ground motion correlation of spatially distributed systems in the seismic risk assessment. Integration of correlation in the proposed framework is illustrated in this chapter.
3. The values of sustainability metrics are sensitive to the parameters used in the evaluation of consequences. For instance, environmental costs and time loss costs contribute significantly to the values of the parameters used in the example.

4. The performance of links is dependent on the performance of the bridges located on the links. The accuracy of the sustainability analysis depends on the relation between the link and bridge performance.

Table 5.1 Bridge damage index, repair-cost ratio, and downtime associated with different damage states

Bridge Damage State	Bridge Damage Index [a]	Repair-Cost Ratio [b]	Downtime (days) [c]	
			Minimum	Maximum
No damage	0.00	0.00	NA	NA
Slight damage	0.10	0.03	10	150
Moderate damage	0.30	0.25	20	200
Major damage	0.75	0.75	60	250
Complete damage	1.00	1.00	75	300

[a] based on Chang *et al.* 2000; [b] based on Werner *et al.* 2006; [c] based on Zhou 2006

Table 5.2 Types of bridges in Figure 5.3 (based on National Bridge Inventory Database)

Bridge ID	Build Year	Classification Type
A	1970	Multiple-span continuous concrete bridge
B	1970	Single-span concrete bridge
C	1970	Multiple-span continuous concrete bridge
D	1970	Multiple-span continuous concrete bridge
E	1970	Multiple-span continuous concrete bridge
F	1970	Multiple-span continuous concrete bridge
G	1965	Multiple-span continuous concrete bridge
H	1966	Single-span concrete bridge
I	1965	Multiple-span continuous concrete bridge
J	1963	Single-span concrete bridge
K	1963	Multiple-span continuous concrete bridge
L	1963	Single-span concrete bridge
M	1962	Multiple-span simply-supported bridge with multi-column bents
N	1961	Single-span concrete bridge
O	1961	Multiple-span continuous concrete bridge

Table 5.3 Average daily traffic data and detour length for the links in Figure 5.3

Link No.	Connecting Nodes	Average Daily Traffic Volume [a]	Year of Traffic	Detour Length (km) [b]
1	(1,2)	147,500	2010	2.0
2	(2,3)	65,700	2010	2.5
3	(3,4)	56,500	2010	1.2
4	(4,5)	155,000	2010	2.5
5	(1,5)	176,000	2010	2.5

[a] based on the California Department of Transportation;
[b] based on the local transportation network

Table 5.4 Parameters of the random variables associated with the consequences.

Random variables	Mean	COV	Distribution type
ADT	Varies [a]	DNA	DNA
ADTT/ADT ratio	0.12 [a]	0.2	LN
Rebuilding costs	1292 USD/m^2 [a]	0.2	LN
Compensation for truck drivers	29.28 USD/h [a]	0.31	LN
Detour speed	30 km/h [a]	0.15	LN
Wage for car drivers	23.36 USD/h [a]	0.28	LN
Vehicle occupancies for cars	1.5 [a]	0.15	LN
Vehicle occupancies for trucks	1.05 [a]	0.15	LN
Running costs for cars	0.4 USD/km [a]	0.2	LN
Running costs for trucks	0.56 USD/km [a]	0.2	LN
Time value of a cargo	3.81 USD/h [a]	0.2	LN
Value of a statistical life	6,200,000USD [a]	0.45	LN
Cars CO_2 emissions	0.22 kg/km [b]	0.2	LN
Trucks CO_2 emissions	0.56 kg/km [b]	0.2	LN

LN=lognormal distribution; COV=coefficient of variation; DNA=do not apply;
[a] based on Decò and Frangol 2011; [b] based on Gallivan *et al.* 2010.

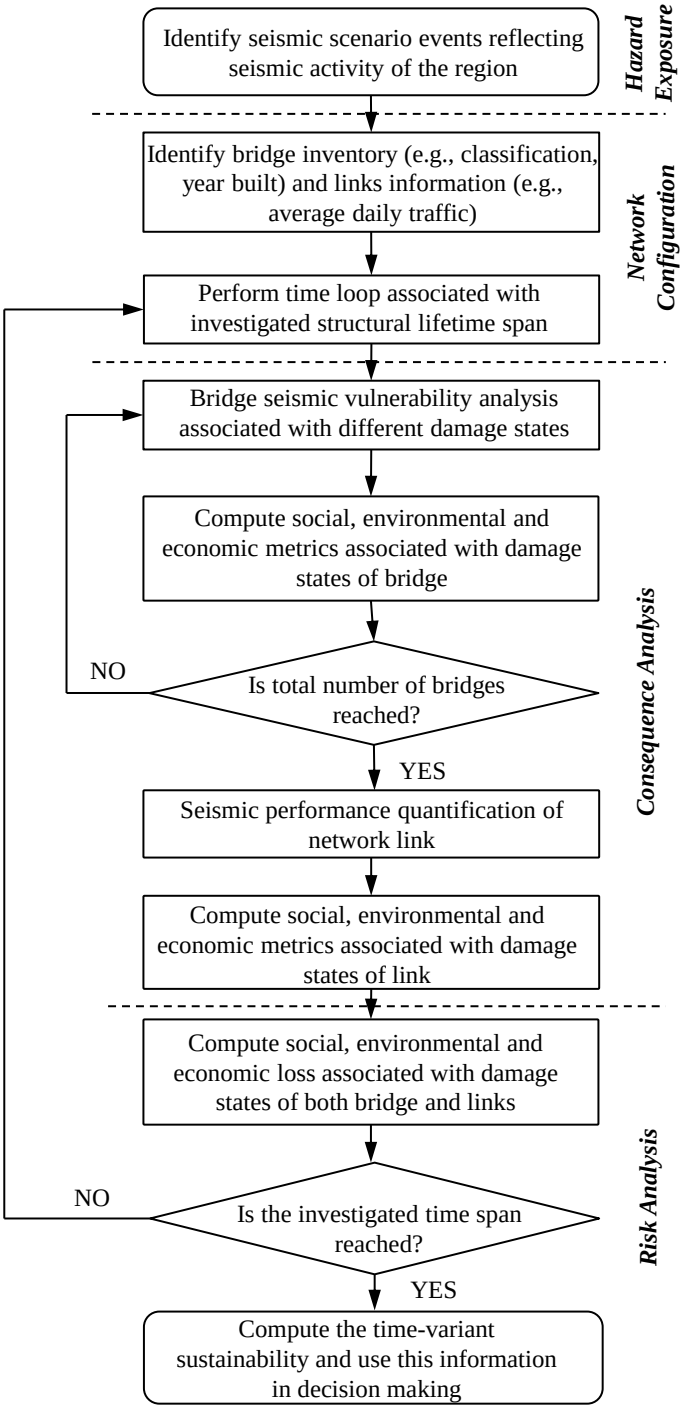

Figure 5.1 Methodology of assessing time-variant sustainability of transportation networks

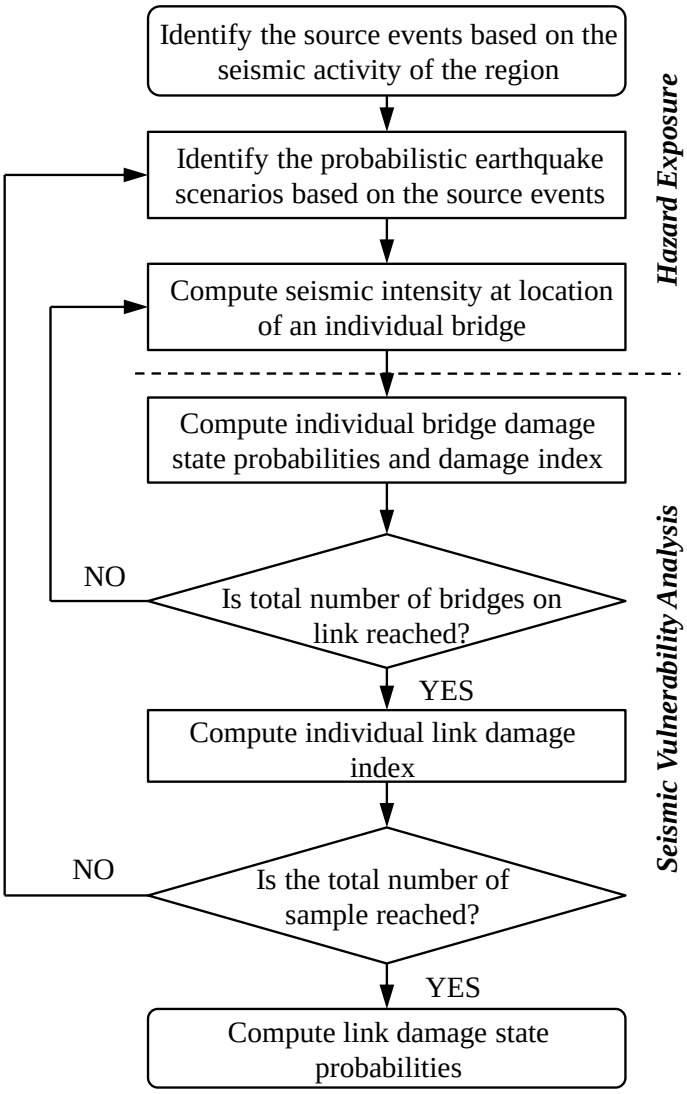

Figure 5.2 Approach for the seismic performance analyses of bridges and links

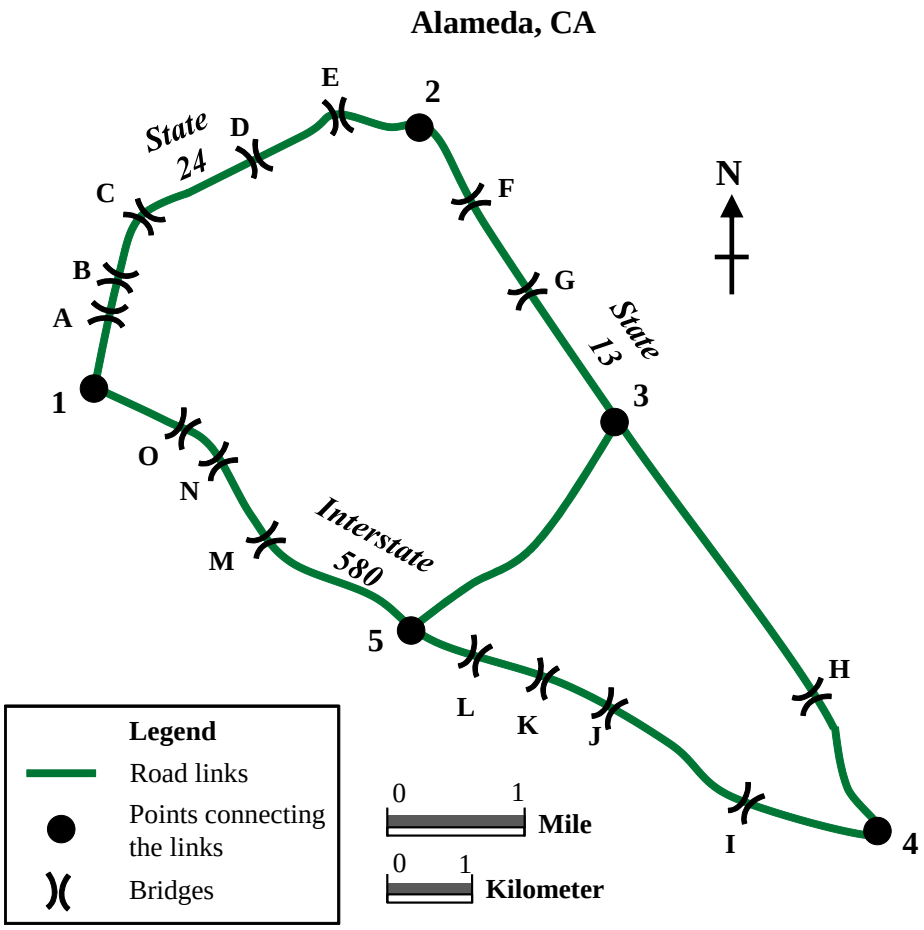

Figure 5.3 Schematic layout of the transportation network

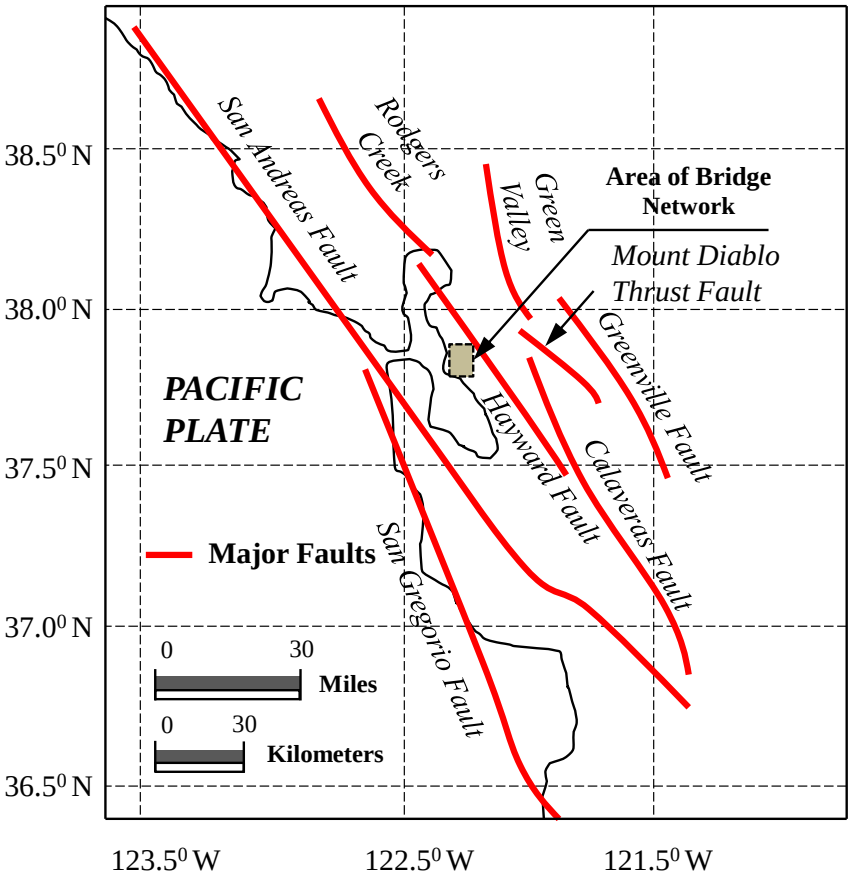

Figure 5.4 Major faults in San Francisco Bay region (based on USGS 2003)

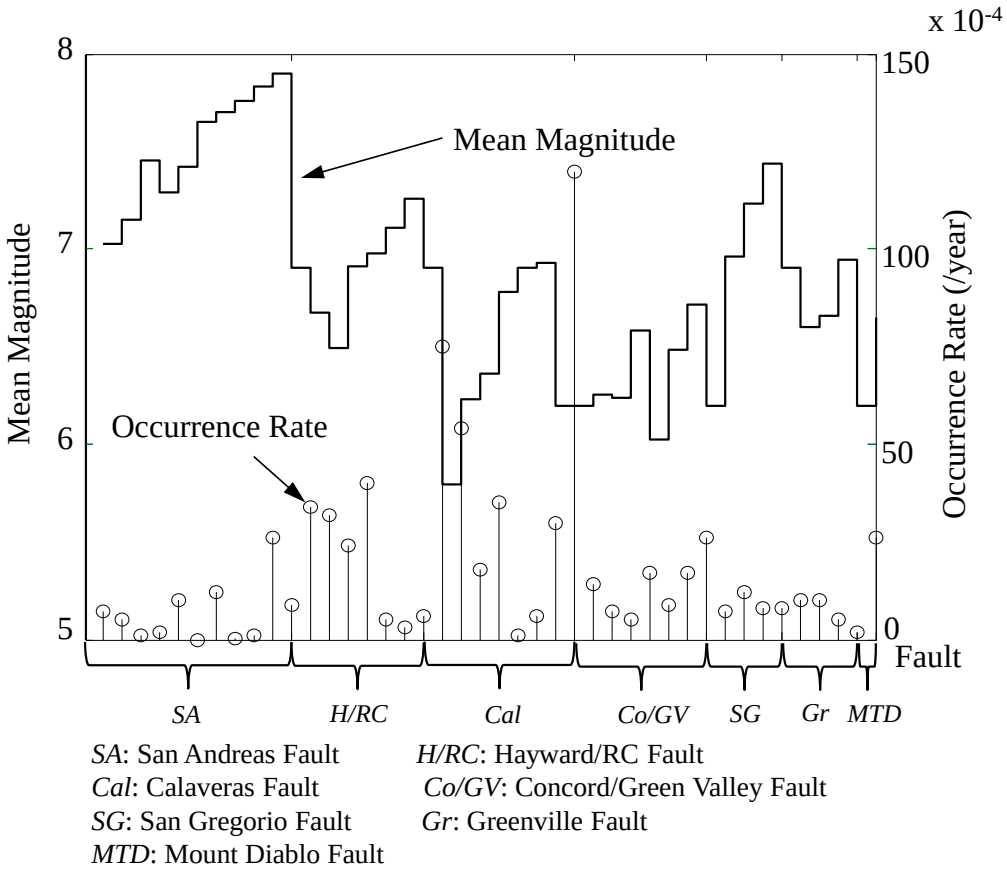

Figure 5.5 Mean magnitudes and occurrence rates (/year) of rupture sources for the San Francisco Bay area (based on data from USGS 2003)

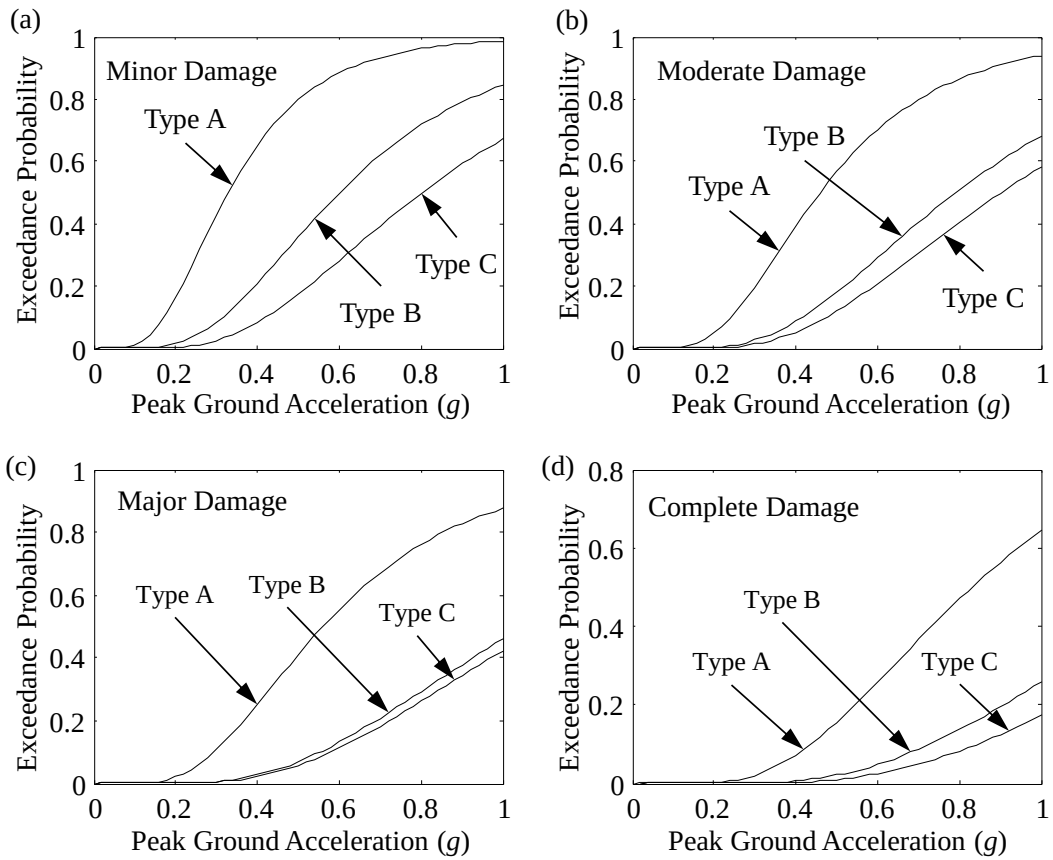

Type A: multi-column bents, simply-supported bridge
Type B: continuous concrete bridge
Type C: single span bridge

Figure 5.6 Fragility curves for bridge types in the investigated network for (a) minor damage state, (b) moderate damage state, (c) major damage state, and (d) complete damage state

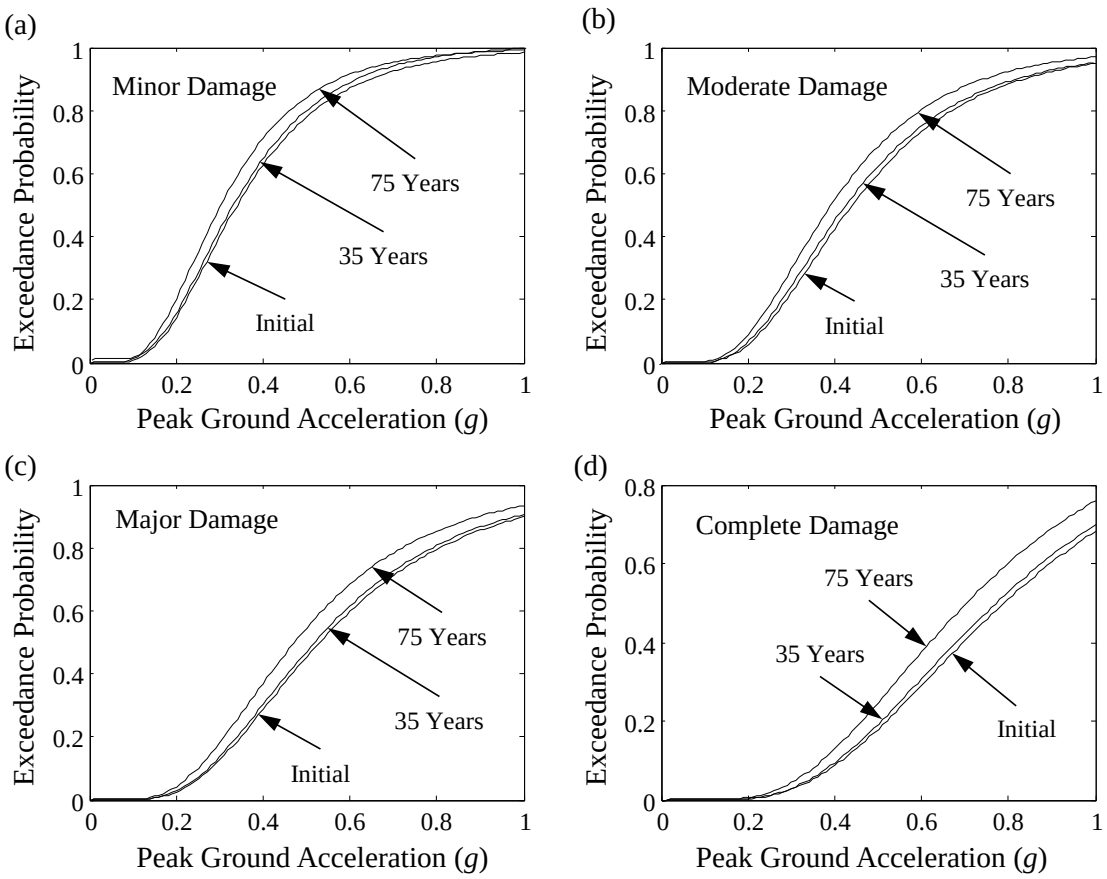

Figure 5.7 Seismic fragility curves of a bridge type A for (a) minor damage state, (b) moderate damage state, (c) major damage state, and (d) complete damage state at different points in time

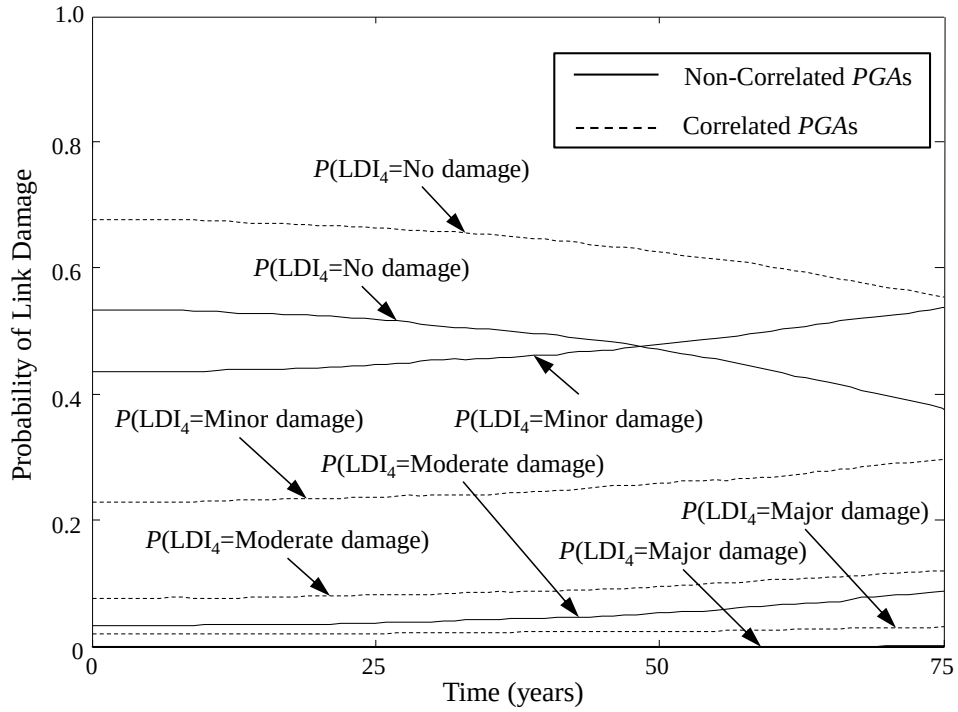

Figure 5.8 Time-variant probability of damage states for link 4 in Table 5.3 with and without correlated *PGA*s

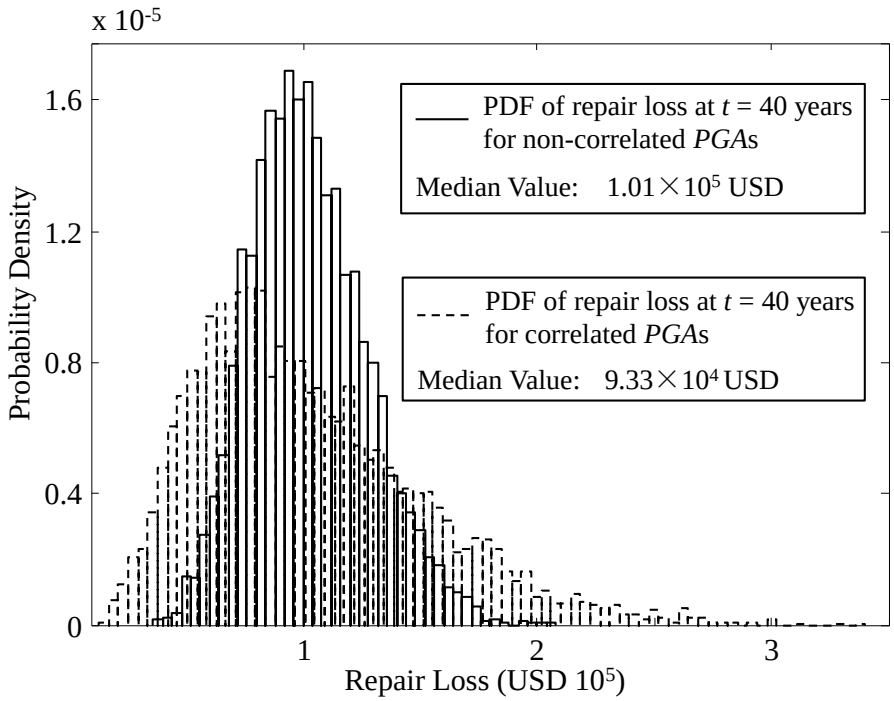

Figure 5.9 Probability density function of repair loss at t = 40 years with and without correlated *PGA*s

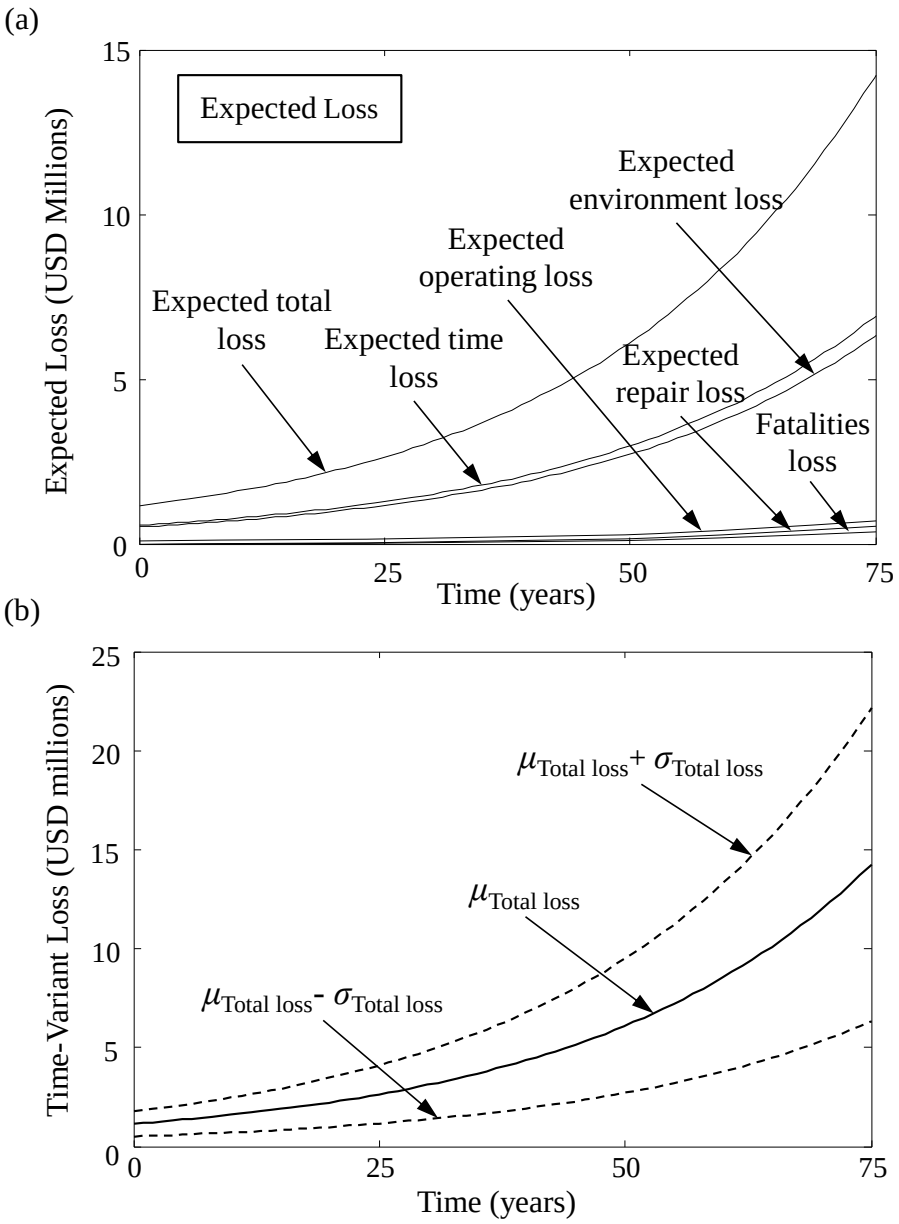

Figure 5.10 (a) Time-variant contributions of different types of losses to the expected total loss; and (b) time-variant of expected total loss, and mean plus and minus one standard deviation

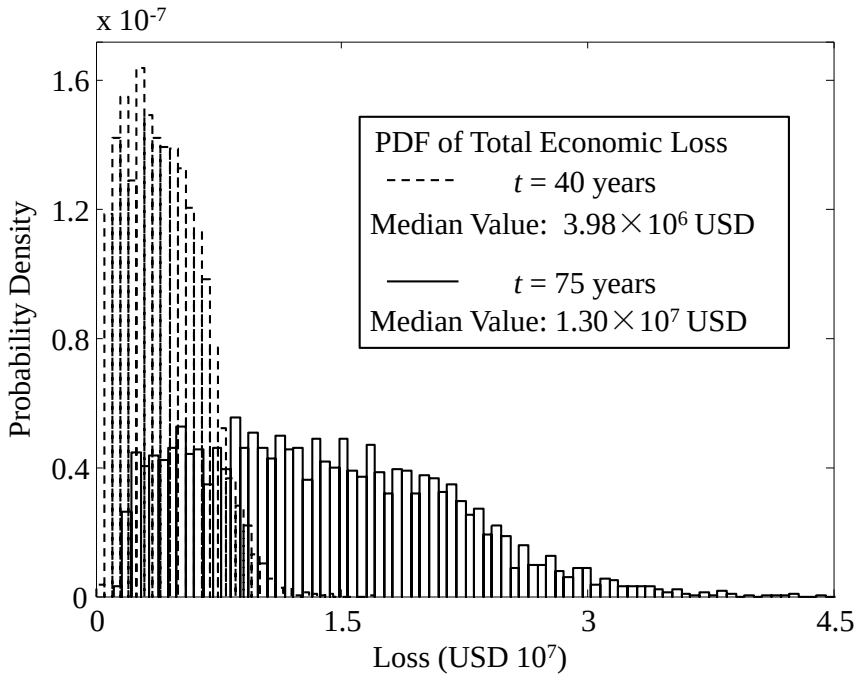

Figure 5.11 PDF of total economic loss at t = 40 and t = 75 years

CHAPTER 6

PERFORMANCE-BASED SEISMIC ASSESSMENT OF CONVENTIONAL AND BASE-ISOLATED STEEL BUILDINGS INCLUDING ENVIRONMENTAL IMPACT AND RESILIENCE

6.1. INTRODUCTION

According to the National Academies (2012), "Impacts of climate change and degradation of natural defenses such as coastal wetlands make the nation more vulnerable". With increase in the global mean annual temperature associated with climate change, the severity of seismic hazard, storm intensity, raising sea levels, and accelerating coastal erosion is likely to worsen (Larsen *et al.* 2011). Consequently, sustainability is an issue that should be recognized worldwide and increased attention should be placed on strategies to design and maintain infrastructure systems that are safe, damage tolerant, and sustainable. The research associated with structural sustainability and hazard resiliency has been an important topic and relevant results are needed in this area.

The Pacific Earthquake Engineering Research Center has developed performance-based seismic design and assessment approaches considering consequences including repair loss, downtime, and fatalities (Porter *et al.* 2001). However, the sustainability metric (e.g., environmental) has not yet been considered in this approach. Building

consumes significant amount of natural resources. Nearly 54% of energy consumption in the United States is caused by building (Horvath 2004). Additionally, buildings account for a paramount portion of greenhouse emission. Although building rating systems, such as LEED (2008), evaluate the greenness of new and existing structural systems, the ratings do not measure building hazard performance, which can impact building sustainability performance as well. Hazard-resistant and green structure design that aim to improve building performance is needed (Comber *et al.* 2012; Hossain and Gencturk 2014). This chapter aims to provide a comprehensive seismic assessment framework of structural systems under earthquake hazard including environmental impact.

Several improvements have been made in codes to increase seismic resistance of buildings (FEMA 2012). Loss associated with non-structural components could be much larger than that of structural components (Liel and Deierlein 2013). The concept of base-isolation can be adopted to reduce the floor acceleration of buildings; consequently, reduce the damage of acceleration sensitive non-structural components. However, due to the high initial construction cost, the performance benefits associated with base-isolated buildings are not recognized. Several studies have investigated the nonlinear seismic performance of isolated systems (Bruno and Valente 2002; Ryan and Chopra 2004; Liel and Deierlein 2013; Terzic *et al.* 2014); the isolation device can reduce the seismic demands compared with a base-fixed building. Smyth *et al.* (2004) investigated the cost and benefit of retrofitting reinforced concrete frame buildings and concluded that this benefit can outweigh the repair cost within the life-cycle. Sayani (2009) concluded that the isolated building is more cost-effective when the life-cycle is longer than 250 years

considering the direct loss only. Liel and Deierlein (2013) evaluated cost benefit of several common retrofit solutions for older RC frame buildings and showed that the cost-effectiveness became more significant when fatalities were considered. However, the sustainability performance of base-isolated buildings has not been investigated in these studies. A methodology to evaluate the seismic sustainability and cost-effectiveness of base-isolated buildings is needed to meet current performance requirements.

The devastating earthquakes have turned attention to the challenge of making buildings more resilient to mitigate loss. Disaster resilience covers the ability of a structural system to mitigate the disaster risks to minimize loss or damage to life, property, infrastructure, economic activity, and surrounding environment (UNISDR 2014). Generally, seismic resilience depends on the duration of downtime of building systems after the destructive earthquake. This duration is affected by the damage states of structural and non-structural components and the efficiency of the repair actions, among others factors (Porter *et al.* 2001). There has been limited work (Moretti *et al.* 2014) conducted to develop an assessment approach that includes losses and resilience of conventional and base-isolated buildings. The seismic resilience associated with isolated buildings is investigated in this chapter and comparative assessment between the conventional and base-isolated buildings is emphasized.

In this chapter, a methodology to evaluate quantitative seismic sustainability and resilience of both conventional and base-isolated buildings is presented. The environmental impact and resilience of buildings under given seismic event are computed. The benefit associated with base-isolated building is realized by considering

the three pillars of sustainability: economic, social, and environmental. The uncertainties associated with performance and consequence evaluation of structural and non-structural components are incorporated within the assessment process. Comprehensive performance-based earthquake evaluation tools are presented to estimate repair costs, downtime, environmental impact, and resilience of buildings under seismic hazard. The proposed approach is illustrated on conventional and base-isolated steel buildings. The work in this chapter is based on a published paper Dong and Frangopol (2016b).

6.2. SEISMIC SUSTAINABILITY AND RESILIENCE ASSESSMENT

6.2.1. Sustainability

Within the civil engineering field, two definitions are commonly used for sustainability. One is the "Brundtland Definition" which is stated as "meeting the needs of the present without compromising the ability of future generations to meet their own needs" (Adams 2006). The other, denoted as the "Triple Bottom Line" treats sustainability as satisfying three objectives: "not only economic, but social and environmental, as well" (Elkington 2004). The PEER approach has provided a framework for assessing building seismic performance by accounting for direct losses, downtime, and fatalities. Sustainability of the structure considers metrics of economic, social, and environmental, such as fatalities, downtime, embodied energy, CO_2 emissions, and damage loss (Dong *et al*. 2015). The sustainability assessment of a building under seismic hazard is investigated herein. A flowchart for sustainability and resilience assessment of structures under natural hazard is introduced in this section as shown in Figure 6.1(a).

Given a seismic hazard, a building can have different performance states, which are characterized by the value of different performance indicators such as inter-story drift ratio and peak floor acceleration. The two extreme cases associated with building performance states under a given seismic scenario are collapse (denoted *C*) and non-collapse (i.e., survival), denoted *NC*. The consequences associated with these states should be assessed. The total sustainability is the sum of consequences weighted with the probability of occurrence of the respective consequences. On the basis of the theorem of total probability, a sustainability metric *SM* of a building under a given seismic event is (Mitrani-Reiser 2007; Dong *et al.* 2013)

$$SM = TC_{Cons|C} \cdot P_{C|IM} + TC_{Cons|NC} \cdot (1 - P_{C|IM}) \tag{6.1}$$

where $TC_{Cons|C}$ and $TC_{Cons|NC}$ is the conditional total consequence *Cons* (e.g., CO_2 emission, downtime) given collapse *C* and non-collapse *NC* of the building, respectively, and $P_{C|IM}$ is the conditional probability of building collapse given the ground motion intensity *IM*.

The environmental impact covers the emissions associated with extraction and production of materials, transportation emission, and construction on sites (Chau *et al.* 2012). Generally, the total CO_2 emissions from the embodied of building material contribute significantly to the total emissions associated with construction and repair (Yan *et al.* 2010). Based on the gaseous emission of a material in terms of unit mass (e.g., kg of CO_2 emission per kg), the masses of the materials associated with different components can be converted to their environmental impact. The basic parameters associated with CO_2 emissions for different structural and nonstructural components have

been investigated by Anderson *et al.* (2002) and Chau *et al.* (2012). Generally, the amount of CO_2 associated with the materials used in a building component can be calculated based on the mass quantity of material and the unit emission coefficient of unit quantity of material (e.g., kg CO_2/kg) (Anderson *et al.* 2002). All the material used in the components should be considered in the environmental consequence assessment process. Then the total CO_2 emissions associated with structural and non-structural components can be computed.

6.2.2. Resilience assessment

To estimate the resilience and indirect losses resulting from the business interruption of a building following an earthquake, downtime needs to be assessed. Building downtime is generally defined as the period of time between the occurrence of a seismic event and the completion of repair efforts. One portion of downtime is attributed to the time needed to repair building damages and is considered as the rational component of building downtime (Comerio 2006). The remaining portion of building downtime is difficult to model because it is highly dependent on several components, which include financing, relocation of functions, human resources, and economic and regulatory uncertainty (Porter *et al.* 2001). The slow-track (i.e., components are repaired serially) and fast-track (i.e., components are repaired in parallel) repair schemes have been investigated by Porter *et al.* (2001), FEMA (2012), and Moretti *et al.* (2014).

The expected total building downtime under a given hazard level is determined considering the collapse and survival cases. After collapse, the building has to be rebuilt. Given building survival, the total repair time associated with a specific component group

is computed. Subsequently, the total repair time of all the groups (e.g., structural and non-structural) can be computed. Then, the repair time in operational unit (e.g., floor) can be computed by dividing the total repair time (i.e., worker-days) by the number of workers allocated to each floor. Repair actions associated with all floors can be assumed to occur either simultaneously or successively. The required repair time (denoted *RT*) for the damaged building in operational unit (e.g., floor) can be computed as follows (Porter *et al.* 2001)

$$RT_{NC|IM} = (\sum_{j=1}^{m} RT_{j,NC|IM}) / (wh \cdot wr \cdot cn) \tag{6.2}$$

$$RT_{j,NC|IM} = n_j \sum_{i=1}^{N} RT_{j,RT|DS_i,IM} \cdot P_{j,DS_i|IM} \tag{6.3}$$

in which $P_{j,DSi|IM}$ is the probability of the building component *j* being in damage state *i* conditioned on the survival of structure under a given *IM*; $RT_{j,NC|IM}$ is the total expected repair time for the building component *j* under a given *IM* conditioned on the survival of the structure; $RT_{j,RT|DSi,IM}$ is the repair time for the building component *j* at damage state *i* conditioned on the survival of the structure and repaired to initial condition under a given *IM*; n_j is the number of component *j* (e.g., structural and non-structural components) that are sensitive to the same seismic demand located in operational unit (e.g., floor); *N* is the number of damage states associated with investigated component; *wh* is the workday hours; *wr* is the workday ratio of calendar days; *cn* is the number of crews available for the repair action; and *m* is the number of assembly groups.

The three recovery states associated with building functionality can be defined as: re-occupancy of the building, pre-earthquake functionality, and full recovery (Bonowitz

2011). Re-occupancy occurs when the building is deemed safe enough to be used for shelter and does not pose a threat to life safety, though functionality may not be restored (Bonowitz 2011). Functional recovery occurs when the building regains its primary function. Lastly, full recovery occurs when the building is restored to its pre-earthquake condition, it follows from functional recovery once additional repairs for aesthetic purposes have been completed. The most widely adopted approach to quantify the resilience of a structural system is to compute it as the integration over time of the functionality under investigation (Cimellaro *et al.* 2010; Frangopol and Bocchini 2011)

$$R_{Resi} = \frac{1}{T_r} \int_{t_0}^{t_0+T_r} Q(t)dt \tag{6.4}$$

where $Q(t)$ is the functionality of the building; t_o is the occurrence time of the extreme event; and T_r is the investigated time horizon. The shape of the performance restoration curve is a function of changes in system performance due to repair and recovery efforts. Three typical recovery functions that are often assumed in resilience studies are linear (Bruneau and Reinhorn 2007), trigonometric (Chang and Shinozuka 2004), and exponential (Cimellaro *et al.* 2010; Bocchini 2013; Decò *et al.* 2013; Dong and Frangopol 2015) functions. The time-variant functionality of structural systems under a given extreme event is qualitatively shown in Figure 6.1(b). T_r is investigated time period range that is usually prescribed by the decision maker. In this figure, t_0 is time instant when resilience starts to be evaluated and the building functionality drops from full functionality Q_{FF} to residual functionality Q_{RF}, which is based on the damage states of the structural systems. The investigated period range $T_r = t_2 - t_0$ is divided into two stages as

shown in this figure. More stages could be defined to meet the requirements determined by the decision maker. Stage I corresponds to the period from t_0 to t_1; at the end of this period necessary repair actions are applied to the damaged building, consequently, it regains partial functionality Q_{PF}. As there are uncertainties associated with downtime, the recovery time interval is probabilistic. The next stage, Stage II, corresponds to the period from t_1 to t_2 and the building is partially functional before reaching full functionality Q_{FF}. Given the time-variant functionality of a building under a seismic hazard, the corresponding resilience can be computed by using Eq. (6.4).

6.3. PERFORMANCE-BASED SEISMIC ASSESSMENT

6.3.1. Performance-based evaluation

As mentioned previously, the two cases associated with building performance under a given earthquake are (a) collapse does not occur (i.e., survival), denoted *NC* and damage in the building is repaired, and (b) collapse occurs and the building is rebuilt. Regarding the performance assessment process, the performance at system level (i.e., building) should be evaluated to determine whether the building is collapsing or not. If it is collapsing, the rebuilding cost and repair time associated with the building failure have to be computed. Given survival, repair actions are applied to the damaged structural and non-structural components. The relevant cost and repair time can be computed. The expected repair loss in the building under a given ground motion intensity is computed as

$$L_{T|IM} = L_{NC|IM} + L_{C|IM} \tag{6.5}$$

$$L_{C|IM} = C_C \cdot P_{C|IM} \tag{6.6}$$

where $L_{NC|IM}$ and $L_{C|IM}$ are the repair loss associated with the non-collapse and collapse of the building under a given *IM*, respectively, and C_C is the rebuilding cost associated with the collapsed building.

The computational process associated with repair loss of a non-collapsing building is introduced herein. The building components are categorized into structural, non-structural, and content components (Mitrani-Reiser 2007). The repair loss associated with different components of a building system is investigated by considering different seismic demand indicators (e.g., story drift, floor acceleration). The damage to structural components is usually correlated with structural drift. The non-structural components refer to the equipment and building facility, such as ceiling, elevators. The damage of non-structural components is generally related with the story drift ratio and/or floor acceleration. The structural response parameters associated with the building components at each story can be calculated using nonlinear time history analyses. Finally, the corresponding repair losses associated with structural components, inter-story drift ratio sensitive non-structural, and floor acceleration sensitive non-structural are computed.

6.3.2. Vulnerability analysis

Given the seismic scenario, the ground motion intensity (e.g., peak ground acceleration (PGA)) can be assessed. Then by using fragility curve, the corresponding probability of a building or component being in different damage states can be computed. A fragility curve defines the conditional probability of exceeding a specified damage state for a given input of ground motion intensity. As indicated previously, a building can be divided into different groups (e.g., structural and nonstructural components) for the

seismic consequence assessment. For a given ground motion intensity, the probability of a building component being in a damage state *i* is given by the difference between the probabilities of exceedance of damage states *i* and *i+1*, where the damage state *i+1* is more severe than the damage state *i*.

6.3.3. Consequence assessment

The building repair loss associated with different groups of structural and nonstructural components is computed. Then, the total expected repair loss given the non-collapse of the building is computed (Mitrani-Reiser 2007)

$$C_{NC|IM} = \sum_{i \in I} P_{StDr,DS_i|IM} \cdot C_{StDr,i} + \sum_{j \in J} P_{NStDr,DS_j|IM} C_{NStDr,j} + \sum_{k \in K} P_{NStAc,DS_k|IM} C_{NStAc,k} \quad (6.7)$$

where $C_{StDr,i}$ is the repair cost of a drift sensitive structural component being in damage state *i*; $C_{NStDr,j}$ is the repair cost associated with drift sensitive non-structural component being in damage state *j*; $C_{NStAc,k}$ is the repair cost associated with acceleration sensitive non-structural component being in damage state *k*; and $P_{StDr,DSi|IM}$, $P_{NStDr,DSj|IM}$, and $P_{NStAc,DSk|IM}$ are the conditional probabilities of being in a given damage state under *IM* associated with drift sensitive structural, drift sensitive non-structural, and acceleration sensitive non-structural components, respectively. The repair cost associated with each damage state is expressed as a percentage of the replacement cost of the component. The total repair loss can be computed by summing the repair losses associated with all the damage states.

In addition to the repair loss, the indirect loss, such as the loss of rental income and fatality is also computed. Generally, the indirect loss depends on the location and use of the building. The total downtime is dependent on the repair scheme chosen by the

building owner. The repair duration for each building operational unit (e.g., floor) is dependent on the repair crew and damage condition of the building as indicated in Eq. (6.2); therefore, the duration should be treated as probabilistic. The corresponding downtime associated with the two investigated repair schedules (i.e., slow-track and quick-track) are computed. The expected repair time given building under a seismic scenario can be computed as

$$RT_{T|IM} = RT_{C|IM} + RT_{NC|IM} \tag{6.8}$$

$$RT_{C|IM} = Tt_C \cdot P_{C|IM} \tag{6.9}$$

where $RT_{T|IM}$ is the total expected repair time of building under given ground motion intensity; $RT_{C|IM}$ is the repair time of the collapsed building under *IM*; $RT_{NC|IM}$ is the repair time of the not collapsed building under *IM*; and Tt_C is the total repair time associated with the collapsed building.

The indirect loss associated with downtime of a building under a seismic hazard is calculated as the sum of the loss for all operational units. Then given the unit loss associated with downtime (e.g., USD/day), the corresponding indirect loss of downtime can be computed. The fatalities associated with a building under a seismic hazard are also considered for the seismic indirect loss assessment. The expected fatalities are computed using the following equation (Mitrani-Reiser 2007)

$$FA_{T|IM} = \sum_{i \in I} PFA_{fa_i|DM_i} \cdot P_{DM_i|IM} \cdot n_{fa} \tag{6.10}$$

where $PFA_{fai|DMi}$ probability of fatality associated with building being in state *i* under *IM*; $P_{DMi|IM}$ is the conditional probability of building being in state *i* under *IM*; and n_{fa} is the

number of people under the fatality risk. Then given the monetary loss associated with a fatality, the expected fatality loss can be computed.

6.4. ILLUSTRATIVE EXAMPLE

The presented performance-based seismic assessment framework is applied to three-story conventional and base-isolated steel buildings. Finite element models able to capture the nonlinear behavior of conventional and base-isolated buildings are established in OpenSees (2012). The seismic performance associated with the two investigated buildings are compared. Furthermore, the environmental impact and resilience are emphasized in the assessment process.

6.4.1. Description of conventional and base-isolated buildings

Three-story conventional and base-isolated moment resisting frame buildings designed by Forell/Elsesser Engineers Inc. are investigated herein as shown in Figure 6.2(a)-(c) (Sayani 2009). The two buildings are both designed for Los Angeles, CA, located on stiff soil. The design force reduction factor is assumed 8 for the conventional building and 1.69 for the isolated building.

The two buildings have the same story height of 4.57 m and bay span of 9.144 m as displayed in Figure 6.2(a)-(c). The steel structural components for the 3-story conventional and base-isolated buildings are described in Sayani (2009). The steel used in the buildings has a nominal strength of f_y = 345 MPa. In the conventional building, moment resisting and gravity columns are fixed and pinned at the base; fixed connections are assumed at all beam-column joints at the base level in the isolated building. The isolators are modeled as the lead rubber bearings, which are commonly used in

engineering practice. The post-yield stiffness k_p and the characteristic strength Q_d are the key parameters (Thompson *et al.* 2000; Constantinou *et al.* 2007; Sayani *et al.* 2011) as shown in Figure 6.2(d). An elastic column element and an elastic-perfectly plastic spring are assembled in parallel to obtain the composite bilinear lateral force-deformation behavior for the isolator as revealed in Figure 6.2(d)-(e). The steel stress-strain and moment-curvature relationships are assumed to be bilinear with a strain hardening ratio of 3%. The columns are modeled by using force-based nonlinear beam-column elements and gravity beams are modeled using elastic beams with moment releases at both ends in OpenSees. The fundamental periods of the conventional and base-isolated building are 0.81s and 3.21s, respectively.

6.4.2. Building seismic vulnerability

The two reference seismic events, 1940 El Centro and 1995 Kobe earthquakes, are used to evaluate the seismic performance of the conventional and base-isolated buildings. The group motion inputs associated with the two earthquakes are selected from the PEER NGA database (Chiou *et al.* 2008; NEES 2009). The PGAs of these two seismic events are 0.663 and 1.258 *g*, respectively. The PGA is selected as ground motion intensity, which has also been used in many previous studies on seismic demand assessment of isolated structures (Sayani *et al.* 2011; Perotti *et al.* 2013). Given the seismic input, the nonlinear time history analyses are performed to compare seismic performance of conventional and base-isolated buildings using OpenSees. The maximum value of story drifts at any of the four corners of the building is adopted as seismic performance indicator. The time-dependent inter-story drift of the conventional building at different

stories under 1940 El Centro earthquake is shown in Figure 6.3(a)-(c). Additionally, time-dependent total floor acceleration of the base-isolated building under the 1940 EI earthquake is presented in Figure 6.3(d)-(f). Similarly, the seismic performance of conventional and base-isolated buildings under 1995 Kobe earthquake can be obtained.

Based on the results presented in Figure 6.3, the peak inter-story drift ratio of the conventional and base-isolated buildings under the two investigated earthquakes are shown in Figure 6.4(a) and (b). As indicated, the inter-story drift ratio associated with base-isolated building is much smaller than that of the conventional building. For the 1940 El Centro event, peak inter-story drift ratio in the isolated building is reduced by 42-53% relative to the conventional building. Given the 1995 Kobe earthquake, the inter-story drift ratio in the base-isolated building are much smaller than that associated with conventional building as shown in Figure 6.4(b). For example, on the first story, the inter-story drift ratio of conventional building is 2.88%, while this value is reduced to 0.647% with respect to base-isolated building.

The peak acceleration of different floors of the conventional and base-isolated buildings is indicated in Figure 6.4(c) and (d). In general, floor acceleration, in terms of *g*, indicates damage of acceleration sensitive non-structural components (Mitrani-Reiser 2007). As indicated in Figure 6.4(c), the peak roof acceleration in the isolated building is attenuated by a factor of 2.07 in the 1940 El Centro earthquake. While the roof acceleration in the conventional building is amplified to 1.225 *g* under the same seismic event. Similar conclusions are drawn for the performance of buildings under 1995 Kobe earthquake. The seismic performance with respect to collapse of the two investigated

buildings is also considered herein. The median value associated with the ground acceleration at collapse for the conventional and base-isolated buildings is 2.39 *g* and 1.93 *g*, respectively (Sayani *et al.* 2011). Based on these values, the conditional probabilities of collapse and non-collapse (i.e., survival) of the building under given seismic intensity can be calculated. Based on the seismic performance of conventional and base-isolated buildings, the seismic loss is obtained and discussed in the following section.

6.4.3. Seismic performance assessment

The structural and non-structural components are divided into three groups: drift-sensitive structural, drift-sensitive non-structural, and acceleration-sensitive non-structural. The peak inter-story drift ratio and acceleration have been obtained in the previous section as shown in Figure 6.4. The fragility functions of the components are represented using lognormal distributions, with given median and dispersion values. Table 6.1 displays the parameters associated with fragility curves of structural and non-structural components under different damage states. Additionally, the number of the components per floor is also indicated in this table. The repair cost associated with each damage state is expressed as a percentage of the replacement cost and the repair cost ratios are also tabulated herein.

The repair loss of structural and non-structural components under given seismic hazard is computed using Eq. (6.7). The relevant parameters used in Eq. (6.7) are provided in Table 6.1. The structural and non-structural repair losses of conventional and base-isolated buildings under 1940 El Centro earthquake are computed. The probability

density functions (PDFs) of the repair loss of structural and non-structural components are shown in Figure 6.5(a). The expected repair losses for structural and non-structural component of conventional building are 1.082×10^5 USD and 6.001×10^5 USD, respectively. As indicated, the repair loss associated with non-structural damage is much larger than that of structural damage in a conventional building. Additionally, the repair loss of non-structural damage within the base-isolated building is reduced to 40.5% of that of conventional building under the El-Centro earthquake. The total expected repair loss of building under the given seismic scenario is computed using Eqs. (6.5) - (6.6). Based on these equations, the repair loss of buildings under seismic hazard is obtained. The probabilistic repair loss of the conventional and base-isolated buildings under 1940 El Centro earthquake is shown in Figure 6.5(b). As indicated, the expected repair loss of the conventional and base-isolated buildings are 7.121×10^5 USD and 2.456×10^5 USD, respectively. Given the same ground motion, the expected repair loss of conventional building is almost 2.9 times of that associated with the base-isolated building.

The structural performance of steel building is generally defined by using three performance states: immediate occupancy, life safety, and collapse prevention, which are defined as 0.7%, 2.5%, and 5% inter-story drift ratio, respectively (FEMA 2000). The probabilities of being in these three performance states can be obtained. In order to compute the total fatality number, the fatality associated with the three performance states should be defined. Based on ATC (1985), the probability of fatality is 0.2 given the building collapse. The probability of fatality is 0.00001 given the immediate occupancy, while this value reaches 0.01 with respect to life safety performance state (ATC 1985).

Regarding a three-story building, the number of occupants under fatality risk is 133 (Mitrani-Reiser 2007). The expected total number of fatalities is computed by using Eq. (6.10). The expected monetary loss associated with a fatality is assumed to the 4.16×10^6 USD and the coefficient of variation is 0.4 (Mitrani-Reiser 2007). By multiplying the fatality number with the monetary loss associated with the fatality, the total fatality loss is shown in Figure 6.5(c). As shown, the expected fatality loss of conventional building is nearly 4 times of that associated with base-isolated building under the same earthquake hazard. The CO_2 emissions of the conventional and base-isolated buildings under given seismic event can be computed. The material types of different building components and the random variables associated with CO_2 emission of building materials are provided in Table 6.2. Based on these parameters, the CO_2 emissions of conventional and base-isolated buildings under 1940 El Centro earthquake are shown in Figure 6.5(d).

The repair time is calculated by using the parallel scheme, assuming simultaneous repair at all three floors, and the serial scheme, assuming sequential repair of floors. These repair schemes can provide a good estimate of the lower and upper bound of the repair time, respectively. The downtime associated with repair actions can be computed using Eqs. (6.2) - (6.3). The random variables associated with repair time of different damage states of structural and non-structural components are shown in Table 6.3. It is assumed that the daily loss due to downtime is 2880 USD for the three-story buildings and the expected downtime of a collapsed building is estimated to be 1.95 years (Mitrani-Reiser 2007). The workday hours *wh* used in Eq. (6.2) is 8 hours. The maximum number of workers associated with floor repair is 15 per floor for low-rise buildings (Almufti and

Willford 2013). Herein, the number of workers is 15 per floor and the workday ratio is 5/7. The total numbers of workers are 15 and 45 for slow- and quick-tracks, respectively. Given all these parameters, the downtime associated with each floor is computed. Then the total downtime of the building considering slow-track and quick-track is obtained. The PDFs of the downtime associated with conventional and base-isolated buildings under 1940 El Centro earthquake are shown in Figure 6.6(a) and (b). As indicated, there is an enormous difference between downtime associated with the fast-track and slow-track scheme. The expected downtime of conventional building using slow-track is 163 days, while this value is reduced to 64 days by using quick-track.

Based on the PDF of seismic loss shown in Figure 6.5 and Figure 6.6, the expected values are obtained. To quantitatively compare the seismic performance of the conventional and base-isolated buildings, the expected repair loss, downtime, fatalities, and environmental impact of the buildings under 1940 El Centro and 1995 Kobe earthquakes are presented in Table 6.4. As indicated, the improvement associated with seismic performance of base-isolated building is significant. Another observation that can be made is that the total loss is substantially higher than the direct loss for each building. Results in Table 6.4 indicate that the base-isolation can substantially reduce the expected repair loss, downtime, fatalities, and CO_2 emissions.

6.4.4. Resilience assessment

The resilience of conventional and base-isolated buildings under seismic hazard is assessed herein. The seismic performance states (e.g., immediate occupancy, life safety, and collapse prevention) are considered in the resilience assessment process. Given the

probability of building being in different performance states and the corresponding functionality, the residual functionality of the conventional and base-isolated buildings is computed on the basis of the theorem of total probability. The uncertainties of functionality associated with different performance states are considered herein. The triangular distribution is used for the functionality assessment associated with three structural performance states: immediate occupancy, life safety, and collapse prevention. The lower limit, upper limit, and mode of triangular distribution for immediate occupancy, life safety, and collapse prevention states are assumed as (0.7, 0.9, 0.8), (0.4, 0.6, 0.5), and (0, 0.2, 0), respectively. The functionality associated with building collapse is 0 while the functionality corresponding to no damage is 1.0. The PDF of residual functionality is shown in Figure 6.7(a) and (b). The expected residual functionalities of conventional and base-isolated buildings under 1940 El Centro earthquake are 0.747 and 0.815, respectively. As indicated in Table 6.4, the difference between the sustainability metrics is much larger than that between the resilience of the two buildings. It is of vital importance to integrate the sustainability metrics with resilience for the performance-based seismic assessment. Repeating the computation process with respect to the 1995 Kobe earthquake, the residual functionality is shown in Figure 6.7(b). The expected residual functionality of the base-isolated building is 0.791, which is about 3.4 times of that associated with the conventional building.

As indicated in Figure 6.1(b), two stages are considered in the time-variant functionality assessment process. If the residual functionality of the damaged building is larger than the partial functionality Q_{PF} = 0.5, the functionality of the building would

reach the full functionality Q_{FF} = 1.0 at the end of the repair time interval. Otherwise, the necessary repair actions are applied to the damaged building to recover its functionality Q_{PF} before reaching Q_{FF}. After the total downtime period, the functionality of the building will reach full functionality. Herein, the repair time is calculated using quick-track and slow-track schemes. Using Monte Carlo simulation, the probabilistic repair time and time-variant functionality can be obtained. Accordingly, the time-variant expected functionality of the conventional building under El Centro earthquake using slow- and quick-tracks is shown in Figure 6.8(a). Then by using Eq. (6.4), the probabilistic resilience is obtained. Given the investigated time-interval *Tr*, the PDF of resilience of conventional building under the 1940 El Centro earthquake using slow-track at 100, 200, and 400 days is shown in Figure 6.8(b). Based on the simulation results, the expected values of resilience of conventional and base-isolated buildings under 1940 El Centro and 1995 Kobe earthquakes are revealed in Figure 6.9(a) and (b), respectively. As indicated, under the seismic event, the expected value of resilience associated with the base-isolated building is substantially larger than that associated with conventional building.

6.5. CONCLUSIONS

This chapter has provided a framework for building seismic performance-based assessment considering environmental impact and resilience. The uncertainties associated with structural performance and consequence evaluation are incorporated within the assessment process. The proposed approach is illustrated on conventional and base-isolated steel buildings under given earthquake scenarios.

The following conclusions are drawn:

1. The seismic performance improvement associated with base-isolated buildings is significant compared with that of the conventional buildings. Based on the results of seismic performance associated with conventional and base-isolated buildings, the base isolation can reduce the seismic repair loss, downtime, fatalities, and environmental impact.
2. The methodology estimates the environmental impact, and economic losses due to repair cost as well as downtime and fatalities. The downtime losses are sensitive to the repair scheme (i.e., quick-track and slow-track). The downtime loss for the conventional building under 1995 Kobe earthquake using slow-track is almost 2.3 times of that associated with quick-track.
3. The seismic repair time and loss associated with structural and non-structural components are computed for the conventional and base-isolated buildings under given earthquake scenario. The base-isolated building can reduce the damage loss of non-structural components.
4. The two performance indicators (i.e., sustainability and resilience) should be investigated for the conventional and base-isolated buildings under seismic hazard and integrated for a more comprehensive performance-based assessment content. There is a need to expand upon the seismic resilience to include the sustainability metrics.

Table 6.1 Parameters associated with fragility curves and repair cost ratios of different damage states associated with structural and non-structural components

Components	Damage state	Number per floor	EDP	Fragility curves		Repair cost ratio		Replacement cost (US $)
				Median	c.o.v	Median	c.o.v	
Reduced beam section connection [1, 2]	Slight	40	IDR (%)	2.2	0.22	0.15	0.3	60000/each
	Moderate			3.6	0.16	0.25	0.3	
	Severe			5.6	0.17	1.0	0.4	
Welded unreinforced flange-welded web connection [3]	Slight	40	IDR (%)	2.5	0.22	0.15	0.3	60000/each
	Moderate			3.7	0.14	0.25	0.3	
	Severe			5.5	0.09	1.0	0.4	
Aluminum framed window [4]	Slight	1060	IDR (%)	1.6	0.29	0.1	0.2	696/Pane
	Moderate			3.2	0.29	0.5	0.2	
	Severe			3.6	0.27	1.0	0.2	
Interior partition [5, 6]	Small cracks	27100	IDR (%)	0.39	0.17	0.2	0.2	3.9/sf
	Extensive cracks (severe)			0.85	0.23	1.0	0.2	
Interior finish [5, 6]	Small cracks	9000	IDR (%)	0.39	0.17	0.2	0.2	2.48/sf
	Extensive cracks (severe)			0.85	0.23	1.0	0.2	
Suspended tile ceiling [4]	Slight	23397	PFA (g)	0.27	0.4	0.1	0.2	3.16/sf
	Moderate			0.65	0.5	0.3	0.2	
	Severe			1.28	0.55	1.0	0.2	

[1]: Engelhardt *et al.* 2000; [2]: Gilton *et al.* 2000; [3]: Ricles *et al.* 2002; [4]: Krawinkler 2005;
[5]: Porter *et al.* 2001; [6]: Mitrani-Reiser 2007;
EDP: engineering demand parameter; c.o.v.: coefficient of variation; sf: square foot
IDR: story drift ratio; PFA: peak floor acceleration.

Table 6.2 Random variables of material types of different building components and CO_2 emissions of different building materials

Building component	Material type	Unit mass (kg/m^2)			CO_2 emission (kg CO_2/kg)		
		Factor I	Factor II	Distribution type	Factor I	Factor II	Distribution type
Interior partition	Bricks and blocks	1.9	0.4 [2]	LN [1]	0.0415	0.4 [2]	LN [1]
	Concrete	1.15	0.4 [2]	LN [1]	0.045	0.06	UF [1]
	Galvanized steel	4.35	0.4 [2]	LN [1]	0.63	0.72	UF [1]
	Glass	1.27	0.4 [2]	LN [1]	0.184	0.4 [2]	LN [1]
	Reinforcing bar	4.5	0.4 [2]	LN [1]	0.46	0.4 [2]	LN [1]
	Stainless steel	0.01	0.8	UF [1]	0.16	0.27	UF [1]
Aluminum framed window	Aluminum	0.35	0.4 [2]	LN [1]	5.035	0.4 [2]	LN [1]
	Glass	17.55	0.4 [2]	LN [1]	0.184	0.4 [2]	LN [1]
Interior finish	Aluminum	0.4	0.4 [2]	LN [1]	5.035	0.4 [2]	LN [1]
	Galvanized steel	0.4	0.4 [2]	LN [1]	0.63	0.72	UF [1]
	Plaster	26.7	0.4 [2]	LN [1]	0.0231	0.4 [2]	LN [1]
	Stone	8.05	0.4 [2]	LN [1]	0.009	0.4 [2]	LN [1]
Suspended ceiling	Aluminum	0.65	0.4 [2]	LN [1]	5.035	0.4 [2]	LN [1]
	Galvanized steel	3.85	0.4 [2]	LN [1]	0.63	0.72	UF [1]
	Plaster	2.8	0.4 [2]	LN [1]	0.0231	0.4 [2]	LN [1]

[1]: Chau *et al.* 2012; [2]: assumed; LN: lognormal distribution; UF: uniform distribution. In the case of the lognormal distribution, Factors I and II refer to mean and coefficient of variation, respectively; in the case of uniform distribution, Factors I and II refer to lower and upper bounds, respectively.

Table 6.3 Parameters of repair time (hours) associated with the investigated components

Component	Damage state	Repair hour Mean	Repair hour c.o.v	Unit
Reduced beam section connection [1, 2]	Slight	44	0.3	Each
	Moderate	190	0.3	
	Severe	240	0.4	
Welded unreinforced flange-welded web connection [2]	Slight	44	0.3	Each
	Moderate	190	0.3	
	Severe	240	0.4	
Aluminum framed window [2]	Slight	1.45	0.3	Pane
	Moderate	5.75	0.3	
	Severe	11.5	0.4	
Interior partition [2]	Small cracks	1	0.4	64 sf
	Extensive cracks	4	0.4	
Interior finish [2]	Small cracks	1	0.4	64 sf
	Extensive cracks	7	0.4	
Suspended ceiling [2]	Slight	0.05	0.5	250 sf
	Moderate	0.1	0.5	
	Severe	0.2	0.5	

[1]: Aslani and Miranda 2005; [2]: Mitrani-Reiser 2007;
c.o.v: coefficient of variation; sf: square foot

Table 6.4 Expected sustainability metrics of conventional and base-isolated buildings under 1940 El Centro and 1995 Kobe earthquakes

Consequences		1940 EI Centro Earthquake		1995 Kobe Earthquake	
		Conventional building	Base-isolated building	Conventional building	Base-isolated building
Repair loss (USD)		7.121×10^5	2.456×10^5	4.818×10^6	6.695×10^5
Fatality loss (USD)		2.164×10^4	5.391×10^3	4.178×10^6	1.600×10^6
Downtime loss (USD)	Slow-track	4.679×10^5	2.121×10^5	1.811×10^6	3.309×10^5
	Quick-track	1.827×10^5	1.157×10^5	7.842×10^5	1.746×10^5
CO_2 emissions (kg)		8.093×10^4	4.543×10^4	1.308×10^5	5.642×10^4

(a)

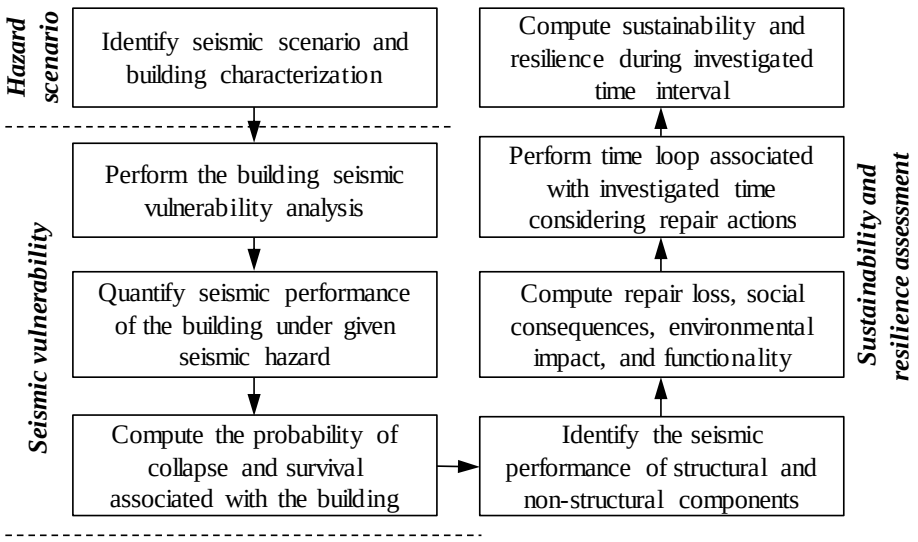

(b)

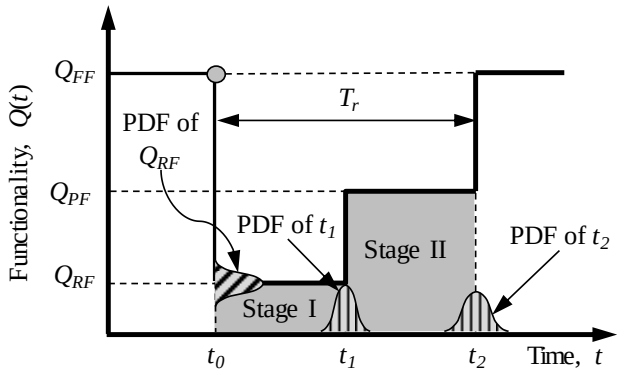

Figure 6.1 (a) Flowchart for sustainability and resilience assessment of buildings under seismic hazard and (b) resilience under extreme event

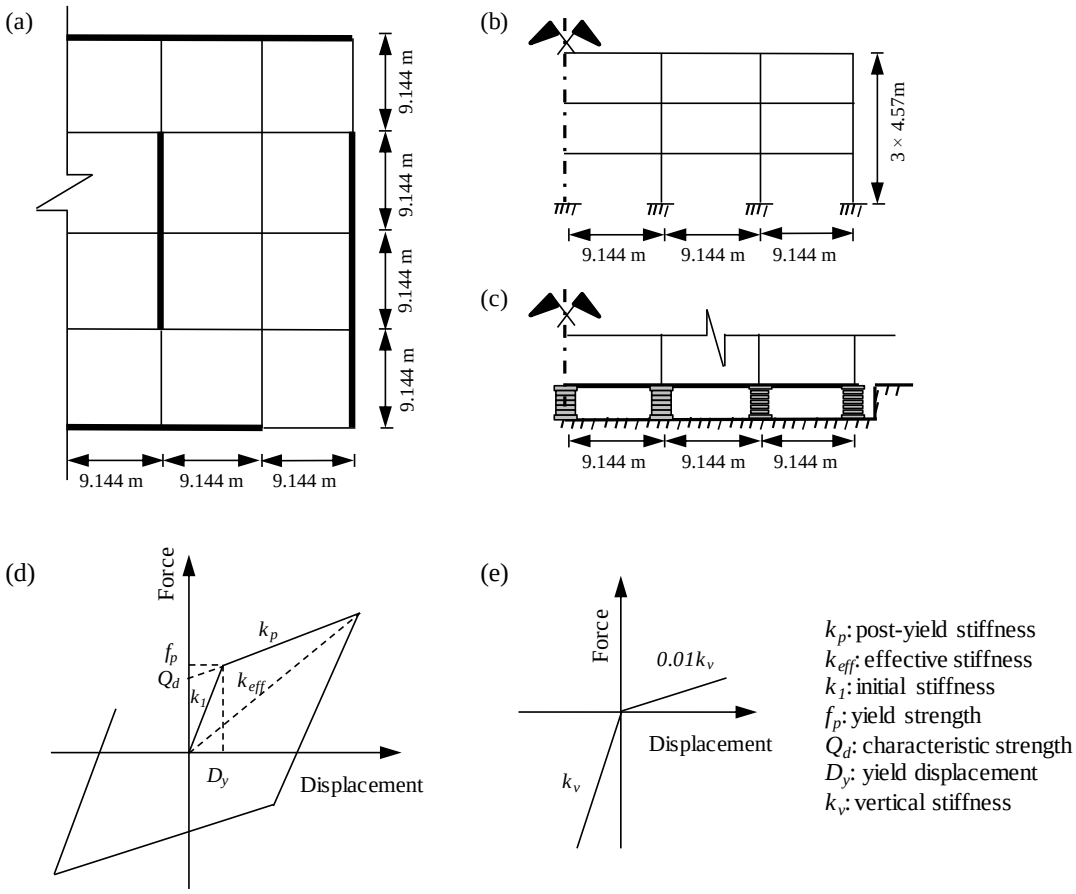

Figure 6.2 (a) Plan and (b) elevation of conventional and (c) based-isolated buildings, (d) lateral, and (e) vertical force-displacement associated with isolation devices (adapted from Sayani 2009)

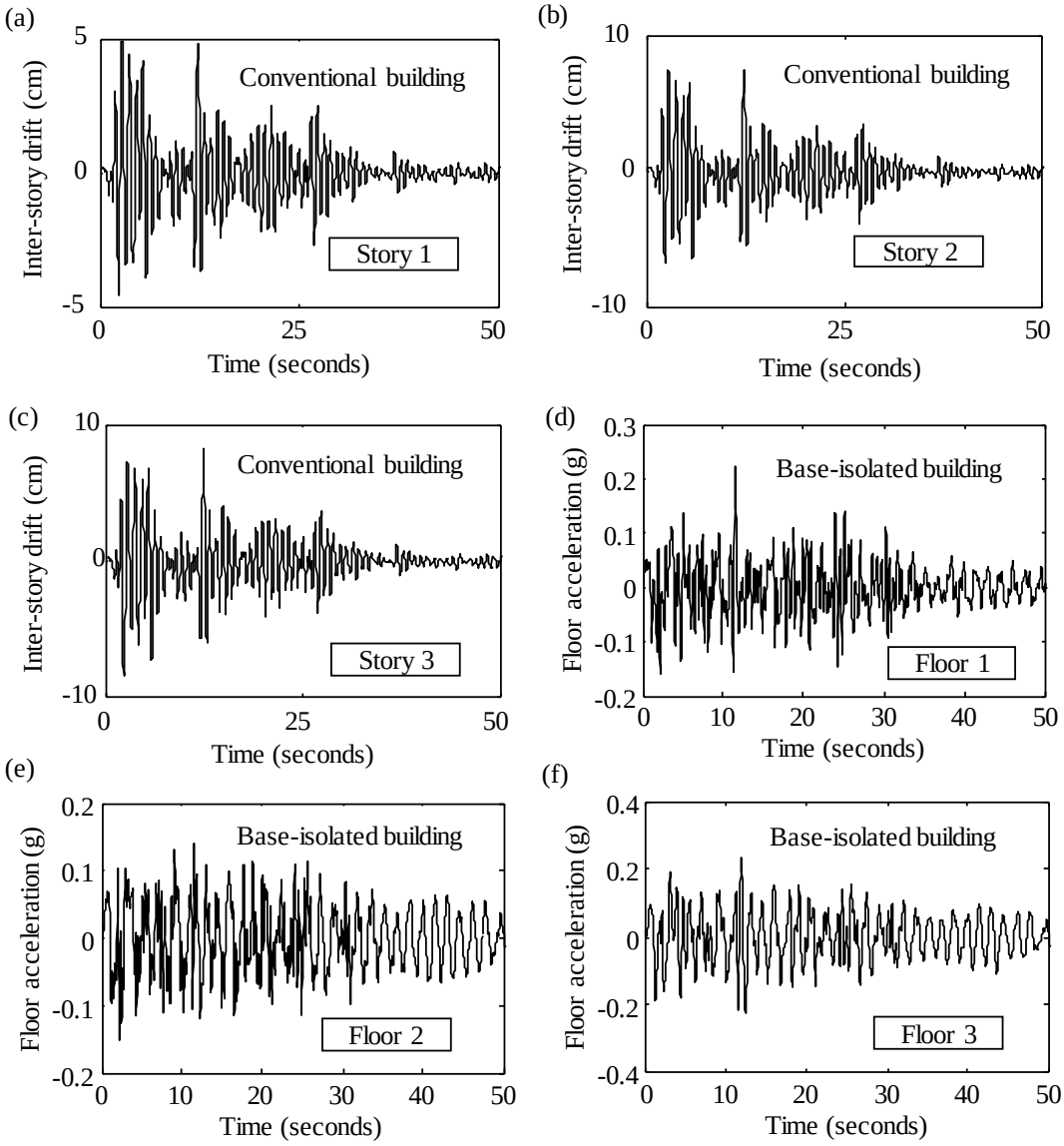

Figure 6.3 Inter-story drift of (a) first, (b) second, and (c) third story of conventional building under 1940 El Centro earthquake and total floor acceleration of (d) first, (e) second, and (f) third floor of base-isolated building under 1940 El Centro earthquake

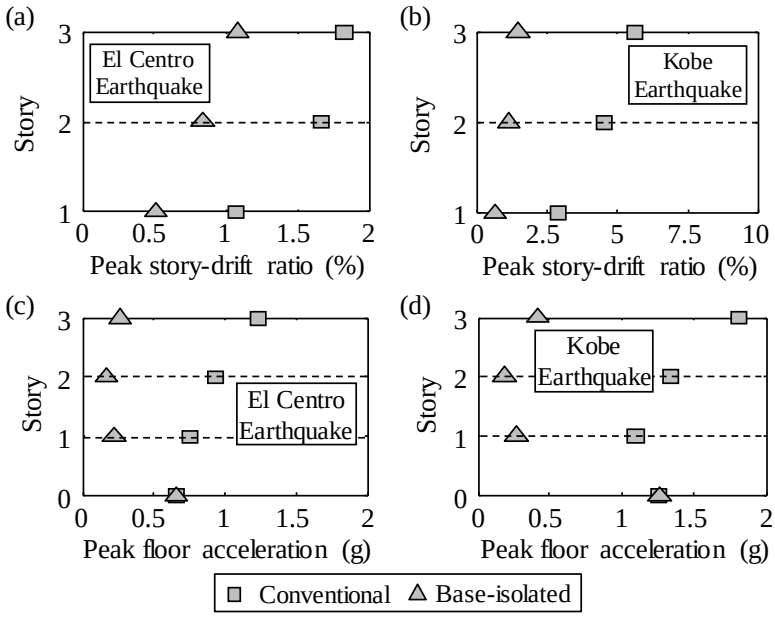

Figure 6.4 Peak inter-story drift ratio of conventional and base isolated building under (a) 1940 El Centro and (b) 1995 Kobe earthquake, and peak floor acceleration of the conventional and base-isolated building under (c) 1940 El earthquake and (d) 1995 Kobe earthquake

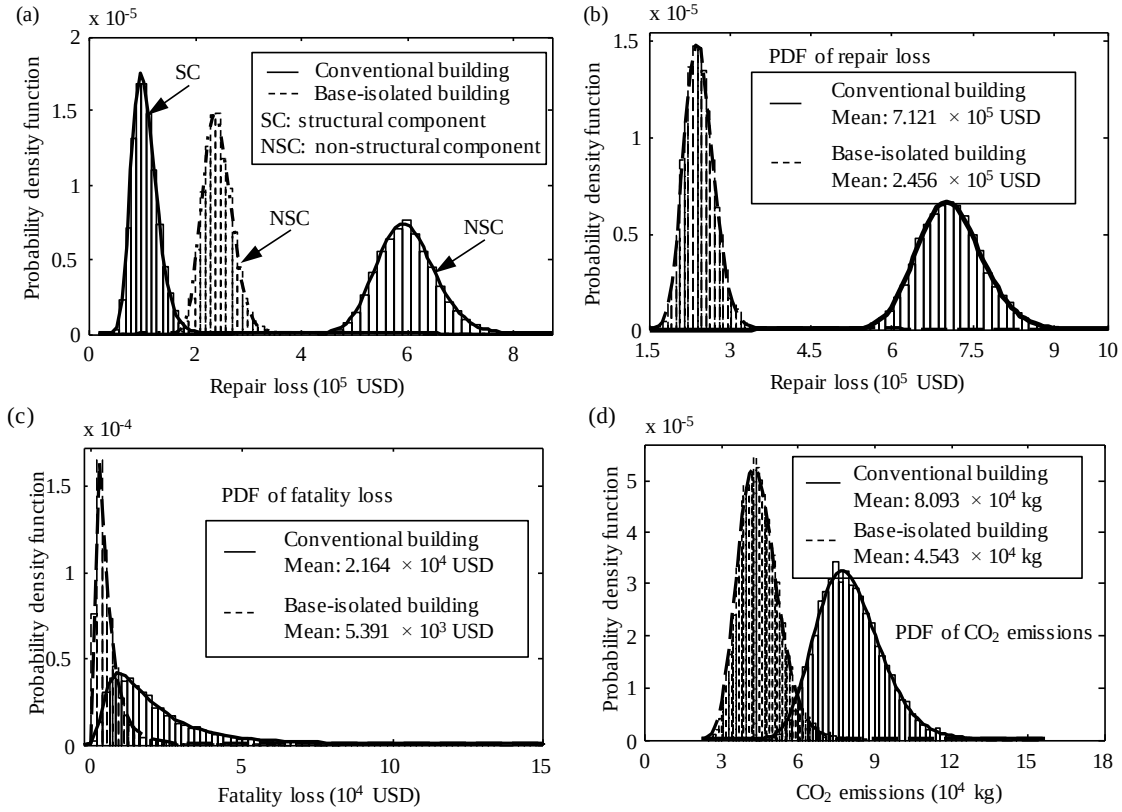

Figure 6.5 (a) PDF of structural component and non-structural component repair loss, (b) structural repair loss, (c) fatality loss, and (d) CO_2 emissions of conventional and base-isolated buildings under 1940 El Centro earthquake

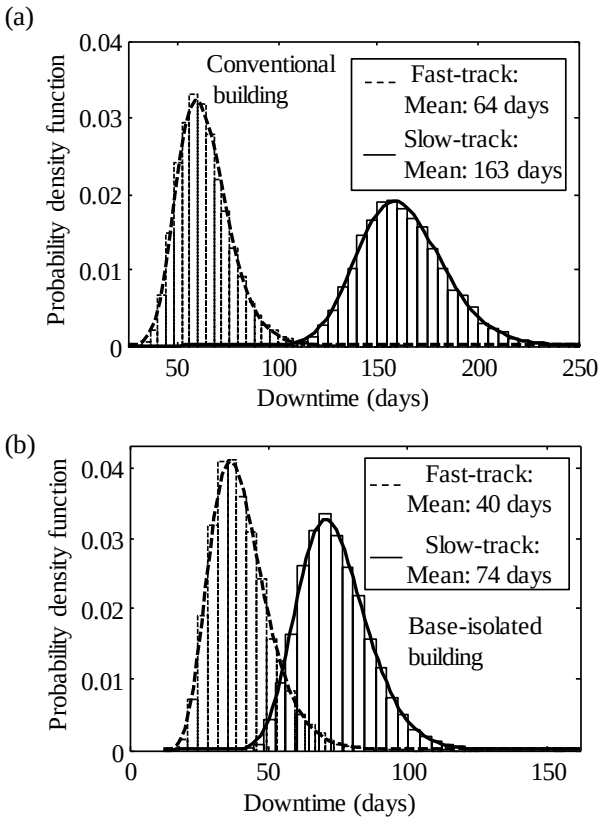

Figure 6.6 Downtime associated with the (a) conventional and (b) base-isolated buildings using fact-track and slow-track repair schemes under 1940 El Centro earthquake

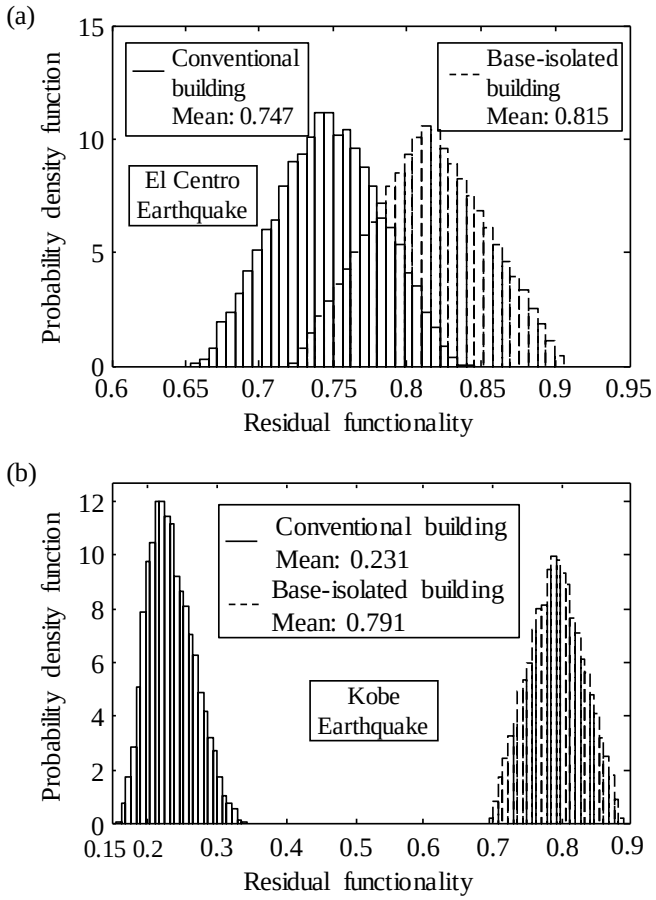

Figure 6.7 PDF of residual functionality of conventional and base-isolated building under (a) 1940 El Centro earthquake and (b) 1995 Kobe earthquake

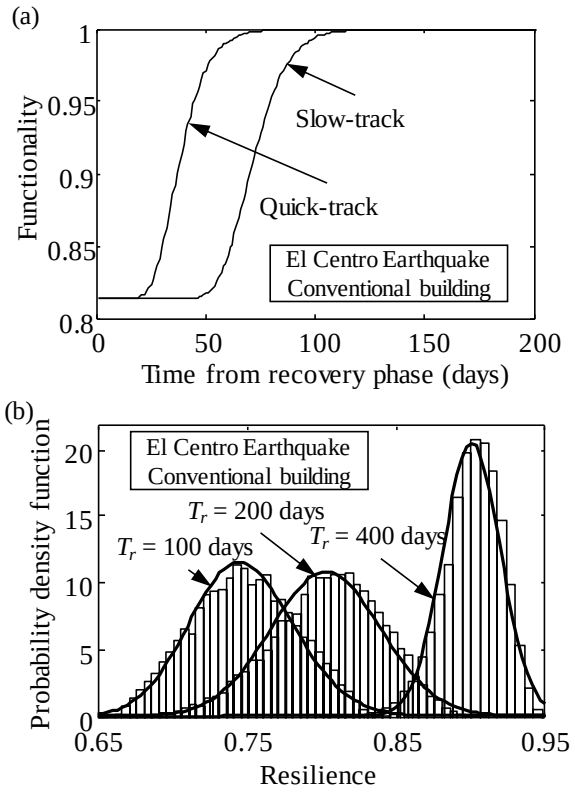

Figure 6.8 (a) Time-variant expected functionality and (b) PDF of resilience of conventional building under 1940 El Centro earthquake considering T_r = 100, 200, and 400 days

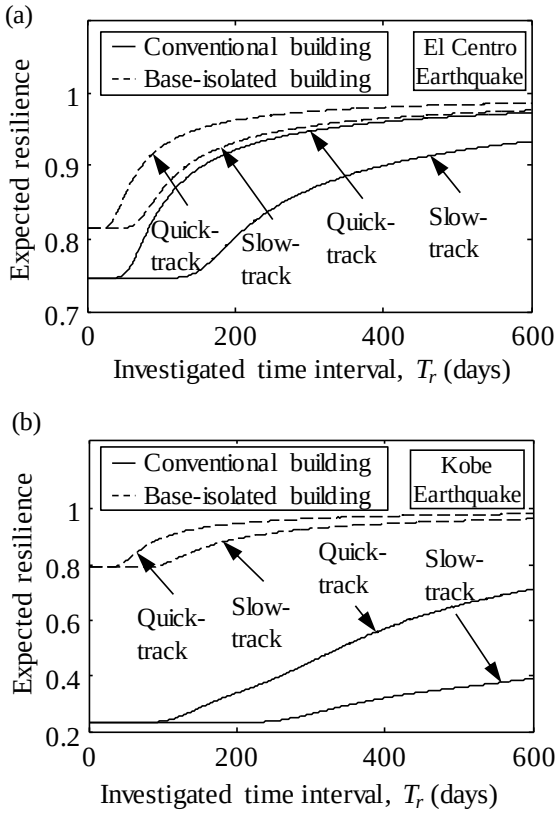

Figure 6.9 Expected resilience of conventional and base-isolated buildings under (a) 1940 El earthquake and (b) 1995 Kobe earthquake considering different time intervals and repair schemes

CHAPTER 7

PROBABILISTIC ASSESSMENT OF AN INTERDEPENDENT HEALTHCARE – BRIDGE NETWORK SYSTEM UNDER SEISMIC HAZARD

7.1. INTRODUCTION

The World Health Organization (WHO) (2007) stated that healthcare systems "must be physically resilient and able to remain operational and continue providing vital health services" after disasters. Thus, healthcare systems need to be resilient enough to cope with earthquakes and to provide timely medical treatment. In this chapter, the seismic performance assessment of a healthcare system located near a bridge network is investigated considering both component and system performance levels.

The assessment of healthcare – bridge network system performance depends on the seismic vulnerability of bridges located in a bridge network and hospital, as well as on the ground motion intensity. After a destructive earthquake, the functionality of a highway network can be affected significantly; this, in turn, may lead to hinder the emergency management. Additional travel time would result due to the damaged bridges and links; consequently, injured persons may not receive treatment in time. Thus, it is important to account for the effects of damage condition associated with highway bridge network on the healthcare system performance. In this chapter, the extra travel time of

injured persons through the damaged bridge network to a hospital under the seismic hazard is investigated.

Myrtle *et al.* (2005) carried out a series of surveys on performance of hospitals during several earthquakes to identify the important components; Yavari *et al.* (2010) investigated performance levels for interacting components (i.e., structural, nonstructural, lifeline, and personnel) using data from past earthquakes; Achour *et al.* (2011) investigated the physical damage of structural and non-structural components of an hospital under seismic hazard; and Cimellaro *et al.* (2011) introduced a model to describe the hospital performance under earthquake considering waiting time. However, the damage conditions associated with bridge networks have not been incorporated within the healthcare system performance assessment process. Additionally, the correlation effects have also not been addressed in these studies.

After an earthquake, it is common to experience a sudden increase in the number of patients for a period of time, which in turn can bring delay in treating them. The estimation of hospital capacity after an extreme event is of vital importance to determine the waiting time of the injured persons. Hospital functionality may be disrupted by damage associated with structural and non-structural components or medical equipment. A proposed approach considering both structural and non-structural components (e.g., medical equipment) is presented in this chapter to investigate the hospital performance under a given seismic scenario. The relationship between structural and non-structural seismic demands (e.g., peak inter story drift ratio and peak floor acceleration) is considered. Additionally, the correlations among the damages of structural and non-

structural components is also considered in the hospital functionality assessment process. Finally, the effects of correlation on the healthcare – bridge network system performance at a system level are investigated.

This chapter aims to assess probabilistically an interdependent healthcare - bridge network system under seismic hazard and to aid the emergency preparedness to cope with the sudden increase of patients. The damage conditions of the bridges, links, and hospital are considered in the overall system performance assessment. Fragility curves are employed to identify the components vulnerability under seismic hazard. The effects of disruption associated with transportation system on the emergency management are investigated. Additionally, the correlations among structural damages and the effect of bridge retrofit actions are considered in the assessment process. The system level performance indicators are expressed in terms of the extra travel and waiting time of the injured persons from the damaged region to the hospital given the occurrence of the earthquake. The approach is illustrated on a healthcare system located near a bridge network in Alameda, California. This chapter is based on a published paper Dong *et al*. (2015). This chapter is based on a paper submitted for possible publication (Dong and Frangopol 2015d).

7.2. EARTHQUAKE SCENARIOS

The first step in seismic performance assessment of a healthcare system located near a bridge network is to identify the seismic scenarios at the location of the system. The seismic scenarios associated with an earthquake fault are introduced herein. The earthquake rupture is given as a characteristic magnitude distribution, modeled as a

Gaussian distribution using the mean, a coefficient of variation of 0.12, and a truncation at ± 2 standard deviations of magnitude above and below the mean (USGS 2003).

The seismic intensities at different sites caused by the same earthquake are correlated. It is necessary to consider the spatial correlation of ground motion intensities within the seismic performance assessment of interdependent hospital – bridge network system. Several studies (e.g., Wang and Takada 2005; Jayaram and Baker 2009) revealed that the peak ground acceleration (PGA) associated with a given seismic scenario at different sites is spatially correlated and this correlation is higher for closer sites. Accordingly, the correlation among the seismic intensities at different locations is modeled as an exponential decay function (Wang and Takada 2005). Given the distribution types associated with the ground motion intensities and correlation coefficients, the correlated ground motion intensities could be generated using straightforward numerical procedures, such as Monte Carlo simulation. In this chapter, the effects of ground motion correlation are accounted for within the seismic assessment of spatially distributed interdependent healthcare - bridge network system.

7.3. BRIDGE, LINK, AND HOSPITAL SEISMIC DAMAGE

7.3.1. Bridge and link seismic vulnerability

A transportation network is composed of nodes, links, and bridges. Nodes describe the locations of highway intersections, while links represent the highway segments connecting two nodes. Generally, bridges are considered to be the most vulnerable components in a transportation network (Liu and Frangopol 2006; Lee and Kiremidjian 2007; Dong *et al.* 2014). Fragility curves are commonly used to quantify structural

performance under seismic hazard and are defined by the exceedance probability of a damage state under a given ground motion intensity (Mander 1999; Dong *et al.* 2013). The correlations among the seismic performance of bridges in terms of fragility have also to be considered. Specifically, bridges in a transportation network can be classified into different subgroups to characterize their fragilities considering structural characteristics, such as number of spans and material types (e.g., steel, concrete). A link is considered as an element connecting the nodes of a network. The performance of network links is related with individual bridge located on the link. The performance of the link after an earthquake can be expressed in terms of link damage index *LDI*, which depends on the *BDI*s of the bridges on the link.

7.3.2. Hospital functionally assessment

The effects of damage states associated with structural and non-structural components on the damage performance of a hospital are introduced in this section. The damage assessment of the hospital should determine the capacity of how many patients it can handle to provide timely treatment to the injured people (Cimellaro *et al.* 2011). The functionality of a hospital could be assessed based on its components (e.g., structural, nonstructural) (Yavari *et al.* 2010). Building components can be categorized into structural, non-structural, and content (Mitrani-Reiser 2007). The performance associated with different components of a hospital system should be investigated by using different seismic demand indicators (e.g., story drift, floor acceleration). The damage to structural components is usually related with structural drift and ground motion acceleration, while

the damage of non-structural components is generally associated with the floor acceleration (Mitrani-Reiser 2007; Dong and Frangopol 2015).

Given the ground motion intensity, the seismic performance of a hospital is investigated by using fragility curves. Based on HAZUS (2003), the PGA is adopted to predict the performance of structural components under earthquakes. The probability of the structural components being in different damage states could be computed accordingly. The peak floor acceleration (PFA) acts as seismic demand for the damage assessment of non-structural components. The peak floor acceleration amplification Ω (i.e. *PFA*/*PGA*) is adopted herein to compute the PFA, which in turn could be utilized for the vulnerability analysis of non-structural components. The peak floor acceleration amplification factor Ω is (Chaudhuri and Hutchinson 2004)

$$\Omega = (1.0 + \alpha_1 \sqrt{h_{nor}})(1.0 - h_{nor}) + (\alpha_2 h_{nor}^{\ 2}) h_{nor} \tag{7.1}$$

where α_1 and α_2 are empirical constants and h_{nor} is normalized height computed as the floor height divided by the total building height. The decreasing shear and increasing bending contributions are considered in Eq. (7.1). Given the detailed information of the investigated hospital and seismic inputs, the PFA could also be obtained using nonlinear time history or incremental dynamic analysis (Dong and Frangopol 2015).

The expected damage indices associated with structural and non-structural components can be expressed, respectively, as follows

$$D_{SC} = \sum_{i=1}^{n_{SD}} HCDI_{SC,i} \cdot P_{SCi|IM} \tag{7.2}$$

$$D_{NSC} = \sum_{i=1}^{n_{NSD}} HCDI_{NSC,i} \cdot P_{NSCi|IM} \tag{7.3}$$

where $HCDI_{SC,i}$ and $HCDI_{NSC,i}$ are the damage indices associated with state i of structural and non-structural components of the hospital, respectively; n_{SD} and n_{NSD} are the numbers of damage states associated with structural and non-structural components, respectively; and $P_{SCi|IM}$ and $P_{NSCi|IM}$ are the probabilities of the structural and non-structural components being in damage state i, respectively. These probabilities are obtained based on the fragility curves considering different seismic demands. The correlation coefficient between the damage indices of structural and non-structural components $\rho(HCDI_{SC}, HCDI_{NSC})$ is considered in the assessment process.

Given the weighting factors associated with structural and non-structural components, the composite expected hospital damage index *HDI* is

$$HDI = r_{SC} \cdot D_{SC} + r_{NSC} \cdot D_{NSC} \tag{7.4}$$

where r_{SC} and r_{NSC} are the weighting factors associated with structural D_{SC} and non-structural D_{NSC} damage indices, respectively. Given the probability density function (PDF) associated with hospital damage index *HDI* and threshold values (i.e., lower and upper bounds), the probability of a hospital being in different functionality levels *HFL*s can be identified. Holmes and Burkett (2006) suggested classifying structural and non-structural damages into four levels: none, minor, affecting hospital operations, and temporary closure. Yavari *et al.* (2010) presented an approach considering the overall facility as fully functional, functional, affected functionality, and not functional.

The capacity of a hospital depends on the classified hospital functionality levels *HFL*s. The waiting time is an important parameter to evaluate the capacity of a hospital during normal and extreme event conditions (Yi 2005). When the number of injured persons is larger than the number of patients treated, additional waiting time is necessary.

The waiting time associated with hospital functional level HFL_i under daily patient rate λ is (Paul *et al.* 2006)

$$WT_i(\lambda) = \exp(A_i + B_i\lambda) \tag{7.5}$$

$$A_i = \frac{\lambda_U \ln(WT_L) - \lambda_L \ln(WT_{Ui})}{\lambda_U - \lambda_L} \tag{7.6}$$

$$B_i = \frac{\ln(WT_{Ui}) - \ln(WT_L)}{\lambda_U - \lambda_L} \tag{7.7}$$

where A_i and B_i are constants associated with the hospital functionality level i; λ_L is the pre-disaster average daily patient arrival number; WT_L is the waiting time associated with the normal hospital operation; λ_U is the maximum daily arrival number; and WT_{Ui} is the waiting time associated with functionality level i under the maximum arrival rate λ_U. Eq. (7.10) is used herein to compute the waiting time; given additional data, other functions could also be adopted.

7.4. SYSTEM LEVEL PERFORMANCE ASSESSMENT

In this section, the effects of the damage states associated with a bridge network and a hospital on system level performance of an interdependent healthcare – bridge network are investigated. The extra travel and waiting time at the system level are computed. Based on the configuration of the investigated bridge network, travel time is defined as the time it takes to transfer the injured people to the hospital immediately after the earthquake. With respect to waiting time analysis, the healthcare system performance is measured by the waiting time needed to get the injured persons treated.

The extra travel time experienced by an injured person is due to the damages of bridges and links in a bridge network. The travel time is representative of the

functionality of a bridge network; large travel time reveals a high reduction of functionality associated with a bridge network (Frangopol and Bocchini 2011; Bocchini and Frangopol 2011; Dong *et al.* 2015). The extra daily travel time *EDTT* for the injured persons in a bridge network can be expressed as (Dong *et al.* 2015)

$$EDTT = \sum_{j=1}^{n_l} \sum_{i=1}^{n_{LD}} P_{LDSj,i|IM} [ADR_{ij} \cdot (\frac{l_j}{S_{Dj,i}} - \frac{l_j}{S_{0j}}) + ADT_{ij} \cdot \frac{D_j}{S}] \quad (7.8)$$

where n_l is the number of links in a bridge network; n_{LD} is the number of damage states associated with link damage; $P_{LDSj,i|IM}$ is the conditional probability of the jth link being in damage state i; ADT_{ij} is average daily number of injured persons that follow detour due to damage state i of the jth link; D_j is the length of the extra detour of jth link (km); S is the detour speed (km/h); ADR_{ij} is the average daily number of injured persons that remain on the jth link under damage state i; l_j is the length of link j (km); S_{0j} is the traffic speed on intact link j (km/h); and $S_{Dj,i}$ is the traffic speed on link j associated with damage state i (km/h).

The waiting time is related with the hospital functionality levels under a given seismic scenario. Given the limited functionality associated with the hospital, the extra waiting time of the injured people could be computed. Based on the theorem of total probability, the extra daily waiting time *EDWT* can be computed as

$$EDWT = \sum_{i=1}^{n_H} [P_{HFi|IM} \cdot WT_i(ATV)] \cdot ATV - ATV \cdot WT_0(ATV) \quad (7.9)$$

where *ATV* is the total number of injured persons transferred though a bridge network to a hospital; WT_i is the waiting time associated with functionality level i given *ATV*; n_H is the number of functionality levels of a hospital under investigation; $WT_0(ATV)$ is the waiting time associated with the intact hospital under *ATV*; and $P_{HFi|IM}$ is the conditional

probability of hospital being in functionality level *i* under *IM*. The flowchart of the computation associated with the extra travel and waiting time of a healthcare system under seismic hazard is shown in Figure 7.1.

During the system level performance assessment process, the correlations associated with the ground motion intensities and seismic damage indices are considered. For example, the correlations among the IMs at different locations are computed using Eq. (7.2). Then by using Monte Carlo simulation, these correlated IMs could be generated. Overall, given the correlation coefficients, the correlated random variables used in the functionality assessment procedure could be generated. The flowchart of generating these random variables using Monte Carlo simulation is shown in Figure 7.2. Finally, the system level performance indicators (e.g., extra travel and waiting time) could be computed using Eqs. (7.8) and (7.9).

Due to the correlations among the random variables of ground motion intensities and seismic damage indices associated with bridges and hospital, the seismic performance of a bridge network and a hospital is correlated. The correlation effects on the conditional seismic performance of a hospital given the damage state of a link is investigated herein. The conditional probability of a hospital being in functionality level *j* given the link in damage state *i* is

$$P(HFL_{j|IM} \left| LDS_{i|IM} \right.) = \frac{P(HFL_{j|IM} \cap LDS_{i|IM})}{P(LDS_{i|IM})} \tag{7.10}$$

where $HFL_{j|IM}$ is the event that a hospital is in functionality level *j* given *IM* and $LDS_{i|IM}$ is the event that a link is in damage state *i* given *IM*. The probability $P(HFL_{j|IM} \cap LDS_{i|IM})$ could be computed by considering the events $HFL_{j|IM}$ and $LDS_{i|IM}$ as a parallel system.

Then, given the correlation coefficients among the random variables (e.g., ground motion intensities, seismic damage indices), the $P(HFL_{j|IM} \cap LDS_{i|IM})$ is computed. When the events $HFL_{j|IM}$ and $LDS_{i|IM}$ are independent $P(HFL_{j|IM} \cap LDS_{i|IM}) = P(HFL_{j|IM}) \times P(LDS_{i|IM})$. Finally, given $P(HFL_{j|IM} \cap LDS_{i|IM})$ and $P(LDS_{i|IM})$, the conditional probability of the hospital being in functionality level j is computed according to Eq. (7.10).

7.5. ILLUSTRATIVE EXAMPLE

7.5.1. Seismic performance of bridges and links

In order to quantify the seismic performance of the bridges and links, the probabilistic earthquake scenarios should be identified. The seismic scenarios are selected based on the seismic rupture sources in the San Francisco bay area (USGS 2003). The investigated earthquake magnitudes are associated with the Northern Hayward Fault as the healthcare – bridge network system is located in this area. The segment length and width of the fault are 50 and 14 km, respectively. The expected magnitude associated with the investigated rupture is 6.88.

The PGA is utilized as ground motion intensity measure and other ground motion intensities (e.g., spectral acceleration) could also be used (Campbell and Bozorgnia 2008). The PGA is assumed lognormal. Its expected value at the location of the hospital is 0.865g and the standard deviation is 0.51g using the attenuation equation (Campbell and Bozorgnia 2008). The probabilistic PGAs at the locations of the bridges and hospital are generated using Monte Carlo simulation. The correlation among the PGAs at the locations of the hospital and bridges is computed. The exponential decay function has

been widely adopted in the assessment of the spatial correlation of PGA (Goda and Hong 2008; Jayaram and Baker 2009; Esposito and Iervolino 2011). Then, the correlated random variables associated with ground motion intensities are generated using Monte Carlo simulation as indicated in Figure 7.2.

The parameters of the fragility curves associated with the bridges located on the network are based on Shinozuka *et al.* (2001). Bridges 2, 7, and 9 are single-span concrete bridges; the remaining bridges are multiple-span continuous concrete bridges. The fragility curves of the basic single and multiple-span continuous concrete bridges are shown in Figure 7.4 (a) and (b). Given the skew angle and soil condition of the specific bridges, the fragility curves could be updated accordingly (Shinozuka *et al.* 2001).

Given the ground motion intensity and fragility curves, the probabilities of the bridges being in different damage states are computed. The damage state index *BDDI* is considered lognormal with a coefficient of variation 0.5 (HAZUS 2003; Shinozuka *et al.* 2008). The expected values of the damage index associated with slight, moderate, major, and complete damage states are 0.1, 0.3, 0.75, and 1, respectively (Shiraki *et al.* 2007). Monte Carlo simulation is adopted to generate these random variables. The bridge damage states associated with bridge 1 (multiple-span continuous concrete) and 2 (single-span concrete bridge) are shown in Figure 7.4 (c) and (d), respectively. The bridge damage indices associated with bridges 1 and 2 are best fitted by a gamma distribution with mean values 0.338 and 0.196, and standard deviations 0.272 and 0.187, respectively. Subsequently, the damage indices of links are computed.

The correlation among the random damage indices *BDDI* of different seismic damage states is now considered. Herein, the correlation coefficients are assumed to be 0, 0.5, and 1, representing uncorrelated, partially, and fully correlated random variables, respectively. These values are adopted to investigate the correlation effects on the network performance under seismic hazard. Additionally, the damage indices of different bridges are also correlated. The probabilistic damage index associated with link 1 under different correlation coefficients among the damage indices *BDDI* is shown in Figure 7.5(a). As indicated, the standard deviation of the link damage index increases as the correlation coefficient among the random variables increases. Given the threshold associated with link performance, the probabilities of the link 1 being in different performance levels (i.e., from no damage to major damage) are shown in Figure 7.5(b). As indicated, without considering the correlation effect, the probabilities of link being in none and major damage states would be underestimated. The probabilities of the links 2 and 3 being in different damage states are shown in Table 7.1.

7.5.2. Hospital damage assessment

In order to quantify the hospital damage index *HDI*, the seismic intensity and vulnerability of structural and non-structural components should be identified. The PGA is adopted as seismic demand indicator for the structural components, while the PFA is used to investigate the seismic performance of non-structural components (HAZUS 2003). The relationship between PFA and PGA is indicated in Eq. (7.1). For the mid-rise hospital building, α_1 and α_2 are assumed 1.63 and 1.53, respectively (Chaudhuri and Hutchinson 2004). The maximum PFA occurs at h_{nor} = 1 for the investigated hospital.

The parameters of the fragility curves associated with structural and non-structural components are based on HAZUS (2003) and shown in Table 7.2. Given moderate-code seismic provision, the median values and standard deviations of fragility curves associated with structural and non-structural components could be obtained. Subsequently, given the PGA and PFA, the seismic vulnerabilities (i.e., $P_{SCi|IM}$ and $P_{NSCi|IM}$) of the structural and non-structural components are computed. Herein, the damage indices of damage states associated with structural and non-structural components are based on Aslani and Miranda (2005). The mean values of slight, moderate, major, and complete damage states of structural components are 0.025, 0.12, 0.6, and 1.2, respectively. The mean values of slight, moderate, major, and complete damage states of non-structural components are 0.02, 0.12, 0.36, and 1.2, respectively. The coefficients of variation of these random variables are 0.7. Then, based on Eqs. (7.2) and (7.3), the damage indices of structural and non-structural components are computed. The PDFs of damage indices of structural and non-structural components are indicated in Figure 7.6.

The correlation coefficient among the damage indices of structural and non-structural components $\rho(HCDI_{SC}, HCDI_{NSC})$ is considered in the assessment process. The three correlation coefficients 0, 0.5, and 1 are considered. Monte Caro simulation is used to generate the random variables considering correlation as indicated in Figure 7.2. Given the damage index of structural and non-structural components, the composite building damage index is computed using Eq. (7.5). This equation is used to compute the hospital damage index. Herein, r_{SC} and r_{NSC} are assumed 0.5. The expected value and standard

deviation of *HDI* associated with $\rho(HCDI_{SC}, HCDI_{NSC}) = 0$ are 0.416 and 0.221, respectively. Given $\rho(HCDI_{SC}, HCDI_{NSC}) = 1$, the expected value and standard deviation of *HDI* are 0.416 and 0.319, respectively.

For the hospital functionality level analysis, none, slight, moderate, and major damage affecting hospital functionality is represented by the values of the hospital damage index $HDI \leq 0.3$, $0.3 < HDI \leq 0.6$, $0.6 < HDI \leq 1$, and $HDI > 1$, respectively. Given the hospital functionality criterion, the probabilities of the hospital being in different functionality levels are identified and shown in Table 7.3. As revealed, the probabilities of being in none and major damaged functionality levels increase when considering correlation effects.

7.5.3. System level performance

The seismic performance of a healthcare – bridge network system is investigated considering two indicators: (a) travel time and (b) waiting time. After the earthquake, the injured persons from nodes 1, 2, and 3 in Figure 7.3 are transferred to node 4, as the hospital is near this node. The extra travel and waiting time associated with the daily patient volume are investigated. The average daily number of injured persons associated with detour *ADT* and remaining number of injured persons *ADR* on the damaged link are based on Chang *et al.* (2000). If the damage state of the link is slight, the remaining patient volume and the flow speed are 100% and 75% of those for the intact link, respectively. In moderate damage state, the remaining volume and the flow speed are 75% and 50% of those for the intact link. In major damage state, the remaining volume and the flow speed are 50% and 50% of those for the intact link (Chang *et al.* 2000; Dong

et al. 2014). The extra detour length of links is 3.5 km. The daily patient volumes after the earthquake from node 1 to 4, 2 to 4, and 3 to 4 are 60, 120, and 60, respectively. The total number of daily injured persons transferred to the hospital is 240 (i.e., 60 + 120 + 60 = 240). Then given the probabilities of links being in different damage states as computed previously, the extra daily travel time considering the number of injured persons through the damaged transportation network is computed using Eq. (7.9). The correlation coefficients $\rho(BDDI_{Bk,i}, BDDI_{Bj,i})$ and $\rho(PGA_i, PGA_j)$ are denoted as ρ_1 and ρ_2, respectively. Given $\rho_1 = \rho_2 = 0$, the extra daily travel time is 15.13 hours; this value reduces to 12.02 hours given $\rho_1 = \rho_2 = 1$. As indicated, the correlation among the random variables could affect the extra travel time significantly. Furthermore, the correlation among the ground motion intensities has a larger effect on the extra travel time. Given $\rho_1 = \rho_2 = 0$, the extra daily travel time is 15.13 hours; this value reduces to 13.22 hours when $\rho_1 = 0$ and $\rho_2 = 1$, and to 14.09 hours when $\rho_1 = 1$ and $\rho_2 = 0$.

Given the hospital being in the performance levels as shown in Table 7.3, the extra daily waiting time is evaluated using Eq. (7.9). The pre-earthquake average patient arrival per day λ_L is 80. The waiting time WT_L associated with the normal operation condition is 20 minutes. Given more information (e.g., number of beds, number of operating rooms) of the investigated hospital, the arrival rate and waiting time could be updated. The maximum arrival per day λ_U is assumed 450. The waiting times associated with none, slight, moderate and major damage levels under maximum arrival rate are 40, 60, 80, and 120 minutes, respectively. Then by using Eqs. (7.5) – (7.7), the waiting times associated with different hospital functional levels are shown in Figure 7.7(a). The waiting time is

expressed using the exponential function (Paul *et al.* 2006). With additional data other models could also be incorporated within the assessment process.

The correlation effects are considered in the extra waiting time assessment process. Herein, $\rho(HCDI_{SC}, HCDI_{NSC})$ is denoted as ρ_3. Given $\rho_3 = 0$, the extra daily waiting time of the injured person is 16.84 hours; this value reduces to 15.46 hours when $\rho_3 = 1$. The extra daily waiting time of the injured people is slightly larger than the extra travel time. The effects of r_{SC} and r_{NSC} on the hospital functionality levels are indicated in Figure 7.7(b). The two parameters (i.e., r_{SC} and r_{NSC}) have a significant effect on the hospital functionality assessment and should be carefully assessed.

The effects of retrofit actions associated with the bridges on extra travel time are also studied. The fragility enhancement of bridges retrofitted by steel jacketing is investigated based on the approach presented in Shinozuka *et al.* (2008). The enhancement ratios associated with fragility median values are 55%, 75%, 104% and 145% considering slight, moderate, major, and complete damage states, respectively (Shinozuka *et al.* 2008). Given $\rho(BDDI_{Bk,i}, BDDI_{Bj,i}) = 0.5$, the extra daily travel time with and without retrofit actions are 3.12 and 13.01 hours, respectively. As revealed, the seismic retrofit actions have a profound effect on the extra travel time and can improve the healthcare – bridge network performance significantly. The probabilistic damage index associated with link 1 under these two scenarios (i.e., with and without retrofit actions) is shown in Figure 7.8(a). Additionally, the effects of seismic vulnerability of hospital on the system level performance are investigated. Medians and standard deviations associated with fragility curves of structural and non-structural components under low- and high-code

design provisions are shown in Table 7.2. Given the fragility curves associated with these design provisions, the extra daily waiting time with low-, moderate-, and high- design codes are 25.41, 16.06, and 10.59 hours, respectively. The PDF of the hospital damage index is shown in Figure 7.8(b). As revealed, the seismic design code has a significant effect on the hospital functionality levels.

Additionally, the effects of correlation on the conditional probabilities of hospital being in different functionality levels given the seismic damage of the link are investigated using Eq. (7.10). Given $\rho(BDDI, HCDI) = \rho(PGA_i, PGA_j) = 0.5$, the conditional probabilities of the hospital being in different functionality levels are shown in Table 7.4

The case without considering the correlation effects is also shown in this table. As indicated, the correlation effects could affect the conditional performance of the hospital significantly. For example, given the link 1 being in damage state 3 (i.e., moderate damage state), the conditional probability of the hospital being in moderate damaged functionality level is 0.2555, while this value is reduced to 0.1526 without considering the correlation effects.

7.6. CONCLUSIONS

This chapter presents an approach for assessment of an interdependent healthcare - bridge network system under seismic hazard considering uncertainties and correlation effects. The functionalities associated with the individual bridges, bridge networks, and hospital are investigated and combined for the system performance assessment. Rather than focusing only on structural damage, the extra travel and waiting time are investigated.

The approach is illustrated on a healthcare system near a bridge network in Alameda, California.

The following conclusions are drawn:

1. The correlation among the random damage indices *BDDI* has an effect on the probabilities of links being in different damage states and should be carefully evaluated.
2. It is necessary to consider the correlation coefficients among the spatial ground motion intensities and component-to-component damage indices for the healthcare – bridge network system performance assessment. The correlation coefficients have an effect on the standard deviations of the damage indices of bridges, links, and hospital.
3. Regarding the system level performance assessment, the extra travel and waiting time decrease when the correlation coefficients (e.g., correlations among the ground motion intensities and seismic damage indices) are accounted for. Additionally, the correlation among the ground motion intensities has a larger effect on the extra travel time than that among the damage indices.
4. The effects of retrofit and seismic strengthening associated with bridges and hospital are significant. Bridge retrofit actions could result in an improvement of the performance of healthcare – bridge network system.

Table 7.1 Probabilities of links 2 and 3 in Figure 7.3 being in different damage states considering correlation among the random damage indices *BDDI*

Link	Correlation coefficient	No damage	Slight damage	Moderate damage	Major damage
Link 2	0.0	0.3514	0.4509	0.1643	0.0334
	0.5	0.4136	0.4001	0.1356	0.0507
	1.0	0.4498	0.3573	0.1277	0.0652
Link 3	0.0	0.4472	0.4223	0.1111	0.0194
	0.5	0.4963	0.3666	0.1051	0.0320
	1.0	0.5327	0.3239	0.0977	0.0457

Table 7.2 Median and standard deviation associated with fragility curves of structural and non-structural components (adapted from HAZUS 2003)

Structural component								
Design level	Slight damage		Moderate damage		Major damage		Complete damage	
	Median	Standard deviation	Median	Standard deviation	Median	Standard deviation	Median	Standard deviation
Moderate -code	0.16	0.64	0.28	0.64	0.6	0.64	1.27	0.64
Low-code	0.15	0.64	0.23	0.64	0.42	0.64	0.73	0.64
High-code	0.17	0.64	0.34	0.64	0.85	0.64	2.1	0.64
Non-structural component								
Design level	Slight damage		Moderate damage		Major damage		Complete damage	
	Median	Standard deviation	Median	Standard deviation	Median	Standard deviation	Median	Standard deviation
Moderate -code	0.38	0.67	0.75	0.67	1.5	0.67	3	0.67
Low-code	0.3	0.65	0.6	0.67	1.2	0.67	2.4	0.67
High-code	0.45	0.66	0.9	0.67	1.8	0.68	3.6	0.66

Table 7.3 Probabilities of the hospital having different functionality levels under different correlation coefficients among the damage indices of structural and non-structural components

Correlation coefficient	No damage	Slight damage	Moderate damage	Major damage
0.0	0.3323	0.4946	0.1526	0.0205
0.5	0.4116	0.3903	0.1569	0.0412
1.0	0.4625	0.3234	0.1527	0.0614

Table 7.4 Conditional probabilities of the hospital being in different functionality levels given the seismic damage of the link 1 considering the correlations among the ground motion intensities and damage indices of bridges and hospital

Correlation coefficient	Hospital functional level	$P(HFL_{i\|IM} \| LDS_{1\|IM})$	$P(HFL_{i\|IM} \| LDS_{2\|IM})$	$P(HFL_{i\|IM} \| LDS_{3\|IM})$	$P(HFL_{i\|IM} \| LDS_{4\|IM})$
$\rho = 0.5$	No	0.6460	0.4032	0.2115	0.0823
	Slight	0.2978	0.4397	0.4681	0.3273
	Moderate	0.0520	0.1367	0.2555	0.3906
	Major	0.0042	0.0204	0.0649	0.1998
$\rho = 0$	No	0.3323	0.3323	0.3323	0.3323
	Slight	0.4946	0.4946	0.4946	0.4946
	Moderate	0.1526	0.1526	0.1526	0.1526
	Major	0.0205	0.0205	0.0205	0.0205

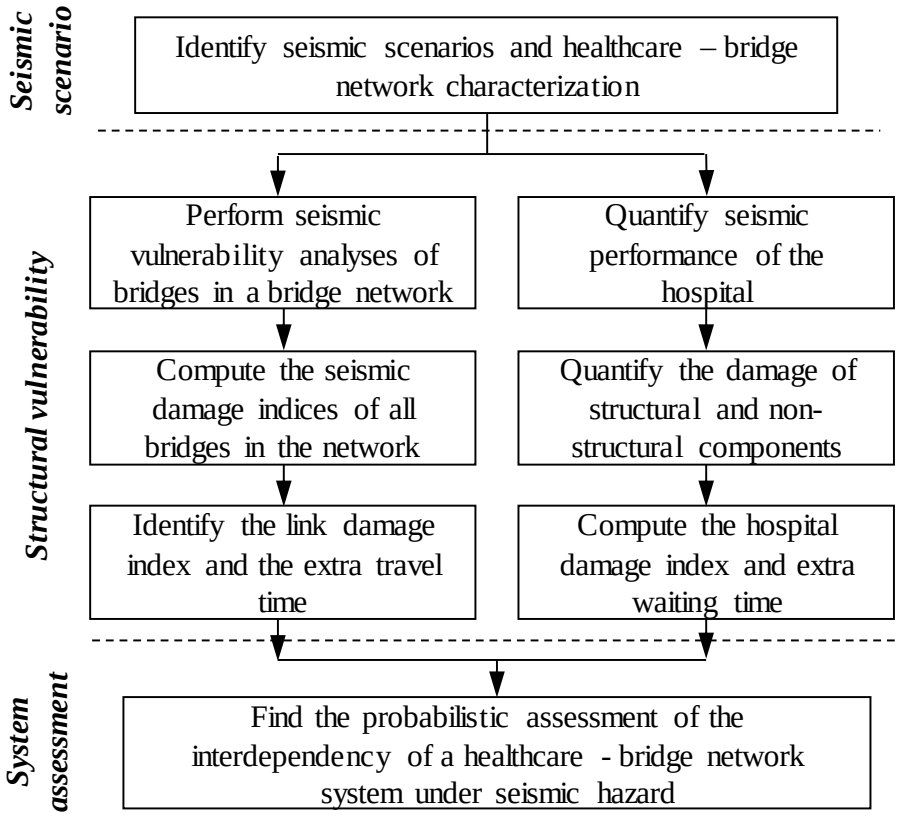

Figure 7.1 Flowchart of component and system levels functionality assessment of an interdependent healthcare – bridge network system under seismic hazard

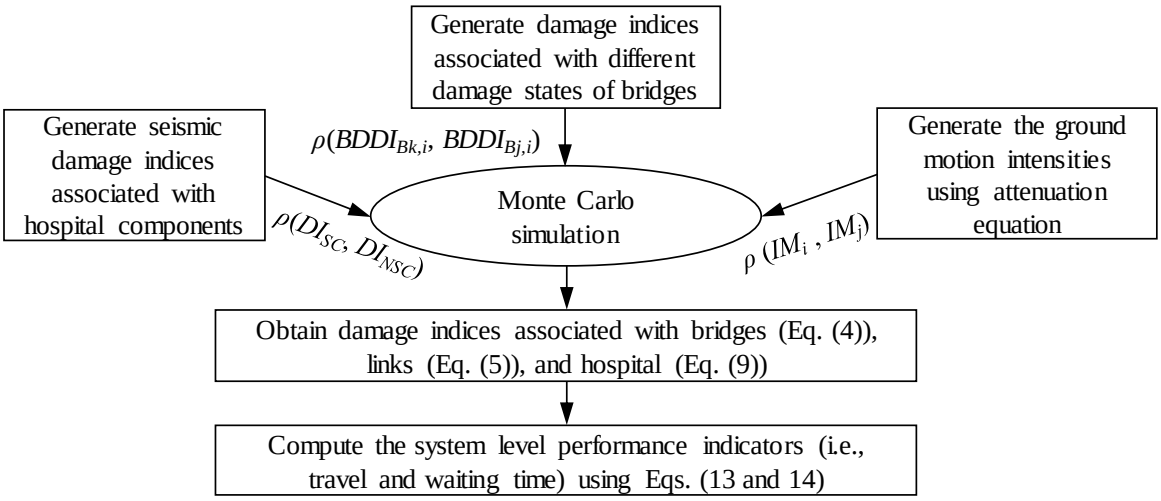

Figure 7.2 Flowchart of generating correlated random variables using Monte Carlo simulation to compute the system level performance indicators

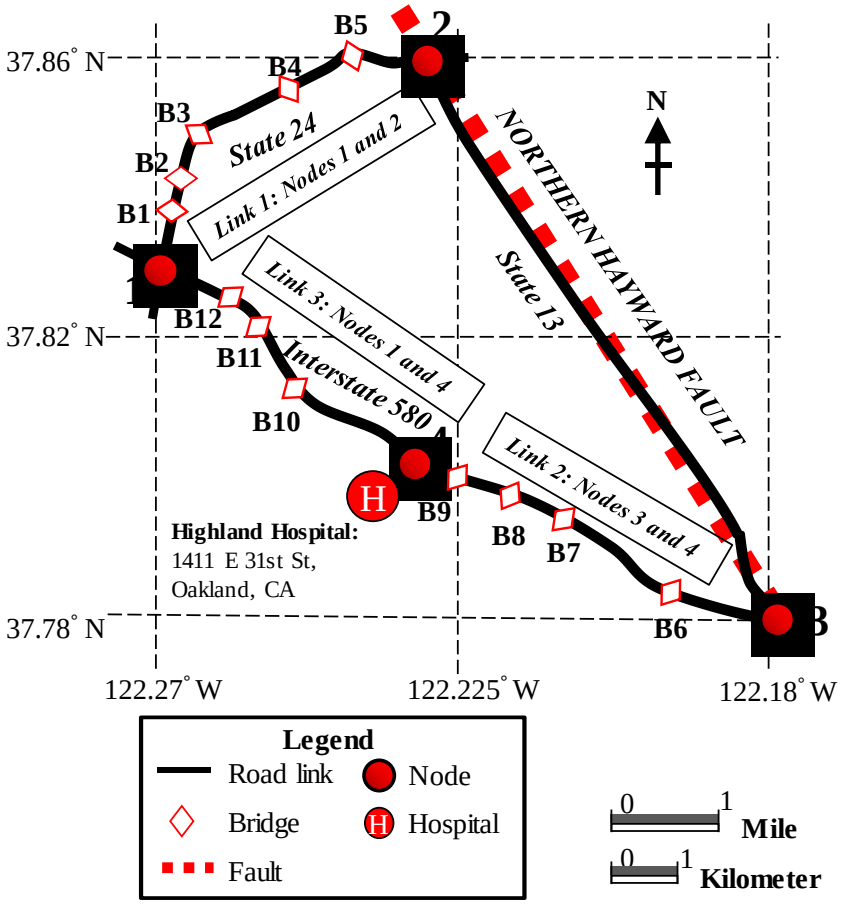

Figure 7.3 Layout of the healthcare – bridge network system under investigation

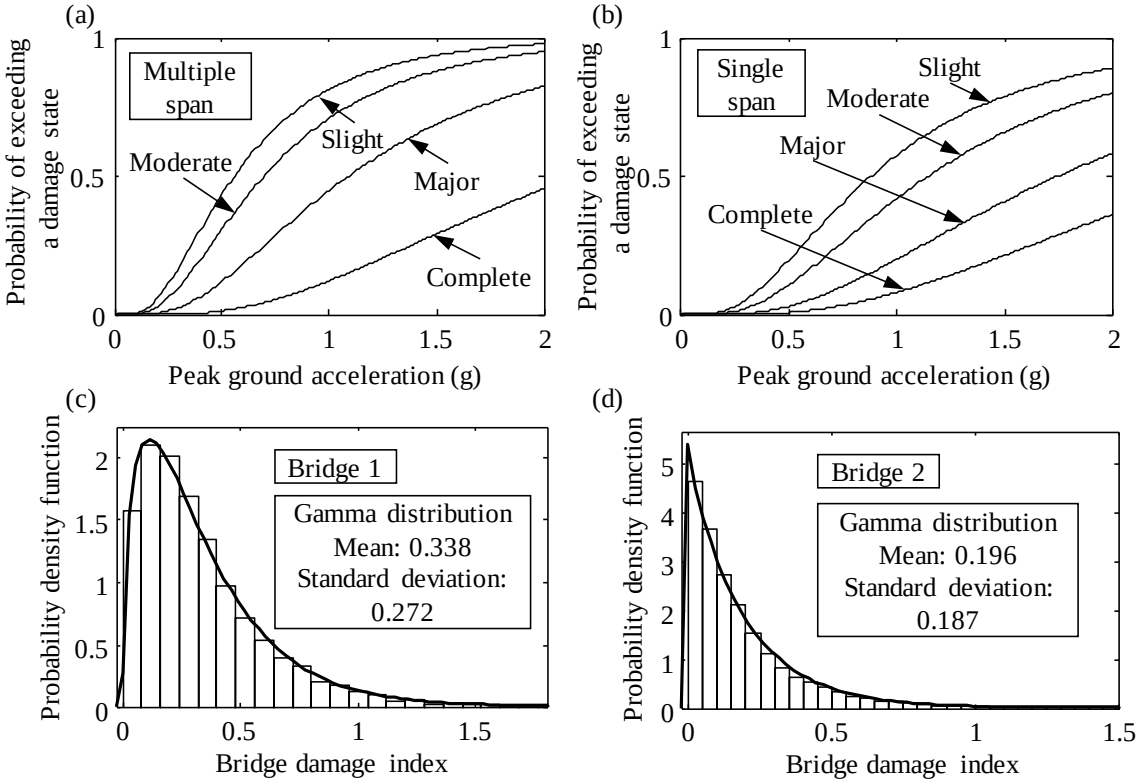

Figure 7.4 Fragility curves of (a) multiple span concrete bridge, (b) single span bridges; probability density functions of damage indices of (c) bridge 1 (B1) and (d) bridge 2 (B2)

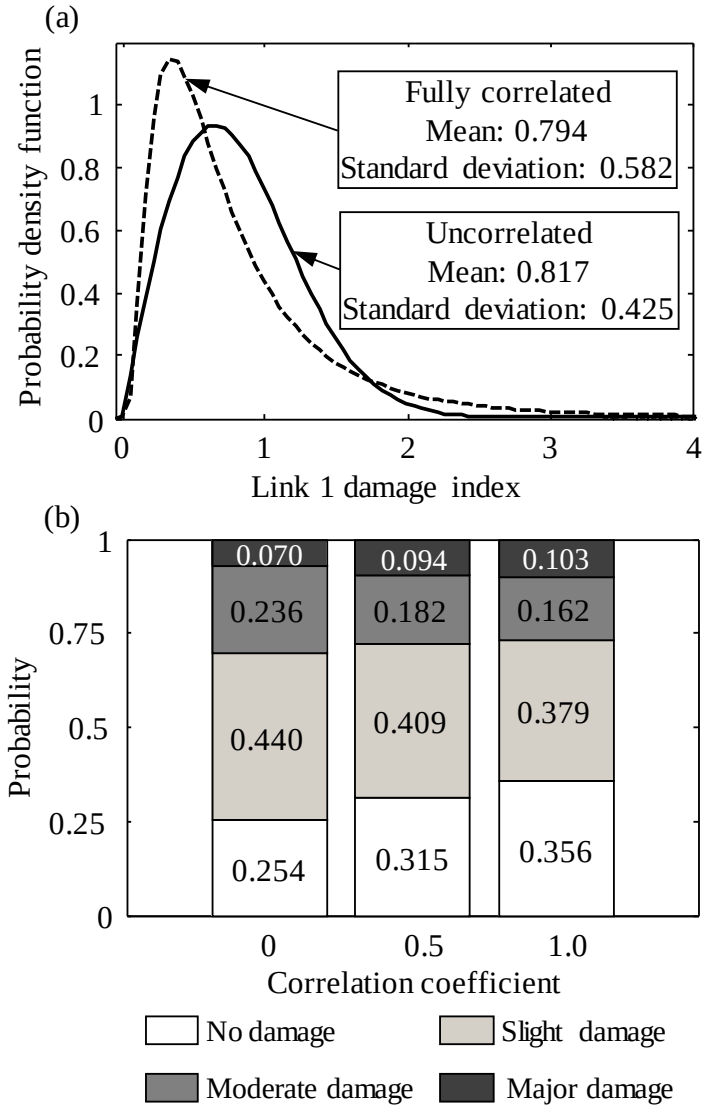

Figure 7.5 (a) Effects of correlation among the damage indices *BDDI* on the link 1 damage index and (b) probabilities of link 1 being in different damage

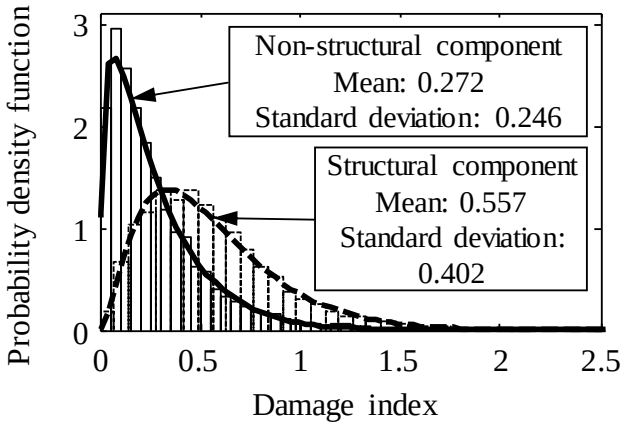

Figure 7.6 Probability density functions of structural and non-structural components damage indices

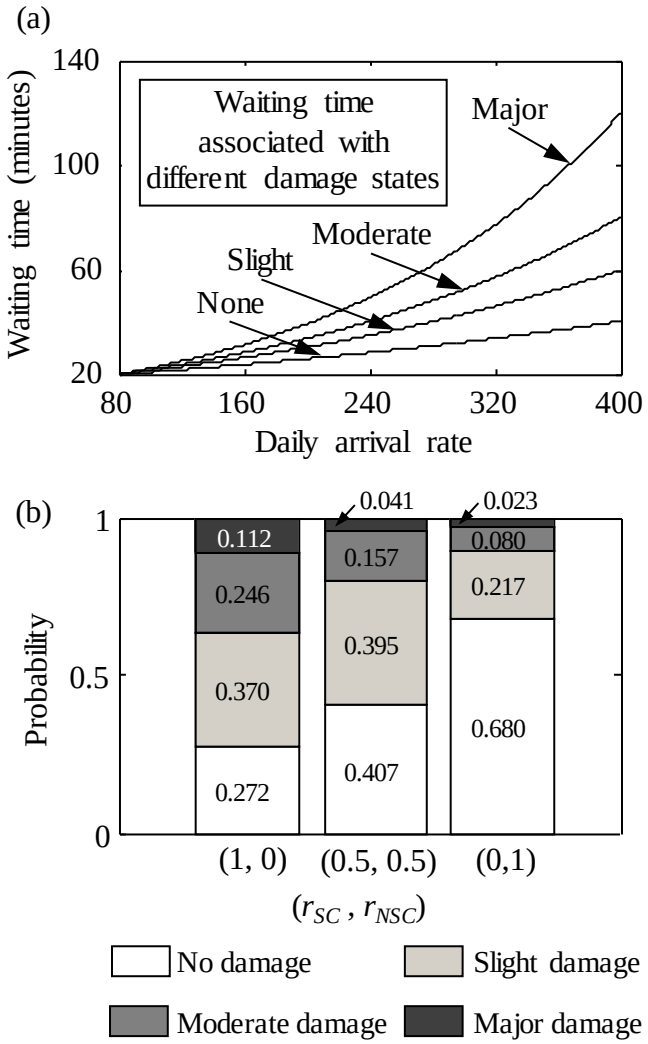

Figure 7.7 (a) Waiting time associated with hospital having different functionality levels (b) effects of r_{SC} and r_{NSC} on the probabilities of hospital being in different functionality levels

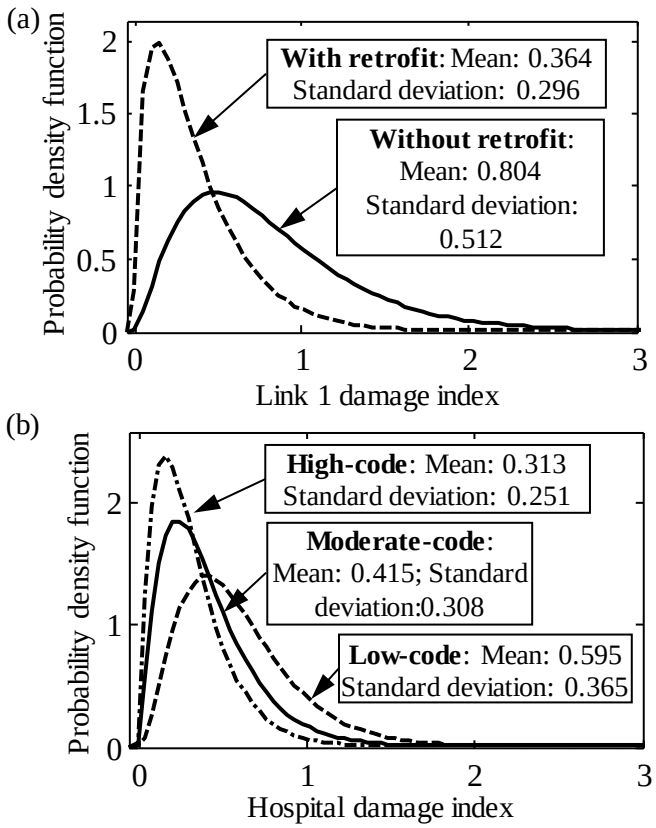

Figure 7.8 Effects of (a) retrofit actions on link 1 damage index and (b) high- and low- design codes on the hospital – bridge network system under seismic hazard

CHAPTER 8

PRE-EARTHQUAKE MULTI-OBJECTIVE PROBABILISTIC RETROFIT OPTIMIZATION OF BRIDGE NETWORKS BASED ON SUSTAINABILITY

8.1. INTRODUCTION

Transportation networks play an important role in sustained economic growth and social development of any country. Maintaining structural reliability and functionality of highway bridge networks under hazard effects is gaining increased attention. Planning retrofit actions under tight budget constraints is a challenging process and can be achieved through a holistic management framework that accounts for uncertainties. This highlights the necessity of effective retrofit strategies to improve structural seismic performance of existing highway bridge networks. The tasks of such a framework include, but are not limited to, quantifying performance at network level in a probabilistic manner and integrating multi-criteria techniques for optimum retrofit strategies to reduce the extent of earthquake damage to society, economy and environment, and total retrofit costs.

Liu and Frangopol (2006) evaluated the bridge network performance based on network connectivity and user satisfaction; Dueñas-Osorio *et al.* (2007) investigated the effect of seismic disruption on the performance of interdependent networks considering the connectivity loss; Zhou *et al.* (2010) analyzed the socio-economic effect of seismic

retrofit associated with a bridge network considering traffic flow redistribution; Bocchini and Frangopol (2011) presented a novel approach to assess the damage level of bridges in a network using fragility and network flow analysis. Sustainability is an appropriate performance indicator for bridge networks to be integrated into the management framework.

Accurate methodologies to quantify probabilistic sustainability of structural systems under seismic hazard are required in order to establish optimum pre-earthquake retrofit plans. Sustainability associated with a bridge network exposed to seismic events can be quantified based on possible seismic scenarios that can occur in the region under investigation. Due to the effects of environmental stressors and aging, structural performance under hazard effects deteriorates in time. The time effects are rarely considered in seismic sustainability assessment (e.g., Decò and Frangopol 2013; Dong *et al.* 2013; 2014a). Based on Dong *et al.* (2014b), the expected value and dispersion of seismic risk associated with a bridge network increase with time if retrofit actions are not applied. This chapter considers retrofit actions in order to plan optimal interventions of bridge networks based on sustainability.

Multi-objective optimization techniques play an important role to allocate limited resources in an efficient way to balance the cost and performance (Frangopol 1999; Frangopol 2011). The optimum retrofit plans can be obtained through an optimization process that integrates economic, social, and environmental metrics of structural performance, and the cost of retrofit actions. Sohn *et al.* (2003) analyzed the retrofit priority of transportation networks considering the final demand loss and transportation

cost under seismic hazard; Liu *et al.* (2009) provided a new formulation of the network retrofit problem using stochastic programing that optimizes a mean-risk objective; Zhou *et al.* (2010) studied the estimated benefit of retrofit actions for a bridge network; Chang *et al.* (2012) investigated the bridge retrofit planning associated with evacuation post-earthquake flow effectiveness of bridge networks. However, to the best of authors' knowledge, there is no research reported to establish the optimum retrofit plans for bridge networks under seismic hazards at network level based on sustainability considering uncertainties.

In this chapter, a probabilistic methodology to establish optimum pre-earthquake retrofit plans for bridge networks based on sustainability is developed. A multi-criteria optimization problem is formulated to find the optimum timing of retrofit actions for bridges within a network. The methodology is illustrated on an existing bridge network. Genetic algorithms are used to solve the multi-criteria optimization problem. The effects of deterioration on the bridge seismic performance are considered. This chapter is based on a published paper Dong *et al*. (2014b)

8.2. PROBABILISTIC TIME-VARIANT SUSTAINABILITY

The first step of the methodology for sustainability based retrofit optimization is evaluating the social and environmental metrics and converting them into the economic metric. Sustainability can be quantified in terms of expected economic loss by converting the social and environmental metrics into monetary value. The time-variant seismic performance of the bridges within the bridge network should be evaluated based on seismic scenarios. The expected economic loss associated with seismic hazard integrates

the probability of occurrence of seismic hazard in the region, time-variant vulnerability of networks (e.g., bridges and links), and consequences of hazards to society, environment, and economy. Corrosion induced deterioration can affect the seismic performance of bridges by increasing the seismic vulnerability over time (Akiyama *et al.* 2012; Akiyama *et al.* 2013). Uncertainties exist in both hazard assessment and structural performance evaluation. The time effects and uncertainties associated with these aspects should be considered.

The time-variant metric of sustainability, in its general form, can be expressed as

$$SM(t) = \sum_H \sum_{LS} \sum_{DS} C_{Cons|DS}(t) \cdot P_{DS|LS}(t) \cdot P_{LS|H}(t) \cdot P_H(t) \qquad (8.1)$$

where $C_{Cons|DS}(t)$ is the conditional consequence (e.g., economic, social, and environmental) given a damage state (e.g., minor, moderate, major, complete) at time t; $P_{DS|LS}(t)$ is the conditional probability of damage state given a structural limit state (e.g., yielding, instability) at time t; $P_{LS|H}(t)$ is the conditional probability of a structural limit state arising from hazard H at time t; and $P_H(t)$ annual mean rate of occurrence of hazard H at time t. In this chapter, Eq. (8.1) is used to calculate the time-variant metrics of sustainability (e.g., annual seismic risk), excluding the retrofit cost. The total sustainability is the sum of consequences weighted with the probability of occurrence of these consequences. Sustainability can be quantified in terms of social, environmental, and economic metrics (Adams 2006) and can provide harmony between structural systems and natural systems for both the present and future generations (Ochsendorf 2005). FEMA (2000) discusses the important linkage between hazard mitigation, disaster resistance, and sustainable development. The metrics of sustainability (economic, social, and environmental) are not usually considered in the design and retrofit processes of

structural systems. It is of vital importance to take the sustainability metrics into account. The following section provides information on the terms in Eq. (8.1). More detailed information associated with the seismic sustainability of bridge networks could be found in Chapter 5.

8.3. EFFECTS OF RETROFIT ON SEISMIC PERFORMANCE

The effects of retrofit actions can be accounted for by modifying the fragility curves associated with different damage states. The median value of ground motion intensity is selected herein as the parameter to be modified in order to reflect the effects of retrofit actions performed on a bridge. The time-variant median value of ground motion intensity including the effects of retrofit actions can be expressed as

$$m_{i,RET}(t) = m_i(t) \cdot (1 + \gamma_{RET,i}) \tag{8.2}$$

where $m_i(t)$ is the median value of ground motion intensity associated with damage state i at time t without retrofit and $\gamma_{RET,i}$ is the retrofit enhancement ratio to decrease seismic vulnerability associated with damage state i. Since the median value of ground motion intensity associated with a damage state increases while the corresponding standard deviation remains the same, the corresponding failure probability is reduced after retrofit. This concept is illustrated qualitatively in Figure 8.1.

8.4. EVALUATING COST OF RETROFIC ACTIONS

The total cost of retrofit actions for an entire bridge network during a time horizon can be expressed as (Liu and Frangopol 2006)

$$C_{Retrofit} = \sum_{i=1}^{k} \sum_{j=1}^{N_i^{Ret}} \frac{C_{ij}^{Ret}(t_{ij})}{(1+r)^{t_{ij}}} \tag{8.3}$$

where k is the number of bridges in the bridge network; N_i^{Ret} is the number of retrofit actions for bridge i during the investigated time span; C_{ij}^{Ret} is the retrofit cost associated with retrofit action j on bridge i; t_{ij} is the application time of the retrofit; and r is the discount rate. The retrofit cost of bridge i associated with retrofit action j can be expressed as (Zhou *et al.* 2010)

$$C_{ij}^{Ret} = r_{Ret,j} W_i L_i c_{REB} \tag{8.4}$$

where W_i and L_i are the width and length of the bridge i; $r_{Ret,j}$ is the ratio of retrofit action j to rebuilding cost; and c_{REB} is the unit rebuilding cost of a bridge.

8.5. FORMULATION OF THE OPTIMIZATION PROBLEM

The optimum prioritization of bridges for seismic retrofit is required under limited resources. For network level retrofit management, effective decisions should be made regarding the application timing of retrofit on each individual bridge within the network. Optimum retrofit planning and prioritization of bridges during certain time horizon can be obtained using a multi-objective optimization approach. Two conflicting objectives are considered in the formulation of this problem (Frangopol 1995; Okasha and Frangopol 2009). The first objective to be minimized is the maximum value of expected economic loss during the investigated time span. Expected economic loss is selected as the metric of sustainability to be included in the formulation of the optimization problem due to the fact that it contains information on all metrics of sustainability including social and environmental metrics. The second objective to be minimized is the total retrofit cost

during the investigated time span. The solutions from the optimization process can provide the information on the sequence of bridge retrofitting. Accordingly, the information regarding bridge importance can be obtained.

The interaction among the modules of the proposed retrofit optimization methodology is illustrated in Figure 8.2. The performance module handles the computations associated with seismic hazard probabilities, seismic fragility, consequences, and expected economic losses. The optimization module sends the candidates for the design variables which are the timeline of retrofit actions for each bridge within the network to the performance module and cost module. The constraint on time span between consecutive actions can reflect the budget constraint. The performance module delivers the value of the first objective function, which is the maximum value of expected economic loss during a specified time horizon to the optimization module. The cost module returns the total cost of retrofit actions for the entire network to the optimization module. After an adequate number of generations, the optimization module provides the Pareto optimum solutions for the timing of retrofit actions for each bridge. The constraint associated with public safety is not considered directly. However, probability of failure, as a measure of safety, is already accounted within the expected economic losses.

The optimization problem is formulated as follows:

***Given**:*

- Bridge network configuration and inventory
- Time-variant seismic vulnerability of each bridge

- Probabilistic seismic scenarios of the region
- Traffic flow on each link
- Time-variant effects of retrofit actions on seismic performance of bridge
- Consequences associated with the damage conditions of bridge network

***Find**:*

- Application timing of retrofit on each bridge within the network
- Type of the retrofit action

***So that**:*

- Total retrofit cost ($C_{Retrofit}$) for entire bridge network is minimized
- Maximum value of expected economic loss during investigated time interval is minimized

***Subject to**:*

- Time span between consecutive retrofit actions is greater than a prescribed time interval
- The retrofit action should be performed within a specified time interval

8.6. ILLUSTRATIVE EXAMPLE

The methodology is illustrated on a highway bridge network located in the Orange County, California. The schematic layout of the network of ten bridges (B1 to B10) is presented in Figure 8.3. The bridges within the network can be classified in two categories. Bridge 1 (B1) and bridge 9 (B9) are single span simply-supported concrete

bridges. The remaining eight bridges are continuous concrete bridges. The steps of the procedure are described in details in this section.

8.6.1. Time-variant probabilistic seismic vulnerability

The fragility curves are used to predict the conditional probability of structure exceeding a certain damage state. The initial median values of ground motion intensity associated with damage states for the two types of bridges located in the investigated bridge network are based on Basöz and Mander (1999). It is assumed that the median value associated with a certain damage state remains 75% of the initial value after 75 years (Decò and Frangopol 2013). The time effects on fragility curves for the continuous concrete bridges are illustrated in Figure 8.4. .Links classified as intact, slightly damaged, moderately damaged, and majorly damaged are represented by the values of the link damage index $LDI \leq 0.5$, $0.5 < LDI \leq 1.0$, $1.0 < LDI \leq 1.5$, and $LDI > 1.5$, respectively. The common used definition associated with link damage state under seismic event is used herein (Chang *et al.* 2000; Shinozuka *et al.* 2003; Shiraki *et al.* 2007). The time-variant probabilities of link damage states under probabilistic seismic scenarios are evaluated in order to be used in the computation of expected economic loss.

8.6.2. Time-variant sustainability assessment

The social metric is evaluated in terms of downtime and fatalities; the environmental metric is evaluated based on the amount of energy waste and carbon dioxide emissions (Dong *et al.* 2013). Social and environmental metrics of sustainability are converted to economic metric by evaluating their associated monetary values. The economic metric is quantified according to Eq. (8.1). The parameters of random variables associated with

consequence evaluation are provided in Table 8.1. The uncertainties associated with these parameters vary for different sources. The discount rate of money is assumed as $r = 0$. The variation of annual expected economic loss for the entire network without retrofit is provided in Figure 8.5. As indicated in this figure, the total economic loss associated with the bridge network increases in time due to the effects of deterioration.

8.6.3. Seismic bridge retrofit actions

As the expected economic loss increases with time, there is a need to apply retrofit action to bridges in network to reduce the potential risk to economy, society, and environment.. It is assumed that the retrofit action will increase the median value of ground motion intensity associated with a certain damage state to a certain level for the bridges in the bridge network. Based on Shinozuka *et al.* (2005), the enhancement ratios associated with steel jacketing for median value of ground motion intensity are 55%, 75%, 104%, and 145% for minor, moderate, major, and complete damage states, respectively. These enhancement ratios for different damage states are assumed for all the bridges in this network to reflect the effects of retrofit actions. The fragility curves for the continuous concrete bridge with and without retrofit are shown in Figure 8.4. As indicated in the Figure 8.4(a), the probability of the bridge being in moderate damage state under $PGA = 0.5g$ is 0.19 without retrofit, while this value reduces to 0.045 with retrofit at $t = 15$ years. Based on Kim *et al.* (2008), the retrofit cost is assumed to be 20% of rebuilding cost of the bridge.

8.6.4. Optimum solutions for retrofit planning

The optimization problem for finding the timeline of retrofit action on bridges of the network is formulated as described previously. The multi-objective optimization problem is solved using Genetic Algorithm provided in Global Optimization Toolbox of *MATLAB* (MathWorks 2011). Figure 8.6 presents the Pareto optimal solution sets for three different time horizons. These include 10, 20, and 30 year intervals, in order to illustrate the effect of the time interval until an expected strong earthquake strikes the region. Each Pareto solution corresponds to a retrofit cost and accordingly leads to different level of bridge network performance in terms of expected annual risk. *Solution A* and *Solution B* represent two different retrofit strategies which belong to the same Pareto set (30 year time interval). *A* represents a low-risk high-cost solution with maximum annual expected economic loss of 1.546 Million USD and total retrofit cost of 0.8794 Million USD. *Solution A* includes the retrofit of Bridge 9 at t = 1 year and the retrofit of Bridges 1, 4, and 8 at t = 13 years. The corresponding annual expected loss profile for *Solution A* is presented in Figure 8.7. *B* represents a high risk low cost solution with maximum annual expected economic loss of 2.663 Million USD and total retrofit cost of 0.1872 Million USD. The decrease in retrofit cost associated with solution *B* results in higher maximum annual expected economic loss compared to solution *A*. *Solution B* includes only the retrofit of Bridge 3 at t = 18 years. The corresponding annual expected loss profile for *Solution B* is also shown in Figure 8.7. It can be concluded from this figure that the risk associated with seismic hazard to bridge network can be reduced significantly by retrofitting the existing bridges within the network; however, the most suitable plan

among the optimum solutions should be selected by the decision maker. In Figure 8.8 (a) and (b), the time-variation of annual expected economic loss for *Solution C* and *Solution D* is presented.

The effect of different retrofit strategies regarding the number of retrofit actions is also investigated. Figure 8.9 illustrates the Pareto optimal solution sets for two different cases considering a 30 year time interval. These cases include: (a) only one retrofit action for each bridge is available during this time interval, and (b) two retrofit actions are available. It is assumed that the repair cost ratio and retrofit enhancement ratio for case (b) are 50% of those for case (a). *Solution E* and *Solution F* in Figure 8.9 yield almost the same retrofit cost, however *Solution E* results in slightly smaller maximum annual expected loss. This indicates that case (b) provides better cost effective solutions. The time-variation of annual expected loss for *Solution E* and *Solution F* is presented in Figure 8.10(a). The 30 year retrofit plans for these two solutions are illustrated in Figure 8.10(b). The effect of the money discount rate (r) on the optimum solutions is also investigated considering a 20 year interval. To illustrate this effect, the optimization problem is solved for different values of r. The corresponding Pareto optimum solutions associated with $r = 0$, $r = 0.01$, and $r = 0.02$ are provided in Figure 8.11.

8.7. CONCLUSIONS

This chapter provides a methodology for pre-earthquake retrofit optimization of bridge networks to mitigate seismic damage to society, economy and environment. Finding optimum pre-earthquake retrofit plans is formulated as a multi-criteria optimization problem, where the total retrofit cost and maximum expected value of economic loss are

considered as conflicting objectives. Genetic algorithms are used to solve the optimization problem. The methodology is illustrated on a bridge network located in Orange County, California.

The following conclusions can be drawn:

1. The prioritization of bridges within a network can be performed based on multi-objective optimization approach. This approach provides the opportunity to observe the optimum solutions with different trade-offs and select the one which fits best the decision maker's needs. Each of the Pareto optimal solutions corresponds to an optimum retrofit plan indicating sequence and timing of bridge retrofitting. These depend on the budget limit and maximum annual loss that the decision maker can tolerate.
2. The economic metric of sustainability (i.e. expected economic loss) increases in time due to deterioration. The retrofit planning depends on the budget limit; a higher budget limit can provide an optimum retrofit planning with a smaller maximum expected annual risk. The importance of the bridges can determine the retrofit prioritization. The multi-objective optimization provides the decision makers a set of different optimum retrofit strategies balancing conflicting objectives to fit their needs.
3. The considered time interval for retrofit actions has impact on the optimal solutions. The longer the time interval considered, the higher risk levels are obtained for same retrofit costs; on the other hand, more resources can be allocated for retrofit of bridges during the investigated time horizon.

4. The number of retrofit actions applied on each bridge within the considered time interval has effects on the optimal solutions. The case with two retrofit actions associated with 50% reduction of the cost and enhancement ratio provides more cost effective solutions than those associated with the case of one retrofit action associated with 100% retrofit effects.

Table 8.1 Parameters of the random variables associated with the consequences.

Random Variables	Mean	COV	Distribution Type
ADT	Varies [a]	DNA [a]	DNA [a]
ADTT/ADT ratio	Varies [a]	DNA [a]	DNA [a]
Rebuilding costs	1292 USD/m^2 [a]	0.2 [a]	LN [a]
Compensation for truck drivers	29.28 USD/h [a]	0.31 [a]	LN [a]
Detour speed	30 km/h [a]	0.15 [a]	LN [a]
Embodied energy for concrete	3022 MJ/m^3 [e]	0.2 [d]	LN [d]
Embodied CO^2 for concrete	414 kg/m^3 [e]	0.2 [d]	LN [d]
Embodied energy for steel	245,757 MJ/m^3 [e]	0.2 [d]	LN [d]
Embodied CO^2 for steel	9,749 kg/m^3 [e]	0.2 [d]	LN [d]
Length of detour	Varies [a]	DNA [a]	DNA [a]
Wage for car drivers	23.36 USD/h [a]	0.28 [a]	LN [a]
Vehicle occupancies for cars	1.5 [a]	0.15 [a]	LN [a]
Vehicle occupancies for trucks	1.05 [a]	0.15 [a]	LN [a]
Running costs for cars	0.4 USD/km [a]	0.2 [a]	LN [a]
Running costs for trucks	0.56 USD/km [a]	0.2 [a]	LN [a]
Time value of a cargo	3.81 USD/h [a]	0.2 [a]	LN [a]
Value of a statistical life	6,200,000 USD [a]	0.45 [a]	LN [a]
Cost value of CO_2 emission	26 USD/t [f]	0.45 [d]	LN [d]
Cars CO_2 emissions	0.22 kg/km [c]	0.2 [d]	LN [d]
Trucks CO_2 emissions	0.56 kg/km [c]	0.2 [d]	LN [d]

Note: LN=lognormal distribution; COV=coefficient of variation; DNA=does not apply;
[a] based on Decò and Frangol 2013; [c] based on Gallivan *et al.* 2010; [d] assumed; [e] based on Alcorn 2003; [f] based on Kendall *et al.* 2008; The costs in USD refer to the year 2012.

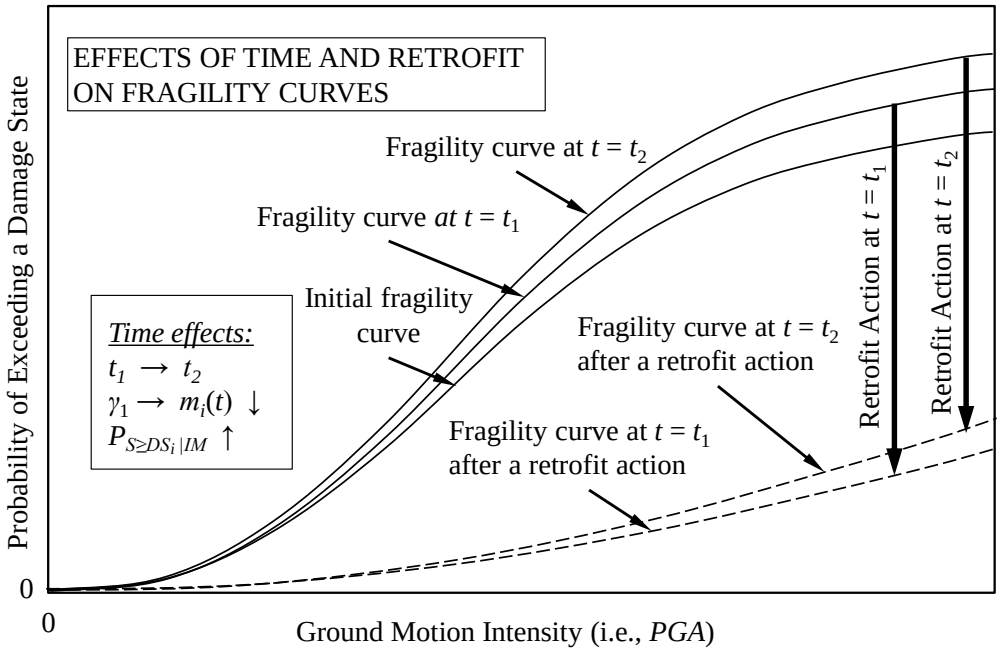

Figure 8.1 Effects of time and retrofit on fragility curves

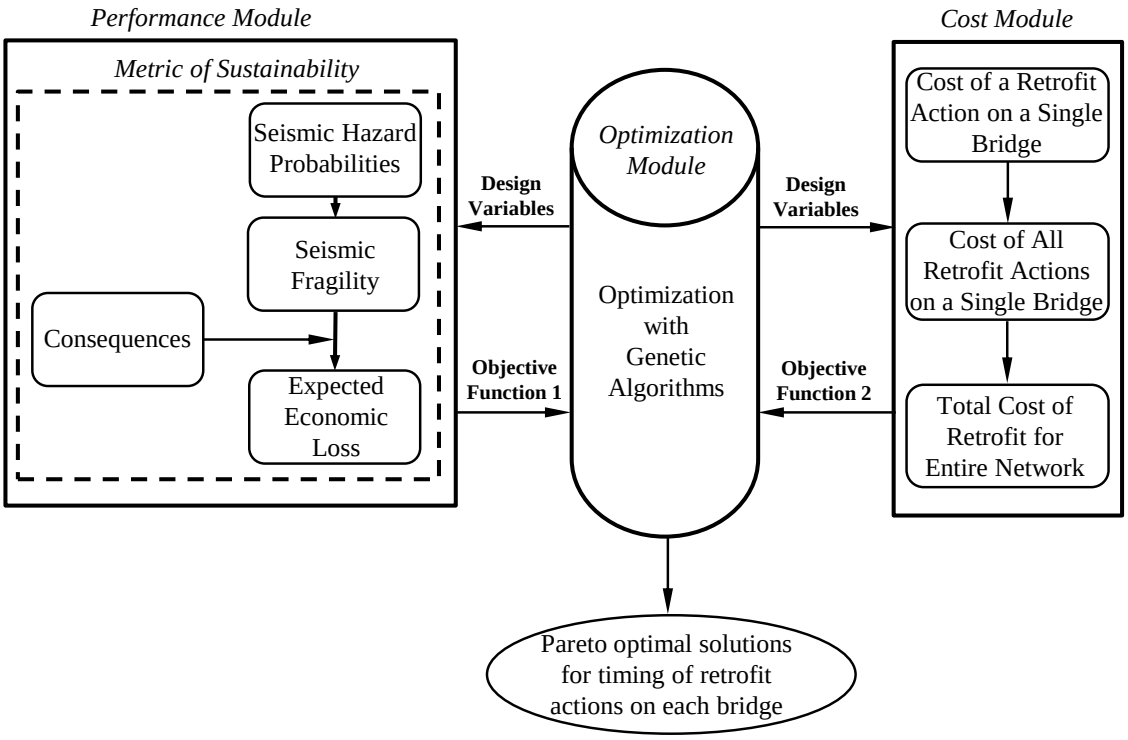

Figure 8.2 Interaction between computational modules

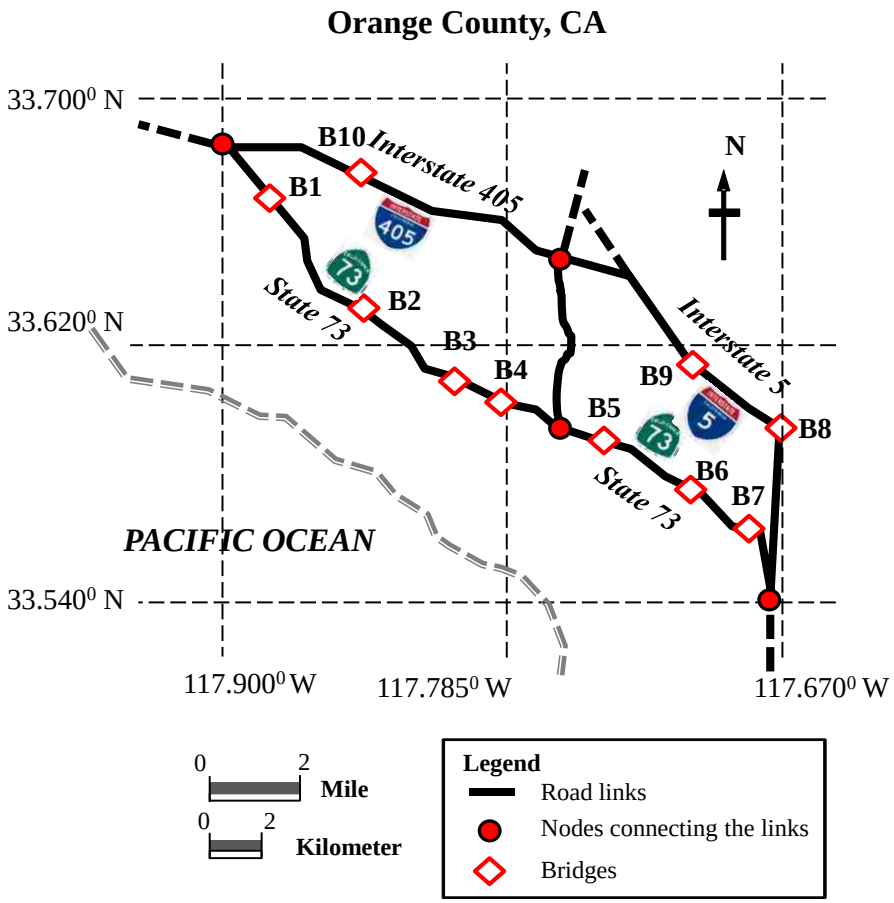

Figure 8.3 Schematic layout of the investigated bridge network

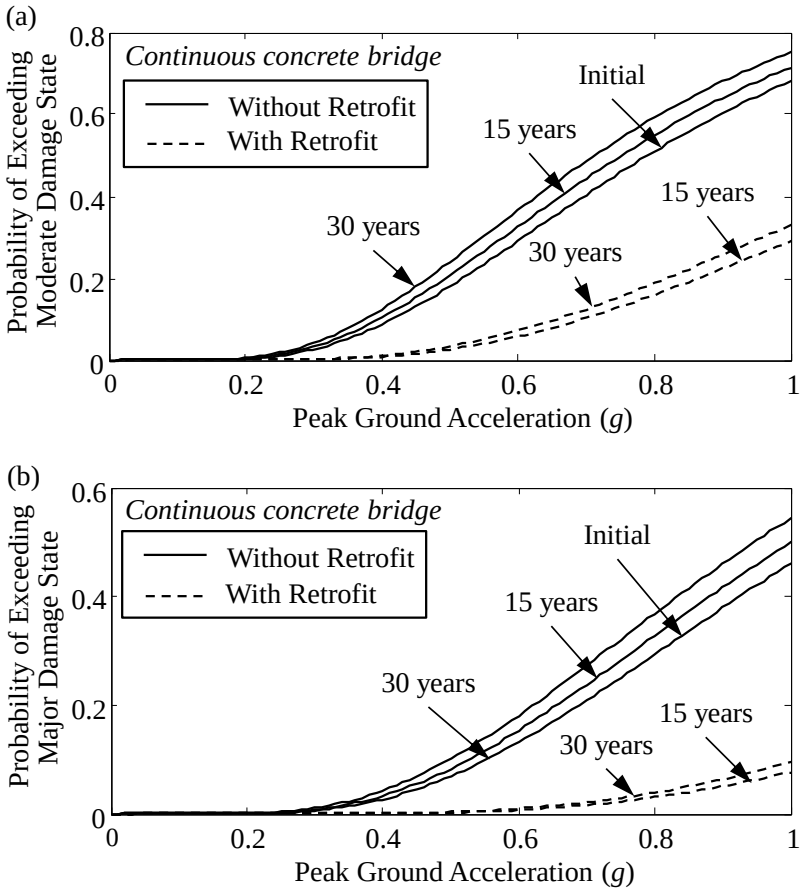

Figure 8.4 Time-variant fragility curves of continuous concrete bridges without/with retrofit for (a) moderate damage state; and (b) major damage state

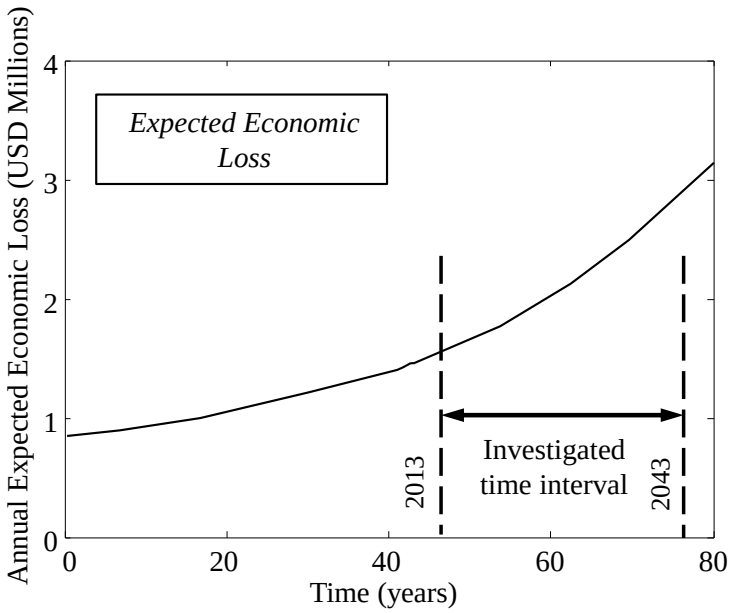

Figure 8.5 Annual expected economic loss for the entire network without retrofit

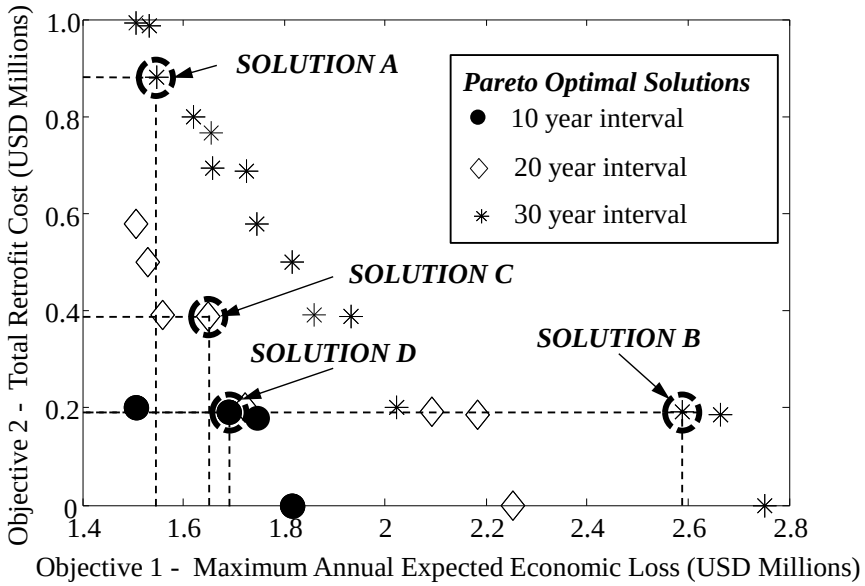

Figure 8.6 Pareto optimal solution sets for different time intervals

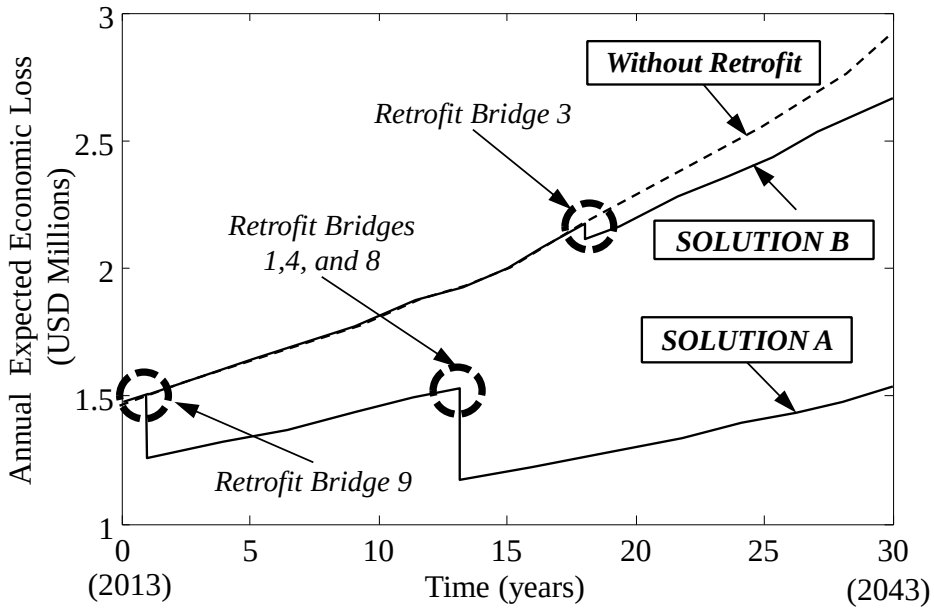

Figure 8.7 Annual expected economic loss associated with *Solution A* and *Solution B* in Figure 8.6

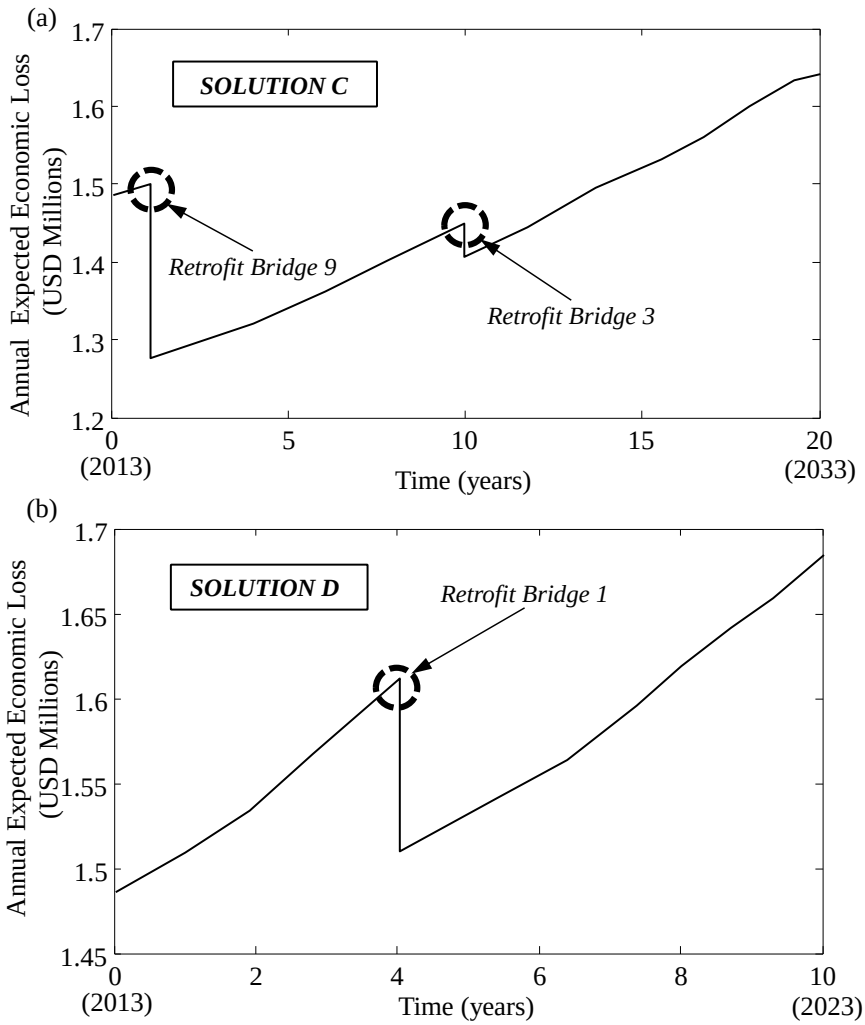

Figure 8.8 Annual expected economic loss associated with (a) *Solution C* and (b) *Solution D* in Figure 8.6

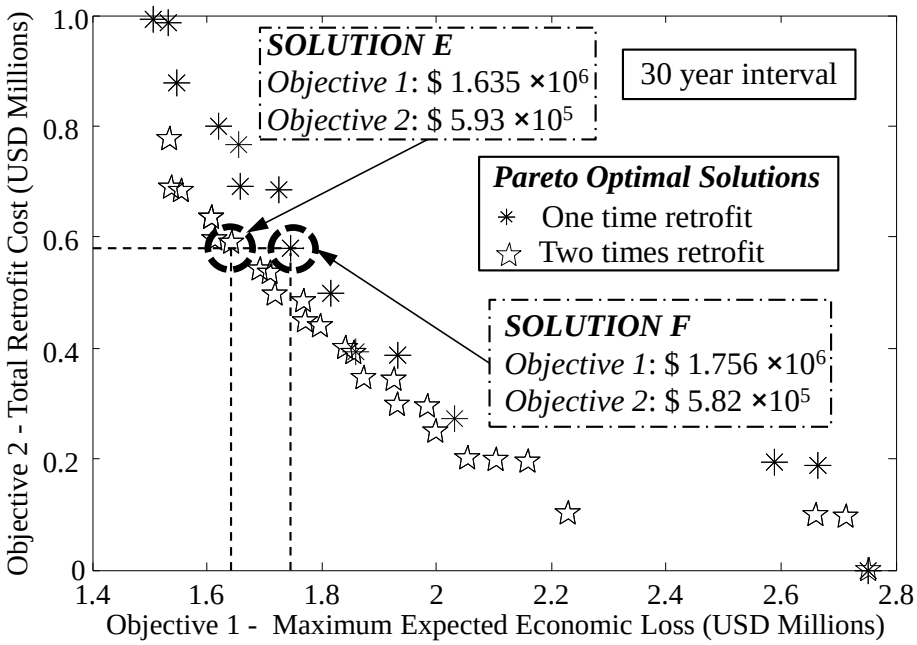

Figure 8.9 Pareto optimal solution sets for retrofit strategies including one time retrofit and two times retrofit during 30 year time interval

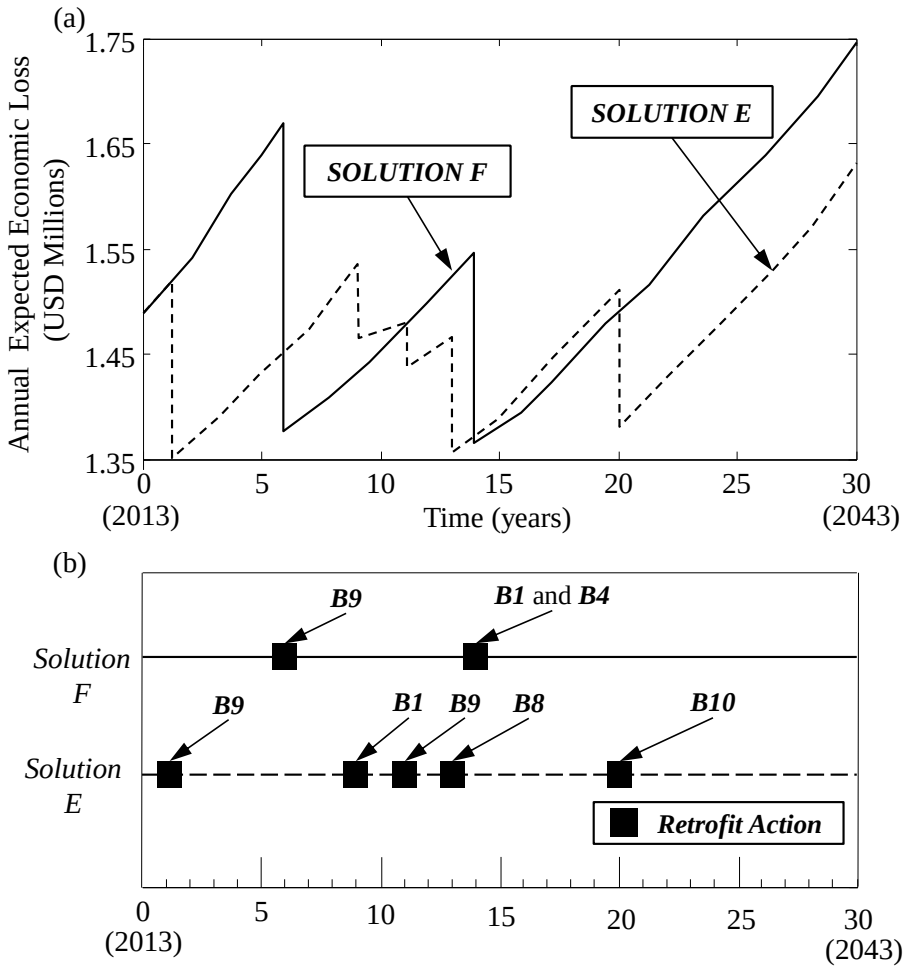

Figure 8.10 (a) Annual expected economic loss of the bridge network associated with *Solution E* and *Solution F* in Figure 9; (b) retrofit plans associated with *Solution E* and *Solution F*

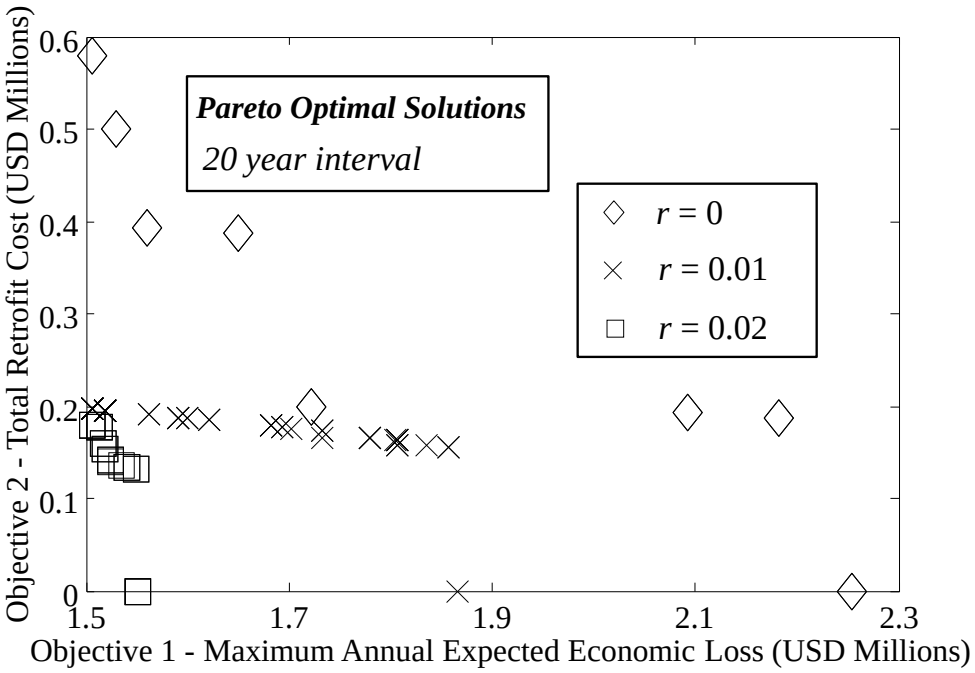

Figure 8.11 Pareto optimal solutions associated with different money discount rates during 20 year time interval

CHAPTER 9

OPTIMIZING BRIDGE NETWORK RETROFIT PLANNING BASED ON COST-BENEFIT AND MULTI-ATTRIBUTE UTILITY

9.1. INTRODUCTION

Seismic mitigation strategies for highway bridges can be compared by carrying out a cost-benefit analysis, in which costs of the intervention actions are directly compared to their benefits. The cost and benefit of each mitigation alternative may be evaluated via a risk assessment that considers a broad variety of consequences of bridge failure. An effective sustainability-based performance indicator must incorporate the consequences associated with structural failure within a risk assessment context. Dong *et al.* (2013, 2014a) investigated the seismic performance of both individual bridges and bridge networks in terms of sustainability by quantifying their associated social and environmental metrics in terms of cost. The accuracy of the results associated with the approach presented in Dong *et al.* (2013, 2014a) depends on the accuracy of the monetary evaluation of the social and environmental metrics. Consequently, a global sustainability performance measure that considers a particular balance between social, economic, and environmental metrics is needed. The ideal combination of the different attributes comprising sustainability can be determined by employing Multi-Attribute Utility Theory (MAUT). The goal of MAUT, within this context, is to transfer the three metrics of

sustainability into one combined value that has a single unit; this multi-attribute performance metric is representative of sustainability under seismic hazard. Kenney and Wood (1977) introduced MAUT with an application involving water resource development planning considering multiple conflicting objectives involving the effect of economic, environmental, social, and technical attributes. Jiménez *et al.* (2003) presented a less demanding approach for the decision maker; within this approach, the decision maker provides acceptable ranges for the weight and utility assessment. Although there have been some efforts to investigate the seismic mitigation of civil infrastructure, there is a lack of research that focuses on the evaluation of sustainability-based seismic performance of transportation networks employing MAUT.

The methodology utilized within this chapter performs a variety of tasks to quantify the sustainability performance of bridge networks and integrate multi-criteria optimization techniques with cost-benefit analysis to find optimum retrofit strategies. Within the presented methodology, the desirability of each alternative (i.e., retrofit plan) depends on three attributes (i.e., social, economic, and environmental impacts), all of which are measured with different units. Thus, there is a need to establish a consistent range of values that each attribute may take so that they are directly comparable to each other. Utility theory may be applied in order to normalize each attribute value to a scale between 0 and 1. The formulation of the utility function corresponding to each attribute greatly depends on the knowledge and preferential characteristics of the decision maker. A multi-attribute utility function can be developed that considers the weighted relative utility value corresponding to each attribute involved. The alternative that provides the

highest utility is the preferred solution (Howard and Matheson 1989). Within this chapter, the resulting multi-attribute utility function represents a sustainability metric that effectively weighs the contribution of impacts to society, the economy, and the environment.

In addition to multi-attribute utility concepts, cost-benefit analysis may be incorporated into an intervention optimization framework. Previous research efforts associated with retrofit cost-benefit analysis evaluated both cost and benefit in terms of monetary values. Liel and Deierlein (2013) evaluated various retrofit strategies in monetary terms for older concrete frame buildings considering repair loss and fatalities. Padgett *et al.* (2010) examined the cost effectiveness of implementing different seismic retrofit strategies to four types of non-seismically designed bridges considering the life-cycle risk as a performance indicator. Zhou *et al.* (2010) proposed a simulation-based approach to evaluate the socio-economic effects of seismic retrofit on highway bridges. These studies concerning cost-benefit analyses were mainly focused on the effects of retrofit actions on the resulting cost-benefit, without performing optimization to obtain the best types of retrofit actions for infrastructure systems. Dong *et al.* (2014b) presented a framework for the pre-earthquake bridge network retrofit optimization based on sustainability; in this framework, the sustainability is evaluated in terms of monetary value and the benefit associated with the retrofit plans is not considered. Explicitly quantifying the relationship between mitigation effectiveness and its cost can facilitate effective decision-making for investment in seismic safety within bridge networks. In this chapter, the cost and benefit corresponding to each alternative are evaluated in terms of

utility measured in consistent units to allow for direct comparison. The benefit of a seismic retrofit action performed on a bridge within a network may be evaluated considering a prescribed time interval, earthquake model, and seismic performance profile specific to the bridge. In order to compute the benefit of a specific alternative, the seismic loss in terms of utility considering no retrofit is subtracted from the utility corresponding to the consequences obtained considering retrofit. The time variability of seismic vulnerability of infrastructure systems is considered herein within a comprehensive risk management planning procedure. The utility values associated with the cost and benefit of retrofit actions may be utilized as objectives within an optimization procedure in order to obtain the best retrofit plan for a bridge network.

In this chapter, a framework for the cost-benefit based retrofit optimization of highway bridge networks is presented. The methodology utilized within this work can quantify sustainability-based seismic performance in terms of utility at the network level. The presented approach effectively employs multi-criteria optimization techniques in order to determine optimum retrofit strategies that reduce the extent of earthquake damage to society, the economy, and the environment, while simultaneously minimizing retrofit costs. The total benefit associated with a retrofit plan is quantified in terms of the reduction in the seismic loss during a given time interval. The utility of both the cost and benefit corresponding to alternatives are utilized within a bi-objective optimization that determines optimal retrofit plans for a bridge network. Additionally, the retrofit actions associated with varying improvement levels are accounted for. A genetic algorithm (GA) based optimization procedure is adopted herein to find the optimal retrofit action for each

bridge with a network. This approach can provide optimal intervention strategies to the decision maker that will ultimately allow for informed decision making regarding retrofit of a highway bridge network. The work in this chapter is based on a published paper Dong *et al*. (2015).

9.2. MULTI-ATTRIBUTE SUSTAINABILITY ASSESSMENT OF BRIDGE NETWORK UNDER SEISMIC HAZARD

The sustainability performance indicator may be quantified in terms of social, economic, and environmental consequences. These consequences include the extra travel time and distance that drivers must endure in addition to any fatalities that may occur (social impact); energy consumption and carbon dioxide emissions (environmental consequences); and rebuilding and repair costs (economic losses). Detailed information concerning the probabilistic evaluation of the annual consequences can be found in Dong *et al.* (2014a). The loss associated with seismic scenarios is computed as the sum of consequences weighted with the probabilities of these consequences occurring. In this chapter, seismic sustainability is calculated considering the possible earthquakes that can occur in a region (Dong *et al.* 2014a). The expected metric of sustainability can be expressed as

$$TSM = \sum_{t=1}^{T_{\max}} \sum_{k=1}^{N} NSM(t) \cdot p_k \tag{9.1}$$

where N is the total number of seismic scenarios under investigation; p_k is the annual probability of occurrence of hazard k; and NSM is the annual sustainability metrics. The *NSM* were computed in Chapter 5. Based on this equation, the total extra travel time *ET*,

extra travel distance *ED*, number of fatalities *FA*, total repair loss R_{REP}, and CO*2* emissions EN could be computed accordingly. For example, the extra travel time for the user in a bridge network can be expressed as (Dong *et al.* 2014a)

$$ET = \sum_{t=1}^{T_{max}} \sum_{k=1}^{N} \sum_{j=1}^{n} \sum_{i=1}^{4} P_{LDSj,i|IM,k}(t) d_{ij} [ADE_{ij}(t)(\frac{l_j}{S_{D,j}} - \frac{l_j}{S_{0,j}}) + ADT_{ij}(t)\frac{D_j}{S}] p_k \quad (9.2)$$

where n is the number of links in the transportation network; N is the total number of seismic scenarios under investigation; p_k is the annual probability of occurrence of hazard k; $P_{LDSj,i|IM,k}(t)$ is the conditional probability of the jth link being in damage state i after an earthquake k occurs at time t; d_{ij} is the downtime associated with the ith damage state of the jth link (days); ADT_{ij} is average daily traffic that is detoured at the jth link in damage state i; D_j is length of the detour for the jth link (km); S is the detour speed (km/h); ADE_{ij} is the average daily traffic remaining at the jth link in damage state i; l_j is the length of link j (km); S_0 is the traffic speed on intact link j (km/h); S_D is the traffic speed on damaged link j (km/h); and T_{max} is the time horizon under investigation (years).

The effects of retrofit actions may be evaluated by modifying the fragility curves associated with different damage states. In order to reflect the effects of retrofit actions performed on a single bridge, the median value of the ground motion intensity is modified accordingly. The time-variant median value of ground motion intensity including the effects of retrofit actions can be expressed as (based on Shinozuka *et al.* 2005)

$$m_{i,RET} = m_i(1 + \gamma_{\boldsymbol{Ret,i}} R_l) \quad (9.3)$$

where m_i is the median value of ground motion intensity associated with damage state i without retrofit; $\gamma_{Ret,i}$ is the retrofit enhancement ratio that proportionally decreases

seismic vulnerability associated with damage state i; and R_l is the retrofit level. R_l may take a value between 0 and 1; a retrofit action with the ability to fully strengthen the seismic performance of a bridge corresponds to a retrofit level equal to 1 (i.e., $R_l = 1.00$). Other retrofit levels may also be considered including $R_l = 0.25$ and $R_l = 0.50$; these intervention options have the capability to strengthen the seismic performance of a bridge by 25% and 50%, respectively. In practice, these two retrofit options correspond to partial steel jacketing of a bridge column. Since the performance of each link is directly related to the performance of the bridges on the link, the seismic performance of the link is improved by considering the retrofit enhancement ratio $\gamma_{Ret,i}$.

Next, the cost of implementing a retrofit action to each bridge is used to calculate the total retrofit cost associated with a bridge network. The total retrofit cost for an entire bridge network can be expressed as (Kim *et al.* 2008; Dong *et al.* 2014b)

$$C_{Ret} = \sum_{j=1}^{m} r_{Ret} R_l W_j L_j c_{REB} \tag{9.4}$$

where r_{Ret} is the ratio of retrofit action to rebuilding cost.

9.3. UTILITY ASSESSMENT FOR COST AND BENEFIT

The computational process adopted herein for the multi-attribute utility assessment of a bridge network under seismic hazard is illustrated in Figure 9.1. This figure highlights the processes of calculating the utility associated with the metrics of sustainability.

9.3.1. Utility function for seismic retrofit costs

The formulation of a utility function that depicts the relative value of retrofit cost investment to the decision maker considering his or her particular risk attitude is

presented in this section. The retrofit strategies associated with high utility values correspond to relatively small retrofit costs and are generally preferred to those associated with small utility values (Howard and Matheson 1989). Given the maximum cost that the decision maker can tolerate, a utility function associated with the retrofit cost considering the attitude of the decision maker may be obtained. The utility associated with a given retrofit cost can be expressed as (Ang and Tang 1984)

$$u_C = \frac{1}{1-\exp(-\gamma)}\left[1-\exp(-\gamma\frac{C_{max}-C_{Ret}}{C_{max}})\right] \quad (9.5)$$

where C_{Ret} is the total expected retrofit cost; γ indicates the risk attitude of the decision maker (i.e., $\gamma > 0$ indicates risk-aversion); and C_{max} denotes the maximum retrofit cost which is utilized to normalize the utility function so that it always takes values between 0 and 1. Considering the same retrofit alternative, a risk averse attitude will always yield a higher utility than that produced from a risk-accepting attitude.

9.3.2. Utility functions associated with metrics of sustainability

The utility functions associated with each attribute considered within the sustainability assessment (social, economic, and environmental metrics) are established considering an exponential form. Other types of utility functions can also be incorporated within this approach. All sub-attributes (e.g., extra travel time, extra travel distance, and number of fatalities are combined to form the social attribute) are analyzed separately and a utility function corresponding to each of them is formulated. The first step in determining appropriate exponential utility functions associated with each sub-attribute is to record the minimum and maximum values each sub-attribute value may take. Additionally, the value of a sub-attribute that corresponds to a utility value of 0.5 is also considered as

input into this problem. Utilizing three points that are assumed to lie along a sub-attribute's utility function, a curve may be fitted, and a closed formulation of this function may be determined considering the following generalized function (Min 1994)

$$u(x) = a + b \cdot \exp(-c \cdot x) \tag{9.6}$$

where *a*, *b*, and *c* represent constants in the generalized form for each sub-attribute's utility function. Then, utility functions corresponding to each attribute (i.e., social, economic, and environmental) are computed considering a weighted average of the utility functions associated with each sub-attribute.

9.3.3. Multi-attribute utility assessment

Once the utility function associated with each attribute of sustainability is appropriately established, a multi-attribute utility that effectively represents all aspects of sustainability can be obtained by combining the utility functions associated with each attribute. Within the additive formulation for the multi-attribute utility function, utility values associated with each attribute are multiplied by weighting factors and summed over all attributes involved (Stewart 1996). The additive form of the multi-attribute utility function is adopted herein. The multi-attribute utility associated with a bridge network's total sustainability without and with retrofit effects can be computed as (Jiménez *et al.* 2003)

$$u_{S,0} = w_{Eco} u_{Eco}(Eco_0) + w_{Soc} u_{Soc}(Soc_0) + w_{Env} u_{Env}(Env_0) \tag{9.7a}$$

$$u_{S,R} = w_{Eco} u_{Eco}(Eco_R) + w_{Soc} u_{Soc}(Soc_R) + w_{Env} u_{Env}(Env_R) \tag{9.7b}$$

where w_{Eco}, w_{Soc}, and w_{Env} are the weighting factors corresponding to each sustainability metric; u_{Eco}, u_{Soc}, *and* u_{Env} are the utility functions for the economic, social, and environmental attributes, respectively; Eco_0, Soc_0, and Env_0 are the expected values of the three metrics of sustainability without retrofit; and Eco_R, Soc_R, and Env_R are the expected values of the three metrics of sustainability considering retrofit.

The weighting factor associated with each sustainability metric is calculated considering information obtained from the decision maker. Typically, these weighting factors are not explicitly known or are difficult to assess for certain decision makers. Jiménez *et al.* (2003) proposed a method where lower and upper bounds for the weighting factors are utilized as input for the decision making problem. A normalized weight associated with each sustainability metric is calculated considering the lower and upper bounds given by the decision maker. The normalized weight for attribute *i* can be computed as (Jiménez *et al.* 2003)

$$w_i = \frac{w_i^L + w_i^U}{\sum_{i=1}^{3} w_i^L + w_i^U} \tag{9.8}$$

where w_i^L and w_i^U are the lower and upper bounds for the weights provided by the decision maker for attribute *i*. Note that this method is just one way to quantify the weighting factors and that it is always ideal to include information about the decision maker's preferences in this process.

9.3.4. Utility value associated with benefit

The final part of the utility assessment involves determining the utility associated with the benefit of retrofit. Quantification of the relationship between mitigation benefit and its cost can facilitate effective decision-making for investment in seismic safety within bridge networks. The benefit of a seismic retrofit action performed on a bridge within a network may be evaluated considering a certain time interval, earthquake model, and the bridge's seismic performance. The utility associated with the sustainability metrics with and without retrofit actions can be assessed using multi-attribute utility in terms of a single utility value. Consequently, the benefit of retrofitting is evaluated by subtracting

the multi-attribute utility associated with expected sustainability considering no retrofit from the utility value corresponding to the expected sustainability of a bridge network with retrofit performed. The benefit associated with retrofit actions in terms of utility can be expressed as

$$u_B(T_{\max}) = u_{S,R}(T_{\max}) - u_{S,0}(T_{\max}) \tag{9.9}$$

where $u_{S,R}$ represents the multi-attribute utility value corresponding to the expected sustainability of a bridge network with retrofit performed and $u_{S,0}$ is the utility associated with expected sustainability considering no retrofit.

In order to directly compare the cost and benefit associated with a retrofit alternative and determine the overall effectiveness of a particular retrofit plan, a cost-benefit indicator is adopted herein. The cost-benefit indicator is calculated as follows

$$CB_{RET}(T_{\max}) = u_B(T_{\max}) - (1 - u_C) \tag{9.10}$$

The first term on the right side of Eq. (9.10) represents the benefit utility associated with retrofit while the second term denotes the cost utility. More specifically, within the parentheses contained in the second term, the integer, 1, corresponds to a cost utility considering no retrofit. The cost-benefit indicator essentially measures the effectiveness of a retrofit plan, taking on values between -1 and 1. Values less than 0 indicate that retrofit is not cost-effective while values greater than 0 denote that it is beneficial to perform retrofit.

9.4. OPTIMIZATION OF BRIDGE NETWORK RETROFIT PLANNING

The result of applying single- and multi-attribute utility approaches are two utility functions: the first quantifies the relative value of retrofit investment costs considering

the risk attitude of the decision maker and the second indicates the benefit of each alternative expressed in terms of the utility of the sustainability metric. These two utility functions are further employed within an optimization procedure as the objective functions selected to be maximized. The optimization process embedded within the proposed retrofit strategy methodology is illustrated in Figure 9.2. The utility value associated with both retrofit cost and benefit are sent to the optimization module in order to determine the set of Pareto optimum solutions detailing retrofit planning for a bridge network. GAs are employed with an adequate number of generations in order to obtain the set of Pareto optimum solutions for the bi-objective problem (Okasha and Frangopol 2009; Frangopol 2011). GAs are tools that are used to solve multi-objective optimization problems; these algorithms are ultimately inspired by the mechanisms of natural selection and the biological theory of evolution (Goldberg 1989).

The bi-objective optimization problem can be formulated as follows:

Given:

- Bridge network configuration including the geometry, physical characteristics, location, and time-variant seismic vulnerability of each bridge (information associated with Eqs. (9.1) and (9.2))
- Representative probabilistic seismic scenarios for the region investigated
- Traffic flow on each link and link damage states
- The effects of retrofit actions on the seismic performance of each bridge ($\gamma_{Ret,i}$ and R_l in Eq. (9.3))

- Consequences associated with the damage state of each bridge within the network
- The utility function (Eq. (9.6)) and weighting factor associated with each attribute and sub-attribute of sustainability (determined by the decision maker; w_i^L and w_i^U in Eq. (9.10))
- Risk attitude of the decision maker toward the total retrofit cost (γ in Eq. (9.5))
- Time horizon under investigation (T_{max})

Find:

- Type of retrofit action performed on each bridge within the network at the beginning of the time interval investigated

So that:

- The utility associated with the retrofit cost for the entire bridge network is maximized
- The utility associated with the retrofit benefit considering a specific time interval is maximized

Subjected to:

- The seismic performance of each bridge within the network should always be larger than a prescribed value
- The total cost of retrofit should be less than a prescribed monetary value

9.5. CASE STUDY

The proposed methodology is illustrated on an existing highway bridge network located in Alameda, California. The schematic layout of the transportation network consisting of 15 bridges (B1, B2, …, B15) is presented in Figure 9.3. The time-variant sustainability of this bridge network under seismic hazard was previously investigated by Dong *et al.* (2014a). This chapter presents a framework that performs retrofit optimization for bridges within the network by employing utility theory and cost-benefit analysis. A more detailed description and discussion of this particular bridge network can be found in Dong *et al.* (2014a).

9.5.1. Seismic vulnerability considering retrofit actions

The initial step in this illustrative study is to determine the time-dependent seismic vulnerability profile associated with each bridge within the network under probabilistic seismic scenarios. An in-depth explanation of the generation of probabilistic seismic scenarios and seismic vulnerability assessment of bridge networks can be found in Dong *et al.* (2014a).

The effects of retrofit actions on the seismic fragility of a single bridge may be calculated using Eq. (9.3). It is assumed that a retrofit action increases the median value of ground motion intensity associated with a certain damage state to a particular level for each bridge in the network. Based on Shinozuka *et al.* (2005), the enhancement ratios (γ_{Ret} in Eq. (9.3)) associated with full steel jacketing for median value of ground motion intensity are assumed to be 55%, 75%, 104%, and 145% for minor, moderate, major, and complete damage states, respectively. Additionally, the retrofit level, represented by R_l in

Eq. (9.3), is considered within this analysis. A retrofit action with the ability to fully restore the seismic performance of a bridge corresponds to a retrofit level equal to 1 (retrofit option 3; $R_l = 1$). Retrofit option 1 ($R_l = 0.25$) and retrofit option 2 ($R_l = 0.50$) are adopted as additional possible retrofit actions. Thus, if a retrofit is performed on a bridge within the network, there are three possible actions that may be implemented that vary by their ability to strengthen bridge seismic performance. The fragility curves associated with continuous concrete bridges considering various retrofit actions are indicated in Figure 9.4. In order to compute the fragility curves corresponding to another type of bridge, Eq. (9.3) is utilized considering that particular bridge's seismic characteristics. As shown in Figure 9.4, the seismic vulnerability of a continuous concrete bridge decreases with an increase in R_l. Additionally, retrofit option 3 provides the highest increase in the seismic strength of the bridge. Based on Kim *et al.* (2008), the retrofit cost ratio (r_{Ret} in Eq. (9.4)) associated with retrofit option 3 ($R_l = 1.0$) is assumed to be 20% of the rebuilding cost of the bridge. Based on this assumption, the retrofit cost ratio is taken as 5% and 10% for retrofit option 1 ($R_l = 0.25$) and retrofit option 2 ($R_l = 0.50$), respectively.

9.5.2. Utility assessment for retrofit costs and sustainability metrics

The next part of the seismic retrofit assessment consists of calculating the utility associated with retrofit cost. A utility function associated with the retrofit cost considering the attitude of the decision maker may be obtained utilizing Eq. (9.5) with C_{max} = \$16M (i.e., 16 Million USD) and $\gamma = 2$. This formulation for the cost utility accounts for the decision maker's preference to investing money in the face of risk.

In addition to the utility associated with the cost of retrofit, the utility corresponding to the seismic sustainability performance metric in terms of social, economic, and environmental attributes must be determined. All the parameters associated with the random variables used in the sustainability assessment are provided in Table 9.1 and the discount rate of the money is taken as r = 0.02. The time-variant expected value corresponding to each sub-attribute of sustainability is shown in Figure 9.5.

Once the expected value of each sustainability sub-attribute is calculated for an investigated time horizon of T_{max} = 30 years, they may be transferred to utility considering the formulation in Eq. (9.6). The utility values associated with all sustainability sub-attributes for every bridge in the network are shown in Table 9.2. This table summarizes the range and mid-point value corresponding to each sub-attribute in addition to the lower and upper bounds associated with their respective weights (w_i^L and w_i^U in Eq. (9.8)). The weighting factors shown in Table 9.2 are dictated by the decision maker's preferences and their values herein are used as examples to illustrate the proposed retrofit optimization framework; ultimately, actual input from the decision maker is needed to perform a complete assessment of retrofit effectiveness in terms of sustainability. Furthermore, the utility associated with each attribute can be computed considering a weighted average of its sub-attributes; each sub-attribute's utility value is weighted with its corresponding ratio shown in Table 9.3 and summed in order to formulate a single utility value associated with each attribute of sustainability. The next step involves calculating a utility value corresponding to the entire sustainability metric (i.e., including impacts to society, the economy, and the environment). Eqs. (9.7a) and

(9.7b) are used to calculate the multi-attribute utility associated with a bridge network's total sustainability without and with retrofit effects. The weighting factors used within Eq. (9.7) are shown in Table 9.3; these weighting factors are determined using Eq. (9.9) and the given upper and lower bounds in Table 9.2. The final part of the utility assessment involves determining the utility associated with the benefit of retrofit. The benefit of retrofitting is evaluated by subtracting the multi-attribute utility associated with expected sustainability considering no retrofit from the utility value corresponding to the expected sustainability of a bridge network with retrofit performed. The benefit in terms of utility value can be computed using Eq. (9.9).

Next, the cost effectiveness of various intervention alternatives are explored based on the cost-benefit indicator calculated using Eq. (9.9). As shown in Table 9.4, the cost-benefit indicators associated with retrofit option 1 (R_I = 0.25) and retrofit option 2 (R_I = 0.50) are larger than those corresponding to retrofit option 3 (R_I = 1.00) considering the same time interval. In this table, it is assumed that all the bridges within the network are retrofit using the same intervention option. Table 9.4 demonstrates that even though retrofit option 1 is the most effective intervention in terms of the cost-benefit indicator, it yields a smaller utility value associated with benefit compared to retrofit option 2 and 3 under the same time interval. As indicated, the cost-benefit indicator increases as the time interval becomes large; it is more beneficial to retrofit when investigating large time horizons. Overall, it is not reasonable to consider just the cost or the benefit alone to determine an optimal solution; rather, the cost and benefit need to be examined together to determine the effectiveness of an alternative.

9.5.3. Pareto optimal retrofit planning

The bi-objective optimization problem is solved utilizing a procedure that employs GAs. The Global Optimization Toolbox created by Matlab (MathWorks 2011) is adopted in this chapter in order to obtain optimal retrofit planning for the bridges located in the network. The illustrative retrofit optimization problem presented in this chapter was solved using Matlab on a Dell Precision R5500 rack workstation equipped with two six cores X5675 Intel Xeon processors with 3.06 GHz clock speed and 24 GB DDR3 memory.

The Pareto optimal solutions obtained considering a time interval of 30 years and a risk averse attitude (γ = 2) are shown in Figure 9.6a. The retrofit planning strategies corresponding to solutions A, B, and C in Figure 9.6a are shown in Figure 9.6b. These three solutions represent retrofit plans that correspond to different values of utility associated with cost and benefit. Solution A represents a low-cost, low-benefit solution with a cost utility equal to 0.993 and a benefit utility equal to 0.370. The retrofit strategy corresponding to solution A is represented in Figure 9.6b. Bridge B2 is retrofit with option 3 (R_l = 1.0), B8 is retrofit using option 1 (R_l = 0.25), and B10 and B14 are retrofit using option 2 (R_l = 0.50). Solutions B and C are also summarized in a similar manner in Figure 9.6b. As evidenced by Figure 9.6, the utility associated with the benefit increases significantly as retrofit actions are applied to more bridges within the network. In addition to the Pareto optimal set of solutions depicted in Figure 9.6, the values corresponding to each sub-attribute of sustainability may also be examined. Table 9.5 tabulates the value of each sub-attribute of sustainability and the total retrofit costs

corresponding to the three representative solutions chosen from Figure 9.6. Solution C is the highest cost alternative; however, it yields relatively low consequences in terms of social, environmental, and economic impacts. Conversely, solution A is associated with the lowest retrofit cost and the highest relative consequences. When comparing solutions A and B, it is evident that solution B results in a larger utility benefit but at the expense of a relatively lower cost utility.

The effects of the investigated time interval on the Pareto optimal solution set are also studied in this chapter. The time intervals examined include 20 and 30 years, while γ = 2 is adopted as the risk attitude parameter within the utility function associated with the retrofit cost (see Eq. (9.5)). The Pareto optimal solutions associated with 20 and 30 year time intervals are indicated in Figure 9.7. As shown in this figure, for the same utility associated with retrofit cost, the 30 year time interval always yields a higher benefit utility than that corresponding to the 20 year time interval. Additionally, there are no Pareto optimal solutions associated with cost utility values smaller than 0.38 considering the 20 year time interval. However, the Pareto front associated with a 30 year time horizon yields optimal solutions for cost utility values less than 0.38. Thus, for a smaller time interval, it is not beneficial to retrofit the bridges within the network. Ultimately, the time interval under investigation has great effects on the Pareto optimal solutions.

In addition to the investigated time horizon, a sensitivity analysis is carried out considering different risk attitudes. Pareto optimum solution sets considering the attitude of the decision maker toward retrofit costs are shown in Figure 9.8a. A risk averse attitude (γ = 2) yields alternatives associated with high benefit utility while a risk

accepting attitude (γ = -2) provides optimal solutions that correspond to smaller utility values associated with benefit. In other words, considering the same utility associated with retrofit costs, a risk averse decision maker will identify with a higher benefit utility value while a risk accepting attitude will be associated with a smaller utility associated with benefit. The corresponding retrofit strategies associated with representative optimal solutions D and E are indicated in Figure 9.8b. Solution E includes the retrofit of 13 bridges while solution D calls for the retrofit of all 15 bridges within the network.

9.6. CONCLUSIONS

This chapter presents a framework for seismic retrofit optimization of bridge networks to mitigate seismic damage to society, the economy, and the environment by MAUT. Optimum seismic retrofit planning is formulated as a multi-criteria optimization problem where the utility associated with total retrofit costs and utility corresponding to benefit of retrofit options are considered as conflicting objectives. Genetic algorithms are used to solve the optimization problem for an existing bridge network located in California.

The following conclusions can be drawn:

1. The three metrics of sustainability (i.e., social, environmental, and economic) are of vital importance for the seismic performance evaluation of infrastructures systems. Multi-attribute utility theory can provide a general approach to evaluate the sustainability of bridge networks in terms of utility value, considering a multi-attribute utility function that employs weighting factors.
2. The consequences associated with the three metrics of sustainability can be evaluated by employing utility theory. Overall, the consequences of bridge network

seismic performance may be evaluated based on professional judgment and existing information while utility theory can be employed to quantify the decision maker's preference.

3. Optimum retrofit plans for bridge networks can be obtained by using a multi-objective optimization approach, resulting in a set of Pareto optimal solutions. This allows decision makers to make informed decisions based on their particular preference between the outcomes of the multiple objectives within the optimization problem.
4. The cost-benefit evaluation and optimization of retrofit actions can produce the best retrofit planning considering the utility associated with both the cost and benefit. The cost and benefit should be considered together to determine the effectiveness of an alternative.
5. The time interval under investigation and risk attitude of the decision maker have great impacts on the optimal solutions resulting from the proposed framework. For retrofit planning of the same bridge network, a longer time interval always yields a higher utility associated with benefit than that corresponding to a shorter time interval.

Table 9.1 Parameters of the random variables associated with the consequences

Random variables	Mean	COV	Distribution type
ADT	Varies [a]	DNA	DNA
ADTT/ADT ratio	Varies [a]	DNA	DNA
Detour additional distance	Varies [a]	DNA	DNA
Rebuilding costs	1292 USD/m^2 [a]	0.2	LN
Fatalities associated with bridge failure	4.154 [a]	0.4	LN
Detour speed	30 km/h [a]	0.15	LN
Carbon emissions associated with construction	159 kg/m^2 [b]	0.2	LN
Energy consumption associated with construction	2.05 GJ/m^2 [b]	0.2	LN
Cars CO_2 emissions	0.22 kg/km [a]	0.2	LN
Trucks CO_2 emissions	0.56 kg/km [a]	0.2	LN
Energy consumption associated with detour	3.80 MJ/km [a]	0.2	LN

Note: LN=lognormal distribution; COV=coefficient of variation; DNA=does not apply; [a] based on Dong *et al.* (2014a); [b] based on Dequidt (2012); the costs in USD refer to the year 2013.

Table 9.2 Information regarding sustainability sub-attributes for utility function formulation

Attribute	Weight interval		Sub-attribute	Measure (units)	Range		Mid-point	
	Lower	Upper			Worst	Best	Level	Utility
Social	0.23	0.46	Extra travel time	hour	1.2×10^5	0	0.6×10^5	0.5
			Extra travel distance	km	6×10^6	0	3	0.5
			Fatalities	number	3.5	0	1.5	0.5
Environment	0.08	0.15	Carbon dioxide emissions	kg	2.5×10^6	0	1.0×10^6	0.5
			Energy consumption	MJ	1.6×10^7	0	0.6×10^7	0.5
Economic	0.25	0.42	Repair loss	USD	5.0×10^6	0	2.0×10^6	0.5

Table 9.3 Utility values associated with the bridge network without retrofit considering a 30-year interval

Attribute		Expected value	Utility	Ratio	Weighting factor	Expected utility
Social	Extra travel time (hour)	1.126×10^5	0.0616	0.25	0.43	0.0643
	Extra travel distance (km)	5.529×10^6	0.0785	0.25		
	Fatalities (no.)	3.01	0.1074	0.5		
Environment	Carbon dioxide emissions (kg)	2.425×10^6	0.0197	0.5	0.15	
	Energy consumption (MJ)	1.520×10^7	0.0293	0.5		
Economic	Repair loss (USD)	4.60×10^6	0.0534	1	0.42	

Table 9.4 Cost-benefit indicators resulting from the same retrofit option being applied to all bridges within the network

Retrofit action	Time interval, T_{max} (years)	Benefit utility, u_B	Cost-benefit indicator, CB_{RET}
1 (R_l = 0.25)	5	0.097	-0.004
	10	0.186	0.086
	20	0.349	0.249
	30	0.501	0.400
2 (R_l = 0.50)	5	0.133	-0.133
	10	0.257	-0.009
	20	0.485	0.220
	30	0.702	0.436
3 (R_l = 1.00)	5	0.158	-0.825
	10	0.306	-0.677
	20	0.583	-0.400
	30	0.846	-0.137

Table 9.5 Expected values of the sub-attributes of sustainability and retrofit costs associated with solution A, B, C, and the case without retrofit

Attribute		Without retrofit	Solution A	Solution B	Solution C
Social	Extra travel time (10^5 hours)	1.126	0.341	0.07	0.0382
	Extra travel distance (10^6 km)	5.529	1.702	0.035	0.0191
	Fatalities (no)	3.01	1	0.0461	0.0354
Environment	Carbon dioxide emissions (10^6 kg)	2.425	1.337	0.364	0.191
	Energy consumption (10^{13}J)	1.52	1.235	0.463	0.245
Economic	Repair loss (millions USD)	4.6	3.373	1.064	0.573
Cost	Retrofit cost (millions USD)	0	0.358	7.059	15.142

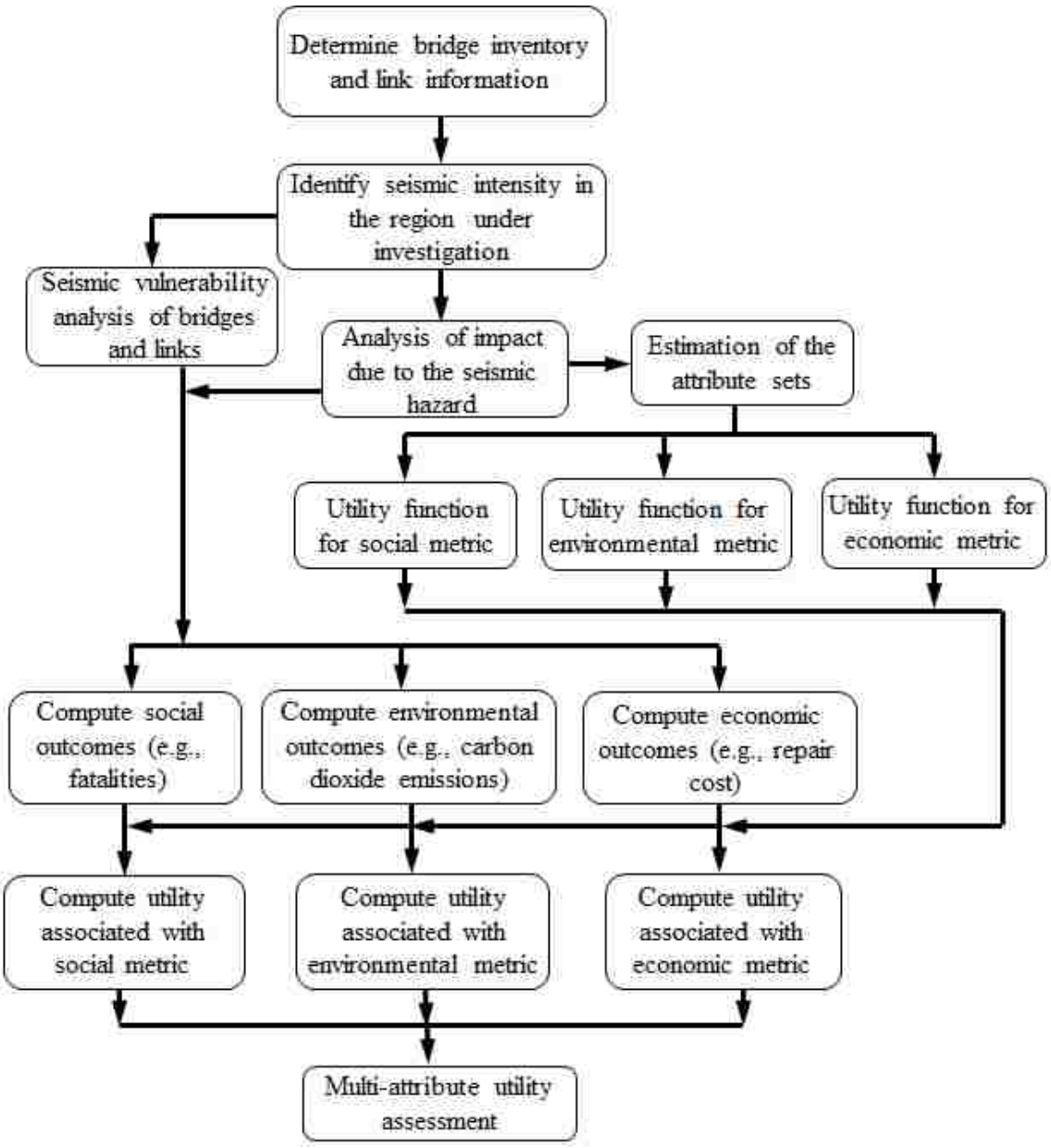

Figure 9.1 Flowchart for the multi-attribute utility assessment of bridge networks under seismic hazard

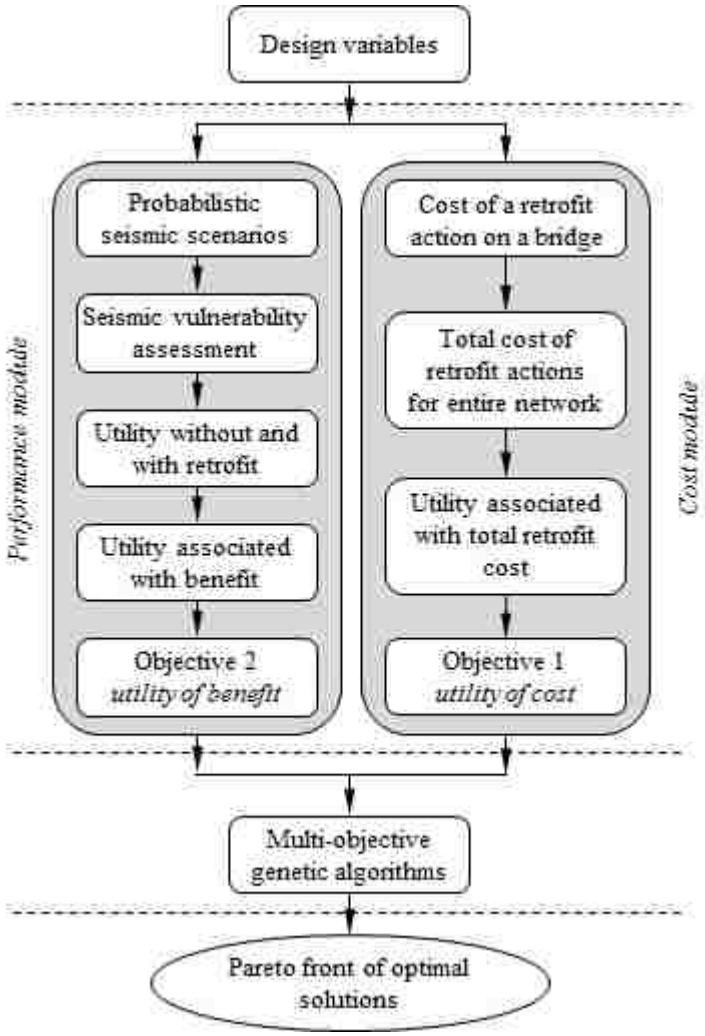

Figure 9.2 Generalized framework for seismic retrofit optimization of bridge networks

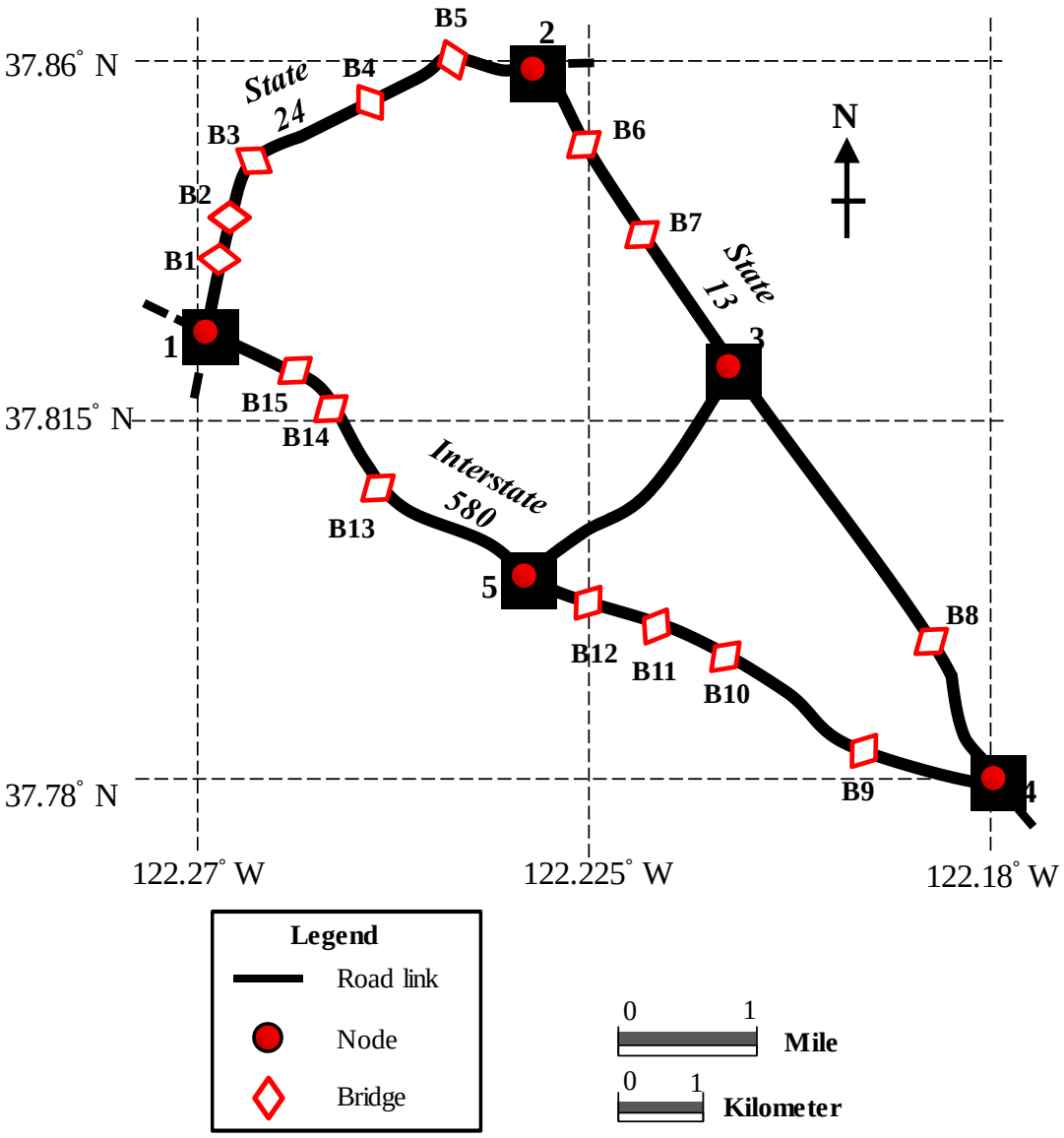

Figure 9.3 Schematic layout of the bridge network under investigation located in Alameda, CA

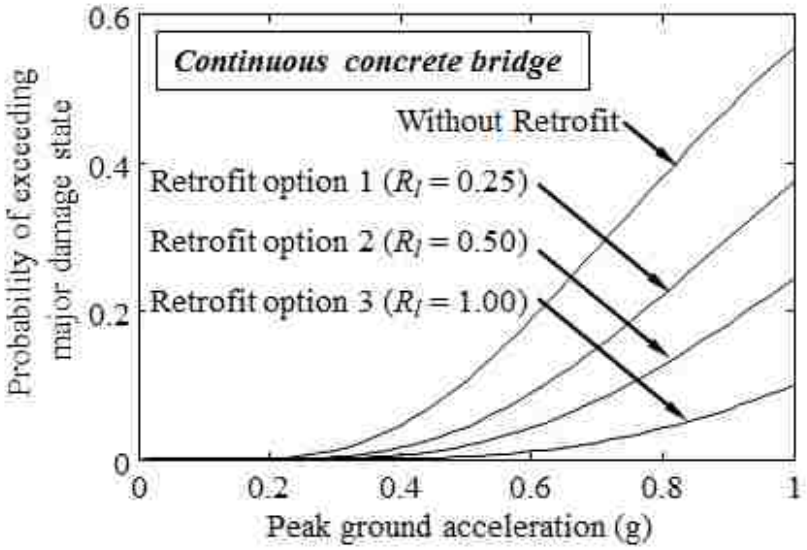

Figure 9.4 Fragility curves of a majorly damaged continuous concrete bridge with different levels of retrofit

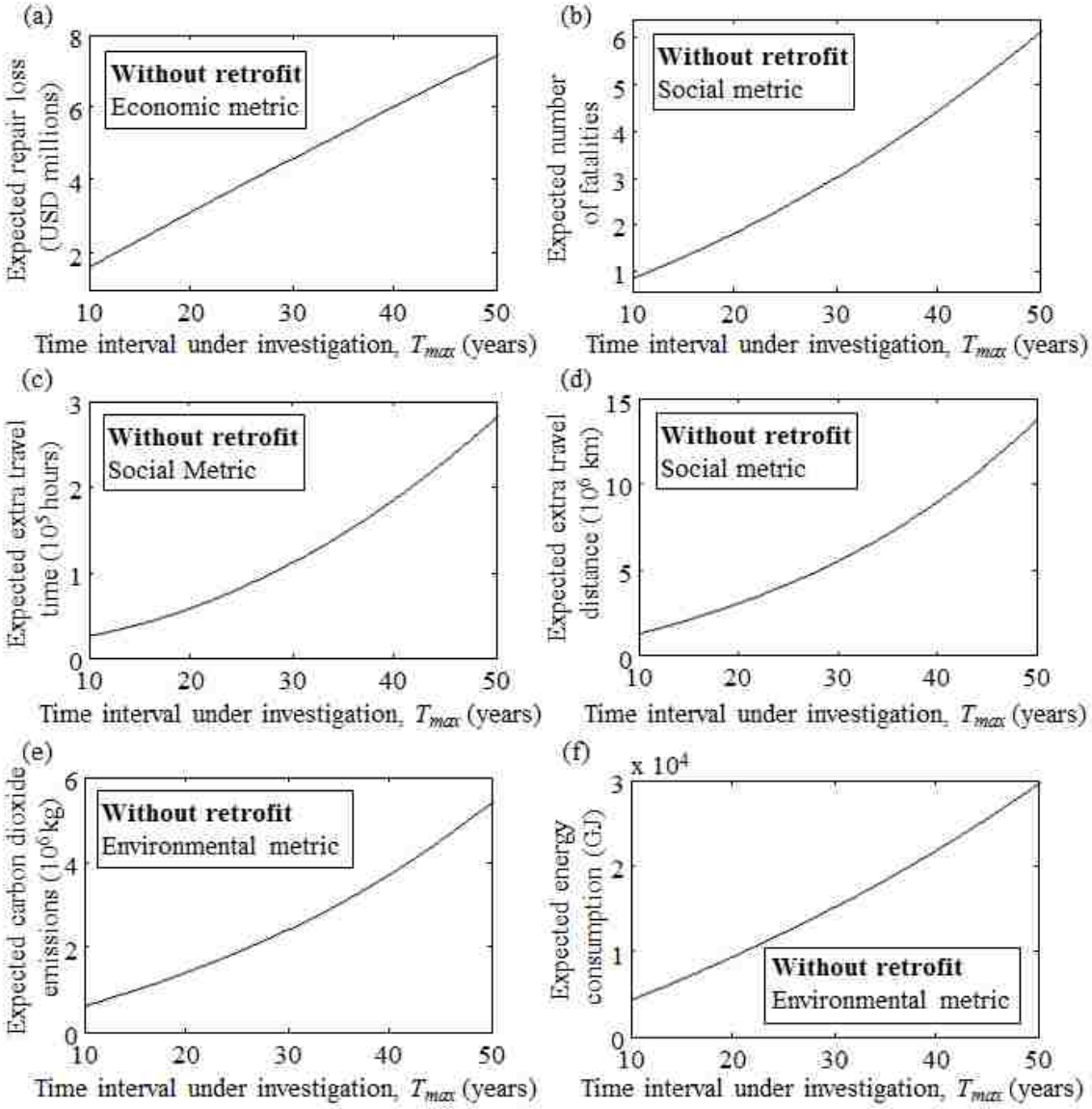

Figure 9.5 (a) The expected repair loss, (b) expected number of fatalities, (c) expected extra travel time, (d) expected extra travel distance, (e) expected carbon dioxide emissions, and (f) expected energy consumption as a function of the time interval under investigation

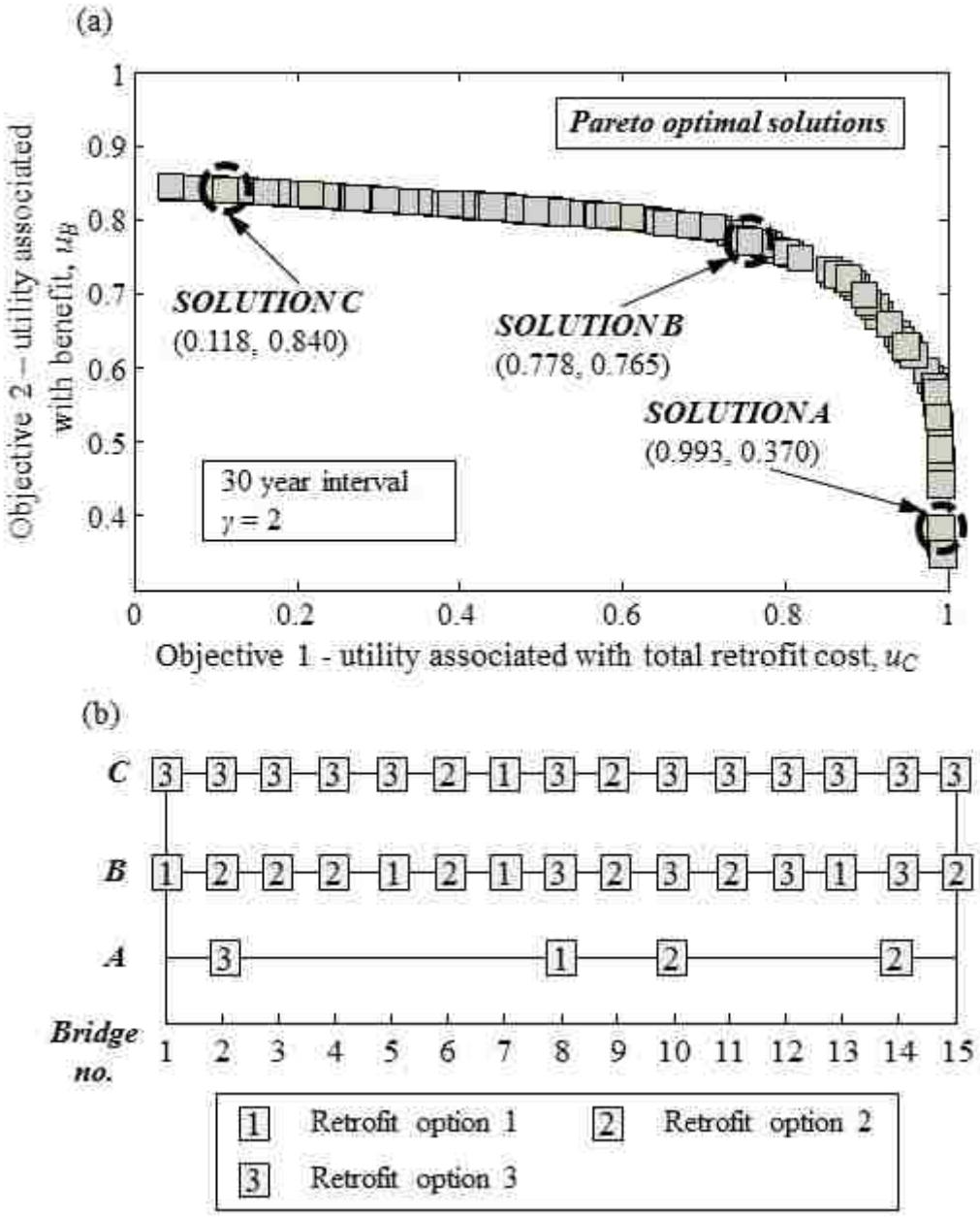

Figure 9.6 (a) Pareto optimal solutions associated with the bridge network considering a 30-year time interval; (b) retrofit plans associated with solution A, B, and C.

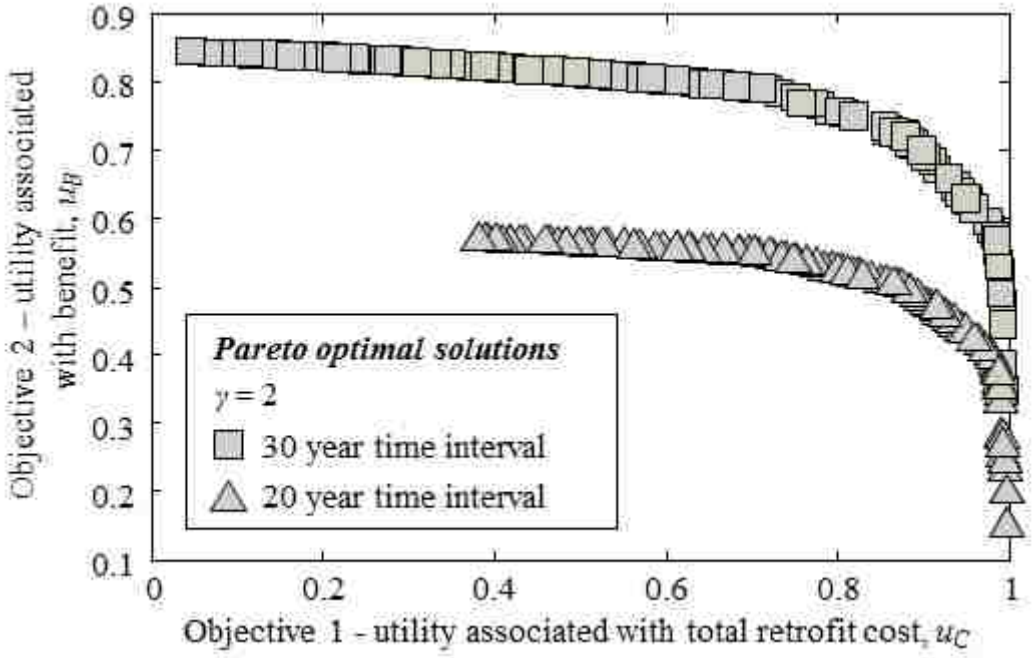

Figure 9.7 Pareto optimal solution sets for retrofit strategies considering 20 and 30 year time intervals

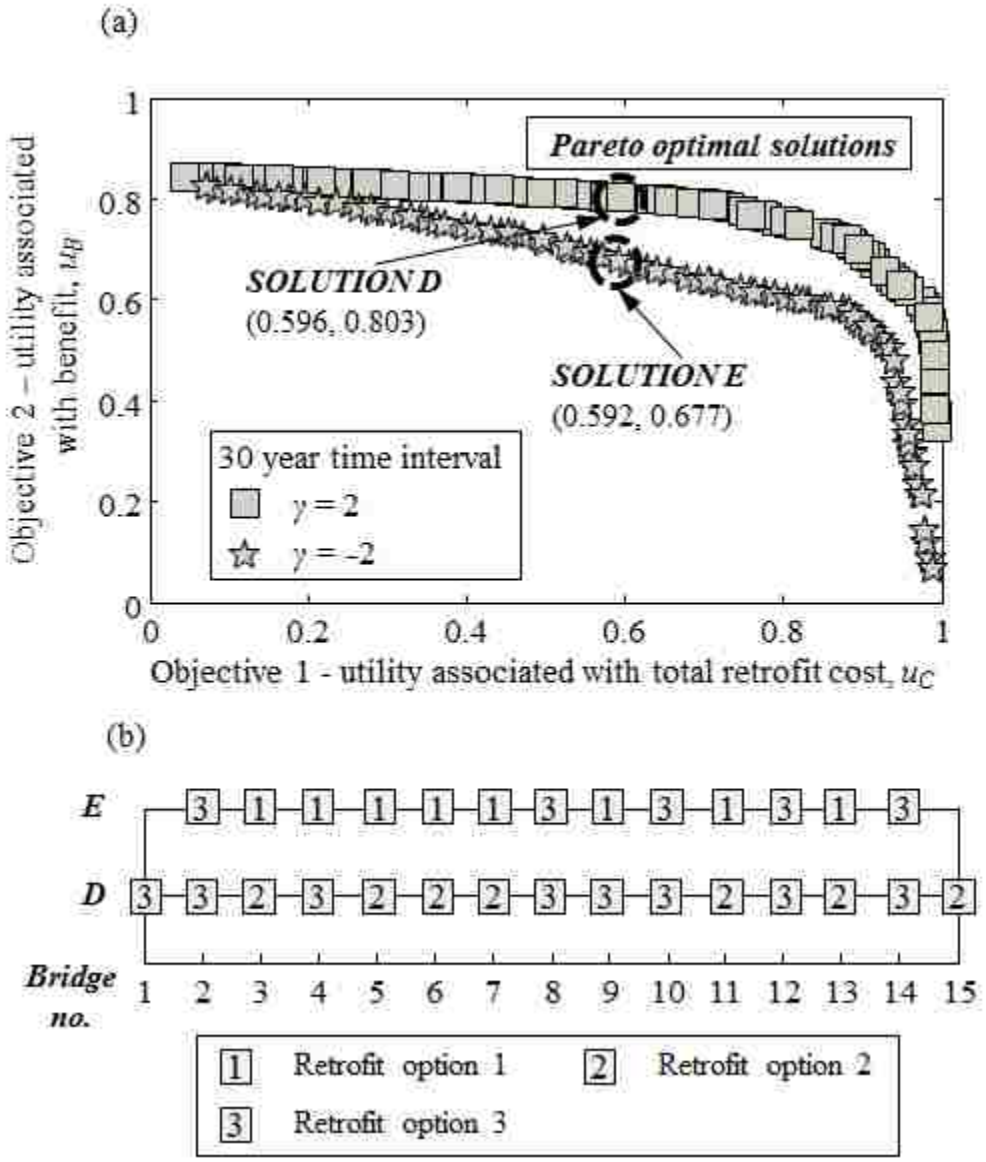

Figure 9.8 (a) Pareto optimal solution sets for retrofit plans associated with different risk attitudes toward retrofit costs considering a 30-year time interval; (b) retrofit plans associated with solution D and E

PART II

RISK-INFORMED LIFE-CYCLE ASSESSMENT, MAINTENANCE, AND UPDATING OF AGING SHIP STRUCTURES UNDER COLLISION, CORROSION, AND FATIGUE

CHAPTER 10

PROBABILISTIC SHIP COLLISION RISK AND SUSTAINABILITY ASSESSMENT CONSIDERING RISK ATTITUDES

10.1. INTRODUCTION

Ship collisions can have detrimental impacts on the environment, society, and economy. It is of vital importance to evaluate collision risk in order to plan preventive actions and be sufficiently prepared for possible oil spills and other associated events with negative consequences. The International Maritime Organization (*IMO*) has paid increasing attention to performance-based standards to ensure adequate safety and reliability of ship structures under extreme events (IMO 2002). In order to evaluate ship collision risk, it is necessary to develop a methodology that integrates the probability of occurrence of collision in a water area, vulnerability assessment of a ship, and probabilistic consequences of collision on society, environment, and economy. In general, sustainability can be quantified in terms of economic, social, and environmental metrics (Pearce and Vanegas 2002; Taylor and Fletcher 2006; Whittmore 2010). Further research must be conducted in order to assess ship collision risk in terms of sustainability and ensure the safety of marine transportation systems.

A predominant part of past studies regarding ship collision focused on determining the probability of this event based on probabilistic scenarios (Fujii and Tanake 1971;

Macduff 1974; Montewka *et al.* 2010). Although these studies described procedures to obtain the probability of ship collision, none has focused on the evaluation of consequences associated with collision. The consequence assessment of damaged ships is crucial for risk-informed decision making after an accident (Saydam and Frangopol 2013). Very little research has been carried out that properly integrates the probability of ship collision with the consequences associated with collision events into a comprehensive risk assessment methodology (Otto *et al.* 2002; Altiok *et al.* 2012). The consequences associated with the collision events can be divided into three categories: social, environmental, and economic impacts. Within this chapter, these three aspects and their associated uncertainties are incorporated within an approach that can evaluate ship collision risk considering the risk attitude of the decision maker. The probabilistic risk and sustainability associated with ship collision is a relatively new area of research.

The perception of risk is determined by the attitude of the decision maker and is an essential component of risk analysis. Based on the willingness of a decision maker, the attitudes toward risk can be classified as risk-averse, risk neutral, or risk taking (Pratt 1964). One of most popular decision theories is the expected utility theory (*UT*) (Von and Morgenstern 1953). The alternative with the highest expected utility value is always preferred. Utility theory is incorporated within the decision making framework presented herein. A utility function that measures the value of a particular alternative to the decision maker is established for the criterion under investigation. Utility theory is applied in order to normalize an attribute value to a uniform scale between 0 and 1. Tversky and Kahneman (1992) developed cumulative prospective theory, an updated version of

prospect theory, which considers the decision maker's risk attitude. The effects of the degree of risk aversion on ship collision risk and sustainability assessment are investigated in this chapter.

An approach to assess the risk associated with ship collision considering the risk attitudes of the decision maker is presented herein. The economic, social and environmental metrics are evaluated separately and then social and environmental metrics are converted into an economic metric considering their associated monetary values. The consequences include downtime, fatalities, human injuries, oil spill, and economic loss. The risk attitude of the decision maker is integrated within risk analysis by using utility functions. The approach is illustrated on a maritime transportation system located within the Delaware River region considering ship collision risk and sustainability. Ultimately, this approach can help the decision maker to make risk-informed choices considering risk attitudes. This chapter is based on a published paper Dong and Frangopol (2015a).

10.2. SHIP COLLISION RISK AND SUSTAINABILITY ASSESSMENT USING UTILITY THEORY

This chapter aims to assess risk due to ship collision by formulating a procedure to compute collision risk and sustainability in a probabilistic manner considering risk attitudes. The methodology for risk and sustainability-informed decision making under extreme events is illustrated in Figure 10.1. The first step for risk-informed decision making is to identify the risk of structural systems under extreme events including natural and man-made hazards.

Risk is defined as the product of consequences of an unwanted event and its probability of occurrence. Risk-based assessment of ships under construction process and operation condition has been recently developed (IACS 2006; Decò and Frangopol 2013). The quantitative risk assessment consists of three main parts: hazard exposure, structural vulnerability analysis, and consequences analysis. The hazard exposure procedure determines the probability of occurrence of an extreme event.. A general formulation of risk *R* was provided by Ellingwood (2007)

$$R = P(H) \cdot \sum_{DS} C(Cons|DS) \cdot P(DS|H) \tag{10.1}$$

where $P(H)$ is the annual rate of occurrence of the extreme event H; $C(Cons|DS)$ is the conditional consequence (e.g., economic, social, and environmental) associated with a given damage state DS (e.g., minor, moderate, major, complete); and $P(DS|H)$ is the conditional probability of damage state given the extreme event H. Based on the theorem of total probability, the total risk is the sum of consequences weighted by the probability of experiencing these consequences associated with different damage states. To clarify this issue, the sample space of all possible damage states and associated consequences is illustrated in Figure 10.2. There have been several research efforts focused on the ship collision probability (Pedersen 1995; COWI 2008). However, more research is needed for ship probabilistic damage conditions and consequences assessment. These topics are covered in the following sections of this chapter.

The input parameters of consequences are random variables. There are uncertainties involved in hazard exposure and the consequences analysis associated with damage states. These uncertainties should be considered in the probabilistic risk assessment

framework. There are two types of uncertainties: (a) aleatory uncertainties associated with natural randomness, and (b) epistemic uncertainties associated with the inaccuracies in the prediction and estimation of reality (Ang and Tang 2007). Based on the random variables involved in the damage states and consequences evaluation, samples of quantitative risk can be obtained by simulation (e.g., Monte Carlo Simulation). Next, distribution parameters (e.g., mean and standard deviation) can be fitted to the generated data. Ultimately, random samples of the economic loss can be obtained by considering the uncertainties. In this chapter, both epistemic and aleatory uncertainties are considered in the sustainability assessment process.

The perception of risk, determined by the attitude of the decision maker, is an essential component of risk analysis (Cha and Ellingwood 2013). The attitudes of most individuals and small groups are supposed to be risk-averse (Slovic 2000). Conversely, government agencies and large corporations are usually risk neutral, indicating an unbias attitude toward negative consequences of extreme events. Utility theory is incorporated within the decision making framework presented herein. The attitude of the decision maker can be incorporated within this approach for the ship collision risk assessment using utility function.

Based on the probability density function (*PDF*) of the ship collision loss and the utility function, the expected utility value can be expressed as

$$E(U) = \int_{-\infty}^{+\infty} u(r) \cdot f_R(r) d(r) \tag{10.2}$$

where $u(r)$ is the utility function associated with ship collision risk and $f_R(r)$ is the *PDF* of R.

10.3. PROBABILITY OF SHIP COLLISION

The ship collision model initially proposed by Macduff (1974) was expressed as the product of geometrical probability and causation probability. Geometrical probability is the probability of a vessel encountering accident scenarios while causation probability is defined as the conditional probability that a collision occurs in an accident scenario. The collision model proposed by *COWI* (2008) is used in this chapter to calculate the probability of ship collision. In the *COWI* model, the geometrical probability is further divided into several separate probabilistic quantities.

10.3.1. Parallel waterways

For collision events associated with parallel waterways, the vessels are navigating along the same route as indicated in Figure 10.3(a, b). There are two basic cases regarding the parallel collision events: a head-on collision and an overtaking collision. These two cases are both considered in the model presented herein. The parallel collision probability depends on length of the route segment, traffic intensity, width and speed of the ships, deviations of the ships from the route axis, and causation probability. For the parallel case, the annual collision probability of two ships can be expressed as (COWI 2008)

$$P_X = P_T P_G P_C k_{RR} \tag{10.3a}$$

$$P_T = L N_1 N_2 \left| \frac{V_1 - V_2}{V_1 V_2} \right| \tag{10.3b}$$

$$P_G = (B_1 + B_2)/c \tag{10.3c}$$

where P_T is the annual probability of meeting within one route segment; L is length of the route segment; N_1 is annual number of ship 1 through the route; N_2 is annual number of

ship 2 through the route; V_1 is the speed of ship 1; V_2 is the speed of ship 2; P_G is the geometrical collision probability; B_1 is the breadth of ship 1; B_2 is the breadth of ship 2; c is the width of the segment of waterway; P_C is the causation probability that two ships sailing on collision route do not undertake any evasive actions; and k_{RR} is a risk reduction factor which depends on the effects of pilotage of the ships, local experience, and safety standards. More detailed information can be found in COWI (2008)

10.3.2. Crossing waterways

The crossing collision considers ships in different routes and involves the cases of full intersection and merging traffic as shown in Figure 10.3(c). The crossing collision probability depends on the crossing pattern, traffic intensity in the two directions, ship width, ship length, ship speed, crossing angle, causation probability, and probability that the two ships intersect. The annual crossing collision probability can be expressed as (COWI 2008)

$$P_X = P_I P_G P_C k_{RR} \tag{10.4}$$

where P_I is the probability that the routes of two ships intersect and P_G is the geometrical collision probability.

Based on *COWI* (2008), the passage of the ship on one of the two routes is assumed to follow a Poisson process. Accordingly, the geometrical collision probability can be expressed as (COWI 2008)

$$P_G = N_1(1 - e^{-N_2 \Delta t}) \tag{10.5}$$

where $\Delta t = \frac{1}{|V_1 V_2|}\left[B_2 \left[\frac{V_2}{\sin\theta} - \frac{V_1}{\tan\theta} \right] + B_1 \left[\frac{V_1}{\sin\theta} - \frac{V_2}{\tan\theta} \right] + L_1 |V_2| + L_2 |V_1| \right]$ and θ is the angle between the routes (see Figure 10.3(c)).

10.4. PROBABILISTIC DAMAGE ASSESSMENT

Pedersen and Zhang (1998) developed a methodology for ship collision assessment based on the analysis of external structural dynamics and internal mechanics. Brown and Chen (2002) proposed an approach to develop a set of parametric equations that define the *PDF*s for damage extent of struck ships. They developed the Simplified Collision Model (*SIMCOL*) by using a time-domain simultaneous solution of external ship dynamics and internal deformation mechanics. The *PDF*s describing the location, extent, and penetration of damage are integrated within this approach in order to properly account for the uncertainty associated with particular probabilistic collision scenarios (Brown and Chen 2002). The probabilistic damage length (*dl*) and damage penetration (*dp*) of several types of ships associated with various collision scenarios can be obtained utilizing this approach.

The damage condition of ships can be quantified by considering the damage penetration area; the larger the penetration area, the more severe the damage condition of the ship. Additionally, according to COWI (2008), the repair costs for the struck ships are related to the damage penetration area. It is reasonable to define the damage state of the collided ships based on damage penetration area associated with specific probabilistic damage condition. In this chapter, the probability of a damaged ship being in a specific damage state is expressed as

$$P(DS_i) = P(DA_{i-1} \leq DA < DA_i) \tag{10.6}$$

where DA is the penetration area of the damaged ship; DA_i is the upper bound of the penetration area for the damage state i and lower bound for damage state i+1 for $i \geq 1$; and DA_{i-1} is lower bound of the penetration area for the damage state i and upper bound for damage state i-1 for $i \geq 2$. Given the information regarding the definition of damage states of a ship, the probability of a ship being in different damage states can be obtained.

10.5. UTILITY OF COLLISION RISK CONSIDERING ATTITUDES

In this section, the consequences associated with different damage conditions are evaluated in terms of social, environmental, and economic metrics. Ship collisions can cause significant damage to ship structures and ultimately hamper their intended function. Moreover, an oil spill resulting from oil tanker collision can negatively impact the environment and local wildlife. The oil can cause water surface contamination and its chemical components can cause acute toxic effects. The oil spills have destructive effects on coastal ecosystems (Biello 2010; Shirley *et al.* 2010). Since most of the parameters used in the evaluation of the cost of various consequence are affected by uncertainties, they have been treated as random variables. According to Ang (2010), a practical evaluation of epistemic uncertainty relies on intuition/engineering judgments and can provide a specific reasonable range of possibilities associated with an associated distribution type.

10.5.1. Social metric

The total number of fatalities, injuries, and downtime resulting from ship collisions are considered as the social impact within the proposed risk and sustainability assessment methodology. Some of the most catastrophic social consequences of ship collisions are fatalities and severe human injuries. The United States Coast Guard (2009) provides the number of injuries resulting from ship collision incidents during the period of 1992 to 2008. The expected number of injuries (N_{inj}) per incident for the ship collision is 2.0. Based on *COWI* (2008), the expected number of fatalities (*FT*) for collisions is approximately 0.01 per accident.

Another social metric considered is the downtime associated with the non-functionality of damaged ships. The downtime associated with ship collision can determined by considering the theory of total probability and damage states of ships as indicated in Table 10.1.

The downtime of a ship due to vessel collision can be expressed as

$$DT = \sum_{i=1}^{N} P(DS_i) \cdot d_i \tag{10.7}$$

where N is the number of damage states considered; i indicates a specific ship damage state; d_i is the downtime of a ship associated with damage state i (days); and $P(DS_i)$ is the probability of a ship being in damage state i after a collision event.

10.5.2. Environmental metric

Due to the damaged condition of a ship after a collision incident, oil can spill into the surrounding water and negatively affect the environment and local ecosystem. The presented risk methodology evaluates environmental metrics in terms of the magnitude of

an oil spill resulting from a ship collision accident. For a given incident, the total oil spill can be estimated based on empirical data for different vessel types. The oil spill distribution data for various types of vessels is provided by the United States Coast Guard (2009). For a given incident, total oil spill is estimated based on empirical distributions for different ship types (e.g., oil tanker). The relative magnitude of an oil spill (O_{spi} (gallon)) associated with ship collision can be assessed as the environmental metric within the proposed risk and sustainability assessment procedure.

10.5.3. Economic metric

The economic consequences resulting from ship collision are evaluated in terms of monetary value. The total economic loss is related to repair costs, costs associated with time loss, environmental costs, and costs of fatalities and injuries. Considering the dependency of future monetary value on the interest rate, the time-variant value of consequences can be calculated as

$$FV(t) = PV(1+r)^t \tag{10.8}$$

where $FV(t)$ is the future monetary value; PV is the present monetary value; and r represents the annual interest rate of money.

The repair costs can be computed based on the damage penetration area of the ship. As more area of the ship is damaged, more repair money is required. The repair loss associated with ship collision is considered as an economic consequence that detrimentally affects the shipping company. The repair cost for the damaged ships can be expressed as

$$C_{Rep} = E_{Rep} \cdot dl \cdot dp \cdot c_{Rep} \tag{10.9}$$

where E_{Rep} is a factor accounting for the epistemic uncertainties associated with repair costs; dl is the damage length of the ship; dp is the damage penetration in the ship; and c_{Rep} is the unit repair cost (USD/m^2).

As a result of collision, a ship may operate with an inadequate performance level, ultimately causing a delay of mission. Accordingly, the economic loss associated with downtime can also be evaluated

$$C_{DT} = E_{dt} \cdot DT \cdot c_{time} \tag{10.10}$$

where E_{dt} is the factor considering the epistemic uncertainties for the downtime loss costs; DT is the downtime/repair for the damaged ship (days); and c_{time} is the monetary value of time loss (USD/day).

The life loss cost depends on the number of fatalities and can be expressed as

$$C_{LL} = E_{fat} \cdot FT \cdot L_C \tag{10.11}$$

where E_{fat} is a factor that considers the epistemic uncertainties for fatalities costs; FT is number of fatalities associated with collisions event; and L_c is the average comprehensive cost of per human death (USD).

Similarly, the cost for the injury can be computed as

$$C_{Inj} = E_{inj} \cdot N_{inj} \cdot c_{inj} \tag{10.12}$$

where E_{inj} is a factor that considers the epistemic uncertainties for injuries costs; N_{inj} is the average number of injury; and c_{inj} is the average comprehensive cost of injury (USD).

Comprehensive oil spill costs per gallon are evaluated in terms of monetary value and shown in Table 10.2. The economic loss associated with an oil spill is computed considering the magnitude of oil spill specific to the damaged ships. In order to determine

the combined effect of sustainability on the risk assessment of damaged ships, the environmental metric is converted to a monetary value and expressed as

$$C_{OS} = E_{os} \cdot O_{spi} \cdot c_{Env} \tag{10.13}$$

where E_{os} is a factor that considers the epistemic uncertainties for costs associated with oil spill; c_{Env} is the cost value of environmental metric per unit volume (e.g., USD/gallon); and O_{spi} is the magnitude of oil spill associated with ship collision (gallon).

The total economic consequence of ship collision is the sum of repair costs (C_{Rep}), time loss costs due to the unavailability of damaged ships (C_{DT}), environmental costs associated with oil spill (C_{OS}), and costs associated with injuries (C_{Inj}) and fatalities (C_{LL}). Therefore, the total economic consequences can be expressed as

$$C_T = C_{Rep} + C_{DT} + C_{OS} + C_{LL} + C_{Inj} \tag{10.14}$$

Generally, risk represents a combined measure of the probability and severity of adverse effects. It can be defined as the product of the consequences and the probability of occurrence of these consequences and can be expressed as

$$R_{Col} = C_T \cdot p_{col} \tag{10.15}$$

where C_T is the total economic consequence associated with the ship collision and p_{col} is the probability of collision.

The input parameters of consequences are random variables. Assuming availability of adequate information on the probability distributions of the input parameters, the proper probabilistic descriptors of total economic loss can be obtained by performing Monte Carlo Simulation. Based on the *PDF* of the economic loss, the expected value of

the collision risk ($E(R_{Col,i})$) associated with a specific interval (e.g., $r_{crit}(i\text{-}1) \leq R_{Col} \leq r_{crit}(i)$) is

$$E(R_{Col,\,i}) = \int_{r_{crit}(i-1)}^{r_{crit}(i)} r_{Col} \cdot f_{R_{Col}}(r_{Col})\, d(r_{Col}) \tag{10.16}$$

where R_{Col} is the probabilistic risk associated with ship collision and $f_{R_{Col}}(r_{Col})$ is the *PDF* of R_{Col}.

10.5.4. Utility analysis

A utility function can reflect the attitude of a decision maker towards specific outcomes (Keeney and Raiffa 1993). The formulation of the utility function under investigation depends on the knowledge and preferential characteristics of the decision maker. Considering an exponential formulation, the utility associated with the given consequence (e.g., economic loss) can be expressed as (Ang and Tang 1984)

$$u(x) = \frac{1}{1-\exp(-\rho)}\left[1-\exp\left(-\rho\frac{x_{max}-x}{x_{max}}\right)\right] \tag{10.17}$$

where x is the value of criterion considered by the decision maker; ρ indicates the attitude of the decision maker; and x_{max} denotes the maximum value associated with the parameter which is utilized to normalize the utility function so that it always takes values between 0 and 1. Utility functions associated with $x_{max} = 1$ and different values of ρ are shown in Figure 10.4. The parameter ρ represents risk attitudes associated with utility function; a positive value of ρ indicates a risk-averse attitude while a negative value indicates a risk-taking attitude. The absolute value of ρ represents the extent of the risk attitude.

Eq. (10.17) provides a deterministic measure of the utility associated with the economic loss under investigation. As mentioned previously, the random samples of the economic loss can be obtained; then the probabilistic utility values associated with these random samples can be computed. The expected utility associated with a specified risk interval is

$$E(U_i) = \int_{r_{crit}(i-1)}^{r_{crit}(i)} u(r_{Col}) \cdot f_{R_{Col}}(r_{Col})\, d(r_{Col}) \tag{10.18}$$

where $u(r_{col})$ is the utility function associated with ship collision risk as indicated in Eq. (10.17).

10.6. AN ILLUSTRATIVE EXAMPLE

The methodology for risk and sustainability assessment of vessel traffic associated with potential collision incidents is illustrated on a particular region of the Delaware River. The layout of the area under investigation is indicated in Figure 10.5. The probability of ship collision and the probabilistic consequences associated with the damage conditions are considered in the risk analysis of this marine infrastructure system. Based on utility theory, the probabilistic risk is evaluated by considering the decision maker's attitude toward risk.

The Delaware River is an important commercial route for the petrochemical facilities located in Delaware City, DE, Paulsboro, NJ, and Marcus Hook, PA. The marine traffic accounts for approximately 12% of the nation's crude oil imports, making this port one of the most critical petroleum infrastructures in the U.S. (USACE 2011). More specifically, oil tankers make up a considerable percentage of the total ship traffic volume in the

Delaware River. The collision risk associated with tankers in the Delaware River is evaluated in this example.

10.6.1. Probability of ship collision and damage states

The collision model developed by COWI (2008) is used herein to calculate the probability of ship collision associated with different scenarios. As mentioned previously, the ship collision associated with parallel and crossing waterway can be computed based on the ship traffic volume and other parameters regarding the operational conditions of ships. The average number of tankers in the water area is approximately 900 per year while the total number of vessels is approximately 3000 per year (Altiok *et al.* 2012). In this example, the collision for tankers in the crossing waterway is related to the Delaware River area. The expected values of the ship speed and breadth used to compute the probability of ship collision are 6 m/s and 30m, respectively. The annual crossing collision can be computed using Eq. (10.4) associated with the parameters (P_I, P_G, P_C, and k_{RR}) involved in this equation. The angle between the routes of ships (θ) is assumed to be $\pi/2$. The general information (e.g., ship average speed) can be assigned for different types of ships considering the operation condition to calculate the geometrical collision probability P_G. The values of P_I, P_C, and k_{RR} can be obtained based on COWI (2008). For example, the causation probability P_C is equal to 3.0×10^{-4}. The probability of collision in the crossing waterway can be computed using Eq. (10.4). The values of P_G, P_I, P_C, and k_{RR} can be obtained using the information mentioned for this illustrative example. Consequently, the annual crossing collision probability P_X is 0.0668.

Brown and Chen (2002) investigated damage properties of different types of ships, including oil-tanker vessels, under probabilistic collision scenarios. The probabilistic damage condition of the struck ships considering damage penetration and length is assessed within this illustrative example. In this chapter, the distributions of the damage parameters (e.g., damage penetration) can be assumed to follow exponential distributions considering tanker collision. The exponential distribution is based on Brown and Chen (2002) and is adopted herein for illustrative purposes. Based on Brown and Chen (2002), the damage *PDF*s for different oil tankers are similar. The larger struck ship can absorb more energy and result in similar damage conditions associated with the smaller ships (Brown and Chen 2002). The probabilistic damage length and penetration of a struck ship are modeled using the exponential distribution. The expected damage penetration is approximately 1.63 *m* and the expected damage length is approximately 2.87 *m*. These values are employed to compute the probabilistic damage condition of a struck ship.

Based on definition of the damage states of a ship, the probability of a struck ship being in a specific damage state can be computed using Eq. (10.6). The critical value for each respective damage state is indicated in Table 10.1. Different damage states denote the damage level by considering penetration area. For example, if the damage penetration area is between 10 m^2 and 20 m^2, the ship can be classified into damage state 3. As the damage penetration area increases, the severity of damage to the ship also increases. As mentioned previously, the distributions of damage length and penetration of the struck ship follow exponential distribution. By performing Monte Carlo Simulation, the penetration area of the struck ship can be computed. Based on the definition of damage

states associated with the struck ship indicated in Table 10.1, the probability of the ship being in damage states 1, 2, 3, and 4 is 0.3662, 0.5087, 0.0808, and 0.0444, respectively.

10.6.2. Collision risk and sustainability assessment

As indicated previously, the consequences are evaluated in terms of social, economic, and environmental metrics. The consequences associated with these three metrics can be evaluated using Eqs. (10.8) to (10.14). The aleatory and epistemic uncertainties are both considered herein. The epistemic uncertainties are considered by introducing a random variable that follows a lognormal distribution with mean value equal to 1. The distributions of the random variables related to the probabilistic consequence evaluation are indicated in Table 10.3. Latin Hypercube Sampling (*LHS*) (McKay *et al.* 1979) is used with 20,000 trials to account for the epistemic and aleatory uncertainties. By performing *LHS*, the corresponding random samples associated with social, environmental, and economic impacts are obtained using Eqs. (10.8) to (10.14). Next, the expected value of these impacts can be computed. In this example, the social and environmental metrics are converted into the economic metric by considering these two metrics in terms of monetary value.

The social metric considered includes the number of fatalities and injuries, and downtime as indicated in Eq. (10.7). The downtime for each damage state is modeled as a triangular distribution as indicated in Table 10.1. By performing *LHS*, the sample of downtime associated with struck ship can be obtained as shown in Figure 10.6. Based on historical data from 1992 to 2008 (USCG 2009), the expected number of injuries per collision incident is 2.0; while the expected number of fatalities in case of collisions is

0.01 (COWI 2008). The environmental metric associated with an oil spill can be evaluated for ship collision events.

The economic metric associated with repair cost, downtime, environmental effects related to an oil spill, fatalities, and injuries cost is evaluated. The annual interest rate of money is assumed to be 2%. The monetary values of annual risk and sustainability refer to year 2013. The repair cost is related to the penetration area of the ship and can be computed based on Eq. (10.9). The calculated *PDF* of repair cost is shown in Figure 10.7(a). Using Eq. (10.13), the costs associated with an oil spill can be obtained. The costs are related to the volume of the oil spill and different probabilistic values are assigned with respect to volume as indicated in Table 10.2. Accordingly, the cost of the environmental consequences considering the monetary value can be evaluated. The consequences regarding the social impact can also be converted into economic metric using Eqs. (10.10) to (10.12). The corresponding calculated *PDF*s are indicated in Figure 10.7(b, c, d). The expected values associated with different consequences regarding the economic loss are shown in Table 10.4. As indicated in this table, the loss associated with the environmental metric significantly contributes to the total loss. The parameters associated with this aspect should be carefully considered. Based on Eqs. (10.14) to (10.15), the total probabilistic economic loss associated with ship collision is indicated in Figure 10.8. The expected value of total economic loss associated with social, environmental, and economic impacts is 423,393 USD. In general, the results in this chapter can be easily updated if more reliable data associated with these parameters becomes available.

10.6.3. Quantification of utility considering attitudes

In this chapter, the risk statistics are used to produce the risk profiles associated with ship collision. The annual risk associated with ship collision is emphasized herein. The uncertainties in the parameters regarding the consequences are incorporated in the methodology to illustrate the variation in the economic loss. As indicated previously, the expected value of the economic loss is 423,393 USD. The probability of the risk being in a given specified interval ($P(r_{crit}(i\text{-}1) \leq R_{Col,i} \leq r_{crit}(i))$) and its expected value ($E(R_{Col,i})$) are also evaluated herein. The outcomes associated with the probabilistic economic loss are shown in Table 10.5. As indicated, the probability of having large risk values is extremely small compared to low or moderate risk. For example, the probability that risk is larger than 2 million USD is 0.0033, while the probability that risk is between 0.5 million USD and 1 million USD is 0.2349.

The utility associated with the economic loss is computed using Eq. (10.17) considering x_{max} = 3 million USD. The effect of the decision maker's risk attitude on the utility value associated the ship collision risk is investigated herein. The expected utility ($E(U_i)$) associated with the economic loss in different risk intervals is shown in Table 10.6 considering two different risk attitudes (i.e., ρ = 2 and ρ = -2). As indicated, the risk attitude can significantly affect the expected utility associated with the same economic loss. The *PDF*s of the utility under different risk attitudes are shown in Figure 10.9. As shown, the risk attitudes have great effects on the distribution of the utility values. Consequently, it is important to consider the attitudes of the decision maker in the utility assessment process.

The effects of severity of risk attitude (i.e., absolute value of ρ) on the utility values associated with different risk intervals are shown in Figure 10.10. The risk intervals considered in this figure are the same as those indicated in Table 10.5. Considering risk averse attitude (i.e., $\rho > 0$), the utility of the expected loss ($u(E(R_{Col,i}))$) is always larger than the expected utility ($E(U_i)$) under the same risk interval. The difference between the expected utility value ($E(U_i)$) and the utility of the expected loss ($u(E(R_{Col,i}))$) for a given risk interval increases with ρ. The distribution of utility values provides useful information to decision makers. Based on this information, the best decision for the management of ship structures can be reached.

10.7. CONCLUSIONS

This chapter presents a methodology for assessing the annual probabilistic ship collision risk and sustainability, incorporating the decision maker's attitudes associated with utility function. The approach is illustrated on a particular region of the Delaware River for ship collision risk and sustainability assessment.

The following conclusions are drawn:

1. The values of sustainability metrics are sensitive to the parameters used in the evaluation of consequences. For instance, environmental costs contribute significantly to the values of the parameters used in the example. Therefore, the parameters involved in the analysis of the environmental costs should be carefully estimated.
2. The results show that it is important to consider the decision maker's risk attitudes in the collision risk and sustainability assessment associated with utility functions.

3. The collision risk and sustainability are dependent on the damage condition of the ship. More emphasis should be placed on developing models for ship damage analysis under probabilistic collision scenarios.
4. The proposed methodology can be used in assisting decision making regarding the traffic control and risk mitigation activities to improve the traffic safety of maritime transportation considering risk attitudes. Sustainability can be used as an objective function to be maximized while simultaneously minimizing the economic loss.

Table 10.1 Downtime associated with different penetration area of ships

Damage state	Penetration area	Repair time (days)		
		Minimum	Maximum	Mean
1	$< 1\ m^2$	0	4	2
2	$1 - 10\ m^2$	2	12	7
3	$10 - 20\ m^2$	8	20	14
4	$> 20\ m^2$	14	28	21

Table 10.2 Comprehensive oil spill cost/gallon associated with oil spill

Oil spill (Gallons)	Mean (USD/Gallon)	COV	Distribution type
< 500	480.40 [a]	0.2 [b]	LN [b]
500 – 1,000	685.88 [a]	0.2 [b]	LN [b]
1,000 – 10,000	814.84 [a]	0.2 [b]	LN [b]
10,000 – 100,000	564.02 [a]	0.2 [b]	LN [b]
100,000 – 1,000,000	316.01 [a]	0.2 [b]	LN [b]
> 1,000,000	243.75 [a]	0.2 [b]	LN [b]

[a] based on Etkin (2004); [b] assumed; LN: lognormal distribution; COV: coefficient of variation.

Table 10.3 Parameters of the random variables associated with the consequences. The costs refer to year 2013

Random variables	Mean	COV	Distribution type
Repair cost (USD/m^2)	2,160 [a]	0.2 [b]	LN [b]
Time loss (USD/day)	95,000 [a]	0.3 [b]	LN [b]
Epistemic uncertainty factor for injury costs	1 [b]	0.3 [b]	LN [b]
Epistemic uncertainty factor for loss of human	1 [b]	0.3 [b]	LN [b]
Epistemic uncertainty factor for material damage repair costs	1 [b]	0.2 [b]	LN [b]
Epistemic uncertainty factor for costs associated with oil spill	1 [b]	0.2 [b]	LN [b]
Epistemic uncertainty factor for operating costs	1 [b]	0.2 [b]	LN [b]
Epistemic uncertainty factor for time loss costs	1 [b]	0.2 [b]	LN [b]
Value of a statistical life (USD)	4,650,000 [c]	0.45 [b]	LN [b]
Cost of injury (USD)	60,000 [c]	0.45 [b]	LN [b]

[a]: COWI (2008); [b]: assumed; [c]: based on Altiok *et al.* (2012);
LN: lognormal distribution; COV: coefficient of variation.

Table 10.4 Expected value and standard deviation of the consequences

Consequences	Expected value (2013 USD)	Standard deviation (2013 USD)
Repair cost	17,492	31,283
Environmental cost	5,284,700	4,757,600
Time loss cost	857,430	217,290
Fatality cost	50,880	22,594
Injury cost	127,740	56,945
Total value	6,338,242	4,760,000

Table 10.5 The expected value and probability of the economic loss associated with different risk intervals

Risk interval (2013 USD)	Expected value, $E(R_{Col,i})$ (2013 USD)	Probability
$0 < R_{Col} \leq 250{,}000$	152,583	0.3355
$250{,}000 < R_{Col} \leq 500{,}000$	374,374	0.3725
$500{,}000 < R_{Col} \leq 1{,}000{,}000$	665,179	0.2349
$1{,}000{,}000 < R_{Col} \leq 1{,}500{,}000$	1,192,308	0.0443
$1{,}500{,}000 < R_{Col} \leq 2{,}000{,}000$	1,678,565	0.0095
$R_{Col} > 2{,}000{,}000$	2,342,731	0.0033

Table 10.6 The expected utility associated with different risk intervals considering different attitudes

Risk interval (2013 USD)	$\rho = 2$ Expected utility, $E(U_i)$	$\rho = -2$ Expected utility, $E(U_i)$
$0 < R_{col} \leq 250{,}000$	0.9831	0.8888
$250{,}000 < R_{col} \leq 500{,}000$	0.9554	0.7455
$500{,}000 < R_{col} \leq 1{,}000{,}000$	0.9116	0.5888
$1{,}000{,}000 < R_{col} \leq 1{,}500{,}000$	0.8084	0.3681
$1{,}500{,}000 < R_{col} \leq 2{,}000{,}000$	0.6753	0.2227
$R_{col} > 2{,}000{,}000$	0.3907	0.0910

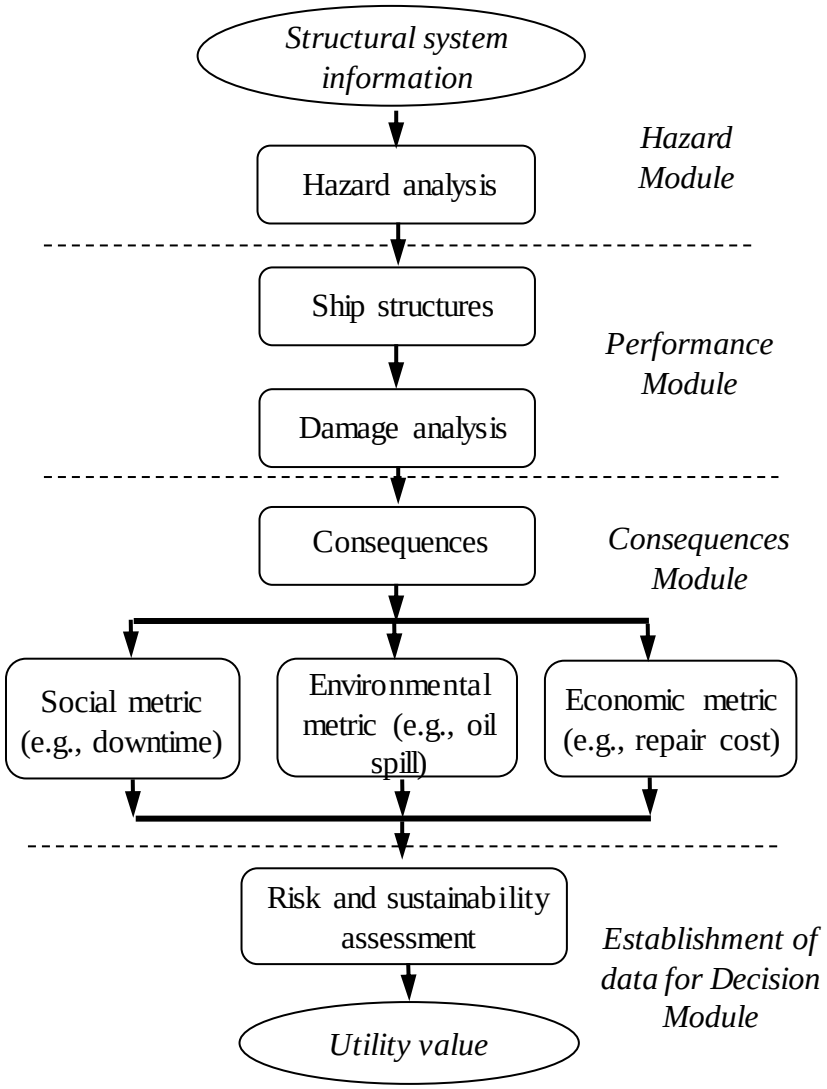

Figure 10.1 The methodology for risk and sustainability assessment considering risk attitudes in terms of utility value

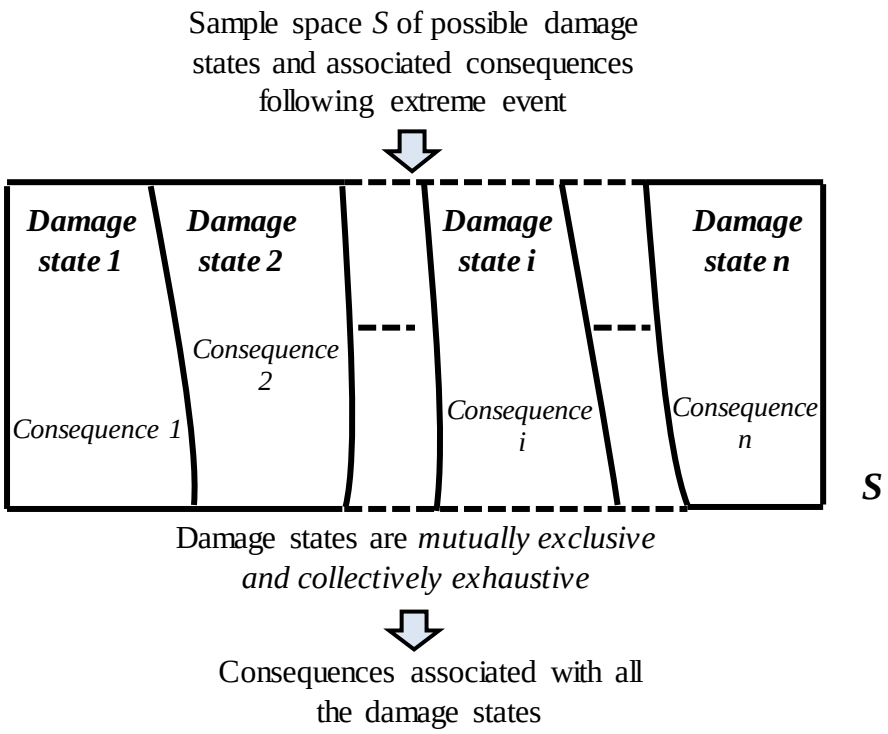

Figure 10.2 Damage states and associated consequences

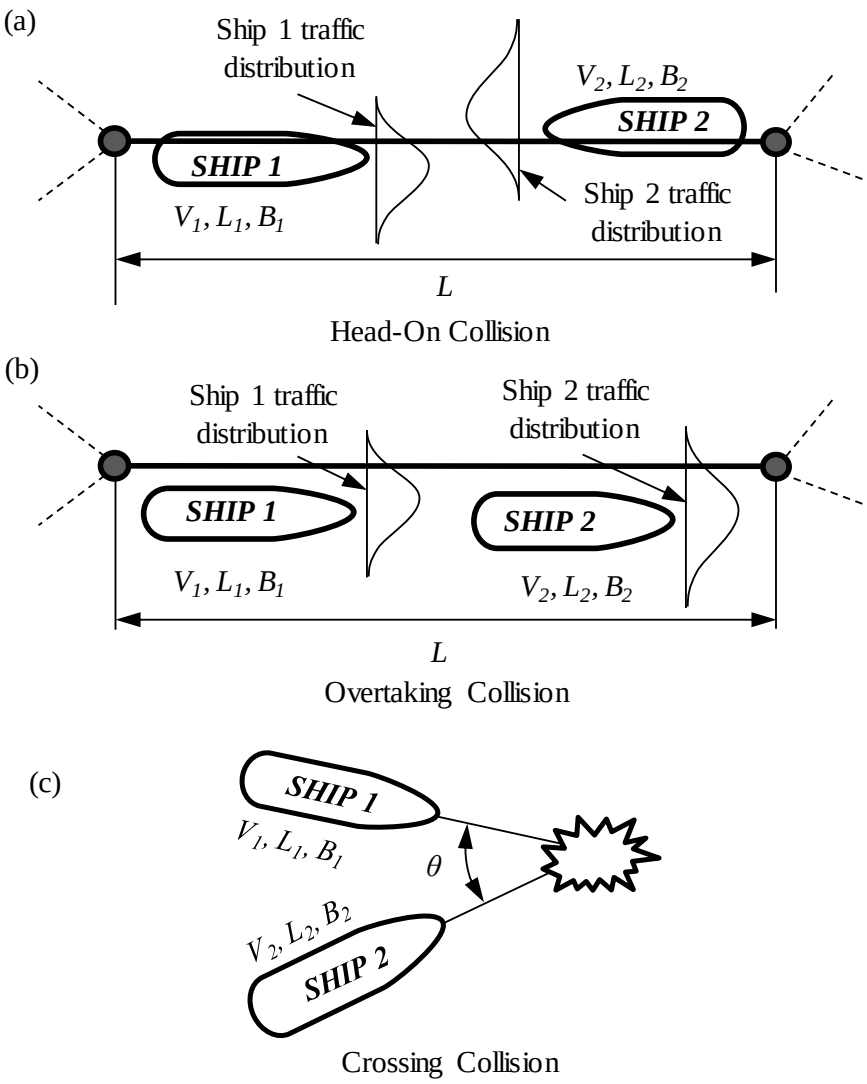

Figure 10.3 Typical waterways for different collision scenarios (adapted from COWI (2008))

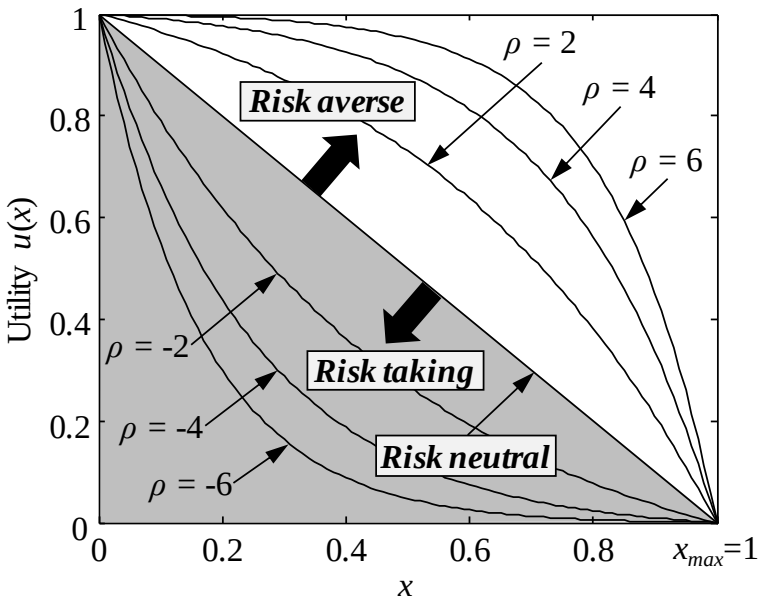

Figure 10.4 Utility functions associated with different risk attitudes

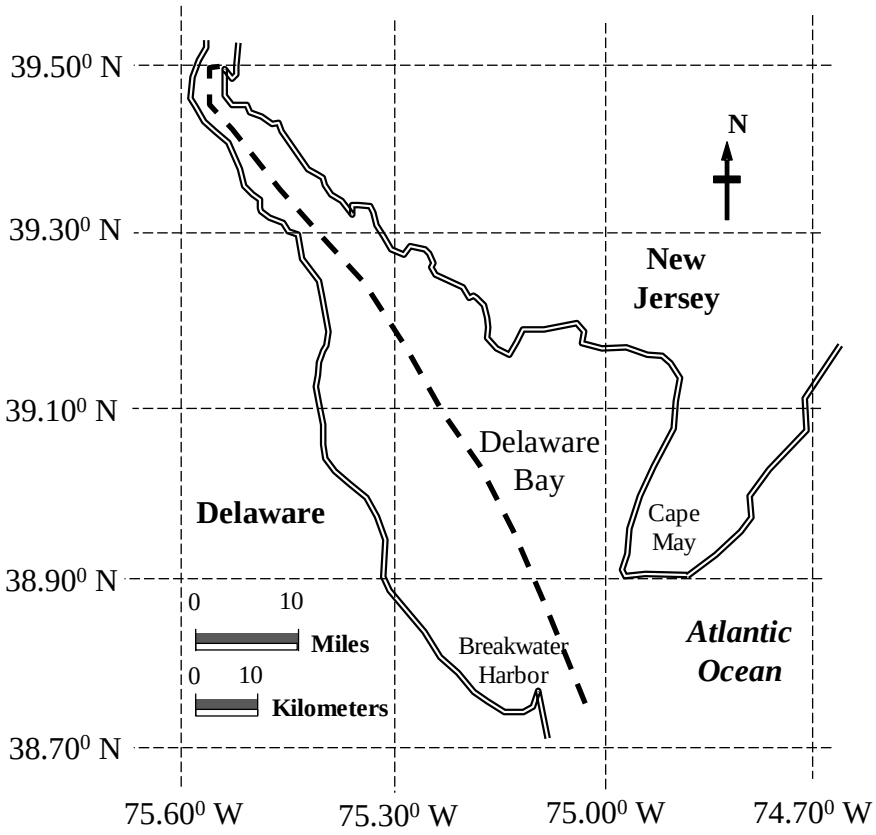

Figure 10.5 Layout of a particular region of Delaware River under investigation (adapted from Google map)

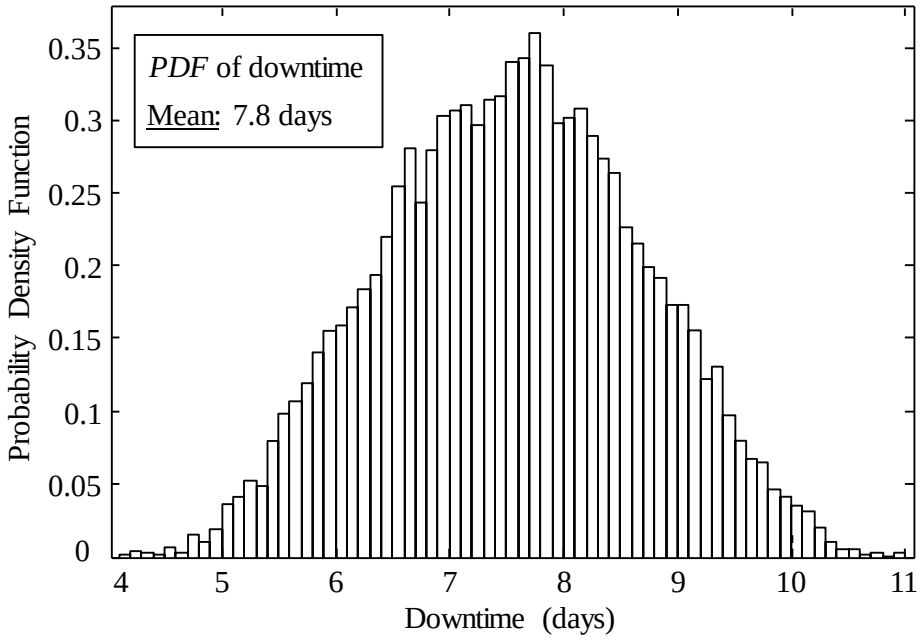

Figure 10.6 Probability density function of the downtime

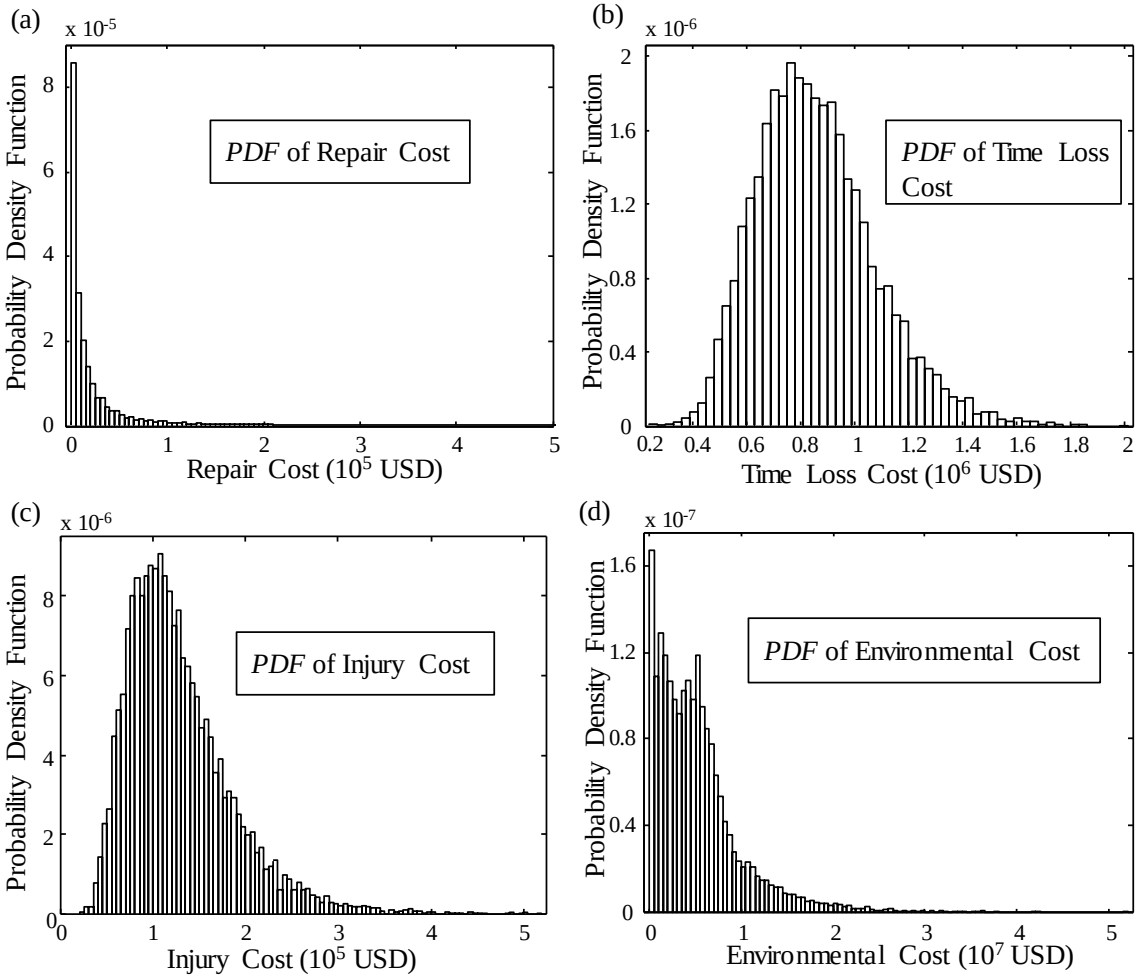

Figure 10.7 Probability density function of the (a) repair cost; (b) time loss cost; (c) injury cost; and (d) environmental cost associated with probabilistic consequences

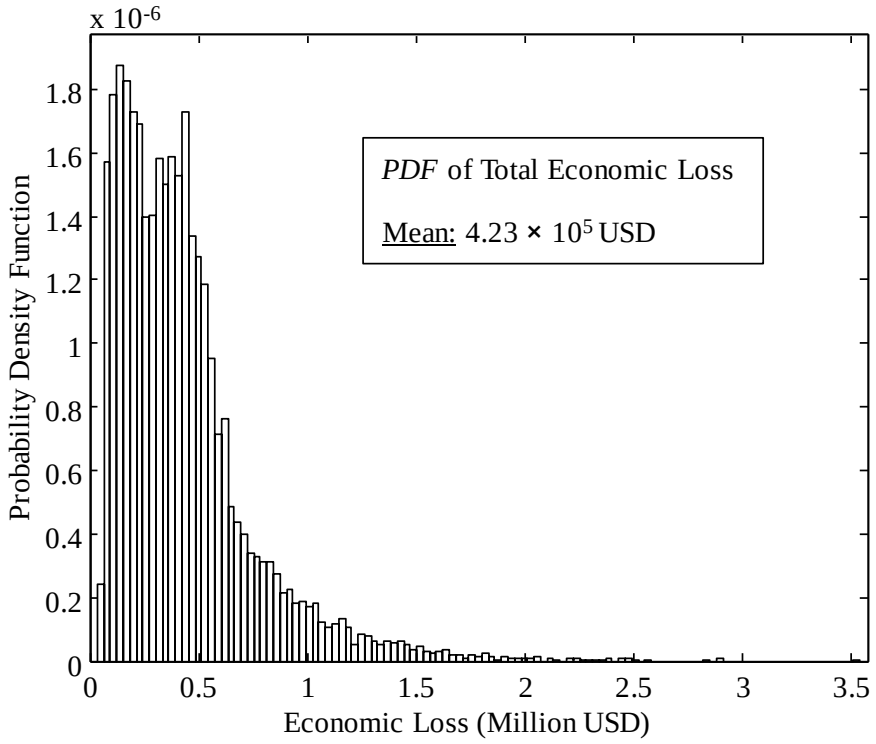

Figure 10.8 Probability density function of the total economic loss

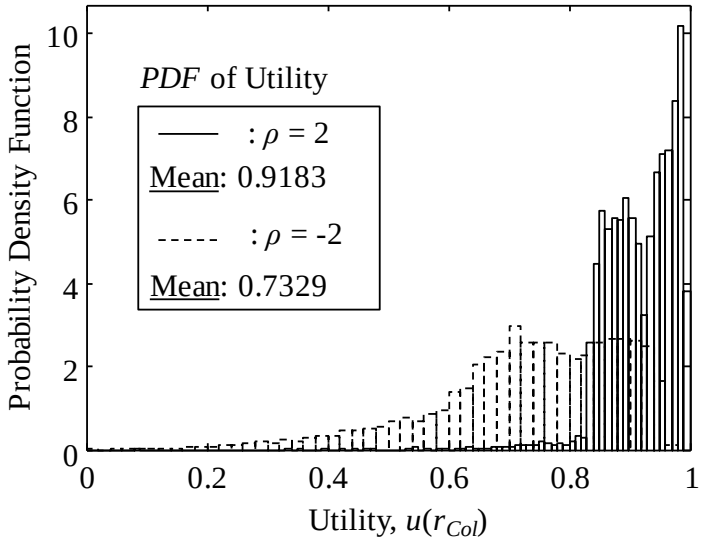

Figure 10.9 Probability density function of the utility considering different risk attitudes

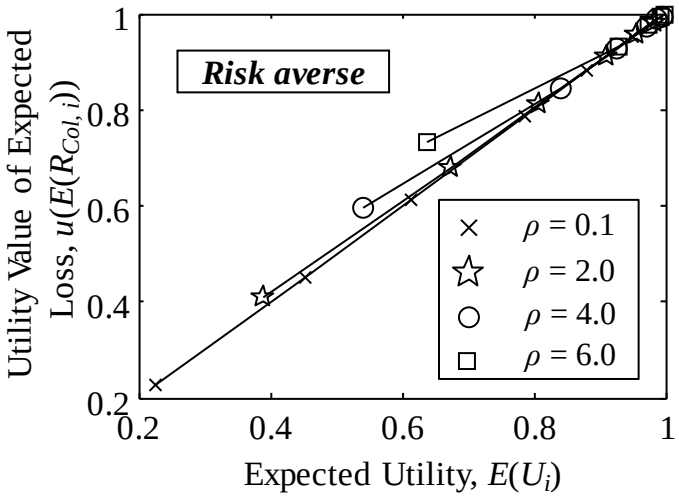

Figure 10.10 Effect of ρ on the utility of the expected loss and the expected utility considering different risk intervals

CHAPTER 11

A DECISION SUPPORT SYSTEM FOR MISSION-BASED SHIP ROUTING CONSIDERING MULTIPLE CRITERIA

11.1. INTRODUCTION

When a ship is deployed on a given mission, the route the vessel traverses is typically a predetermined path with known potential sea conditions (e.g., sea states). Thus, a decision maker must determine, before the mission, which route a ship may take. It is crucial to evaluate the risk associated with marine vessels subjected to inclement weather and sea conditions when developing a decision management system for ship routing. Ship mission routing can be established considering the strength of the hull, accounting for both flexural and fatigue damage. Additionally, a multi-attribute decision making process may be incorporated to form a robust framework for ship routing that accounts for a wide range of consequences (e.g., total travel time and repair loss). The uncertainties associated with the risk evaluation process must also be included within a generalized ship routing decision making framework. During a mission, a ship must always satisfy safety and serviceability requirements. In some cases, marine vessels are forced to follow certain routes while simultaneously handling time and distance constraints; this combination of dire conditions puts ships in danger of accruing damage that may negatively impact society and the surrounding environment. Ultimately, ship mission performance assessment is of vital importance for ship managers since it provides them guidance for the real-time decision making.

Often, marine vessels are used beyond their intended design life and are, therefore, found under-performing in terms of mission reliability. Consequently, it is of the utmost importance to assess the safety of ship structures by employing a holistic management program to ensure their functionality considering both flexural failure and fatigue damage. Ship performance associated with ultimate flexural failure of the hull's mid-ship section is considered as one of the most critical criteria regarding mission safety assessment (Decò *et al.* 2011). Although the reliability of ship structures considering flexural failure has been previously studied (Paik *et al.* 1998; Akpan *et al.* 2002; Ayyub *et al.* 2000; Decò *et al.* 2012; Saydam and Frangopol 2013), fatigue failure has yet to be comprehensively examined in a marine vessel routing context. Moreover, since ship structures are continuously subjected to oscillatory environmental loads, the risk associated with fatigue damage under the loading cases must be carefully considered (Kwon and Frangopol 2012; Guedes Soares *et al.* 2003). The evaluation of fatigue damage associated with a ship's midsection is integral to ship routing performance assessment (Mao *et al.* 2012). Overall, the failure associated with both hull girder collapse and fatigue damage must be considered simultaneously in order to capture the true performance of a marine vessel.

The spectral-based fatigue method is widely used in the fatigue damage evaluation of marine structures. In practice, the fatigue damage analysis of ship structures is often treated as a linear process and assessed using the spectral method (ABS 2010; DNV 2010; IACS 2009). Fatigue damage assessment may be implemented by utilizing a linear model to compute the response of a ship under wave loading (Nguyen *et al.* 2013). The

linear assumption ultimately allows for the solution of the hydrodynamic problem to be represented in the frequency domain. Several previous research efforts have investigated the role of the wave-induced vertical bending moment in the spectral fatigue analysis of marine vessels (Kukkanen and Mikkola 2004; Mao *et al.* 2012; Nguyen *et al.* 2013). Furthermore, the combined effects of both the vertical and horizontal hull girder bending moments were considered in the fatigue damage assessment by Wang (2010) and Xue *et al.* (1994). Additionally, the cumulative fatigue damage associated with a ship structure prior to and during a mission should be considered within the proposed framework. Since existing ship structures already have accumulated some fatigue damage, they may not be able to handle additional damage, especially if they are at late stages within their lifetimes. Accordingly, it is the decision maker's responsibility to determine whether a ship can still embark on a mission considering the cumulative fatigue damage.

The emissions associated with an operating marine vessel are regulated by the International Maritime Organization (IMO); the IMO states that it is essential to restrict the amount of carbon dioxide emissions and other greenhouse gases produced by a ship route (IMO 2008). Since air pollutants are amongst the most common forms of emissions from ship structures and there is a propensity for atmospheric levels of greenhouse gases to increase significantly in the next 20 years, the environmental consequences must be investigated for the ship mission decision making process. Within the proposed multi-attribute risk assessment of marine vessels, the repair loss, fatigue damage, total travel time, and CO_2 emissions are considered as consequences. Since there have been no significant research efforts regarding risk-based, multi-attribute shipping route decision

making, it is necessary to develop sound approaches to effectively assess the risk associated with marine vessels.

The ship routing decision making procedure also greatly depends upon the risk attitude of the decision maker toward the consequences associated with structural performance. Utility theory is incorporated within the decision making framework to account for the attitudes of a decision maker. A utility function that measures the value of a particular alternative to the decision maker is established for each attribute. In order to account for various sets of units corresponding to each type of consequence, Multi-Attribute Utility Theory (MAUT) is employed to convert each attribute (i.e., repair loss, fatigue damage, travel time, and carbon dioxide emissions) to a consistent unit. A balanced combination of various attributes can be determined by employing MAUT (Jiménez *et al.* 2003). By employing utility theory, the decision maker's attitude can be incorporated into the decision making process. Furthermore, attributes with various units can be all converted into a singular utility value that is always bounded by 0 and 1.

Overall, the approach adopted within this chapter focuses on the estimation of ship safety considering flexural and fatigue damage and provides a sound ship routing risk assessment procedure. Additionally, the generalized framework developed herein performs a variety of tasks, including, but not limited to quantifying the flexural and fatigue performance of the ship structure and employing MAUT to evaluate ship mission performance. The attitude of the decision maker is also considered herein using utility theory. The approach is applied to the Joint High-speed Sealift Ship (Devine 2009) in

order to illustrate the capabilities of the proposed methodology. This chapter is based on Dong *et al*. (2016d)

11.2. FRAMEWORK OF MULTI-CRITERIA DECISION MAKING

A flowchart outlining the proposed framework is shown in Figure 11.1. The environmental conditions (e.g., sea states) must be identified in order to determine the loading scenarios. Each sea state is regarded as the general condition of the free surface on a large body of water and may be characterized by certain significant wave heights and frequencies of these waves. The limit state corresponding to flexural failure is incorporated within this approach. Additionally, the uncertainties involved with this limit state are considered within the risk assessment procedure. Risk is defined as the product of adverse consequences and probability of occurrence associated with a given limit state. In order to quantify the risk performance indicator, the probability of failure associated with a given limit state should be determined first by using simulation and/or first/second order reliability analysis. Then, given the specific consequences of structural failure, the risk can be assessed accordingly. Finally, each decision should be made on basis of risk. The spectral-based fatigue damage is also included as a performance criterion regarding ship routing decision making. The next step includes determining the consequences associated with the ship routing process. Furthermore, the attitude of the decision maker is also considered herein; the attitude of the decision maker can significantly affect the results of the consequence evaluation, risk assessment, and, ultimately, decision making regarding ship routing. The consequences under investigation are multiplied by the probabilities of occurrence in order to calculate the risk performance metric. There are

several types of attributes (i.e., repair loss, fatigue damage, travel time, and carbon dioxide emissions) considered within this analysis, all with different units.

11.2.1. Single attribute utility function

A utility function that measures the value of a particular alternative to the decision maker is established for each attribute. Generally, the utility function contains information about the decision maker's attitude toward risk (Keeney and Raiffa 1993; Park 2004). Within the presented methodology, the desirability of each alternative depends on the values of four attributes (i.e., repair loss, cumulative fatigue damage, total travel time, and CO_2 emissions), all of which are measured with different units. Thus, there is a need to establish a consistent range of values that each attribute may take so that all attributes are directly comparable to each other. A utility function that measures the value of a particular alternative to the decision maker must be defined for each attribute. The formulation of the utility function corresponding to each attribute greatly depends on the knowledge and preferential characteristics of the decision maker.

Considering an exponential formulation, the utility associated with a single attribute (e.g., repair loss and total travel time) can be expressed as (Ang and Tang 1984)

$$u(x) = \frac{1}{1-\exp(-\rho)}\left[1-\exp\left(-\rho\frac{x_{max}-x}{x_{max}}\right)\right] \tag{11.1}$$

where x is the attribute value under investigation; ρ indicates the attitude of the decision maker; and x_{max} denotes the maximum value of the attribute. x_{max} is included within this formulation in order to normalize the utility function so that it always takes values between 0 and 1. An illustrative example of a utility function associated with a general loss is shown in Figure 11.2(a). The risk attitude of the decision maker is reflected within

the parameter ρ; a positive value of ρ indicates a risk averse attitude while a negative value indicates a risk taking attitude. Additionally, the absolute value of ρ represents the severity of the risk attitude.

11.2.2. Multi-attribute utility theory

MAUT is commonly used in the field of decision making and allows for the incorporation of multiple criteria into a decision. Decision making regarding mission routing depends on the encountered sea states, ship capacity (e.g., flexural and fatigue strength), and prescribed constraints associated with all attributes. The ideal combination of the different attributes comprising risk can be determined by employing MAUT. The goal of MAUT, within this context, is to transfer these four metrics (i.e., repair loss, fatigue damage accumulation, total travel time, and CO_2 emissions) into one combined value. Once the utility function associated with each attribute is appropriately established, they may be combined into one multi-attribute utility that effectively represents all aspects under investigation. The flowchart regarding MAUT in the context of this chapter is shown in Figure 11.2(b). Considering an additive formulation, the multi-attribute utility function utilized within the presented decision making framework can be computed as (Jiménez *et al.* 2003)

$$u(x_1, x_2, x_3, x_4) = k_1 u_1(x_1) + k_2 u_2(x_2) + k_3 u_3(x_3) + k_4 u_4(x_4) \tag{11.2}$$

where $u(x_1, x_2, x_3, x_4)$ is the multi-attribute utility function and k_i is the weighting factor corresponding to the ith attribute. The weighting factor associated with each attribute is calculated considering information obtained from the decision maker. The alternative that provides the highest multi-attribute utility value is the preferred solution. Overall, the

consequences considered in this chapter may be evaluated based on professional judgment and existing information while utility theory can be used to quantify the decision maker's preference.

11.3. SHIP PERFORMANCE ASSOCIATED WITH FLEXURAL FAILURE AND FATIGUE DAMAGE

11.3.1. Load effects

The effects induced by the sea on the hull are due to two separate events: still water and waves. Safety evaluation of ship structures operating in different sea conditions requires an accurate estimation of the load effects due to still water and waves (Guedes Soares 1992). As recognized by previous study (Guedes Soares and Teixeira 2000), the primary load effects within the hull are the sagging and hogging vertical bending moments (VBMs). According to the International Association of Classification Societies (IACS 2008), the VBMs $M_{sw,sag}$ and $M_{sw,hog}$ (associated with sagging and hogging, respectively) for a specific ship cross-section (*CS*) under still water can be expressed as

$$M_{sw,sag} = 0.05185 f_{sw,CS} C_{wv} L^2 B(C_b + 0.7) \tag{11.3}$$

$$M_{sw,hog} = 0.01 f_{sw,CS} C_{wv} L^2 B(11.97 - 1.9C_b) \tag{11.4}$$

where $f_{sw,CS}$ is a factor accounting for the variation of VBMs along the vessel length (equal to 1.0 at mid-ship); C_b is the ship block coefficient; L is the ship length (m); B is the ship breadth (m); and C_{wv} is the wave coefficient. The VBM associated with still water is assumed to follow the normal distribution with a mean and standard deviation

equal to 70% and 20% of the maximum still water bending moment, respectively (Hørte *et al.* 2007; Hussein and Guedes Soares and 2009).

The load effects on ship structures associated with waves are related to many factors, including ship geometry, heading angle, speed, and encountered sea state. The linear response theory is commonly employed to compute structural performance of marine vessels (Salvesen *et al.* 1970; Hughes 1983); a widely used approach for ship performance evaluation based on linear response theory is the strip method (Fonseca and Guedes Soares 1998). The relationship between input and output, which is described by a spectral density function, may be established from the results of applying the strip method. In addition to the strip method, other methods have been established to account for the non-linear effects (Jensen and Pedersen 1978; Guedes Soares and Schellin 1988).

The main goal of the load assessment procedure is to obtain response amplitude operators (RAOs) corresponding to a particular cross-section of a marine vessel. The RAOs can be determined by converting the time domain response of a ship to the frequency domain. Based on the RAOs, a ship's response to a particular sea state can be computed. Using the linear superposition theory, a ship's response in a given sea state can be obtained. RAOs are calculated as a vessel's response considering excitation waves with unitary amplitude. The response spectrum can be computed as (Hughes 1983)

$$S_Y(\omega) = \left|RAO(\omega)\right|^2 S_X(\omega) \tag{11.5}$$

where $S_Y(\omega)$ and $S_X(\omega)$ are the spectral density functions of the output and input, respectively and ω is the circular frequency of excitation waves (rad/s).

The spectrum for a fully developed sea may be computed using the guidelines established by the International Ship and Offshore Structures Congress (ISSC). A modified version of the Pierson-Moskowitz sea spectrum is used to formulate the following expression describing the sea spectrum (Faltinsen 1990)

$$S_{\omega}(\omega) = \frac{0.11 H_s{}^2 T_1}{2\pi} \left(\frac{\omega T_1}{2\pi}\right)^{-5} \exp\left[-0.44\left(\frac{\omega T_1}{2\pi}\right)^{-4}\right] \tag{11.6}$$

where $S_{\omega}(\omega)$ is the sea spectrum for a given sea state; T_1 is the wave mean period (s); and H_s is the significant wave height corresponding to the mean of the one third highest waves (m). The values of the mean period and significant height associated with excitation waves depend upon the intensity of the sea states encountered. For a particular operational condition, the wave spectrum is usually expressed in terms of the encountered frequency ω_e, instead of the circular frequency ω, accounting for a ship's speed and heading angle. The encountered wave frequency ω_e is defined as follows (ABS 2010)

$$\omega_e = \left|\omega - U\frac{\omega^2}{g}\cos\theta\right| \tag{11.7}$$

where g is gravitational acceleration (m/s^2); U is the forward ship speed (m/s); and θ is the heading angle (e.g., 0º, 90º, 180º for following, beam, and head seas, respectively). Although the Pierson-Moskowitz sea spectrum is utilized herein for load analyses, other sea spectrums (e.g., JONSWAP) could also be used.

For the spectral-based fatigue analysis, a linear model assumption of loading is generally adequate and the non-linear effects can be neglected (Nguyen *et al.* 2013). FREE!ship (2006), an open source surface-modeling program based on subdivision surfaces, can be used to model a ship's body and estimate its hydrodynamic parameters.

Based on the given sea spectrum, load descriptors due to wave effects are evaluated using a developed MATLAB (MathWorks 2013) code linked with PDSTRIP (2006), a program that performs strip analysis. As an example, a qualitative representation of the VBM RAOs associated with a ship's cross section considering certain operational cases is shown in Figure 11.3. The vertical bending stress $RAO_{\sigma,ver}$ at the structural component associated with a particular cross section is given as (Rasmus 1998)

$$RAO_{\sigma,ver} = \frac{z - z_0}{I_{yy}} RAO_{M,ver} \tag{11.8}$$

where z is the vertical distance from the structural detail to the baseline (m); z_0 is the vertical distance from the neutral axis to the baseline (m); and I_{yy} is the moment of inertia with respect to the horizontal axis of the section (m^4).

The evaluation of probabilistic hull strength with respect to ultimate flexural failure can be carried out utilizing a classical incremental curvature method (IACS 2008). In order to significantly reduce the total computational time, Okasha and Frangopol (2010) developed an optimization-based approach that yields results that are as accurate as those obtained from the incremental curvature method. The safety evaluation of ship structures operating in different sea and cargo conditions requires a probabilistic estimation of various parameters. The uncertainties associated with vessel dimensions, material properties, and applied loads should be treated as random variables (Decò *et al.* 2012). Furthermore, the load effects due to still water and waves must be probabilistically simulated to account for uncertainties in the loading conditions (Guedes Soares 1992).

Based on the short-term statistics and the assumption that the instantaneous value of ocean elevation follows a Gaussian distribution (Faltinsen 1990), the probability density

function (PDF) of the peak response under given operational conditions can be estimated using a Rayleigh distribution as follows (Guedes Soares and Moan 1991)

$$f(M_w) = \frac{M_w}{m_{o,M}} \exp(-\frac{M_w^{\ 2}}{2m_{o,M}}) \tag{11.9}$$

where M_w is the wave-induced VBM response and $m_{0,M}$ is the zeroth moment of the VBM response spectrum. Accordingly, the mean μ_M and standard deviation σ_M associated with the random variable M_w can be obtained as

$$\mu_M = \sqrt{\frac{\pi \cdot m_{o,M}}{2}} \tag{11.10}$$

$$\sigma_M = \sqrt{\frac{(4-\pi) \cdot m_{o,M}}{2}} \tag{11.11}$$

The zeroth moment of the wave spectrum regarding the VBM spectrum can be computed as

$$m_{0,M} = \int_0^\infty \omega_e^{\ 0} S_W(w_e) dw_e \tag{11.12}$$

Furthermore, the response spectrum for the wave-induced VBMs is

$$S_M(w_e) = \left|H_M(w_e|U,\theta)\right|^2 S_w(w_e) \tag{11.13}$$

where $H_M(w_e|U, \theta)$ is the RAO for the VBMs under given ship speed U and heading angle θ.

11.3.2. Reliability analysis associated with flexural failure

The first step within the reliability analysis involves determining the probability of flexural failure based on the ultimate failure limit state. Considering modeling uncertainties associated with resistance and load effects, the limit state equation for the

ultimate failure of a particular ship cross section can be expressed as (Paik and Frieze 2001)

$$x_R M_{UR} - x_{SW} M_{SW} - x_W M_W = 0 \tag{11.14}$$

where M_{UR} is the resisting bending moment associated with ultimate failure; M_{SW} is the still water bending moment; M_W is the wave-induced bending moment; x_{SW} and x_W are the model uncertainties associated with still water and wave-induced bending moment prediction, respectively; and x_R is the model uncertainty associated with hull resistance determination. The geometric parameters and material properties, such as plating thickness, elastic modulus, plating yielding stress, and stiffener yielding stress, are treated as random variables. Additionally, the model uncertainty is considered by using coefficients x_R, x_{SW}, and x_W, which are assumed normally distributed with mean values of 1.0, 1.0, and 0.9, respectively, and coefficients of variation equal to 0.10, 0.05, and 0.15, respectively (Paik and Frieze 2001). The probability of failure p_f corresponding to the flexural limit state may be obtained using simulation techniques. The reliability index β is

$$\beta = \Phi^{-1}(1 - p_f) \tag{11.15}$$

where Φ^{-1} denotes the inverse standard normal cumulative distribution function.

11.3.3. Spectral-based fatigue damage assessment

In order to avoid structural failure and adverse consequences, it is essential to assess and predict the fatigue performance and safety of marine vessels. A ship may be subjected to a variety of load effects, including vertical and horizontal bending moments, in addition to torsional moments. Typically, wave-induced loads are the main source of fatigue damage to ship structures. In this chapter, the vertical bending moments induced from

encountered waves are emphasized for the fatigue assessment. The linear model assumption is generally adequate for fatigue analysis of marine vessels (Guedes 1993; Nguyen *et al.* 2013).

Within the context of this chapter, the spectral-based fatigue analysis involves a method for the direct calculation of fatigue damage (Bai 2003; Wang 2010). The whole history of stress associated with the ship's operating condition is considered in the cumulative fatigue damage assessment. Based on the spectral approach, the Rayleigh PDF associated with the short-term stress range distribution, zero-up crossing frequency, and spectral bandwidth parameters for the wide band random process can be obtained (Siddiqui and Ahmad 2001). Additionally, considering the short-term stress range distribution, the fatigue damage accumulation associated with a structural detail with a linear S-N curve in a specific sea state can be expressed as (ABS 2010)

$$D_i = \frac{T}{A}(2\sqrt{2})^m \Gamma(1+\frac{m}{2})\lambda(m,\nu_i) f_{oi} p_i (\sigma_i)^m \tag{11.16}$$

where T represents the service time of a ship structure; A is fatigue strength coefficient; m is the fatigue strength exponent; λ is the cycle counting correction factor; f_{oi} is the zero-up crossing frequency of the stress response; p_i is the probability of occurrence of sea state i; σ_i is the standard deviation of the stress process associated with sea state i; ν_i is spectral width parameter; and Γ is the gamma function.

The standard deviation σ and zero crossing frequency f_0 associated with the stress response can be expressed as

$$\sigma = \sqrt{m_0} \tag{11.17}$$

$$f_0 = \frac{1}{2\pi}\sqrt{\frac{m_2}{m_0}} \tag{11.18}$$

where m_o and m_2 are the spectral moments of the stress process. Accordingly, these two parameters are (ABS 2010)

$$m_n = \int_0^\infty w_e{}^n S_\sigma(w_e) dw_e \tag{11.19}$$

$$S_\sigma(w_e) = \left|H_\sigma(w_e|\theta,U)\right|^2 S_W(w_e) \tag{11.20}$$

where H_σ $(w_e|\theta,H)$ is the stress transfer function obtained by the linear hydrodynamic analysis.

The total fatigue damage of a structural detail is computed by summing the fatigue damage over all the k possible sea states. The closed form expression of the total fatigue damage can be computed as (ABS 2010)

$$D = \frac{T}{A}(2\sqrt{2})^m \Gamma(1+\frac{m}{2})\sum_{i=1}^{k}\lambda(m,\nu_i) f_{0i}\, p_i(\sigma_i)^m \tag{11.21}$$

11.4. MULTI-ATTRIBUTE RISK ASSESSMENT

11.4.1. Repair loss associated with flexural failure

The first attribute investigated in detail is the repair loss which describes the direct monetary loss associated with structural failure. In order to calculate the economic risk, the construction cost of a ship must be computed considering its preliminary design and work breakdown system (Decò and Frangopol 2013). The costs associated with the ship work breakdown system (SWBS) are subdivided into several categories, including propulsion, structural, and electrical systems. The construction cost C_{Cons} is the sum of all

the labor and material costs involved in the construction process and is computed as follows (Miroyannis 2006)

$$C_{Cons} = 5747.19 \times STF \times DISP^{-0.3792} \times WGT_{100}{}^{0.862} + 800 \times WGT_{100} \qquad (11.22)$$

where WGT_{100} is the weight of SWBS 100 (long tons); STF is the ship type factor; and $DISP$ is the ship full load displacement (long tons).

In this chapter, the repair loss is associated with the ultimate flexural failure; the probabilities of ultimate flexural failure under different sea states are first calculated and then the repair loss is computed by multiplying these probabilities by the associated repair costs and summing over all sea state and operational conditions. The repair loss of a ship structure considering the contribution of all sea states and ship operational cases can be computed as

$$RL = \sum_{SS} \sum_{U,\theta} P(SS) \cdot P(U, \theta | SS) \cdot P(f | SS, U, \theta) \cdot C_{Cons} \qquad (11.23)$$

where $P(SS)$ is the probability of occurrence of sea state (SS) during a ship route; $P(U, \theta|SS)$ is the probability of ship operation cases (i.e., speed U and heading angle θ) given the sea state; $P(f|SS, U, \theta)$ is the conditional probability of ship section failure given the occurrence of a specific set of SS, U, and θ.

11.4.2. Fatigue damage accumulation

In order to ensure structural safety, when conducting a fatigue analysis on a marine vessel, it is necessary to identify fatigue-critical structural details (e.g., the connections of the deck longitudinal to transverse web) associated with stress analysis under wave-induced loading. In this chapter, the spectral-based fatigue damage method is employed. For a given ship mission process, the fatigue damage associated with specific sea state

conditions can be computed by considering the total time a ship encounters the prescribed sea states (Mao *et al.* 2012). The total fatigue damage associated with a ship detail is computed by summing the fatigue damage over all encountered sea states. The closed form expression corresponding to the total fatigue damage can be computed using Eq. (21). Within this formulation, the total fatigue damage is calculated using strip theory considering the total time of travel, ship speed, wave spectrum, and scatter diagrams (ABS 2010).

11.4.3. Total travel time

The third attribute considered in the risk analysis is the total travel time associated with a ship mission. The ship route planning relies on decision making tools that estimate the time of arrival for a ship mission. The expected speed loss experienced by a ship structure during a route is influenced by the significant wave height of the surrounding water and heading angle of the ship. Determining a ship's operational speed within different sea states is of vital importance for the economic and environmental risk assessment. Ultimately, severe sea states yield relatively high reductions of ship speed (Prpić-Oršić and Faltinsen 2012). The percentage of time spent in each possible sea state may be estimated based on the fraction of the route distance corresponding to each possible sea state (Mansour and Preston 1994). The total travel time required for a ship to complete a particular route may be considered as a social impact of ship routing. The total travel time is computed as

$$TT = \sum_{SS} \sum_{U,\theta} P(SS) \cdot P(U,\theta|SS) \cdot \frac{l}{U(SS)} \tag{11.24}$$

where U is the speed of the ship at a given sea state and l is the length of the route.

11.4.4. Carbon dioxide emissions

The fourth and final attribute is the total carbon dioxide emissions produced during a ship mission. The speed of a ship is dynamic and may change based on current sea state conditions. In general, the speed loss associated with each possible sea state is related to the greenhouse gas emissions produced by a ship. Severe sea states can yield a large increase in CO_2 emissions (Prpić-Oršić and Faltinsen 2012). Consequently, the CO_2 emissions of a ship operating in different sea states and operational conditions must be considered when calculating the environmental attribute within the proposed multi-attribute risk assessment procedure. The carbon dioxide emissions can be expressed as (Prpić-Oršić and Faltinsen 2012)

$$CDE = \sum_{SS} \sum_{U,\theta} P(SS) \cdot P(U,\theta | SS) \cdot l \cdot cde(U) \tag{11.25}$$

where *cde* is the carbon dioxide emission per unit distance (i.e., kg/km) for a ship structure associated with specific sea states and ship operational conditions.

11.5. ILLUSTRATIVE EXAMPLE

The proposed approach is applied to the Joint High-Speed Sealift (JHSS) (Devine 2009) to illustrate ship routing decision making using MAUT. This particular marine vessel measures 290 m in length, 22.3 m in height, and 32 m in breadth. The block coefficient is taken as 0.4835. The ship's body and a representative transverse cross-section at mid-ship are shown in Figure 11.4(a) and (b), respectively. The ship performance under different operational and sea states is depicted using a polar representation, which presents the ship's response as a function of wave direction under given conditions. The sea

conditions adopted in Decò and Frangopol (2013) are utilized herein; a stationary storm system that yields severe sea states is considered to occur at a location along the straight-line path between the origin and destination points. The straight-line route that takes the ship directly through the storm is considered as Route 3. The possible shipping courses considered in this chapter are Routes 1, 2, and 3 (see Figure 11.4(c)). Route 1 is associated with the longest travel time and largest CO_2 emissions; it is considered to be the safest shipping course. Conversely, Route 3 is regarded as the most dangerous route, but results in the lowest travel time and CO_2 emissions. Route 2 may be considered as another alternative. Additionally, the effects of the decision maker's risk attitude (i.e., ρ in Eq. (11.1)) and the weighting factors (i.e., k_1, k_2, k_3, and k_4 in Eq. (11.2)) on the multi-attribute utility value corresponding to each route are investigated.

11.5.1. Performance of ultimate flexural failure and fatigue

The load effects associated with still water and wave loads in terms of the VBMs corresponding to sagging and hogging are investigated herein. The optimization-based method is adopted herein to compute the probabilistic hull strength. The elastic modulus E, the yielding stresses of plating and stiffener s_{Yp} and s_{Ys}, respectively, and the plating thickness t_p are considered to be lognormal random variables with the coefficients of variation of 0.03, 0.1, 0.1, and 0.05, respectively (Decò *et al.* 2011). The mean values of the variates E, s_{Yp}, and s_{Ys} are assumed to be 2.1×10^5, 351.6, and 351.6 MPa, respectively (Decò *et al.* 2011). Additionally, the model uncertainty is considered by using the coefficients x_R, x_{SW}, and x_W, which are assumed normally distributed with mean values of 1.0, 1.0, and 0.9, respectively, and the coefficients of variation equal to 0.10,

0.05, and 0.15, respectively (Paik and Frieze 2011). Within this chapter, Latin-Hypercube sampling techniques are utilized with 5,000 samples to compute the moment capacity of the mid-section of the JHSS under wave loading in a probabilistic manner. The generated samples of flexural capacities are fitted to a lognormal distribution with mean values equal to 99.83×10^8 Nm and 95.05×10^8 Nm for hogging and sagging, respectively. The COV corresponding to the hogging and sagging bending moment capacity are 8.9% and 8.3%, respectively. Furthermore, the bending moment associated with still water can be computed using Eq. (11.3) and (11.4). The expected value for the hogging and sagging under still water conditions are 20.1×10^8 Nm and 11.15×10^8 Nm, respectively. The RAO curves are formulated considering the VBM load effects under given operational conditions. Additionally, the Pierson-Moskowitz spectrum is applied in this chapter to describe irregular wave patterns. Heading angles between 0º (following sea) and 180º (head sea), in increments of 15º, are accounted for within the RAO curves. Using PDSTRIP, the linear response of the ship structure under regular wave loading is obtained. Due to the implementation of linear theory, the resulting bending moments are the same for both sagging and hogging (Hughes 1983; Lua and Hess 2006). More detailed information regarding the VBM evaluation using linear strip theory can be found in Decò *et al.* (2012). Within this chapter, the mean and standard deviation of the JHSS's VBM response distribution are computed using Eqs. (11.10) and (11.11).

The reliability index associated with sagging and hogging for the mid-ship section is determined given the sea state, ship speed, and heading as shown in Eq. (11.14). The reliability analysis is performed using the computer program RELSYS (Estes and

Frangopol 1998), based on the First-Order Reliability Method (FORM). The intensity of the sea may be expressed in terms of significant wave height. Within the illustrative example, the intensity of the sea in terms of significant wave height ranges from 1.07 and 7.10 m. Given the weather conditions outlined in Decò and Frangopol (2013), it is determined that sea states 4, 5, 6, and 7 may be used to represent the possible sea conditions. The significant wave height, period, and length associated with each sea state are shown in Table 11.1. Herein, the ocean conditions are based on a hypothetical sea map. With new measurement techniques and if more data associated with wind and waves becomes available, the uncertainties related to ocean condition could be well developed and incorporated within the decision making process. Overall, sea state 7 yields relatively low reliability, which indicates poor operational conditions for each considered heading angle. Figure 11.5 shows the reliability index associated with the load effects under still water and waves. It is evident from this figure that as the ship's speed increases, the VBM typically increases considering head sea, whereas for following sea, relatively larger VBM responses are obtained for lower speeds. The lowest reliability index with respect to heading angle is obtained when the heading angle equals to 180º. Furthermore, the reliability index associated with sagging is overall larger than the reliability index calculated with respect to hogging.

A spectral-based method is used in this chapter for the fatigue damage assessment of the JHSS. The structural detail considered within the fatigue analysis is a connection that joins the main deck longitudinally to a transverse web at the mid-ship section. The linear model assumption is adopted herein since the nonlinear effects are considered negligible.

In this chapter the wave-induced VBMs are considered as the main source of fatigue damage. For illustrative purposes, the cumulative service time under investigation (T in Eq. (11.16)) is taken as 20 years and the fraction of time that this vessel is out at sea is assumed to be 85%. The RAOs associated with the VBM stress at a fatigue-critical structural component are obtained considering given operational cases by using Eq. (11.8). The probabilities of encountering certain sea states during a ship's service life are obtained from a wave scatter diagram associated with unrestricted service classification provided by the ABS (2010). Considering these wave scatter diagrams, the annual largest significant wave height investigated within this illustrative example is assumed to be 3.5 m for the fatigue damage accumulation of the JHSS during its service time. Additionally, the average service speed of the JHSS is assumed to be 15 m/s for calm seas. Based on Prpić-Oršić and Faltinsen (2012), the ship's speed as a function of significant wave height is shown in Figure 11.6. As indicated, there is a significant reduction of the ship's speed in severe sea states. The fatigue damage accumulation for the structural component is computed using Eq. (11.21); the correction factor to account for the wide band process is considered in this equation. The linear S-N approach is also applied in this chapter, with curve slope parameters defined as $m = 3$ and $A = 4.31 \times 10^{11}$. Note that the fatigue damage accumulation associated with ship structures increases with time if no repair or maintenance actions are applied. The fatigue damage accumulated by the JHSS's fatigue critical component is 0.6238 after the assumed 20 year service time.

11.5.2. Risk assessment considering multiple performance criteria

The consequences associated with a ship's mission are outlined within this section; impacts to the surrounding social setting, environment, and economy are accounted for in the presented approach. The first step within the attribute evaluation procedure is to calculate the direct monetary loss corresponding to ship routing. This attribute, measured in monetary terms, is computed utilizing Eq. (11.23) for Routes 1, 2, and 3. The ship type *STF* and WGT_{100} associated with the JHSS regarding its construction costs are 7 and 10,300, respectively (Decò and Frangopol 2013). The second detrimental attribute included within this risk analysis is the fatigue damage accrued by a marine vessel. The fatigue damage is represented by the fatigue damage accumulation calculated using Eq. (11.21). In this illustrative example, the fatigue damage prior to the mission is significantly larger than that during the ship mission process. Overall, the fatigue damage is highly dependent upon sea and ship operational states.

The third attribute considered within this analysis is the travel time experienced by a ship. The total travel time is considered as a social impact herein and is calculated using Eq. (11.24). The factors that affect this social risk metric include the sea conditions and vessel velocity. The fourth and final consequence examined in detail within this chapter is the total amount of carbon dioxide emissions associated with a specific route. Environmental impacts of a marine vessel's mission may be represented by the greenhouse gas emissions associated with a specific route in addition to ship speed and heading angle. The carbon dioxide emissions associated with ship routing is calculated with Eq. (11.25). The expected CO_2 emissions from the JHSS are assumed to be 355

kg/km considering calm sea conditions (Prpić-Oršić and Faltinsen 2012). Additionally, significant wave heights are associated with specific reductions of ship speed as shown in Figure 11.6. The mean values of the risk metrics calculated with Eqs. (11.21) and (11.23) - (11.25) are then utilized as attribute values within the single attribute utility assignment. For instance, as indicated in Table 11.2, the expected value of the repair loss and total travel time corresponding to Route 1 are 2.0385×10^5 USD and 9.7841×10^4 seconds, respectively. The expected repair losses associated with Route 2 and 3 are 3.1595×10^5 and 4.1754×10^5 USD, respectively.

11.5.3. Decision making using multi-attribute utility theory

MAUT is utilized within the route decision making framework presented herein. The expected values of the attributes (i.e., repair loss, fatigue damage, travel delay, and carbon dioxide emissions), all of which are represented in different units, are transferred to a uniform scale ranging from 0 to 1 by employing separate single attribute utility functions. The utility assignment for each attribute is facilitated by Eq. (11.1) with varying x_{max} values as outlined in Table 11.3. This formulation for single-attribute utility accounts for the risk attitude of the decision maker. Figure 11.7 depicts the utility values associated with the expected values of each attribute considering two different risk averse attitudes (ρ = 2 and ρ = 4). The effect of the decision maker's risk attitude on the utility function associated each attribute of risk is investigated herein. Figure 11.7 shows the resulting utility functions corresponding to each attribute considering two different risk taking attitudes (ρ = -2 and ρ = -4). Comparing Figure 11.7 and Figure 11.8 reveals that utility functions associated with attributes follow the general trends shown in Figure 11.2

(a); a concave utility function corresponds to a risk averse attitude, while a convex utility function indicates a risk taking attitude.

Once the single attribute utility functions are formulated, the marginal utility values are then combined into one multi-attribute utility value utilizing Eq. (11.2). Note that subscripts 1, 2, 3, and 4 on u and k in Eq. (11.2) correspond to the repair loss, cumulative fatigue damage, total travel time, and carbon dioxide emissions, respectively. For Route 1, the multi-attribute utility values associated with a risk averse decision maker are shown in Table 11.2 considering weighting factors (k_1, k_2, k_3, k_4) = (0.25, 0.25, 0.25, 0.25). This combination of weighting factors indicates equal contributions of all four attributes within the multi-attribute utility assessment.

In order to determine which route the ship should take, the multi-attribute utility values associated with Routes 1, 2, and 3 must be compared; the Route that corresponds to the largest multi-attribute utility value is the one that should be chosen. Table 11.4 shows the result of applying the proposed methodology to all three Routes considering different risk attitudes and weighting factor combinations. Within Table 11.4, each column represents a decision maker that has a certain risk attitude ρ and assigns particular weighting factors to the consequences investigated (e.g., k_1, k_2, k_3, k_4). Additionally, within each column, the largest multi-attribute utility value is bolded; this value corresponds to the best route for the ship. For instance, considering a risk taking attitude with weighting factors (0.3, 0.3, 0.2, 0.2), the decision maker will always choose Route 1 since it corresponds to the largest utility value. However, if the same risk taking decision maker weighs the consequences slightly differently with weighting factors equal to (0.2,

0.2, 0.3, 0.3), then Route 3 is determined as the best shipping route. Furthermore, a risk averse decision maker with attribute weighting (0.2, 0.2, 0.3, 0.3) will always choose Route 1.

As an extension of the results obtained in Table 11.4, Figure 11.9 depicts the effects of the severity of the decision maker's risk averse attitude on the ship routing. This figure presents the multi-attribute utility value as a function of the decision maker's risk averse attitude ρ. Figure 11.9(a) considers a risk averse decision maker with consequences weighting (0.2, 0.2, 0.3, 0.3). As evidenced by Figure 11.9(a), as a decision maker becomes more risk averse (increasing values of ρ), the multi-attribute utility value corresponding to each Route increases. Additionally, the difference between the multi-attribute utility values corresponding to Route 1 and Route 3 increases as the decision maker becomes more risk averse. For the scenario presented in Figure 11.9(a), Route 1 is always chosen as the best route. When the consequence weighting is changed to (0.1, 0.1, 0.4, 0.4), the effect on the resulting multi-attribute utility values associated with Routes 1 and 3, is investigated in Figure 11.9(b). For this combination of consequence contributions, a decision maker with a risk averse attitude characterized by $0 < \rho \leq 4$ will choose Route 3, while a decision maker with a more severe risk averse attitude (i.e., $\rho >$ 4) will choose Route 1 as the best shipping course. Overall, the decision maker's risk attitude and the weighting factors involved in the multi-attribute utility assessment have great effects on the final ship route decision.

11.6. CONCLUSIONS

This chapter presents an efficient approach for ship routing decision support by using MAUT. The strip theory is used for the assessment of the RAOs associated with VBMs and stresses at the mid-ship cross section. The repair loss, fatigue damage accumulation, total travel time, and CO_2 emissions are considered as performance criteria for ship routing decision making.

The following conclusions are obtained:

1. Ship structures are sometimes forced to follow certain routes with severe sea states while simultaneously handling time and distance constraints; this combination of dire conditions puts ships in danger of accruing damage that may negatively impact society and the surrounding environment. Ultimately, ship mission performance assessment is of vital importance for ship managers since it provides them guidance for the decision making of marine vessels under uncertainty.
2. The consequences associated with structural damage may be represented by the four attributes considered herein. MAUT is utilized to combine all single-attribute utilities into a uniform metric that reflects the overall utility associated with a specific ship route. Overall, the consequences of decision making regarding ship routing may be evaluated based on professional judgment and existing information while utility theory can be employed to quantify the decision maker's preference.
3. Both the attitude of the decision maker and weighting factors employed in the multi-attribute utility assessment have significant effects on the multi-attribute utility value obtained for a route. The proposed methodology may be used to assist

decision making regarding traffic control and risk mitigation activities, and to ultimately improve the traffic safety of maritime transportation.

Table 11.1 Statistical information corresponding to sea states (based on information from Resolute Weather 2014)

Sea state	Significant wave height (m)	Average wave period (s)	Average wave length (m)
4	1.83	5	24.08
5	2.44	5.5	32
6	4.27	7.5	56.09
7	7.62	10	100.13

Table 11.2 Multi-attribute utility values associated with Route 1, 2, and 3 considering equal weighting factors (0.25, 0.25, 0.25, 0.25) under different risk attitudes

Alternative	Attribute	Expected value	$\rho = 2$		$\rho = -2$	
			Single attribute utility	$u(x_1, x_2, x_3, x_4)$	Single attribute utility	$u(x_1, x_2, x_3, x_4)$
Route 1	A_1 (10^5 USD)	2.0385	0.8028	0.7134	0.3552	0.2604
	A_2	0.6238	0.6116		0.1757	
	A_3 (10^4 second)	9.7841	0.7401		0.2782	
	A_4 (10^5 kg)	5.4058	0.6951		0.2358	
Route 2	A_1 (10^5 USD)	3.1595	0.6026	0.6961	0.1703	0.2470
	A_2	0.6238	0.6238		0.7570	
	A_3 (10^4 second)	8.8277	0.7781		0.3219	
	A_4 (10^5 kg)	4.9793	0.7328		0.2707	
Route 3	A_1 (10^5 USD)	4.1754	0.3249	0.6724	0.0612	0.2666
	A_2	0.6238	0.6116		0.1757	
	A_3 (10^4 second)	7.4117	0.8281		0.3946	
	A_4 (10^5 kg)	4.2679	0.7890		0.3360	

Note: A_1: repair loss; A_2: fatigue damage accumulation; A_3: total travel time; A_4: carbon dioxide emissions.

Table 11.3 Information regarding the single attribute utility functions

Attribute	Maximum Value	Minimum value
Repair loss (USD)	5.0×10^5	0
Fatigue damage accumulation	1	0
Total travel time (second)	2.0×10^5	0
Carbon dioxide emissions (kg)	1.0×10^6	0

Table 11.4 Multi-attribute utility values associated with Routes 1, 2, and 3 considering different risk attitudes ρ and various weighting factors

Alternative	Multi-attribute utility value					
	ρ = -2	ρ = -4	ρ = -2	ρ = -4	ρ = 2	ρ = 4
Weighting factor	(0.3, 0.3, 0.2, 0.2)		(0.2, 0.2, 0.3, 0.3)		(0.2, 0.2, 0.3, 0.3)	
Route 1	**0.2621**	**0.1186**	0.2604	0.1164	**0.7134**	**0.8661**
Route 2	0.2223	0.0936	0.2471	0.1084	0.6961	0.8531
Route 3	0.2172	0.1006	**0.2666**	**0.1302**	0.6724	0.8126

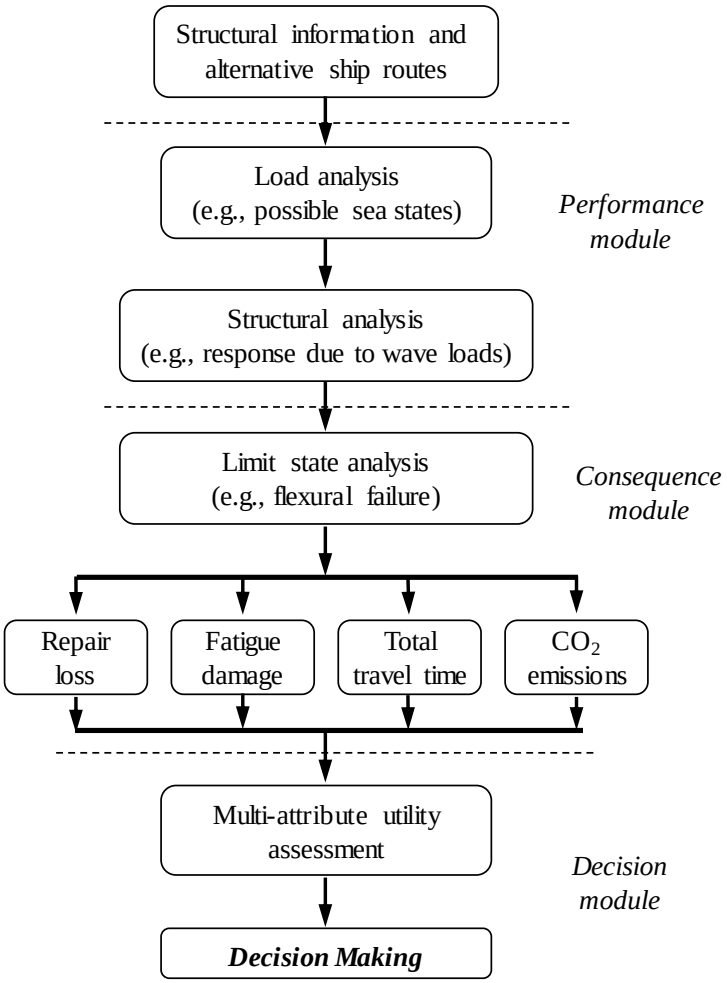

Figure 11.1 Flowchart for the decision support system

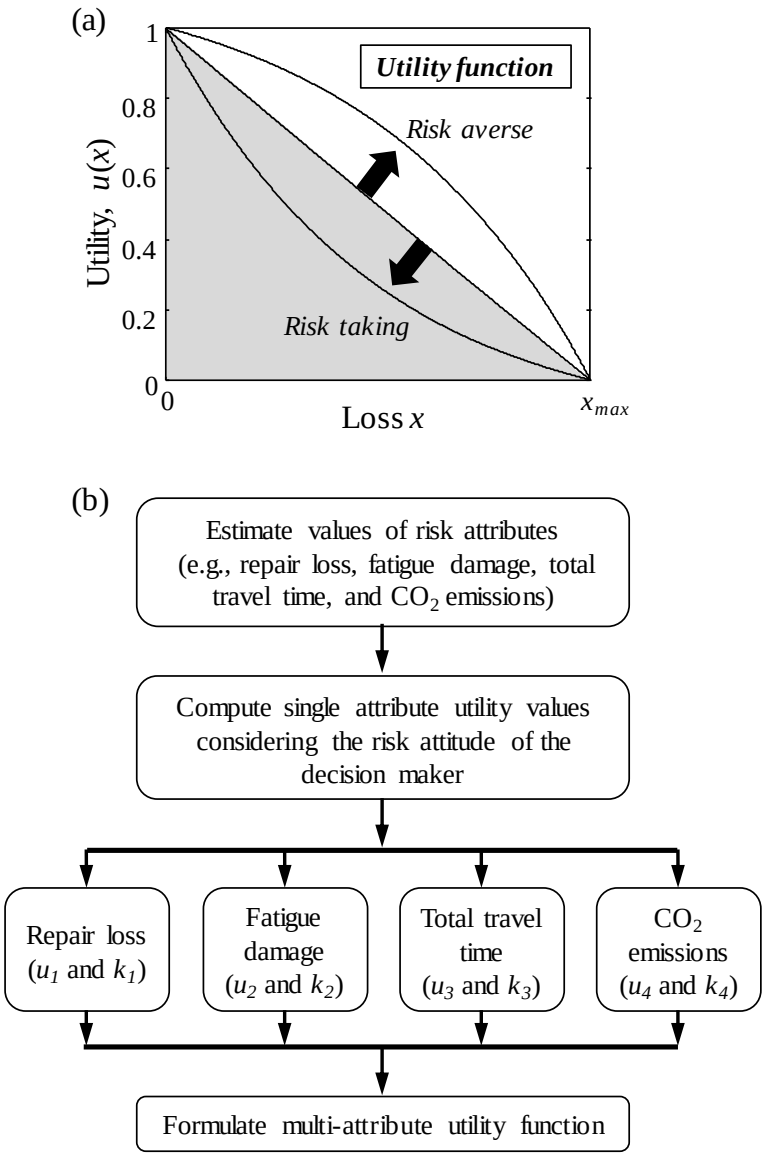

Figure 11.2 (a) Utility functions associated with different risk attitudes and (b) flowchart for the multi-attribute utility assessment

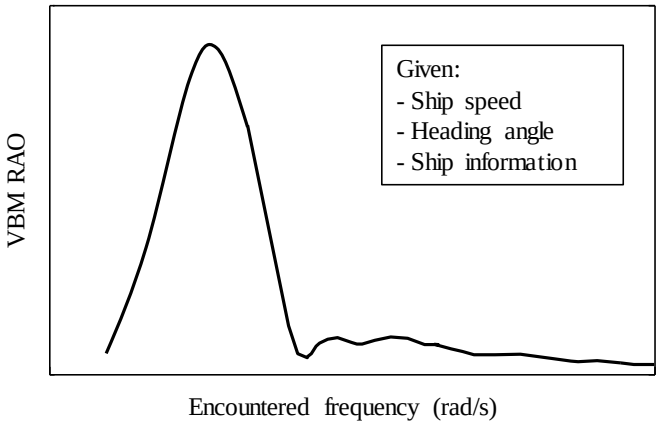

Figure 11.3 The qualitative VBM RAOs associated with given cross section

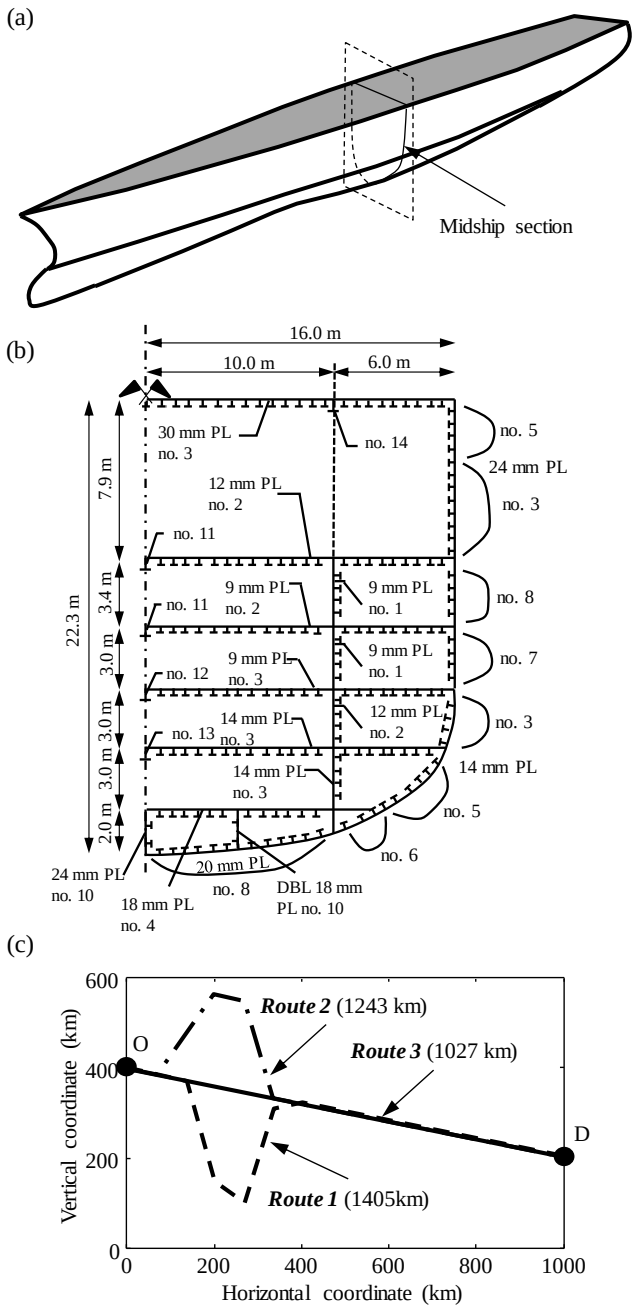

Figure 11.4 (a) The ship body under investigation; (b) mid-ship cross-section of the JHSS; and (c) alternative ship routes

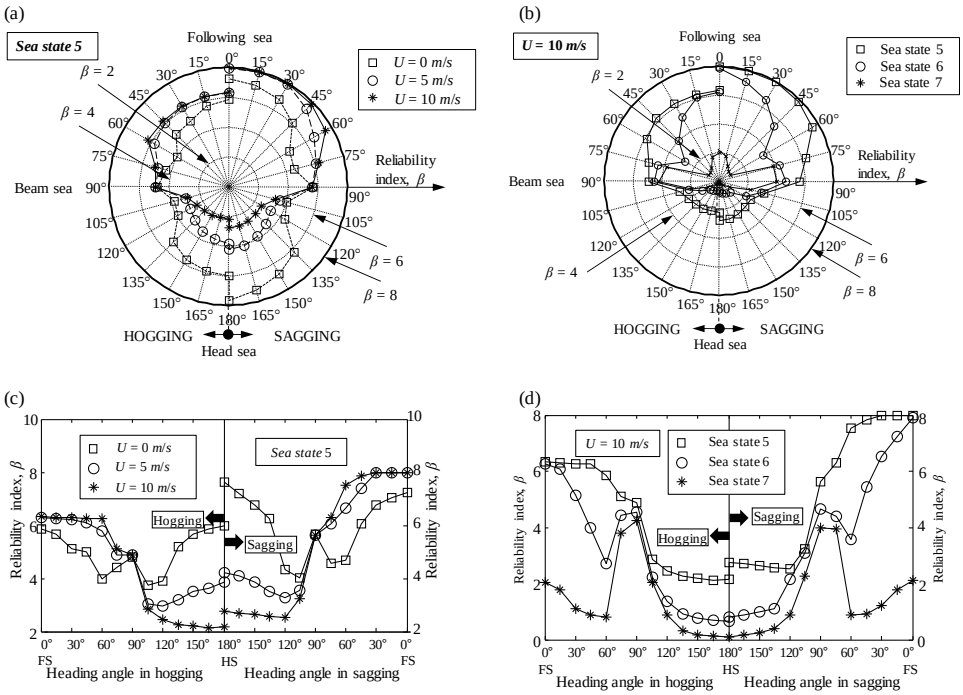

Figure 11.5 Polar representation of the reliability index corresponding to the mid-ship cross-section under sea state 5 considering different ship speeds and (b) profiles of the reliability index for different sea states considering a ship speed of 10 m/s. Associated Cartesian plots of the reliability indices for the ship with respect to different (c) ship speeds, and (d) sea states.

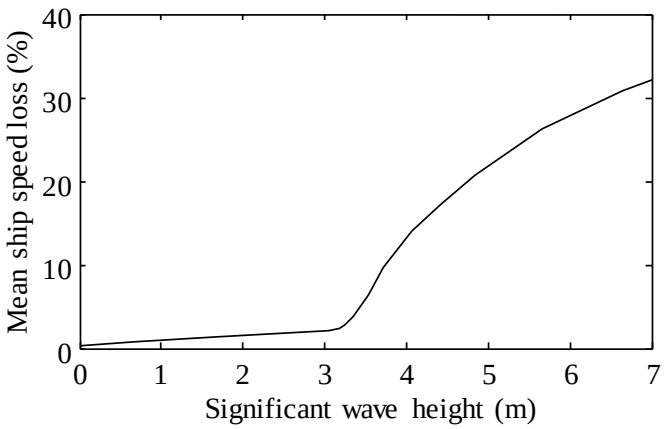

Figure 11.6 Expected ship speed reduction as a function of significant wave height

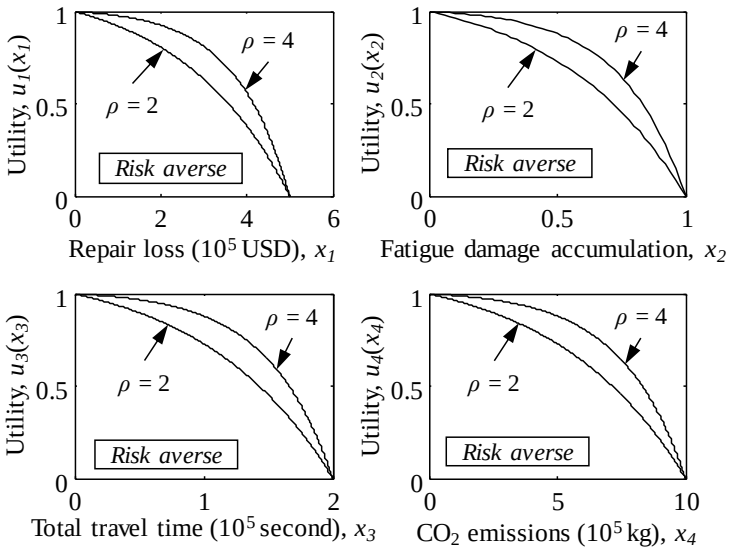

Figure 11.7 Utility functions for the four attributes considering a risk averse attitude

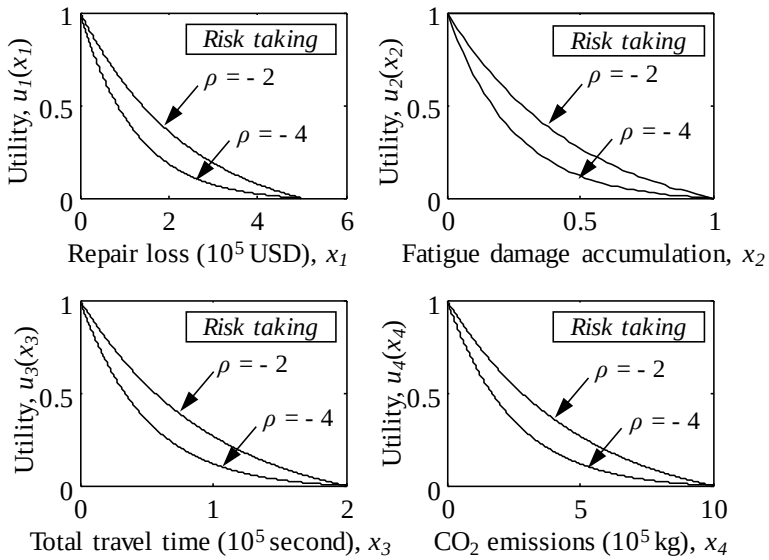

Figure 11.8 Utility functions for the four attributes considering a risk taking attitude

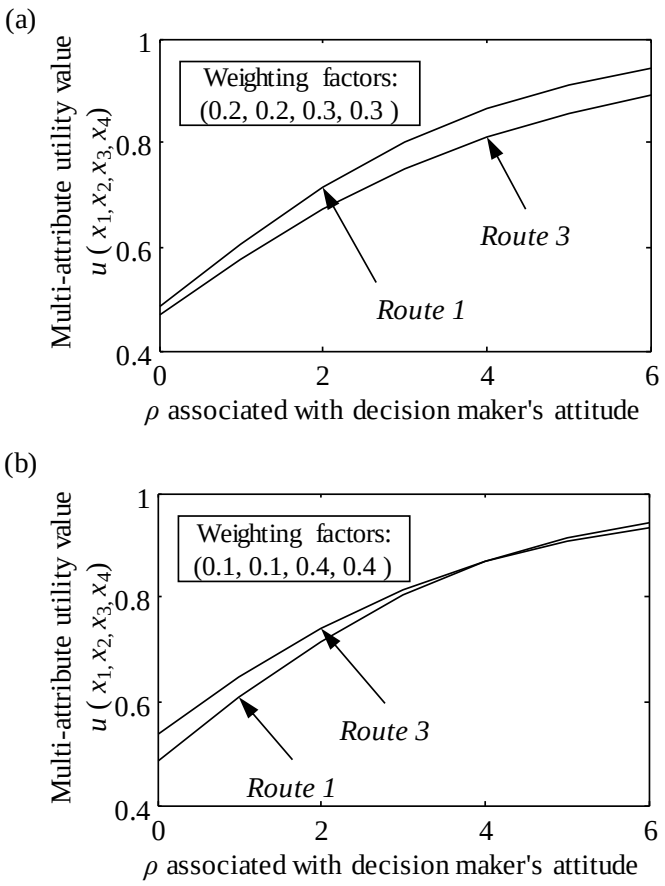

Figure 11.9 Multi-attribute utility values as a function of risk averse attitude ρ considering weighting factors equal to (a) (0.2, 0.2, 0.3, 0.3) and (b) (0.1, 0.1, 0.4, 0.4)

CHAPTER 12

RISK-INFORMED LIFE-CYCLE OPTIMUM INSPECTION AND MAINTENANCE OF SHIP STRUCTURES CONSIDERING CORROSION AND FATIGUE

12.1. INTRODUCTION

Aging ships may suffer from structural deterioration associated with corrosion and/or fatigue, resulting in a reduction of their resistance. This reduction can lead to structural failure. Moreover, load effects on ship structures contain high levels of uncertainty and may exceed the associated design loads. Inspection and maintenance of aging ship structures are needed to ensure satisfactory structural performance during their life-cycle. In general, the most significant strength deterioration mechanisms associated with ship structures are corrosion and fatigue (Guedes Soares and Garbatov, 1999; Kwon and Frangopol, 2012). Therefore, it is essential to mitigate the adverse consequences associated with structural failure under corrosion and fatigue. Furthermore, there are significant uncertainties associated with corrosion and fatigue models. The corrosion of a ship structure is affected by many factors such as corrosion protection, temperature and humidity. Fatigue crack propagation is also affected by many parameters such as initial crack size, history of local nominal stresses, and load sequence. Consequently, uncertainties must be incorporated within the structural performance deterioration process. This chapter aims to provide a probabilistic methodology for optimum

inspection and maintenance planning of ship structures to mitigate risk under corrosion and fatigue.

Crack growth at a critical structural detail can be predicted using fracture mechanics. The most commonly used mechanistic model is based on the Paris-Erdogan formula (Paris and Erdogan 1963). Overall, fatigue cracks can propagate under repetitive loadings and affect structural integrity associated with ship hulls, while corrosion can also affect the ultimate strength of ship structures. Therefore, it is of vital importance to control the relevant fatigue cracks and corrosion level to meet the design and operational tolerance levels for ship structures. The fatigue model that predicts cracking damage considered in this chapter is incorporated within a corrosion model to investigate the ship performance level associated with ultimate flexural failure. In general, structural damage associated with corrosion and fatigue can reduce the ship load-carrying capacity. Moreover, such damage may lead to partial failure or total loss of marine vessels. In order to minimize the economic loss and fatalities associated with structural failure, it is of vital importance to investigate ship performance under corrosion and fatigue. In this chapter, the separate and combined effects of corrosion and fatigue on ship structural ultimate flexural failure are considered.

During the past few decades, the field of ship structural reliability assessment has been developed considerably (Paik and Frieze 2001; Okasha *et al.* 2011; Frangopol and Soliman 2014). In its most broad terms, structural reliability is a measure of the probability of a system's survival under a given limit state. Ship performance associated with ultimate flexural failure of the hull's mid-ship section is considered as one of the

most critical criteria regarding ship safety assessment (Decò *et al.* 2011). The probability of failure and reliability index of ships have been previously investigated by Ayyub *et al.* (2000), Paik and Frieze (2001), and Okasha *et al.* (2011). Reliability-based structural performance indicators reflect the uncertainty in load, resistance, and modelling. However, these indicators do not account for the outcome of a failure event in terms of economic losses. A risk-based performance indicator provides means of combining the probability of component or system failure with consequences of this event. Nowadays, risk is an essential structural performance indicator (IACS 2006; Decò and Frangopol 2013). Although there have been significant efforts to investigate reliability of ship structures, there has been a lack of research that focuses on risk-based performance assessment of ship structures. The importance of risk as a performance indicator is emphasized in this chapter. The flowchart for risk assessment of ship structures considering corrosion and fatigue is shown in Figure 12.1. Since failures associated with ship structures have significant impacts on surrounding economic, social, and environmental networks, risk-based methodologies are more appropriate for life-cycle management of ships. Accordingly, risk-based methodologies can be used to determine the optimal intervention strategies. However, to the best of authors' knowledge, there have been no studies to establish a framework for risk-based optimum inspection and maintenance planning of ship structures considering corrosion and fatigue.

Overall, inspection and maintenance planning focuses on estimating the timing and types of these inspection actions to ensure structural safety and serviceability under corrosion and fatigue. Multi-objective optimization concepts and sensitivity analysis

method play an important role in allocating limited resources in an efficient way to balance both cost and performance (Bucher and Frangopol 2006; Frangopol 2011). Within the adopted bi-objective framework, the risk is aimed to be minimized during an investigated time horizon. Recent efforts have performed optimization procedures that minimize the life-cycle cost of a structure under given constraints on performance (Okasha and Frangopol 2009; Kim and Frangopol 2011; Kim *et al.* 2013). Although extensive research has been conducted on the optimization of intervention strategies based on life-cycle costs, there is very limited research regarding risk-informed life-cycle optimization of ship structures. The best inspection and maintenance plans can be obtained through an optimization process that considers risk and cost of keeping structural performance above prescribed thresholds during the life-cycle of marine vessels.

In this chapter, a probabilistic framework for risk-informed life-cycle optimum maintenance of ship structures is presented. The effects of corrosion and fatigue on the ultimate strength of ships are considered in the framework; additionally, uncertainties associated with these two deteriorating mechanisms are incorporated within the risk assessment process. The effects of inspection and repair on the ultimate bending moment are assessed. The methodology proposed in this chapter can quantify risk-based structural performance of ships during their life-cycles. A bi-objective optimization problem accounting for common deterioration mechanisms and their associated uncertainties is formulated to find the best lifetime inspection and repair plan for ship structures. The maximum annual risk associated with ship structural failure during the investigated time

interval, in addition to expected total inspection and repair costs are considered as conflicting criteria. The proposed probabilistic approach uses optimization techniques based on genetic algorithms (GAs) in order to determine optimum inspection planning that reduces the extent of adverse consequence associated with ship failure while simultaneously minimizing the expected total maintenance cost. Decision makers can use the results of the proposed approach to make optimal risk-informed decisions regarding life-cycle inspection and repair of ships. The capabilities of the approach are demonstrated through its application to a real vessel, the Very Large Crude Carrier (VLCC) ship structure. GAs are used to solve the bi-objective optimization problem. The work in this chapter is based on a published paper Dong and Frangopol (2015b).

12.2. RISK ASSESSMENT

Risk-based performance measures combine the probability of system failure with the consequences associated with this particular event. In general, since failures associated with structural systems result in significant economic and social impacts, risk-based methodologies are most appropriate for structural system management. The aim of risk-based management is to develop a management plan that can prevent failures and, consequently, reduce the impact of adverse consequences. The importance of risk as a performance indicator is emphasized in this chapter. The evaluation of the consequences associated with potential failure plays a fundamental role in the risk assessment process. Generally, the risk R associated with a structural system can be expressed as (CIB 2001)

$$R = \int\int\cdots\int \delta(X)\cdot f(X)dx \tag{12.1}$$

where $\delta(\mathbf{X})$ represents the consequences and $f(\mathbf{X})$ is the joint probability density function (PDF) of the considered random variables $\mathbf{X} = (x_1, x_2, \ldots, x_k)$. Generally, the solution of this equation is not obvious; therefore, risk can be evaluated by considering an approach that accounts for discrete condition states. Ship performance associated with ultimate flexural failure of the hull's mid-ship section is considered as one of the most critical criteria regarding ship safety. Therefore, the risk associated with ultimate strength failure is emphasized herein.

12.2.1. Reliability analysis

Reliability analysis of ship structures is performed based on knowledge of the probability distributions associated with hull structural resistance and statistical descriptors of load effects. The first step within the reliability analysis involves determining the probability of flexural failure based on the ultimate limit state. Considering modeling uncertainties associated with resistance and load effects, the limit state equation for the ultimate failure of a particular ship cross-section can be expressed as (Paik and Frieze 2001)

$$G_U = x_R M_{UR} - x_{SW} M_{SW} - x_W M_W = 0 \tag{12.2}$$

where M_{UR} is the resisting bending moment associated with ultimate failure; M_{SW} is the still water bending moment; M_W is the wave-induced bending moment; x_{SW} and x_W are the model uncertainties associated with still water and wave-induced bending moment, respectively; and x_R is the model uncertainty associated with hull resistance determination. The probability of failure p_f corresponding to flexural limit state may be obtained using simulation techniques. Furthermore, the reliability index β is

$$\beta = \Phi^{-1}(1 - p_f) \tag{12.3}$$

where Φ^{-1} denotes the inverse of the standard normal cumulative distribution function.

The ultimate bending moment capacity associated with ship hull is introduced in this section. Paik and Mansour (1995) proposed a distribution of longitudinal stresses associated with hull section at the collapse state. In this approach, material in compression was assumed to reach ultimate buckling strength; while material in tension was assumed to result in full yielding. The ultimate moment capacity of the hull associated with sagging M_{us} and hogging bending moment M_{uh} can be expressed as (Paik and Mansour 1995)

$$M_{us} = -A_D(D-g)\sigma_{uD} - \frac{A_S}{D}(D-H)(D+H-2g)\sigma_{uS} - A_B g\sigma_{yB} + \frac{A'_B}{H}(g-D_B)[D_B\sigma_{uS} - (H-D_B)\sigma_{yS}] - \frac{A_S H}{3D}[(2H-3g)\sigma_{uS} - (H-3g)\sigma_{yS}] \quad (12.4)$$

$$M_{uh} = A_D g\sigma_{yD} + A_B(D-g)\sigma_{uB} + A'_B(D-g-D_B)\sigma'_{uB} + \frac{A_S H}{3D}[(2H-3g)\sigma_{uS} - (H-3g)\sigma_{yS}] + \frac{A_S}{D}(D-H)(D+H-2g)\sigma_{uS} \quad (12.5)$$

where A_D, A_B, A'_B, and A_S are the total sectional area of deck, outer bottom, inner bottom, and half-sides, respectively; D is the hull depth; g is the neutral axis position above the base line associated with the sagging condition or below the deck in the hogging condition; σ_{yB}, σ'_{yB}, σ_{yD}, and σ_{yS} are the yield strengthes of outer bottom, inner bottom, decks and side, respectively; σ_{uB}, σ'_{uB}, σ_{uD}, and σ_{uS} are the ultimate buckling strength of outer bottom, inner bottom, decks, and side, respectively; D_B is the height of double bottom; and H is depth of non-collapse side of the hull section. Detailed information concerning the ultimate moment capacity calculation can be found in Paik and Mansour (1995).

The next step associated with ship structural reliability analysis is to determine the load effect. The load effects induced by the sea on the hull are due to two events: still water and waves. Safety evaluation of ship structures operating in different sea conditions requires an accurate estimation of the load effects due to still water and waves (Guedes Soares, 1992). As emphasized by Guedes Soares and Teixeira (2000), the primary load effects within the hull are the sagging and hogging vertical bending moments (VBMs). According to the International Association of Classification Societies (IACS, 2008), the VBMs $M_{sw,sag}$ and $M_{sw,hog}$ associated with sagging and hogging, respectively for a specific ship cross-section under still water can be expressed as

$$M_{sw,sag} = -0.05185 f_{sw,CS} C_{wv} L^2 B(C_b + 0.7) \tag{12.6}$$

$$M_{sw,hog} = 0.01 f_{sw,CS} C_{wv} L^2 B(11.97 - 1.9 C_b) \tag{12.7}$$

where $f_{sw,CS}$ is a factor accounting for the variation of VBMs along the vessel length (i.e., equal to 1.0 at mid-ship); C_b is the ship block coefficient; L is the ship length (m); B is the ship breadth (m); and C_{wv} is the wave coefficient. The load effect on ship structures associated with waves is related to many factors, including ship geometry, heading angle, speed, and encountered sea state. The linear response theory is commonly employed to compute the structural performance of marine vessels (Hughes, 1983); a widely used approach for ship performance evaluation based on linear response theory is the strip method (Fonseca and Guedes Soares 1998). In addition to the strip method, other methodologies have been established to account for the non-linear effects (Jensen and Pedersen 1978).

12.2.2. Consequence evaluation

As mentioned previously, risk is regarded as an important performance indicator within the fields of civil and marine structural engineering. This section presents the consequence evaluation regarding ship flexural failure. The repair loss (i.e., economic impact) of the entire ship structure is considered in this chapter.

The main consequence investigated in this chapter is the repair loss, which describes the direct monetary loss associated with structural failure. The construction cost of a ship is computed considering its preliminary design and work breakdown system (Decò and Frangopol 2013). The costs associated with the ship work breakdown system (SWBS) are subdivided into several categories, including propulsion, structural, and electrical systems. Using this information, the construction cost of a ship structure is calculated as (Miroyannis 2006)

$$C_{Cons} = 5747.19 \times STF \times DISP^{-0.3792} \times WGT_{100}{}^{0.862} + 800 \times WGT_{100} \tag{12.8}$$

where WGT_{100} is the weight of Ship Work Breakdown Structure (SWBS) (long tons); *STF* is the ship type factor; and *DISP* is the ship full load displacement (long tons).

The repair loss (i.e., direct loss) associated with complete structure failure of marine vessels is emphasized. The probability of occurrence of this event is first calculated and then the repair loss is computed by multiplying this probability by the associated repair cost of the entire ship structure. The repair loss R of a ship structure associated with ultimate flexural failure at time t is

$$R(t) = P_f(t) \cdot Cons(t) \tag{12.9}$$

where $P_f(t)$ is the conditional probability of ship cross-section failure given specific load effects at time t; and $Cons(t)$ is the monetary consequence associated with ship structural failure at time t.

12.3. CORROSION AND FATIGUE CRACKING

12.3.1. Corrosion

Over time, corrosion effects cause the gradual loss of thickness of plates and stiffeners that are parts of a ship's hull structure; in turn, this leads to a reduction in the ultimate failure moments. The ultimate strength behavior of ship structures exposed to uniform corrosion is emphasized herein; however pitting corrosion can also be incorporated within the presented framework. Guedes Soares and Garbatov (1999) investigated a nonlinear function that relates corrosion depth with time. Additionally, Akpan *et al.* (2002) proposed an equation to compute the thickness loss within a cross-section of a ship as follows:

$$d(t) = C_1(t - t_0)^{C_2} \tag{12.10}$$

where $d(t)$ is thickness loss (mm); t is the time (year); t_0 is the corrosion initiation time depending on coating life (year); C_1 is the annual corrosion rate (mm/year); and C_2 is a constant set to unity. Although this corrosion model is adopted in this chapter, other models can also be incorporated within this study.

12.3.2. Fatigue

For fatigue cracking damage, the fracture mechanics approach can be used to establish crack growth equations associated with the stress intensity factor, stress range, material,

and environmental properties. Typically, the Paris equation is used to predict fatigue crack propagation (Paris and Erdogan 1963)

$$\frac{da}{dN} = C \cdot (\Delta K)^m \tag{12.11}$$

where a is the crack size; N is the number of cycles; ΔK is the stress range intensity factor; C is the fatigue coefficient; and m is the fatigue exponent (i.e., material constant). The stress intensity factor range can be computed as

$$\Delta K = \Delta\sigma Y(a)\sqrt{\pi a} \tag{12.12}$$

where $\Delta\sigma$ is the stress range and $Y(a)$ is the geometric factor.

Subsequently, the crack size at time t is (Ayyub *et al.* 2002)

$$a(t) = [a_0^{1-m/2} + (1-\frac{m}{2}) \cdot C \cdot C_{corr} \cdot \Delta\sigma^m Y^m \pi^{m/2} \upsilon_0 t]^{2/(2-m)} \qquad m \neq 2 \tag{12.13}$$

$$a(t) = a_0 \exp(CY^2 \Delta\sigma^2 \pi \upsilon_0 t) \qquad m = 2 \tag{12.14}$$

$$\upsilon_0 = 365 \cdot \alpha \cdot N_{avg} \tag{12.15}$$

where a_0 is the initial crack size; C_{corr} is the corrosion-enhanced crack growth parameter; α is the annual ship operation rate; and N_{avg} is average daily number of cycles.

Numerical and experimental studies have to be developed in order to investigate the effect of fatigue on the residual strength of steel plated structures under axial tensile/compressive loads. Another method to account for the effect of fatigue is simply subtracting the crack area from the total area (Guedes Soares and Garbatov 1999; Akpan *et al.* 2002). This simplified method is adopted in this chapter for illustrative purposes. The time-variant parameters associated with the plate and web of hull stiffeners,

considering fatigue and corrosion, can be expressed as (Guedes Soares and Garbatov 1999)

$$b_p(t) = b_{p,0} - a_p(t) \tag{12.16}$$

$$t_p(t) = t_{p,0} - d_p(t) \tag{12.17}$$

$$h_w(t) = h_{w,0} - a_w(t) \tag{12.18}$$

$$t_w(t) = t_{w,0} - d_w(t) \tag{12.19}$$

where $b_{p,0}$ and $t_{p,0}$ are the plate breadth and thickness, respectively; $h_{w,0}$ and $t_{w,0}$ are the stiffener height and thickness, respectively; a_p and a_w are the crack length associated with the plate and web, respectively; and d_p and d_w are the corrosion depth of the plate and web, respectively. Consequently, the structural deteriorations mechanisms (e.g., corrosion and fatigue) can reduce the flexural capacity of ship structures on basis of Eqs. (12.4) and (12.5).

12.4. INSEPECTION AND MAINTENANCE ACTIONS

Inspections are used to detect corroded components and fatigue cracks in order to ultimately ensure structural safety of critical structures. The uncertainties involved in inspection activities can be approximately modeled in terms of the probability of damage detection. Once the structural deterioration (e.g., corrosion and fatigue crack) associated with the inspected components exceeds the prescribed critical value, they are replaced with new components, thus decreasing the risk associated with ship structures. Regarding welded structures, initial cracks are assumed to be present after fabrication and thus, fatigue damage is indicated by crack size, which increases with time. In the methodology

presented herein, once a fatigue crack is detected and exceeds a prescribed critical size, the affected components should be repaired and restored to their original conditions in order to increase the overall reliability of the ship. A decision tree model is used here to illustrate the inspection and maintenance process as shown in Figure 12.2(a). In the decision tree, probabilities of damage detection and repair are considered. The relation among damage intensity, quality of an inspection method and probability of damage detection is expressed as a damage detectability function. This model represents all the possible events. Each path has a particular outcome that associated with a probability of occurrence.

12.4.1. Corrosion inspection and repair action

The quality of inspection depends on the specific damage detection technique used for ship structures. In general, inspections for corrosion are scheduled for ship structures during their service time in order to ensure that corrosion thickness is smaller than a prescribed acceptable value. The probability of detecting corroded components can be computed as (Guedes Soares and Garbatov 1999)

$$P_{D,CR,i}(t) = 1 - \exp(-\frac{ds_i}{\lambda_s}) \qquad t > t_{0,i} \tag{12.20}$$

where $t_{o,i}$ is the coating life for ship structure; ds_i is the corrosion level of the component i under investigation; and λ_s is a parameter that is associated with the corrosion damage detection method. λ_s can be calculated using the following expression(Guedes Soares and Garbatov, 1999)

$$\lambda_s = \frac{ds_p}{\ln(1-p)} \tag{12.21}$$

where ds_p is the fraction of thickness that is detected associated with probability p. The average probability of repair $P_{RE,CR}(t)$ of corroded components at time t can be computed as (Guedes Soares and Garbatov 1999)

$$P_{RE,CR}(t) = \frac{n_{0,CR}}{N_{Tot}} P_{ED,CR}(t) \tag{12.22}$$

$$P_{ED,CR}(t) = \frac{\sum_{i=1}^{n_{0,CR}} P_{D,\,CR,i}(t)}{N_{Tot}} \tag{12.23}$$

where $n_{0,CR}$ is the number of components associated with corrosion loss larger than a prescribed critical value; N_{Tot} is the total number of the components inspected at a given time t; and $P_{ED,CR}(t)$ is the expected probability of detecting corroded components at the given inspection time t.

12.4.2. Fatigue inspection and repair action

Among the available nondestructive inspection techniques, liquid penetrant, ultrasonic, magnetic particle, and acoustic emission inspection methods are commonly employed for fatigue crack detection (Mohamed and Frangopol 2014). The quality of an inspection type is effectively expressed by the probability of detection associated with a given crack. In general, the probability of detection associated with a fatigue crack can be expressed as (Packman *et al.* 1969; Guedes Soares and Garbatov 1999)

$$P_{D,\,FC,i}(t) = 1 - \exp\left(-\frac{E[a_i(t)] - a_l}{\lambda_d}\right) \tag{12.24}$$

where a_l is the limit size of fatigue crack size that can be detected; $a_i(t)$ is the fatigue crack at time t; and λ_d is a parameter that is associated with the specific fatigue crack

detection method employed. The average probability of repair associated with fatigue crack, at time of inspection t, can be expressed as (Guedes Soares and Garbatov 1999)

$$P_{RE,FC}(t) = \frac{n_{0,FC}}{N_{Tot}} P_{ED,FC}(t) \tag{12.25}$$

$$P_{ED,FC}(t) = \frac{\sum_{i=1}^{n_{0,FC}} P_{D,\,FC,i}(t)}{N_{Tot}} \tag{12.26}$$

where $n_{0,FC}$ is the number of components associated with cracks larger than a_l; and $P_{ED,FC}(t)$ is the expected probability of detecting crack sizes larger than the critical value at the given inspection time t.

Considering corrosion and fatigue, the probability of repair at inspection time t can be expressed as (Guedes Soares and Garbatov 1999)

$$P_{RE}(t) = P_{RE,CR}(t) + P_{RE,FC}(t) - P_{RE,CR}(t) \cdot P_{RE,FC}(t) \tag{12.27}$$

where $P_{RE,CR}(t)$ and $P_{RE,FC}(t)$ are the probabilities of repair at the inspection time t considering corrosion and fatigue, respectively. Other inspection methods associated with corrosion and fatigue can also be implemented within this methodology. The inspection method based on Guedes Soares and Garbatov (1999) is adopted herein. Detection of critically degraded components should be followed by the replacement of the affected components with new ones. Consequently, the risk associated with ship structural failure can be reduced by applying maintenance actions after an inspection at time t_{insp}, as is qualitatively shown in Figure 12.2(b). As evidenced by Figure 12.2(b), the risk R_1 at time $t_{life,nm}$, considering the case with maintenance, is relatively smaller than the risk threshold

R_2. Generally, the risk associated with ship structures can be reduced significantly by implementing maintenance actions.

12.4.3. Inspection and repair costs

The total cost of inspection effectively integrates the access, equipment, and operator costs for ship structures. The total cost of inspection can be obtained by summing up these costs. The life-cycle inspection cost associated with component *j* of a ship structure can be expressed as

$$C_{Insp,j}^{T} = \sum_{i=1}^{n} \frac{c_{Insp,j}}{(1+r)^{t_{insp,i}}} \tag{12.28}$$

where *r* is the annual discount rate of money; *n* is the number of inspections; $c_{Insp,j}$ is the inspection cost of component *j*; $t_{insp,i}$ is the time of inspection *i*; and *T* is the investigated time interval (e.g., life-cycle). The life-cycle expected repair cost associated with component *j* during the investigated time interval *T* can be expressed as

$$C_{\boldsymbol{Rep,j}}^{T} = \sum_{i=1}^{n} \frac{c_{\boldsymbol{Rep,j}}}{(1+r)^{t_{insp,i}}} \cdot P_{RE,j}(t) \tag{12.29}$$

where $c_{Rep,j}$ is the repair cost for component *j* and $P_{RE,j}(t)$ is the probability of repairing the component under inspection action at time *t*. Generally, the repair cost for a ship component can be computed as (Rigterink *et al.* 2013)

$$c_{\boldsymbol{Rep,j}} = c_{Cons} \cdot W_j \cdot L_j \tag{12.30}$$

where c_{Cons} is the construction cost per unit area (e.g., USD/m^2); and L_j and W_j are the length and width associated with component *j* under investigation, respectively. In the optimization process adopted herein, the life-cycle maintenance cost is considered as an

objective to be minimized within the decision making process. The expected maintenance cost during the investigated time interval T (e.g., life-cycle) can be formulated as

$$C_{LCMC} = \sum_{j=1}^{N_{Tot}} (C_{Insp,j}^{T} + C_{\boldsymbol{Rep,j}}^{T}) \tag{12.31}$$

12.5. LIFETIME OPTIMUM INSPECTION AND REPAIR PLANNING

The life-cycle maintenance of ship structures is of vital importance in preventing their ultimate failure considering corrosion and fatigue. Risk is emphasized herein as a performance indicator associated with ultimate flexural failure. The structural deterioration effects associated with corrosion and fatigue are incorporated within this process. Overall, this optimization process aims to determine optimum lifetime inspection schedules for ship structures. Two objectives have to be minimized simultaneously in this bi-objective optimization procedure: (a) the expected life-cycle maintenance costs considering inspection and repair, and (b) the maximum annual value of risk during a ship's life-cycle. Risk is selected as the main performance indicator to be included in the optimization process due to the fact that it contains information regarding both structural failure and its consequences. The solution of the optimization process provides information concerning the optimal sequence and timing of ship inspection and repair planning. The optimization process embedded within the proposed life-cycle maintenance strategy methodology is illustrated in Figure 12.3.

Within this optimization procedure, the design variables are inspection and repair timings. The maximum number of nondestructive inspections, in addition to time, cost, and reliability constraints is specified. GAs are adopted herein to solve the bi-objective

problem. The optimization module sends the candidates for the design variables to risk and cost modules. Next, the performance module delivers the value of one objective, which is the maximum annual risk value experienced during the investigated time horizon, to the optimization module. The cost module returns the total expected maintenance costs for the ship structure to the optimization module. Finally, after an adequate number of iterations, the optimization module provides the Pareto optimum front for the lifetime inspection planning (Kwon and Frangopol 2011; Frangopol 2011; Dong *et al.* 2014). The solutions associated with the bi-objective optimization are solved using Matlab (MathWorks 2013). This approach can be utilized to provide multiple choices to the decision maker.

Generally, the optimization process associated with optimal inspection and maintenance planning of ship structures can be formulated as follows (Kim and Frangopol, 2011; Kim *et al.* 2013):

***Given*:**

- Ship configuration including the geometry, physical characteristics (information associated with Eqs. (12.6) and (12.7))
- Ship operation scenarios (e.g., ship speed, heading angle, encountered sea states)
- Representative probabilistic corrosion scenarios for given cross-section (see Eq. (12.10))
- Fatigue crack propagation associated with ship details under investigation (calculated using Eqs. (12.11) to (12.15))

- Time-variant reliability index of the ship structure associated with flexural failure under corrosion and/or fatigue
- Consequence evaluation associated with the construction cost for the ship structure (see Eq. (12.8))
- The inspection method for the ship details under corrosion and fatigue with probability of detection calculated using Eqs. (12.20) and (12.24), respectively
- The repair criterion for the repair associated with ship details under corrosion and fatigue (see Eq. (12.27))
- The inspection and repair cost for the details under investigation (see Eqs. (12.28) and (12.29))
- Time horizon under investigation (T) and the maximum number of inspections during T

***Find*:**

- The timings of inspection and repair performed on each structural detail during the investigated time interval

***So that*:**

- The inspection and repair cost associated with the given cross-section is minimized
- The maximum annual value of the risk during a specific time interval is minimized

***Subjected to*:**

- Time interval between consecutive inspection actions should be larger than or equal to a given value
- The structural performance (e.g., reliability index) of components under investigation considering corrosion and/or fatigue should always be larger than a prescribed value
- The total cost of the inspection and repair costs should be less than a prescribed monetary value.

12.6. ILLUSTRATIVE EXAMPLE

The proposed approach is applied to the Very Large Crude Carrier (VLCC) (Khan and Parmentier 2006). The ship length and dead weight are 326.75 m and 216,269 tonnes respectively. The deck and bottom are made of high strength steel with yield strength equal to 315 MPa, while the side shell and bulkheads are made of mild steel with yield strength of 235 MPa. The mid-ship section of the tanker investigated in this chapter is shown in Figure 12.4. The primary failure mode (i.e., hull girder collapse), taking into account the influence of corrosion and fatigue, is emphasized in this chapter. Performance associated with ultimate flexural failure of the hull's mid-ship section is considered as the most critical criterion regarding ship safety. To compute the risk associated with the ship's flexural failure, the probability of this failure under wave and still water loading should be obtained first.

12.6.1. Reliability analysis under corrosion and/or fatigue

By using Eq. (12.2), the limit state function regarding the ship's ultimate flexural failure can be established. The ultimate bending strength, M_u, of the intact VLCC is computed for sagging and hogging, respectively, on basis of Eqs. (12.4) and (12.5). The cross-sectional areas of the deck, outer bottom, and side are 20,382, 20,790, and 16,471 cm^2, respectively (Paik and Mansour 1995). The random variables parameters considered within this analysis are presented in Table 12.1. For sagging and hogging moments, the computed expected values of M_{us} and M_{uh} are 22,601 MN-m and 22,405 MN-m, respectively. Based on Eq. (12.6) and (12.7), the still water induced moments are estimated. For sagging and hogging conditions, the computed mean values of M_{sw} are 3,763 MN-m and 5,371 MN-m, respectively. Within this illustrative example, the ship's wave load is obtained based on data presented in Kwon and Frangopol (2012). The expected wave load is 1,161 MN-m for both sagging and hogging conditions.

The effects of corrosion and fatigue on the ship flexural failure are considered herein. The components comprising the ship are exposed to different aggressive environments; consequently, the corrosion rate varies over the components. The entire hull cross-section is divided into five different sections as shown in Figure 12.4. Section 1 (S1) includes the deck area; sections 2, 3, and 4 correspond to the side area; and section 5 (S5) is bottom area of the ship structure. The parameters associated with the corrosion model considering different component groups as a part of the whole cross-section are shown in Table 12.2. The ultimate strength behavior of ship structures exposed to uniform corrosion is considered in this chapter by using Eq. (12.10), while pitting

corrosion can be incorporated within the presented framework for maintenance optimization.

Under repetitive loading effects, a crack can initiate and propagate at the connection between the plate and stiffener within a ship's structural detail (Guedes Soares and Garbatov, 1999). In order to model uncertainties in the assessment process, the size of a fatigue crack should be random. The uncertainties with respect to load effects and material properties are incorporated within this process. Monte Carlo simulation is adopted to predict the probability of fatigue damage crack growth with time. Then the statistical descriptors of crack propagation (e.g., expected value of fatigue crack size) are computed. The actual crack size is predicted utilizing a closed-formulation expression, as indicated in Eq. (12.13). For the specific ship considered in this illustrative example, the material constant (i.e., m in Eq. (12.11)) equals 3 and the annual ship operation rate is 0.75 (Kwon and Frangopol, 2012). The fatigue scenario and parameters (e.g., stress intensity factor) associated with fatigue crack analysis for this specific ship are based on the work that has been done by the second author of this chapter (Kwon and Frangopol 2012). The similar approach has also been used by Kwon and Frangopol (2012) and Akpan *et al.* (2002). More detailed information can be found in Kwon and Frangopol (2012), while the risk assessment is not considered in that chapter. The probabilistic random variables associated with fatigue considered in this chapter are shown in Table 12.2. Regarding the fatigue analysis, the wave-induced vertical bending moment is emphasized herein to compute the stress range associated with the components of the

ship structure under investigation. The hull girder stress range associated with wave-induced vertical load is computed as (DNV, 2014)

$$\Delta\sigma_v = K_{axial}(M_{wl,hog} - M_{wl,sag}) \cdot 10^{-3} \frac{|Z - n_0|}{I_Y} \tag{12.32}$$

where $|Z - n_0|$ is the vertical distance from the horizontal neutral axis of hull cross section to the component under investigation (m); I_Y is the moment of inertia of hull cross-section about transverse axis (m^4); and K_{axial} is the stress concentration factor for the structural detail considered.

Due to corrosion and/or fatigue, the thickness of the plate and web of the structural details within a ship are reduced with time as indicated in Eq. (12.16) to (12.19). Assuming that no repair actions are applied to the investigated ship structure, the ultimate bending moment of the ship is reduced with time. Therefore, the probability of structural failure increases with time. The capacity and load effect associated with sagging and hogging for the mid-ship cross-section are first computed. Next, the reliability analysis is performed using the computer program RELSYS (Estes and Frangopol 1998) based on the First-Order Reliability Method (FORM). As indicated in Figure 12.5(a), it is observed that the reliability index associated with the sagging case is greater than that with respect to hogging. Consequently, the hogging moment is emphasized herein for risk assessment. The time-variant reliability index associated with the ship under corrosion, fatigue, and both corrosion and fatigue decrease with time as shown in Figure 12.5(b). The reliability index of the ship structure under corrosion only is relatively larger than that under fatigue only. Consequently, the structural deterioration associated with corrosion should be paid

special attention to during the investigated time interval. After approximately 28 years, fatigue has a greater effect on the reliability index than corrosion.

12.6.2. Risk assessment

The risk (i.e., direct loss) associated with complete structure failure of marine vessels is computed herein. The risk is computed as the product of the probability of occurrence of failure and the repair cost associated with ship structural failure. The probabilities of the ship structural failure under corrosion only, fatigue only, and combined corrosion and fatigue have been obtained previously. Then risk can be computed by taking the consequence into consideration. The flowchart regarding the overall risk assessment process is shown in Figure 12.6. The risks associated with the combined and separate effects of corrosion and fatigue are computed for the investigated marine vessel using Eq. (12.9) considering $r = 0$. The parameters regarding the consequences associated with the ship failure can be found in Table 12.3. Quantitative risk values associated with the combined and separate impacts of corrosion and fatigue are shown in Figure 12.7. As observed in this figure, the risk increases gradually with time since no maintenance action is applied. Consequently, it is of vital importance to reduce the risk of the ship structure under corrosion and/or fatigue to ensure the structural performance above the prescribed performance level during the investigated time interval. The optimal maintenance strategies are addressed in the following section.

12.6.3. Pareto optimum inspection planning

The optimal maintenance strategy for the investigated ship structure is obtained by using optimization techniques. In this chapter, the bi-objective optimization problem is solved

using the GAs provided in the MATLAB Global Optimization Toolbox (MathWorks 2013). Generally, the mid-ship section is divided into five different sections (see Figure 12.4), each with a corresponding corrosion rate and separate fatigue damage conditions. The optimization process aims to find the optimal inspection timings for the respective section of the entire hull structure and simultaneously to meet the prescribed constrains (e.g., performance level). Moreover, the inspection plans associated with the Pareto optimal solutions are compared with fixed inspection plans.

The input with respect to the optimization problem should be identified first. The risk associated with the ship structure under corrosion and fatigue has already been obtained. Next, the inspection and maintenance actions should be identified. Regarding the inspection and repair associated with corrosion, the components that have corrosion loss larger than 25 percent of the original thickness are repaired. It is assumed that the thickness of a structural detail, within 75% of its initial thickness, can be detected with 99.9% probability (Guedes Soares and Garbatov 1999). By substituting these values into Eq. (12.21), the parameters λ_s associated with the given corrosion detection method can be obtained. Consequently, the probability of repair associated with corrosion is computed using Eq. (12.22). Additionally, the fatigue crack sizes that propagate in the plate and web are inspected. The maximum critical crack size is assumed to be equal to 70% of the height of the web and 70% of the breadth of the plate. Given the inspection method for the fatigue (Guedes Soares and Garbatov 1999), the detected crack size with probability 0.999 is 0.3 m. Within the proposed framework, at the time of inspection, if a crack is detected and is larger than a prescribed critical size, the component affected by

this crack is replaced as described previously. Overall, these values and associated probabilities are commonly used in practice (Guedes Soares and Garbatov 1999). Then, the probability to repair the damaged components associated with fatigue cracks can be computed using Eq. (12.25). Finally, the probability of repairing the ship's components considering both corrosion and fatigue at inspection time t can be computed using Eq. (12.27), while its corresponding repair cost is provided by Eq. (12.29). Within this illustrative example, the inspection cost is assumed as 10% of the repair cost (Kwon and Frangopol 2012). Given these input parameters, the optimum solutions for inspection and maintenance planning considering corrosion and fatigue of the VLCC ship are determined.

Figure 12.8 shows the Pareto optimal solution sets considering a maximum of three inspections during a 30 year time interval. Each Pareto solution represents a unique inspection and repair plan leading to various levels of structural performance in terms of risk. In order to analyze the results, two representative solutions, A and B (see Figure 12.8), are investigated in detail. Solution A represents a low-risk high-cost solution with maximum annual expected economic risk of 7.67×10^4 USD and total maintenance cost of 6.05×10^4 USD. Additionally, Solution A corresponds to inspecting sections S1 and S5 at t = 9 years; sections S1, S3, S4, and S5 at t = 18 years; and sections S1 and S3 at t = 25 years. The corresponding annual risk profile for solution A is shown in Figure 12.9(a). Conversely, Solution B represents a high-risk low-cost solution with maximum annual risk of 1.29×10^5 USD and total maintenance cost of 1.21×10^4 USD. The decrease in the maintenance cost associated with solution B corresponds to a higher maximum annual

risk compared to solution A. As indicated in Figure 12.9(b), solution B is associated with only two inspections: inspections of section S5 at t = 17 years and section S1 at t = 22 years. The annual risk associated with solution B is shown in Figure 12.9(a). The probability of repair of S1 associated with Solution A at inspection times t = 9, 18, and 25 years is shown in Figure 12.10.

The inspection plans associated with the Pareto optimal solutions are compared with that with respect to regular (i.e., non-optimized) inspection plans. Figure 12.11 shows the time-variant risk under regular inspection plans (i.e., Plan D and E). Plan D represents the inspection of sections S1, S2, and S5 at t = 8, 16, and 23 years. Plan E dictates the inspection of sections S1, S2, and S3 at the schedule associated with plan D. The inspection plan associated with plan D has a maximum annual expected risk of 8.41×10^4 USD and total maintenance cost of 7.03×10^4 USD. Plan E is associated with a maximum annual expected risk of 9.41×10^4 USD and total maintenance cost of 4.82×10^4 USD. Solution C in Figure 12.8 and Figure 12.10 an optimal solution obtained from the Pareto solutions with similar maintenance cost as plan D. As shown in Figure 12.11, this optimal solution yields a much smaller maximum annual risk at the end of the investigated time interval compared to plan D.

12.7. CONCLUSIONS

This chapter presents a framework for optimum inspection and repair planning of ship structures to mitigate life-cycle risk. The proposed approach integrates life-cycle probabilistic risk assessment with multi-objective optimization techniques to determine

optimum maintenance planning that can ultimately assist the decision maker in making risk-informed choices.

The following conclusions can be drawn:

1. Optimum inspection plans can be obtained based on the proposed bi-objective optimization approach. This approach provides the opportunity to observe the optimum solutions with different trade-offs and select the one which best fits the decision maker's needs. Each of the Pareto optimal solutions corresponds to an optimum inspection and repair plan.
2. Corrosion and fatigue have an impact on the risk of ships. In the example considered the effect of corrosion is larger than that associated with fatigue cracking, while fatigue cracking acts as the main factor for risk assessment close to the end of the service life when considering both corrosion and fatigue.
3. The structural deteriorations associated with both corrosion and fatigue should be considered for the risk assessment of ship structures. Otherwise, the risk would be underestimated.
4. The risk associated with structural failure increases with time due to corrosion and fatigue. The optimum inspection and repair planning depends on the budget limit. Several inspection actions are needed for a ship structure to meet the risk-based performance assessment. The risk associated with ship failure can be reduced significantly by optimum inspection and repair planning.

Table 12.1 Characteristics of the VLCC and parameters of random variables associated with ultimate bending moment assessment

Random variable	Mean	C.O.V.	Distribution type	Reference
Yield strength at deck and bottom	315 MPa	0.1	Normal	Paik and Frieze, 2001
Yield strength at side shell	235 MPa	0.1	Normal	Paik and Frieze, 2001
Young's modulus	205,800 MPa	0.03	Lognormal	Paik and Frieze, 2001
Ultimate bending moment for sagging	22,601 MN-m	0.089	Lognormal	Computed
Ultimate bending moment for hogging	22,405 MN-m	0.088	Lognormal	Computed

Note: C.O.V.: coefficient of variation.

Table 12.2 Parameters associated with corrosion and fatigue crack assessment (based on Kwon and Frangopol, 2012)

Random variable	Mean	C.O.V.	Distribution type
Deck plating and longitudinal annual corrosion rate	0.065 mm/year	0.5	Weibull
Side annual corrosion rate	0.03 mm/year	0.5	Weibull
Bottom plating annual corrosion rate	0.12 mm/year	0.5	Weibull
Bottom shell annual corrosion rate	0.065 mm/year	0.5	Weibull
Initial crack length	0.882 mm	0.36	Lognormal
Crack growth parameter, C	2.37E-13	0.5	Lognormal

Table 12.3 Parameters of the random variable associated with consequence evaluation; the costs in USD refer to the year 2014

Random variable	Mean	C.O.V	Distribution type	Reference
Modelling uncertainty of ultimate strength	1	0.15	Normal	Paik and Frieze, 2001
Modelling uncertainty in still water bending moment	1	0.05	Normal	Paik and Frieze, 2001
Modelling uncertainties of wave-induced bending moment	0.9	0.15	Normal	Paik and Frieze, 2001
Still water bending moment of sagging	3,865 MN-m	0.38	Normal	Computed
Still water bending moment of hogging	5,472 MN-m	0.4	Normal	Computed
Wave induced bending moment	1,161 MN-m	0.4	Gumbel	Kwon and Frangopol, 2012
Construction cost	400 USD/m^2	0.2	Lognormal	Rigterink *et al.* 2013
Ship type factor *STF*	7	DNA	DNA	Miroyannis, 2006

Note: DNA: does not apply.

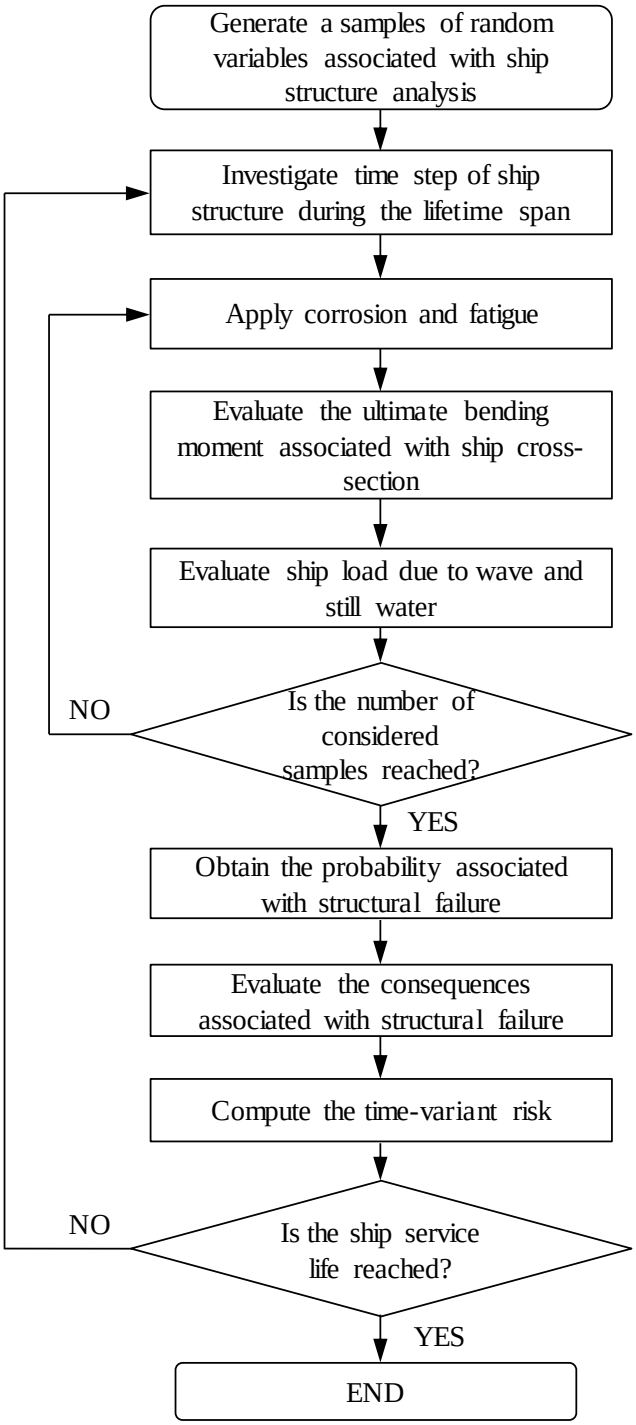

Figure 12.1 Flowchart for the life-cycle risk assessment of ship structures considering corrosion and fatigue

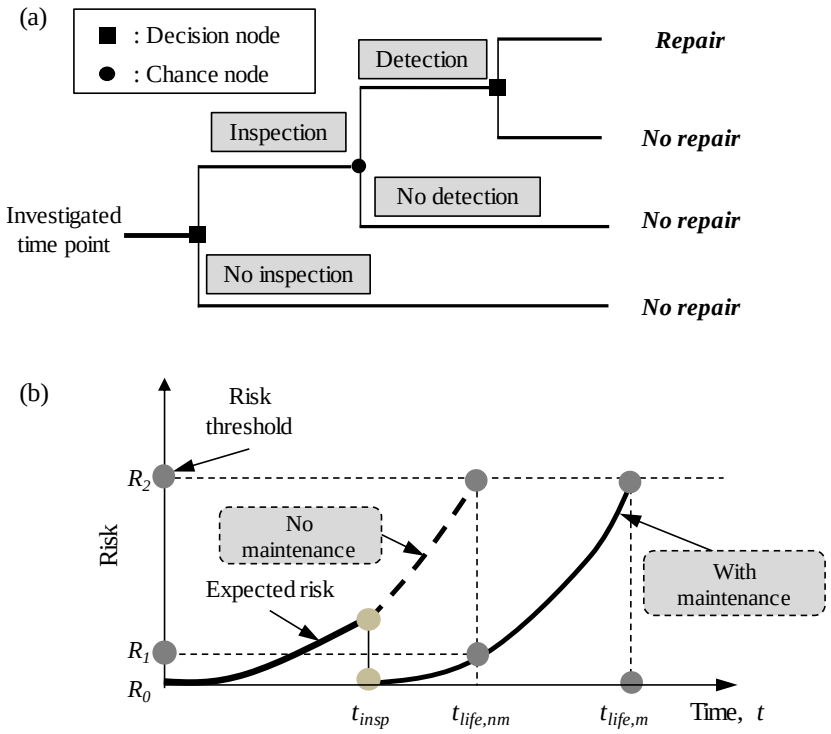

Figure 12.2 (a) Decision tree model to formulate the inspection and maintenance planning and (b) effect of maintenance on time-variant risk

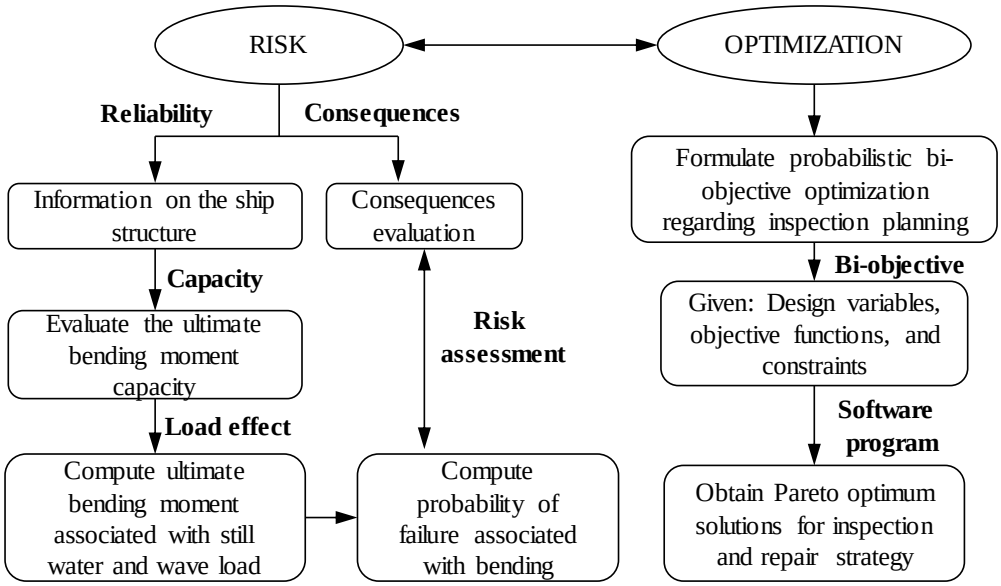

Figure 12.3 Flowchart for the life-cycle optimal inspection and maintenance planning

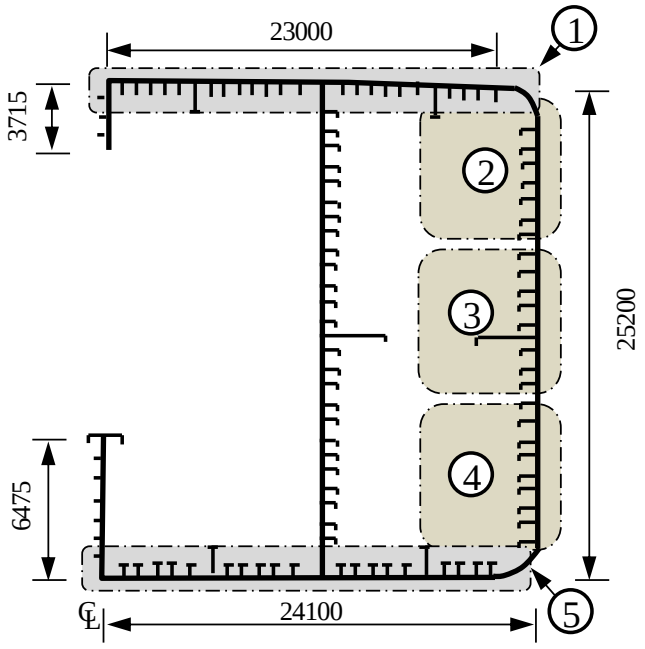

Note: all dimensions are in mm

Figure 12.4 Mid-ship section details under investigation (adapted from Khan and Parmentier, 2006)

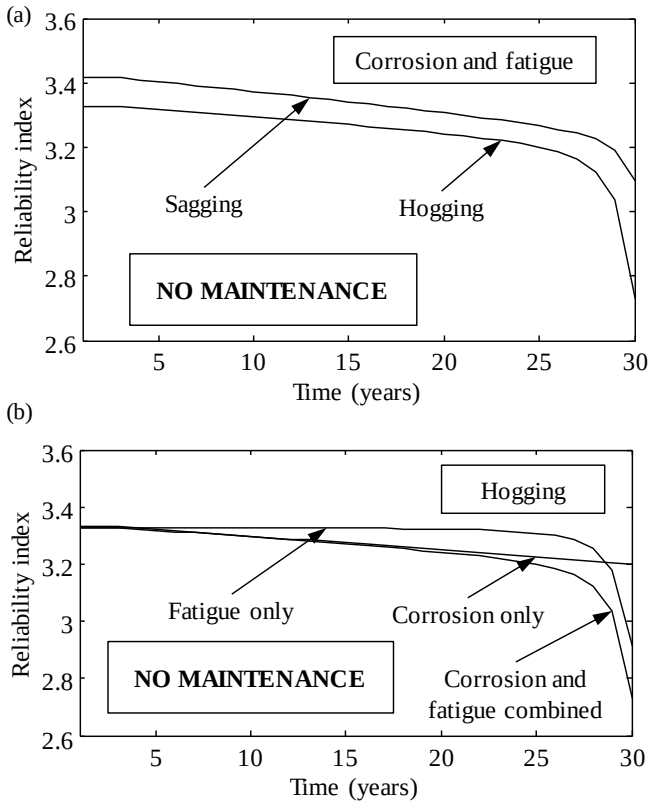

Figure 12.5 (a) Life-cycle reliability index for sagging and hogging and (b) time-variant reliability index for hogging of the VLCC considering corrosion, fatigue, and both corrosion and fatigue

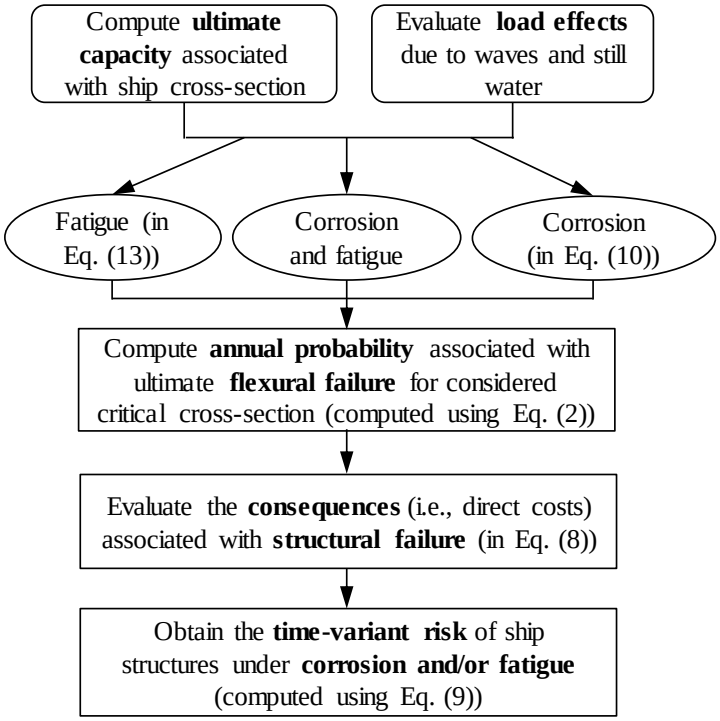

Figure 12.6 Framework for risk assessment of ship structures under corrosion and/or fatigue

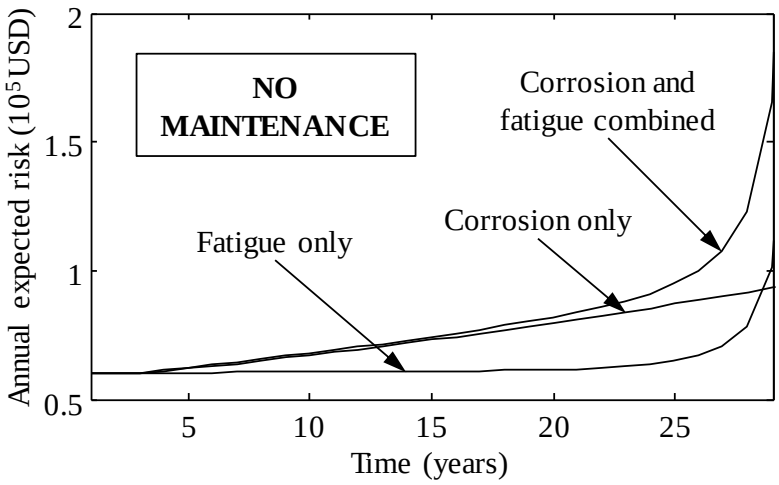

Figure 12.7 Time-variant risk of the VLCC without maintenance considering corrosion and fatigue separately and together

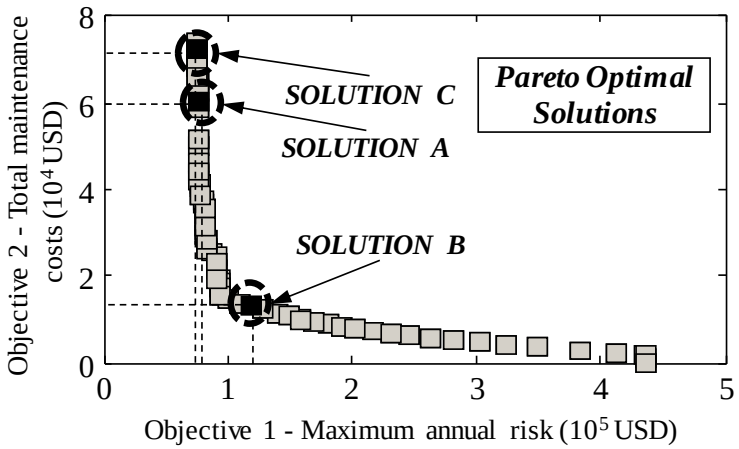

Figure 12.8 Pareto optimal solutions associated with the VLCC with a 30-year time interval

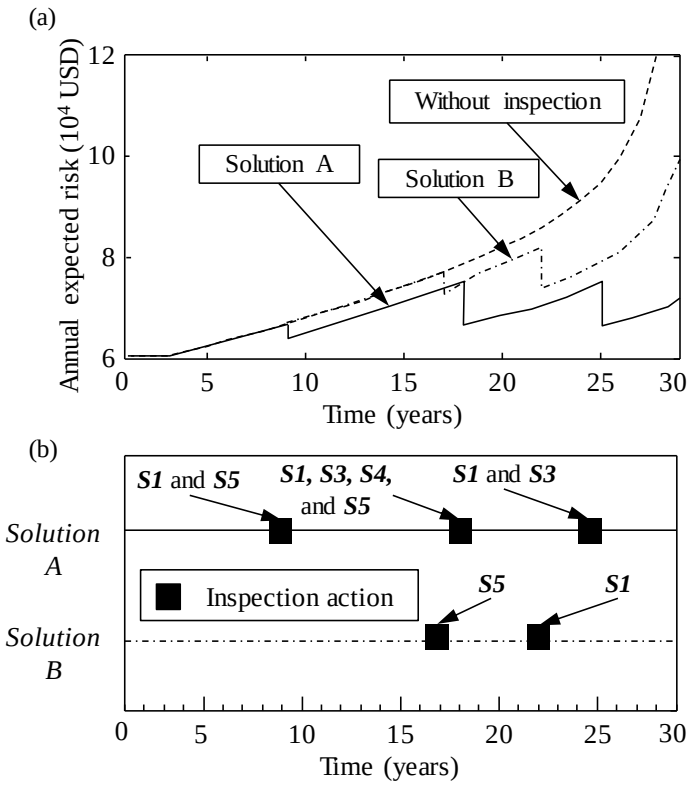

Figure 12.9 (a) Time-variant risk of the ship and (b) inspection schedules associated with Solution A and B considering a 30-year time interval

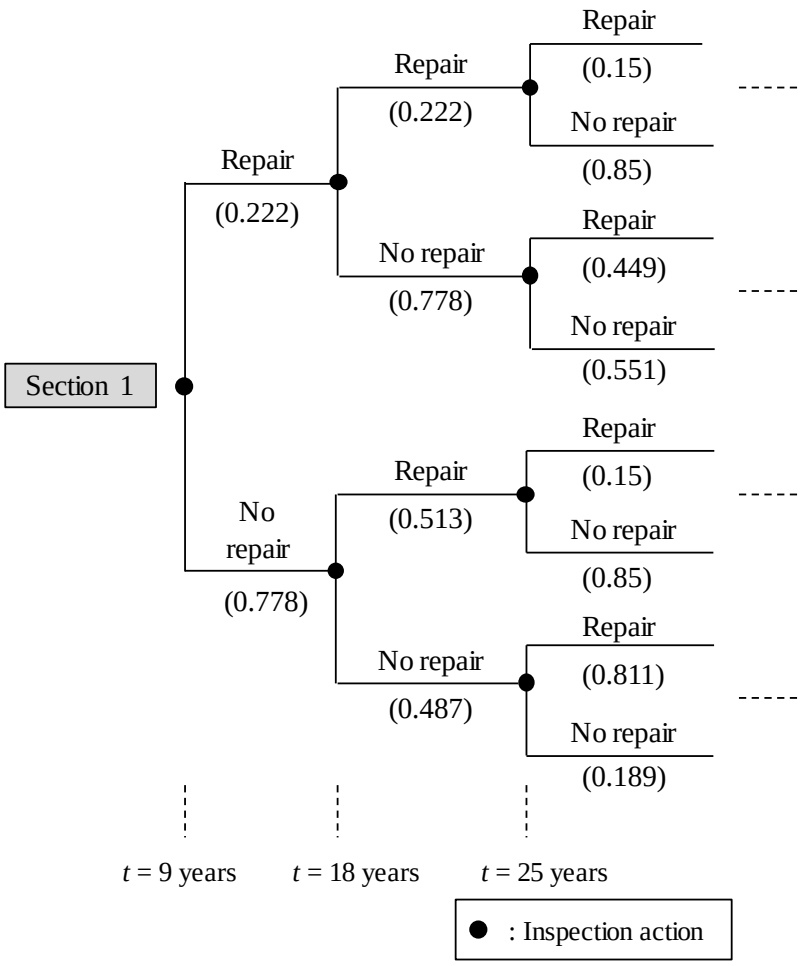

Figure 12.10 Probability of repair Section 1 associated with Solution A at t = 9, 18, and 25 years (probabilities are indicated in parentheses)

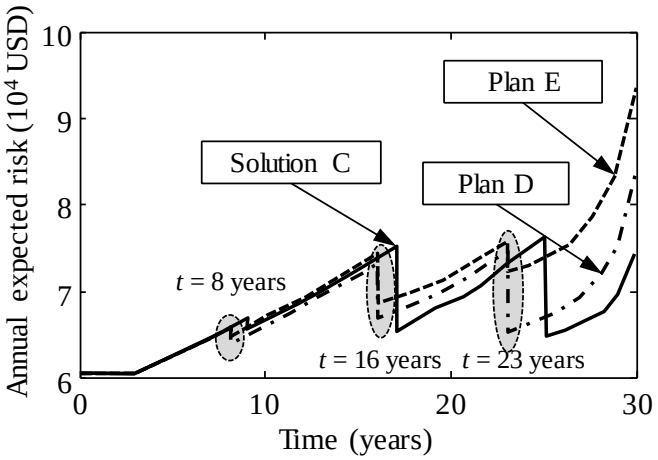

Figure 12.11 Time-variant risk of the ship associated with optimal Solution C and non-optimized plan D and E considering a 30-year time interval

CHAPTER 13

INCORPORATION OF RISK AND UPDATING IN INSPECTION OF FATIGUE-SENSITIVE DETAILS

13.1. INTRODUCTION

Fatigue crack of ship critical details has always been a main concern associated with ship operation and is one of the deterioration mechanisms that can affect structural performance. Fatigue cracks may propagate and reach critical sizes; ultimately they can lead to unstable crack growth and/or unanticipated out of service. Generally, these cracks are prone to initiate at welded details due to the existence of initial defects, as qualitatively shown in Figure 13.1(a), caused by several factors such as welding, fatigue loading, and/or environment (SSC 1995; DNV 2010). Traditionally, non-destructive inspections (NDIs) are applied to ship structures periodically without considering the damage level associated with time. Inspection results can be used to update fatigue reliability and risk of investigated structural systems during their remaining service life using Bayes' techniques. Fatigue crack assessment should be performed during service life of ship structures in order to prevent loss of survivability and to achieve economic and reliable performance. This chapter aims to develop a probabilistic framework incorporating risk and updating in the inspection of fatigue-sensitive details of ship structures.

The fatigue deterioration process of structural systems is highly uncertain. Therefore, a probabilistic approach is necessary for considering this deterioration process. The

assessment of fatigue crack size under uncertainty is qualitatively shown in Figure 13.1(b). As indicated, the fatigue crack size increases significantly with time and uncertainties are incorporated within the process. The uncertainties are also associated with inspection events. The outcomes of an inspection event are affected by many factors, such as type of inspection method, human factors, and inspection quality. Consequently, uncertainties should be incorporated within the risk-informed decision making and updating. During the past few decades, the field of ship structural reliability assessment has been developed considerably (Cramer and Friis-Hansen 1994; Mansour *et al.* 1996; Wirsching *et al.* 1987; Lukic and Cremona 2001a; Ku *et al.* 2004; Kwon and Frangopol 2012; Rabiei and Modarres 2013). In its most broad terms, structural reliability is a measure of the probability of a system's survival given a limit state. Reliability-based structural performance indicators reflect the uncertainty in load, resistance, and modelling. A risk-based performance indicator provides means of combining the probability of components or system failure with consequences of this event (Dong and Frangopol 2015b).

There has been a lack of research that focuses on risk-based performance assessment of ship structures. The importance of risk as a performance indicator for the inspection planning decision making is emphasized in this chapter. The schematic flowchart of risk-informed inspection decision making process is shown in Figure 13.2. The first step associated with the proposed methodology is to identify structural deterioration, possible hazard scenarios, and structural details that should be inspected. Subsequently, qualitative and quantitative risk assessments are conducted for the investigated details. Generally,

qualitative risk assessment requires approximate estimates of failure likelihood and its consequences, while quantitative indicators of failure likelihood and consequences are needed for quantitative assessment associated with fatigue-sensitive details under high qualitative risk. To the best knowledge of the authors, there have been no studies focusing on the risk assessment and updating of multiple fatigue-sensitive details at system level using inspection information. This chapter addresses this issue in detail. Finally, given the performance threshold associated with risk, the inspection decision can be made in a probabilistic life-cycle context (Frangopol 2011).

The information on inspected details can be used to update deterioration models of a structural system to reduce epistemic uncertainty. The fatigue details associated with a given structural system are correlated due to common parameters associated with materials, design, fabrication, loading, and operational conditions. Based on these correlations, the inspection information of one particular detail can be used to update deterioration performance of others uninspected details. Probabilistic models have been used to evaluate and update the fatigue reliability using inspection information. These models can be used to determine the optimal number of inspected details to make the inspection strategies efficient and economic. Ayala-Uraga and Moan (2002) and Moan and Song (2000) investigated system fatigue reliability issues considering fatigue failure and updating based on inspection; Chen *et al.* (2011) proposed a methodology for inspection planning on the basis of Palmgren-Miner's rule and fracture mechanics; Huang *et al.* (2013) computed the fatigue reliability index of a complex welded structure as a series model under multiple cracks; Maljaars and Vrouwenvelder (2014) presented a

reliability-based updating considering multiple critical locations in a bridge. While previous studies have emphasized on reliability-based decision making process using updating, there is limited research regarding transferring the information associated with a given inspection event to risk assessment of other details and/or system performance assessment considering numerous details. Another novelty of this chapter derives from the risk assessment at system level under a specific system failure event. Based on the system risk, the inspection planning and repair priority among the investigated fatigue sensitive systems can be identified. In turn, the inspection results can be used to update risk and the timing for the following inspection.

This chapter presents a probabilistic framework for fatigue reliability and risk assessment and updating through inspection events. The flowchart for risk-informed inspection planning for a structural system under fatigue damage considering updating under multiple fatigue-sensitive details is shown in Figure 13.3. The computation associated with fatigue damage is performed using probabilistic fracture mechanics. Bayesian techniques are adopted for reliability and risk updating of both inspected and uninspected fatigue-sensitive details. Additionally, correlation of fatigue damage among different critical details is considered and incorporated within risk assessment and updating. A number of analyses have been performed to investigate the fatigue risk assessment and updating. A methodology to quantify the risk using rating functions, which have the ability to take different consequences into account, is proposed in this chapter. By using rating functions, the consequences with different units can all be transferred into the rating values. Additionally, the decision maker's preference can also

be incorporated within the rating assessment process. The optimal inspection plan can be established on the basis of the comparison between the updated risk and target risk. Moreover, the inspection decision making process involves consideration of economic, environmental, and other factors. Applications are made on an existing tanker with multiple fatigue-sensitive details. Overall, this approach can aid in risk-informed decision making of ship structures under fatigue damage. The work in this chapter is based on a published paper Dong and Frangopol (2016a).

13.2. FATIGUE RELIABILITY ANALYSIS: A REVIEW

Fatigue cracks generally initiate at structural discontinuities such as the welded detail of the intersection of longitudinal and transverse internal supporting members as shown in Figure 13.1(a). One of the commonly used methods is Paris law which uses linear elastic fracture mechanics to predict the crack growth (Paris and Erdogan 1963). The fatigue crack reliability analysis is related to various factors such as stress range, material property, welding residual stress, loading history, and environmental condition. Generally, all uncertainties involved in loading, material property, crack size and stress intensity factor should be considered in this process. The performance function of an individual structural detail is defined as

$$M_i(t) = a_{ci} - a_i(t) \tag{13.1}$$

where a_{ci} is the critical crack size and $a_i(t)$ is the crack size of fatigue-sensitive detail i at time t. The critical crack size is often selected as through-thickness crack associated with a plate or weld. It can also depend on the size associated with brittle or ductile failure of

details under specified loading effect. Given an initial crack size a_0, the random crack size after time t can be computed using a crack growth propagation model. The performance function associated with fatigue detail i can be expressed as (Moan and Song 2000)

$$M_i(t) = \int_{a_{0i}}^{a_{ci}} \frac{da}{(\varepsilon_{Yi} \cdot Y(a) \cdot M_k \cdot \sqrt{\pi a})^m} - C_i \cdot \nu_{0i} \cdot t \cdot {\varepsilon_{Si}}^m \cdot {A_i}^m \cdot \Gamma(1 + m_i / B_i) \quad (13.2)$$

where a_{oi} is the initial fatigue crack size associated with detail i; ν_{0i} is the average zero-crossing rate of stress cycle; ε_S is the modeling uncertainty associated with stress modeling; ε_Y is the modeling uncertainty associated with geometry function; Γ is the Gamma function; a is crack size; C and m are material constants which can be obtained from the experiments on simple specimens; A and B are the parameters associated with Weibull scale and shape, respectively; $Y(a)$ is geometrical correction factor depending on the geometry of cracked detail, nature of load distribution (e.g., bending and membrane), and the crack size with respect to the detail dimension; and M_k is a stress magnification factor which is associated with local weld geometry. The probability that the fatigue crack size exceeds a critical size within the time t is

$$P_i(t) = P(M_i(t) \le 0) \quad (13.3)$$

In general, P_i can be computed using Monte Carlo simulation, or by first or second-order reliability methods (Estes and Frangopol 1998). The reliability index β is

$$\beta_i = \Phi^{-1}(1 - P_{f,detail\,i}) \quad (13.4)$$

where Φ^{-1} denotes the inverse of the standard normal cumulative distribution function.

The previous studies associated with reliability-based damage analysis of fatigue-sensitive details are reviewed herein. Wirsching *et al.* (1987) proposed an approach for the reliability-based fatigue analysis based on fracture mechanics considering service life of a detail; Cramer and Friis-Hansen (1994) presented a computational procedure for the optimum design and inspection of a welded fatigue-sensitive component using reliability analysis; Lukic and Cremona (2001a) presented a method for the fatigue reliability assessment of welded joints using probabilistic fracture mechanics; and Kwon and Frangopol (2012) incorporated the component level fatigue reliability analysis in the life-cycle maintenance of aluminum ships. As revealed, the reliability index was used as a performance indicator for the damage assessment of fatigue-sensitive details. Additionally, the reliability index was widely adopted in the inspection planning considering the updating process at the component level. Moan *et al.* (1997), Moan and Song (2000), and Ayala-Uraga and Moan (2002) developed a series of reliability-based fatigue damage updatings for ships and offshore structures considering different environmental conditions and inspection methods; Ku *et al.* (2004) developed an inspection plan for a floating structure based on reliability-informed decision and updating; Chen *et al.* (2011) investigated the inspection planning at component level considering reliability index and fracture mechanics; Berg *et al.* (2014) investigated the updated fatigue reliability of uninspected joints using the inspection data; and Maljaars and Vrouwenvelder (2014) investigated reliability of multiple fatigue details using Bayesian updating techniques considering different inspection methods. As indicated, risk, as a performance indicator, has not been adopted in these studies for the fatigue

damage and updating assessment. The number of studies considering risk-based fatigue assessment and updating is very limited. Goyet *et al.* (2002) presented an approach for risk-based inspection planning of offshore production using qualitative failure consequence at the component level; Tammer and Kaminski (2013) presented a general approach associated with the risk-based inspection considering fatigue damage at the component level where the consequences were assessed, without an explicit expression, based on the severity levels; and Lassen (2013) presented a framework for risk-based inspection planning of fatigue cracks in welded steel structures at component level without quantifying the consequences associated with failure. The system level risk assessment and detailed quantification of probability of failure and consequences associated with failure have not been well documented in these studies. Furthermore, to the best knowledge of the authors, there have been no studies focusing on the risk-informed updating of multiple fatigue-sensitive details at system level.

13.3. UPDATING BASED ON INSPECTION EVENT

13.3.1. Inspection modelling

Generally, the probability of detecting a crack depends on crack size and inspection method. Many efforts have been devoted to evaluate the quality of nondestructive inspection methods of fatigue cracks. Among the available nondestructive inspection techniques, liquid penetrant, ultrasonic, magnetic particle (MP), and acoustic emission are commonly employed for fatigue crack detection (Soliman and Frangopol 2014). The probability of detection (PoD) associated with different inspection methods has been indicated in previous studies, including BS-7910 (2013), Moan *et al.* (1997), and Visser

(2002). There are different types of PoD associated with fatigue cracks. The commonly used exponential form is adopted in this chapter (Moan and Song 2000; Chen *et al.* 2011)

$$PoD(a) = 1 - \exp(-a/\lambda_D) \tag{13.5}$$

in which λ_D is the mean detectable crack size. This PoD is applicable to several inspection types including close visual and MP inspections. These two inspection methods are adopted herein.

13.3.2. Reliability updating

In this chapter, the event based inspection updating is adopted based on two inspection results: (a) no crack detected, and (b) crack detected and repaired. If no fatigue crack is detected, the updating can be performed within the original fatigue limit state. If repair actions are conducted, the physical changes need to be considered in the estimation of limit state function. In this chapter, it is assumed that once the fatigue crack is detected, it will be immediately repaired. The updated probability of failure of the *i*th detail under fatigue given inspection event *j* can be formulated as follows (Moan and Song 2000)

$$P_{i,up} = P[M_i(t) \le 0 \,|\, IE_j(t_{IE})] = \frac{P[(M_i(t) \le 0) \cap IE_j(t_{IE})]}{P[IE_j(t_{IE})]} \tag{13.6}$$

where M_i is limit state function associated with detail i; IE_j is the inspection event j; and t_{IE} is the inspection time.

Generally, fatigue failure modes associated with individual details of a structural system are correlated due to the common uncertain factors. The initial crack sizes are correlated among all the investigated details due to the common fabrication quality. Additionally, the fatigue failure modes are also partly correlated due to the statistical

dependence associated with common material characteristics. The loading effects of these investigated details are also correlated, leading to the correlation of the stress range associated with the investigated details. Eq. (13.6) can be applied to the inspected and uninspected fatigue-sensitive details.

The inspection event associated with no fatigue crack detected can be expressed as (Moan and Song 2000)

$$IR_{i,no}(t_{IE}) = a_D - a_i(t_{IE}) = \int_{a_{0i}}^{a_D} \frac{da}{(\varepsilon_{Yi} \cdot Y(a,X) \cdot M_k \cdot \sqrt{\pi a})^m} - C_i \nu_0 t_{IE} \varepsilon_S{}^m A_i{}^m \Gamma(1+m/B) > 0 \quad (13.7)$$

where a_D is the detectable crack size and $a_i(t_{IE})$ is the predicted crack size associated with detail i at inspection time t_{IE}. Given the repair actions, the reliability index associated with fatigue crack damage should be recomputed. Then, the limit state associated with repaired details can be established.

As indicated previously, the failure modes associated with fatigue cracks of individual details are generally statistically dependent due to common random variables. The initial crack sizes are correlated. The correlation coefficient $\rho(a_{0i}, a_{0j})$ is used to quantify the statistical dependence due to common fabrication among initial fatigue crack sizes associated with different fatigue-sensitive details. The crack growth parameters are also correlated; the correlation coefficient $\rho(\ln C_i, \ln C_j)$ reflects the dependence associated with common material characteristics. Additionally, the scale parameters of the stress ranges are correlated due to common loading effects of individual details. Finally, the modelling uncertainty factors are considered to be correlated among all fatigue-sensitive details. Given correlation coefficients of the common random variables used in fatigue

reliability assessment and inspection event (i.e., Eqs. (13.2) and (13.7)), the fatigue reliability index of inspected and uninspected fatigue-sensitive details can be updated using Eq. (13.6). Regarding the inspected detail, the correlation coefficient among the common random variables associated with Eqs. (13.2) and (13.7) is 1.0 (e.g., $\rho(\ln C_i, \ln C_j) = \rho(a_{0i}, a_{0j}) = 1.0$).

As there are many structural details with potentially dangerous cracks, the inspection actions are applied to these fatigue-sensitive details simultaneously. It is assumed that among the N_{insp} inspected details, r do not show cracks while fatigue cracks are detected at the remaining $N_{insp} - r = s$ inspected details. Inspections are applied to the N_{insp} fatigue sensitive details simultaneously. The updated reliability of the investigated detail (e.g., inspected, uninspected) under this scenario associated with N_{insp} inspected fatigue-sensitive details can be computed as

$$P_{i,up} = P[M_i(t) \le 0 \,|\, IR_{1,no} \cap IR_{2,no} \cap ... \cap IR_{r,no} \cap IR_{r+1,yes} \cap IR_{r+2,yes} \cap ... \cap IR_{r+s,yes}] \quad (13.8)$$

where $IR_{i,no}$ is the inspection event associated with no fatigue crack detected at fatigue-sensitive detail i and $IR_{i,yes}$ is the inspection event associated with fatigue crack detected.

13.4. RISK ASSESSMENT

Risk-based performance indicators combine the probability of failure with the consequences associated with this particular event. Although SSC (SSC 2000) proposed an approach for risk-based management of ship structures, the uncertainties associated with consequence evaluation and quantification of probability of failure were not discussed in detail. The risk assessment process depends on various factors such as

environmental loading conditions, failure mode, loss of life, environmental pollution and possible economic and social loss (Dong and Frangopol 2015a). For example, the fatigue crack may lead to cargo oil spill. The consequences associated with oil spill are significantly adverse and in turn the fatigue crack detail should be inspected and paid special attention to prevent hazardous consequences.

Risk, which combines the probability of occurrence of a specific event with the consequence associated with this event, is a crucial performance indicator for structural systems. A formulation of risk is (Ang and De Leon 2005)

$$R = P \cdot C_f \tag{13.9}$$

where P is probability of occurrence of an adverse event and C_f is the consequence of this event.

13.4.1. Consequence evaluation

As mentioned previously, risk is regarded as an important performance indicator within the fields of civil and marine structural engineering. Based on the reliability approach, the probability of failure (i.e., probability that the fatigue crack size secedes a critical size) can be computed. The probability of failure associated with fatigue crack can be obtained using Eq. (13.3). The second key factor to be assessed for risk assessment is consequence. The potential major consequences of failure include economic loss (e.g., loss of vessel), social (e.g., downtime), and environmental impact (e.g., oil spill and pollution). The consequence value can range from low, which is very unlikely to have a significant effect on safety and serviceability, through severe, where the threats to safety and life are significant. Generally, assessing consequence associated with a structural

detail failure is a challenging process. Evaluation of the potential consequences may be based on historical data and analyses to define critical details to hull structural integrity (SSC 2000). Consequence assessment is of vital importance in risk ranking of structural details since similar details at two different locations can have significantly different consequences. For example, a crack in the side shell of a cargo oil tank may have much more serious consequences than a similar crack in a deck. This is because the former can cause oil spill and pollution.

The repair cost C_{rep} is generally computed as percentage of a construction cost C_{cons}. The ratio C_{rep}/C_{cons} is considered to be random. The repair action considered is replacing the cracked detail with a new one. The total cost of a repair should include material, labor, dry dock charge, tank cleaning, staging and down time. Consequently, the cost to replace the damaged details is larger than the construction cost. Generally, the repair cost for a ship detail can be computed as (Lukic and Cremona 2001b; Rigterink *et al.* 2013)

$$C_{rep} = c_{Cons} \cdot W \cdot L \cdot r_{cr} \tag{13.10}$$

where c_{Cons} is the construction cost per unit area (e.g., USD/m^2); L and W are the length (e.g., m) and width (e.g., m) associated with structural detail under investigation, respectively; and r_{cr} is ratio between repair and construction cost.

The consequences are assessed using different units. The repair cost can be established using the monetary value; while the consequence associated with oil spill can be computed in terms of the amount (e.g., tons). A rating system that measures the consequence of failure can be developed. Expert opinion and experience from classification society rules could be adopted as guides in consequences evaluation

process. An example of rating system associated with consequences resulting from fatigue crack damage is provided in Table 13.1. The rating factor associated with oil spill is much larger than that associated with repair cost. Based on this table, different types of consequences can be converted into rating factor. Within the defined boundaries associated with the rating factor, the decision maker should specify the value of this factor. Based on these values, a consistent matrix is developed and the rating factor associated with consequences can be estimated.

Typically, a larger rating factor should be assigned to a larger repair cost. The rating can be defined using linear and exponential functions. The hypothetical value could be adjusted considering the decision maker's value and experienced engineers' input. Rating functions are adopted herein to quantify the consequence associated with fatigue failure; consequently different types of consequences could be transferred into rating factors incorporating the preference of the decision maker. For example, an exponential rating function associated with repair cost C can be expressed as follows (Ang and Tang 1984)

$$Rt_c(C) = \left(\alpha_1 + \alpha_2 \exp(\alpha_3 \cdot \frac{C - C_{\min}}{C_{\max} - C_{\min}}) \right) \cdot (Rt_{\max} - Rt_{\min}) + Rt_{\min} \qquad (13.11)$$

where α_1, α_2, and α_3 are parameters associated with rating functions; C is the consequence under investigation (e.g., repair cost); $Rt_c(C)$ is the rating factor associated with consequence C; Rt_{min} and Rt_{max} are the minimum and maximum values associated with rating factor, respectively; and C_{min} and C_{max} are the minimum and maximum cost values, respectively.

13.4.2. Expected risk ranking

Ship structures have various fatigue-sensitive details. Correlation among the performance functions of these details should be considered in the system reliability and risk analyses processes. The uncertainties and correlations among the common random variables used in fatigue reliability analysis of different fatigue-sensitive details should be considered in the total risk ranking assessment of a given structural system. The correlation metric associated with the fatigue reliability analysis of different details should also be considered in the risk assessment process. The expected risk ranking associated with failure of a single detail among *n* details can be computed as

$$R_{rk,1} = P(\overline{E_{D1,S}}E_{D2,S}E_{D3,S}\cdots E_{Dn,S})\cdot Rt_c(C_{D1,F}) + P(E_{D1,S}\overline{E_{D2,S}}E_{D3,S}\cdots E_{Dn,S})\cdot Rt_c(C_{D2,F}) + \ldots + P(E_{D1,S}E_{D2,S}E_{D3,S}\cdots\overline{E_{Dn,S}})\cdot Rt_c(C_{Dn,F}) \quad (13.12)$$

where $C_{Di,F}$ is the consequence considering the fatigue-sensitive detail *i* failure while all other details survived; Rt_c is the rating factor associated with the cost as indicated in Eq. (13.11); $E_{Di,F}$ and $E_{Di,S}$ are the events of failure and survival of detail *i*, respectively; and $\overline{E_{Di,S}}$ is the complement of $E_{Di,S}$. The probability $P(\overline{E_{D1,S}}E_{D2,S}E_{D3,S}\cdots E_{Dn,S})$ associated with one component failure can be computed using a parallel system. The probability of failure of a parallel system can be expressed by the probability of intersections of component failure events

$$P_{PS} = P\left(\bigcap_{i=1}^{N}\{g_i(\boldsymbol{X})\le 0\}\right) \quad (13.13)$$

where $g_i(\boldsymbol{X})$ is the performance function associated with fatigue-sensitive detail *i* under investigation. The probability of system failure associated with series, parallel, and

series-parallel systems can be calculated using first/second order reliability method or simulation methods. The correlation between the random variables used in the fatigue limit state is considered in the reliability computational methods. Due to the common random variables (e.g., $\ln C_i$ and $\ln C_j$) used in the failure modes associated with different fatigue-sensitive details, these failure modes are also correlated. The methodology proposed by Ditlevsen (1979) is employed herein to account for the correlation among the components of a system. The same approach has been adopted by Estes and Frangopol (1998) to compute the system reliability. The probability of system failure can be computed accordingly. Given the adverse consequence associated with the failure event, the risk associated with one component failure can be computed by using Eq. (13.12).

The risk ranking associated with repair loss due to fatigue sensitive details is emphasized herein. The total expected risk ranking of n fatigue-sensitive details can be computed as

$$R_{RK} = \sum_{D1,i=1}^{2} \sum_{D2,i=1}^{2} \sum_{D3,i=1}^{2} \cdots \sum_{Dn,i=1}^{2} P(E_{D1,i} \bigcap E_{D2,i} \bigcap E_{D3,i} \cdots \bigcap E_{Dn,i}) \cdot Rt_c(C_{D1,i;D2,i;\cdots;Dn,i}) \quad (13.14a)$$

$$E_{D1,1} = E_{D1,F} = \overline{E_{D1,S}} \quad (13.14b)$$

$$E_{D1,2} = E_{D1,S} \quad (13.14c)$$

where n is the number of fatigue-sensitive details. Given the consequence with respect to the specified system condition, the total expected risk ranking can be computed.

13.4.3. Decision making criteria and optimal inspection

Most of the previous studies emphasized on the reliability-based inspection planning for marine structures without considering correlation among the inspected and uninspected

details and failure consequences (Kim *et al.* 2011; Soliman *et al.* 2013). Risk is a better structural performance indicator than reliability. The risk associated with repair loss of fatigue-sensitive details at both component and system levels is emphasized herein.

Risk is selected as the main performance indicator to be included in the decision making process due to the fact that it contains information regarding both the probability of failure and its associated consequences. Threshold values for classifying the risk levels at the fatigue-sensitive details have to be set. Generally, acceptable risk levels for fatigue critical details must be determined using expert opinion, engineering judgment, vessel cost, and classification rules. The fatigue reliability and risk ranking are updated using Bayesian approach, and then the time interval to the subsequent inspection action can be obtained. Risk ranking assessment and relevant management strategies associated with different risk performance threshold are indicated in ABS (2003). A structural detail with a high-risk priority rating has high risk associated with it, implying a high expected loss when it fails. A risk-based management strategy implies that these decisions are based on the risk ranking associated with each fatigue-sensitive detail. The risk-based priority ranking can be used to determine how the various fatigue-sensitive details should be maintained. According to SSC (2000), the low, moderate, high, and extreme risk levels are associated with the rating intervals $0 < R_{RK} \leq 10$, $10 < R_{RK} \leq 1000$, $1000 < R_{RK} \leq 10000$, and $R_{RK} > 10000$, respectively. The low, moderate, high, and extreme risks are associated with maintenance strategies that should give the lowest, moderate, high, and the highest priority for maintenance, respectively.

The risk assessment and decision making process at the system level are also investigated herein. In order to quantify the risk associated with a system composed of multiple fatigue-sensitive details, the system failure mode should be identified firstly. A system of *n* fatigue-sensitive details is assumed to fail if m adjacent details fail. The configuration of the series-parallel system is shown in Figure 13.4. The event associated with system failure can be expressed as follows:

$$E_{SysF} = (E_{D1,F} \cap E_{D2,F} \cdots \cap E_{Dm_{ad},F}) \cup (E_{D2,F} \cap E_{D3,F} \cdots \cap E_{Dm_{ad}+1,F}) \cup \cdots \cup (E_{Dn-m_{ad}+1,F} \cap E_{Dn-m_{ad}+2,F} \cdots \cap E_{Dn,F}) \quad (13.15)$$

where E_{SysF} is the event associated with system failure and m_{ad} is the number of adjacent details. The probability of system failure $P(E_{SysF})$ can be determined by using simulation and/or first/second order reliability analysis. Due to the correlation among the random variables used in fatigue assessment associated with different fatigue-sensitive details and the fact that the same variables are present in failure modes of parallel sub-systems in Figure 13.4, the events in Eq. (13.15) are also correlated. Given the consequence associated with system failure, the risk can be computed as the product of the probability of occurrence of failure and its associated consequence. Based on this risk, the inspection priority and planning can be obtained. Most of the previous studies considered one detail at a time, while a structure would have multiple fatigue-sensitive details. Due to the similar geometry and loading, the inspection information could be used to update the fatigue reliability and risk associated with multiple potential crack locations at system level.

13.5. ILLUSTRATIVE EXAMPLE

The proposed approach is illustrated on fatigue-sensitive details of an existing tanker. The investigated fatigue prone details are located at deck, bottom, and side shell. Generally, fatigue cracks are concentrated at the welded details (ABS 2003; DNV 2010). The location and dimensions of the investigated stiffeners are as follows (Chen *et al.* 2011): (a) Deck (web: 400 mm x 30 mm); (b) Bottom (web: 550 mm x 14.5 mm, flange: 180 mm x 22 mm); and (c) Side Shell (web: 540 mm x 12 mm; flange 120 mm x 18 mm). The fatigue reliability and risk ranking of the fatigue details are investigated considering uncertainties. The updating is also conducted in the illustrative example. Subsequently, the risk-informed optimal inspection is obtained by using the updating results.

13.5.1. Probabilistic fatigue crack growth and risk ranking assessment

In this section, the reliability index and risk ranking of the fatigue-sensitive detail located at the deck of the investigated tanker are computed. The time interval is assumed to be 30 years. According to Chen *et al.* 2011, the mean values of ln$A$ and 1/B for deck fatigue-sensitive detail are 2.05 and 2.17, and their coefficients of variation are 13.8% and 10%, respectively. The probability of fatigue failure of the deck $P_{f,Deck}$ is computed using Eqs. (13.2) and (13.3). The parameters involved in these equations are shown in Table 13.2. An equivalent initial flaw size distribution is adopted in the fatigue crack assessment and assumed to follow the Weibull distribution (Moan and Song 2000; Soliman *et al.* 2014). The geometrical correction factor Y is a function associated with crack size as well as other geometric parameters, such as the crack half-length and flange thickness. The stress magnification factor M_k depends on the crack depth and other geometric parameters, such

as flange thickness, weld height, and weld angle. The values of Y and M_k are based on Newman and Raju (1981) and have been widely used in previous studies for the fatigue damage assessment process. Given the random variables associated with geometric and fatigue crack growth, Y and M_k can be generated using Monte Carlo simulation (Lukic and Cremona 2001b; Maljaars and Vrouwenvelder 2014). Given all the parameters involved in fatigue reliability analysis, the probabilistic fatigue damage of the investigated deck fatigue-sensitive detail is obtained. The reliability index of this detail is computed using Eq. (13.4). The time-variant probability of fatigue failure and its associated reliability index are both shown in Figure 13.5. As indicated, the reliability index of the deck fatigue-sensitive detail decreases significantly with time.

The repair cost is computed using Eq. (13.10). Then based on Eq. (13.11), the rating factor is obtained. The parameters used in Eqs. (13.10) and (13.11) are shown in Table 13.2. The uncertainties associated with the unit construction cost and repair cost ratio are considered in the risk assessment process as indicated in this table. Herein, the boundary values Rt_{min} and Rt_{max} are 5,000 and 15,000, respectively. The risk ranking is computed as a product of probability of fatigue failure and the consequence rating factor associated with repair cost. Based on the results shown in Figure 13.5(a) and using Eq. (13.9), the risk ranking of the given detail is shown in Figure 13.6(a). As indicated, the ranking increases dramatically with time as no repair action is applied to the deck fatigue-sensitive detail. The mean, mean plus and minus one standard deviation of risk ranking are also shown in this figure. The probability density functions (PDFs) of risk ranking at t = 10 and 20 years are revealed in Figure 13.6(b) and their expected values are 125 and

496, respectively. As indicated, the dispersion of risk ranking increases significantly with time.

The rating factor associated with the failure consequence depends on the severity of this consequence as shown in Table 13.1. In order to demonstrate the advantage of using quantitative risk as a performance indicator, the risk rankings of two fatigue-sensitive details are evaluated. Detail A refers to the deck fatigue-sensitive detail investigated previously. The load parameters $\ln A$ and $1/B$ of detail B are 1.85 and 1.16, respectively. All other parameters involved in fatigue reliability analysis of detail B are the same as those associated with detail A. Following the same process of fatigue reliability analysis of detail A, the results of detail B are obtained and shown in Figure 13.7(a). As indicated, the reliability index of detail B is much larger than that of detail A during the investigated time interval. The detail A is more critical than detail B considering only the reliability index. The consequence of detail B fatigue failure can result in a high damage intensity associated with oil spill. The expected rating factor associated with detail B fatigue failure is 1,000,000 as indicated in Table 13.1. In order to compare the inspection priority of these two details using risk ranking, the quantitative risks are computed for details A and B and are shown in Figure 13.7(b). As indicated, although the reliability index of detail A is always smaller than that of detail B, the risk ranking of detail B is larger than that of detail A after t = 10 years. Consequently, different inspection priorities of these two details can be obtained using the reliability and quantitative risk-informed performance thresholds after 10 years. The PDFs of risk ranking of details A and B at t =

12 years are indicated in Figure 13.8. The dispersion of risk ranking of detail B is larger than that of detail A.

13.5.2. Fatigue reliability and risk ranking updating

The fatigue reliability and risk ranking of the fatigue-sensitive detail considering updating are investigated in this section. The detectable fatigue crack size follows an exponential distribution (Moan and Song 2000; Chen *et al.* 2011). Mean values of detectable crack size a_d associated with close visual and MPI methods are 2 and 0.89 mm, respectively. The inspection is performed at t = 4 years; it is assumed that no fatigue crack is detected. The conditional updated reliability index associated with the inspected deck fatigue-sensitive detail given no crack detected is computed using Eq. (13.6) and shown in Figure 13.9(a). As expected, the reliability index increases significantly given no crack is detected using MPI. The effect of inspection methods on the reliability updating is also investigated herein. As indicated in Eq. (13.7), the detectable crack associated with given inspection method affects the probability of detecting a crack within a fatigue-sensitive detail. This would affect the updated probability of failure of the investigated detail using Eq. (13.6). For a more advanced inspection method (e.g., MPI), the increase of reliability index is much larger than that associated with a less advanced method (e.g., visual inspection) given no crack detected. The updated reliability index at t = 4 years using MPI is larger than the initial value at t = 1 year due to the fact that the detail has a significant amount of fatigue capacity remaining. Additionally, the updated expected risk ranking of the inspected detail located at the deck using different inspection methods is shown in Figure 13.9(b). As indicated, there is a huge difference

between the expected risk rankings of the inspected detail using different inspection methods.

The fatigue failure modes of individual detail of a structural system are correlated due to common uncertainties. The correlation coefficients for slight, moderate, and strong correlation among random variables in different fatigue-sensitive details are assumed 0.3, 0.5, and 0.8, respectively. Due to the common random variables used in the computational process of safety margins (e.g., Eq. (13.2)) and inspection events (e.g., Eq. (13.7)), the information obtained from inspection is used to update the fatigue performance of inspected and uninspected details systematically. As indicated previously, the initial crack sizes (i.e., a_0 associated with fatigue details i and j) are correlated among all investigated details. Additionally, material characteristics (e.g., $\ln C_i$ and $\ln C_j$ associated with fatigue-sensitive details i and j) are correlated among the fatigue details in the investigated tanker. The loading characteristics of investigated details are also correlated, leading to the correlation of random variables associated with stress range (e.g., $\ln A_i$ and $\ln A_j$). The modeling error ε_S and geometry error ε_Y factors of various fatigue-sensitive details are correlated. The results obtained are based on a correlation model suggested by Moan and Song (2000) and Schneider *et al.* (2013). The inspection is applied to the deck fatigue-sensitive detail at t = 4 years assuming that no crack is detected using MPI. The updated reliability index of the uninspected deck fatigue-sensitive detail is computed using Eq. (13.6) and is shown in Figure 13.10. As indicated, the updated reliability index of the uninspected detail at t = 4 years increases given the inspection event compared to that without updating. Additionally, the reliability index

increases as the correlation coefficient becomes larger. When ρ = 0.3, the updated reliability index of the uninspected reliability index is close to that associated with the case without updating.

The scenario associated with fatigue crack detected at the deck fatigue-sensitive detail is also investigated herein. It is assumed that once the fatigue crack is detected, the repair action is applied. The new material variables (e.g., a_{0r}, C_r and m_r) associated with the repaired detail are modelled using the same original properties (e.g., a_0, C and m), but these random variables are statistically independent (e.g., $\rho(C_r, C) = 0$) (Moan and Song 2000). At t = 4 years, if a crack is detected using MPI, the updated reliability of the inspected detail is shown in Figure 13.11(a). Given no repair action, the reliability index decreases significantly due to the existence of the detected crack. When the repair action is applied to the detected fatigue-sensitive detail at 4 years, the reliability index of the detail increases as indicated in Figure 13.11(a). Shortly after the repair, the reliability index decreases more significantly than that associated with the case without repair. This specific conclusion is based on the parameters adopted in the illustrative example. The expected risk ranking for different correlation cases is shown in Figure 13.11(b).

The effects of the number of inspected details on updated reliability index associated with an uninspected fatigue-sensitive detail are also investigated. It is assumed that no crack is found on the inspected deck fatigue details at t = 4 years and the correlation coefficients among the random variables are 0.5. The updated reliability index is computed using Eq. (13.6). As shown in Figure 13.12(a), the reliability index of the uninspected detail increases with the number of inspected details N_{insp}. The risk ranking

associated with the uninspected detail under fatigue damage is also computed. As shown in Figure 13.12(b), the difference between the expected risk rankings is decreasing with N_{insp}. Given the risk threshold associated with fatigue damage, the timing of the following inspection can be obtained accordingly as shown in Figure 13.12(b). Herein risk replaces reliability as a performance indicator for the inspection decision making process. The relevant results for 1, 10, 20, 30, 40, and 50 inspected details are shown in Figure 13.13(a). The effects of N_{insp} on the risk ranking of the inspected detail are also conducted. The relevant results are shown in Figure 13.13(b). The updated risk ranking of the inspected detail is slightly lower than that of the uninspected detail given no fatigue crack detected at year 4.

A more general scenario that involves inspection results associated with fatigue crack detected and not detected is investigated using Eq. (13.8). The updated reliability index of the uninspected detail under different inspection outcomes is shown in Figure 13.14(a). It is assumed that among the 5 inspected details (i.e., $N_{insp} = 5$), six outcomes associated with inspection at $t = 4$ years are considered. These outcomes correspond to $r = 0$, $r = 1$, $r = 2$, $r = 3$, $r = 4$, and $r = 5$ details out of the 5 inspected fatigue-sensitive detail do not show damage and fatigue cracks are detected at the remaining details $s = 5$, $s = 4$, $s = 3$, $s = 2$, $s = 1$, and $s = 0$, respectively, where $s + r = 5$. As more fatigue-sensitive details are detected with crack (i.e., s increases), the reliability index of the uninspected fatigue detail drops significantly. If more than 2 out of the 5 details are detected with crack (i.e., $s > 2$), the reliability index of the uninspected detail is generally smaller than that without updating. The results associated with 10 fatigue-sensitive details

inspected are also computed and shown in Figure 13.14(b). Finally, the updated expected risk rankings of the uninspected detail under different inspection outcomes of 5 inspected details at year 4 are indicated in Figure 13.15.

13.5.3. Risk-informed inspection decision making

The risk associated with the three fatigue details of the tanker (i.e., deck, bottom, and side shell) is investigated herein. According to Chen *et al.* 2011, the mean values of ln$A$ and 1/B for Deck, Bottom, and Side Shell are 2.05 and 2.17, 2.26 and 1.29, 1.22 and 1.16, respectively; and the coefficients of variation of ln$A$ and 1/B are 13.8% and 10%, respectively. For tankers, the side shell plates can protect cargo oil and, therefore, are considered as having a high failure consequence. As shown in Table 13.1, the damage intensity associated with side shell detail failure is high. The repair loss for the fatigue-sensitive details located at bottom and deck corresponds to moderated damage intensity. As expected, the risk associated with the side shell is much larger than that of the other two details as shown in Figure 13.16(a). Given the risk threshold, the details at the side shell should be treated as the priority detail for the inspection.

If multiple fatigue-sensitive details are investigated in a ship structure, it is of vital importance to take the correlation among the random variables involved in fatigue damage assessment and inspection into account for fatigue risk assessment. The total expected risk of two fatigue-sensitive details located at the deck considering correlation coefficients 0.1, 0.5, 0.8, and 1.0 among the random variables are computed using Eqs. (13.12) and (13.14). The expected risk ranking of the two deck fatigue-sensitive details given one or two details failure is shown in Figure 13.16(b). When the correlation is

considered in risk ranking for the case with one detail failure, the expected risk ranking decreases as the correlation increases. The opposite conclusion is drawn for the case associated with failure of two details. The results associated with n = 10, 20, 50, and 100 deck, bottom, and side shell fatigue-sensitive details are presented in Table 13.3 at t = 4 years. Two scenarios are investigated herein: (a) risk associated with one fatigue-sensitive detail failure, and (b) failure of two details among 10, 20, 50, and 100 details, respectively. Although the consequence associated with two details failure is much larger than that involving one detail failure, the risk ranking associated with failure of one detail is generally larger than that associated with failure of two details. As indicated, the expected risk ranking of a system depends on many factors, such as the number of fatigue-sensitive details, the correlation coefficients, and the fatigue failure scenarios.

Given a risk ranking threshold associated with a fatigue-sensitive detail failure, the timing for inspection can be obtained. Considering 10 as the minimum acceptable risk ranking per fatigue-sensitive detail, the first inspection is required at t = 4 years for the details located at the deck and bottom as shown in Figure 13.11 and Figure 13.15(a). As indicated in Figure 13.12, the required time interval between inspections increases as more details are inspected simultaneously. Given that 1 out of 10, 20, 50, and 100 inspected fatigue-sensitive details at the deck is detected with damage at t = 4 years, the next inspection associated with an uninspected detail at the deck is at t = 8, 10, 13, and 14 years, respectively.

Based on the system failure event defined in Eq. (13.15), the probability of system failure can be computed. Then, given the consequence associated with system failure, the

risk ranking is obtained. The reliability analysis is performed using the computer program RELSYS (Estes and Frangopol 1998). The risk ranking associated with a system composed of 10 deck fatigue-sensitive details is shown in Figure 13.17. The failure modes associated with fatigue-sensitive details are generally statistically dependent due to common random variables. Herein, the correlation coefficient among the random variables (e.g., $\rho(\ln C_i, \ln C_j)$, $\rho(a_{0i}, a_{0j})$, $\rho(A_i, A_j)$) is assumed 0.5. The effect of the number of adjacent fatigue-sensitive details considered to fail in parallel m on the system reliability is shown in Figure 13.17(a). In this figure, the system failure is defined as the failure of m = 2, 3, and 4 adjacent fatigue-sensitive details. As indicated, m has significant effect on the system fatigue reliability. The scenario associated with m = 2 reveals the largest probability of system failure during the investigated time interval. The risk ranking of these failure modes is also computed. As more details fail, the consequence associated with system failure becomes larger. For example, oil spill could arise from system failure. The probability of system failure increases with increasing the number of failures of adjacent fatigue-sensitive details. The consequences associated with system failure when m = 2, 3, and 4 are assumed 10,000, 100,000, and 1,000,000, respectively for illustrative purposes. The risk ranking is shown in Figure 13.17(b). The risk ranking associated with m = 4 is much larger than that associated with m = 2 and 3 after about 8 years. Accordingly, the inspection priority could be different when reliability and risk indicators are used. The probability of system failure and the associated consequences have significant effects on the risk ranking assessment. Additionally, the effects of inspection on the system reliability are investigated. For m = 3

and n = 10, the updated system reliability indices at t = 4 years detection and no detection of cracks at all 3 fatigue-sensitive details are shown in Figure 13.17(c) along with the system reliability index that was not updated.

13.6. CONCLUSIONS

This chapter provides a probabilistic framework for risk-informed decision making of ship structures under fatigue damage incorporating inspection information. The uncertainties and correlations among the random variables involved in fatigue damage assessment and inspection are incorporated within the framework. The total expected risk ranking of structural systems associated with multiple fatigue-sensitive details is also investigated. The proposed framework is applied to an existing tanker with multiple fatigue-sensitive details. The following conclusions are obtained.

1. The inspection methods and associated mean detectable crack sizes have effects on reliability and risk updating. Additionally, correlation among the random variables used in fatigue reliability and inspection should be considered in the fatigue damage and risk assessment. Given no fatigue crack detected, the inspection interval of uninspected fatigue-sensitive details increases if correlations are considered. . Neglecting correlation can significantly affect the reliability and risk ranking of fatigue-sensitive details.
2. Given no crack detected, the updated reliability of a fatigue-sensitive detail increases as the number of inspected details becomes larger. Bayesian updating shows the effect of inspections on the reliability and risk ranking assessment of structures considering fatigue failure. The updating information has to be

incorporated within the decision making process associated with inspection priority and planning.

3. It should be noted that the inspection priority among fatigue-sensitive details considering risk ranking is sensitive to consequence evaluation associated with failure of details. The parameters and uncertainties associated with consequence rating factor should be carefully evaluated.
4. An approach for computing the reliability and risk of a system composed of multiple fatigue-sensitive details is proposed. The system failure event and associated consequences can significantly affect the risk. Given the system reliability and risk thresholds, the inspection priority and planning can be obtained and updated using inspection information.
5. The information associated with inspection can be used to update the deterioration models to reduce the epistemic uncertainty. If no fatigue crack is detected, the reliability of the detail after inspection would increase. Overall, Bayesian approach can be adopted to update the reliability and risk ranking associated with inspected and uninspected fatigue-sensitive details.

Table 13.1 Conseqences rating factors for structural detail failure associated with fatigue damage

Damage intensity	Rating factor	Consequences (SSC 2000)
Low	$[5\times10^{2}; 15\times10^{2}]$	Temporary repair, and/or no immediate repair
Moderate	$[5\times10^{3}; 15\times10^{3}]$	Unscheduled repair and/or reduction of serviceability
High	$[5\times10^{5}; 15\times10^{5}]$	Minor oil spill, major structural failure, cargo loss, loss of serviceability and/or salvage
Extreme	$[5\times10^{7}; 15\times10^{7}]$	Loss of ship, cargo, lives, and/or major oil spill involving cargo tanks

Note: lower and upper bounds are provided in square brackets

Table 13.2 Random variables associated with fatigue crack limit state and consequence assessment

Random variables	Distribution type	Mean	COV
Initial crack size, a_0 (mm) [1]	Exponential	0.11	1
Detectable crack size, a_d (mm) [1]	Exponential	0.89	1
Average stress cycle rate, υ_0	Normal	1×10^6	0.07
Material parameter, m [1]	DNA	3.1	DNA
Material parameter, ln$C$ [1]	Normal	-29.97	0.017
Stress modeling error, ε_S [2]	Lognormal	1	0.1
Stress geometry error, ε_Y [2]	Lognormal	1	0.1
Repair cost ratio, r_{cr} [3]	Lognormal	2.5	0.2
Unit construction cost, c_{Cons} [4]	Lognormal	447	0.2
Minimal cost value, C_{min}	DNA	200	DNA
Maximal cost value, C_{max}	DNA	2000	DNA
Structural dimension, W (m)	DNA	0.6	DNA
Structural dimension, L (m)	DNA	2.0	DNA

COV: coefficient of variation; DNA: does not apply;
[1]: Moan and Song (2000); [2]: JCCS (2000); [3]: Lukic and Cremona (2001b);
[4]: Maljaars and Vrouwenvelder (2014)

Table 13.3 Risk ranking of deck, bottom, and side shell with different numbers of fatigue-sensitive details and correlation coefficients at t = 4 years

Number of details, n	Detail	One detail failure			Failure of two details		
		$\rho = 0$	$\rho = 0.5$	$\rho = 0.8$	$\rho = 0$	$\rho = 0.5$	$\rho = 0.8$
10	*Deck*	126.2	68.9	24.5	1.3	27.7	20.6
10	*Bottom*	109.6	57.3	22.4	0.8	23.8	17.7
10	*Side shell*	4615.7	2479.7	923.4	50.0	1067.5	660.6
20	*Deck*	250.2	92.8	30.4	9.8	52.7	22.5
20	*Bottom*	220.5	84.7	25.9	7.2	39.0	17.0
20	*Side shell*	9345.5	3641.9	1086.3	212.1	1779.7	909.2
50	*Deck*	611.4	138.5	33.8	29.3	98.3	20.5
50	*Bottom*	530.9	122.6	28.9	18.4	87.1	14.3
50	*Side shell*	22745.0	5457.2	1298.1	1247.5	3242.8	873.8
100	*Deck*	1140.5	178.3	39.5	187.2	140.3	23.5
100	*Bottom*	1005.2	163.4	33.2	82.5	70.8	28.6
100	*Side shell*	42314.0	7121.8	1664.6	2519.9	4535.8	1511.9

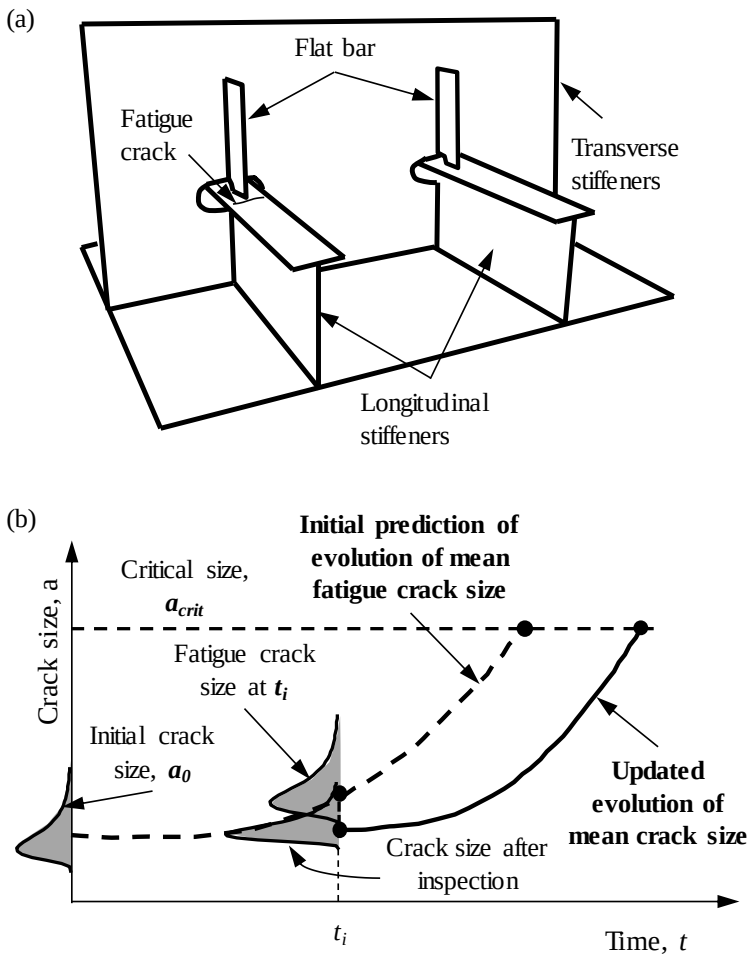

Figure 13.1 (a) Typical fatigue crack of structural detail of a ship structure and (b) fatigue crack size evolution with and without inspection under uncertainty

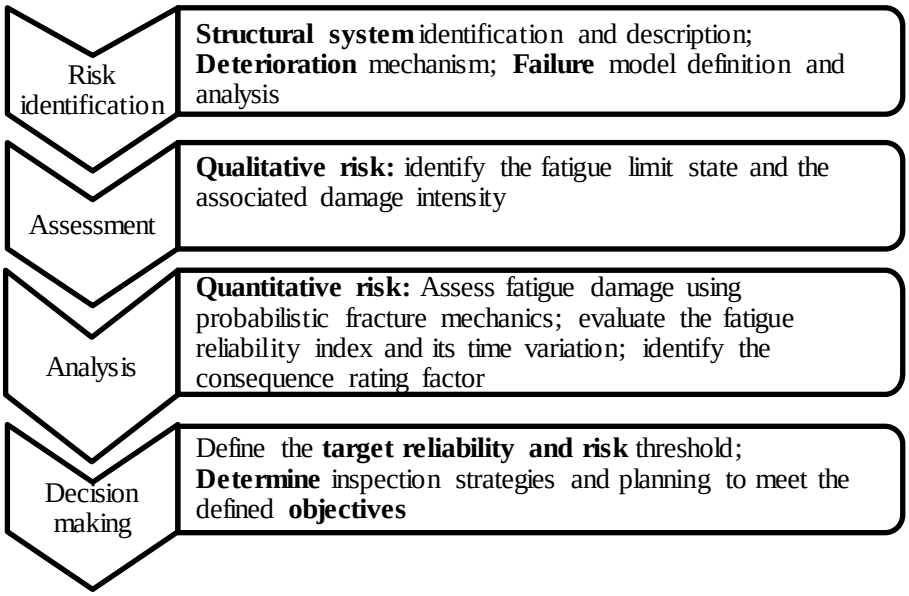

Figure 13.2 Schematic flowchart of risk-informed decision making using a qualitative/quantitative model

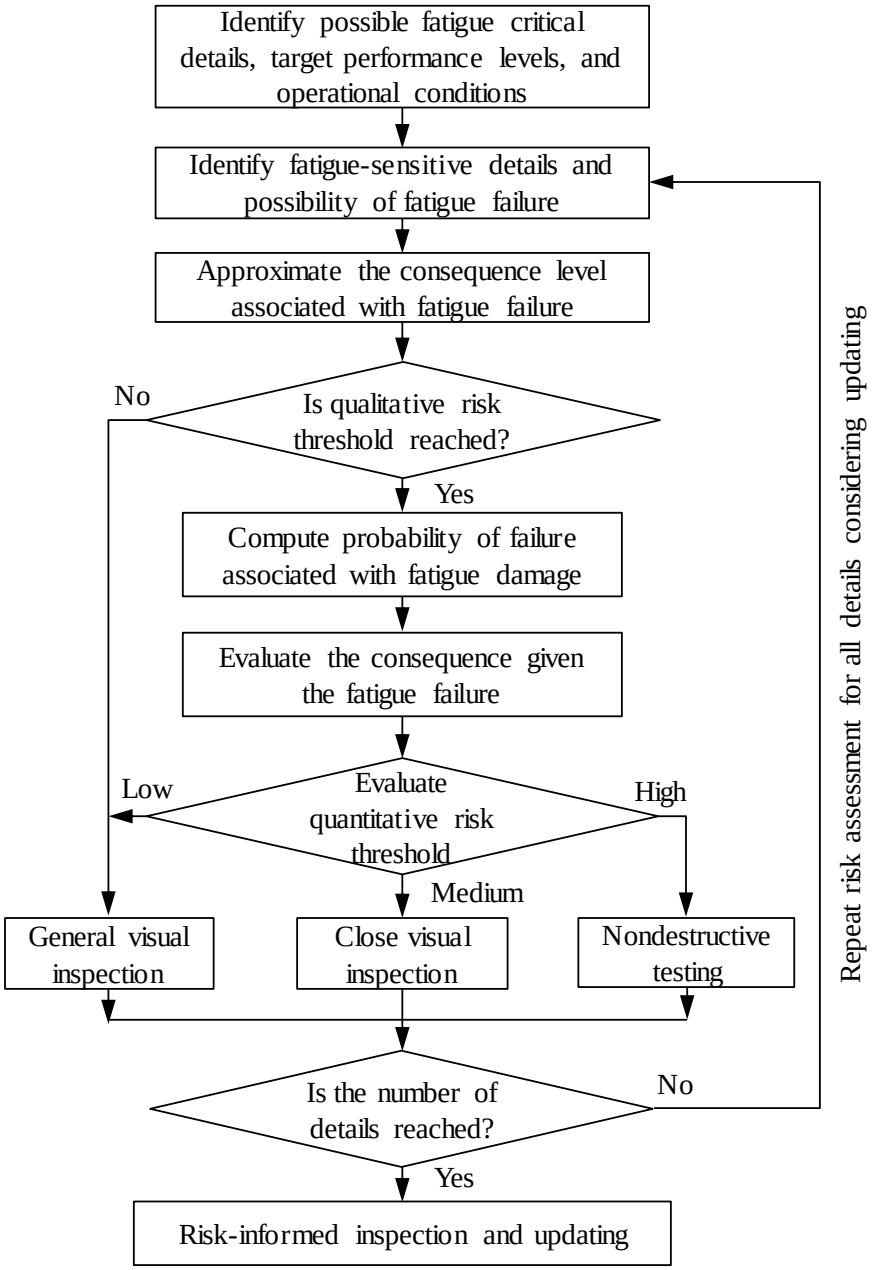

Figure 13.3 Flowchart for risk-informed inspection planning of fatigue-sensitive details

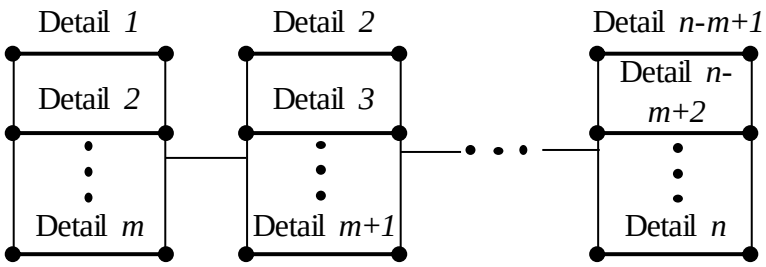

Figure 13.4 Series-parallel model of a system of *n* fatigue-sensitive details, where system failure consists of failure of *m* adjacent details

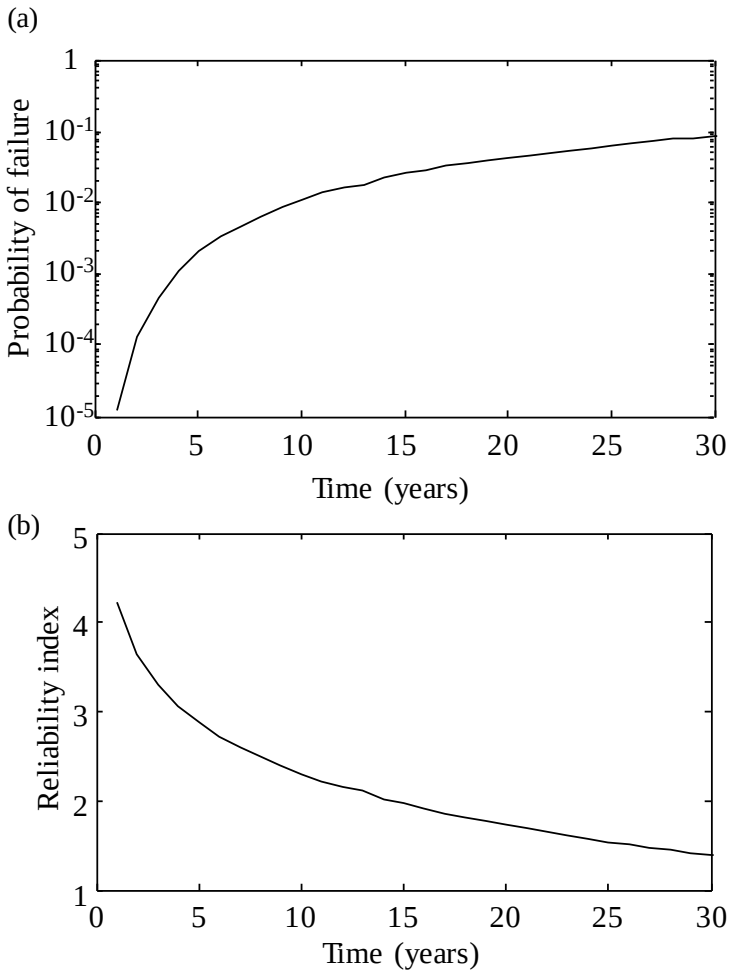

Figure 13.5 Time-variant (a) probability of failure and (b) its associated reliability index of the fatigue-sensitive detail located at the deck

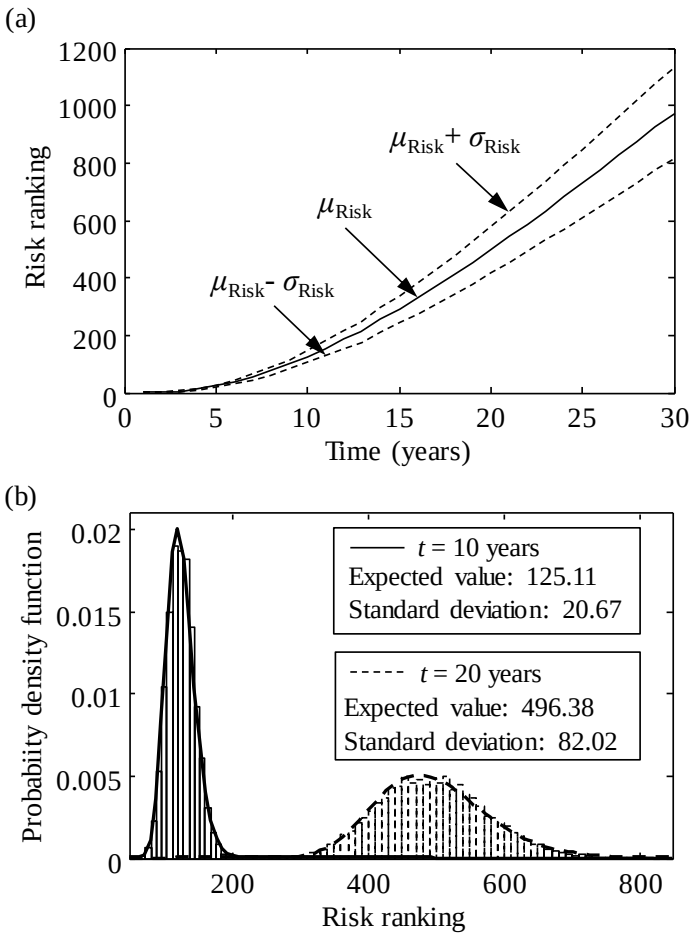

Figure 13.6 (a) Fatigue risk ranking during the investigated time interval and (b) the probability density function associated with risk ranking at t = 10 and 20 years

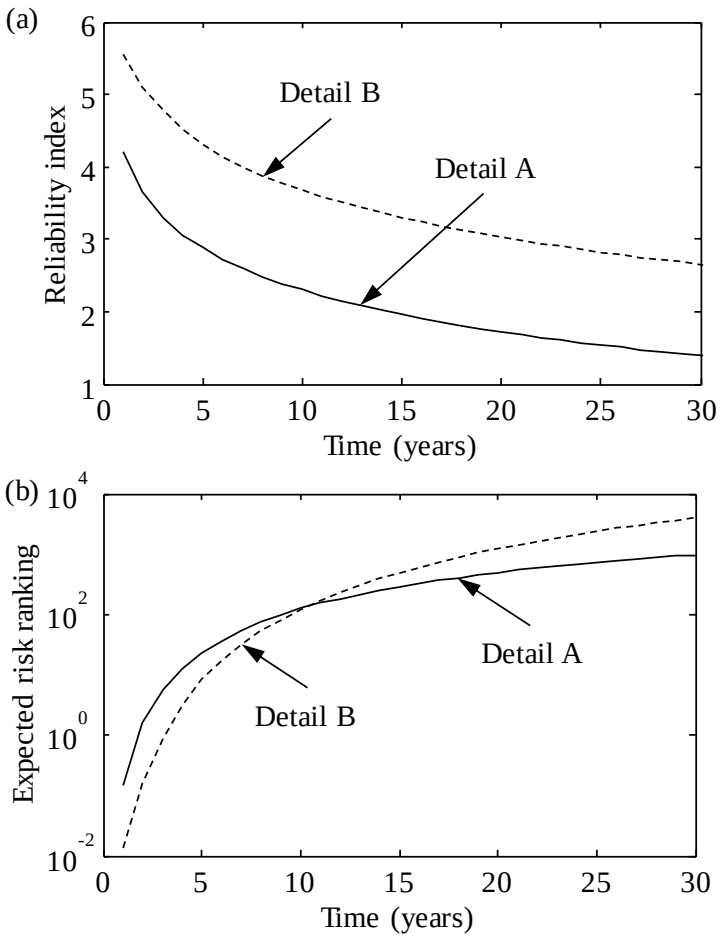

Figure 13.7 (a) Time-variant fatigue reliability of two investigated details (i.e., A and B) and (b) time-variant expected fatigue risk ranking

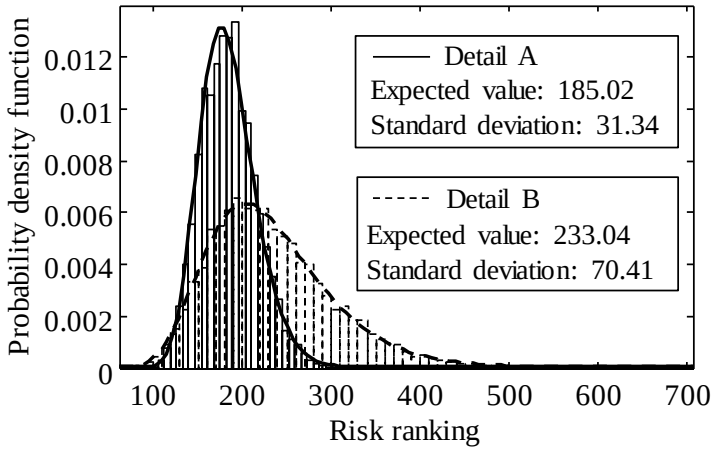

Figure 13.8 Probability density function of risk ranking at t = 12 years for details A and B.

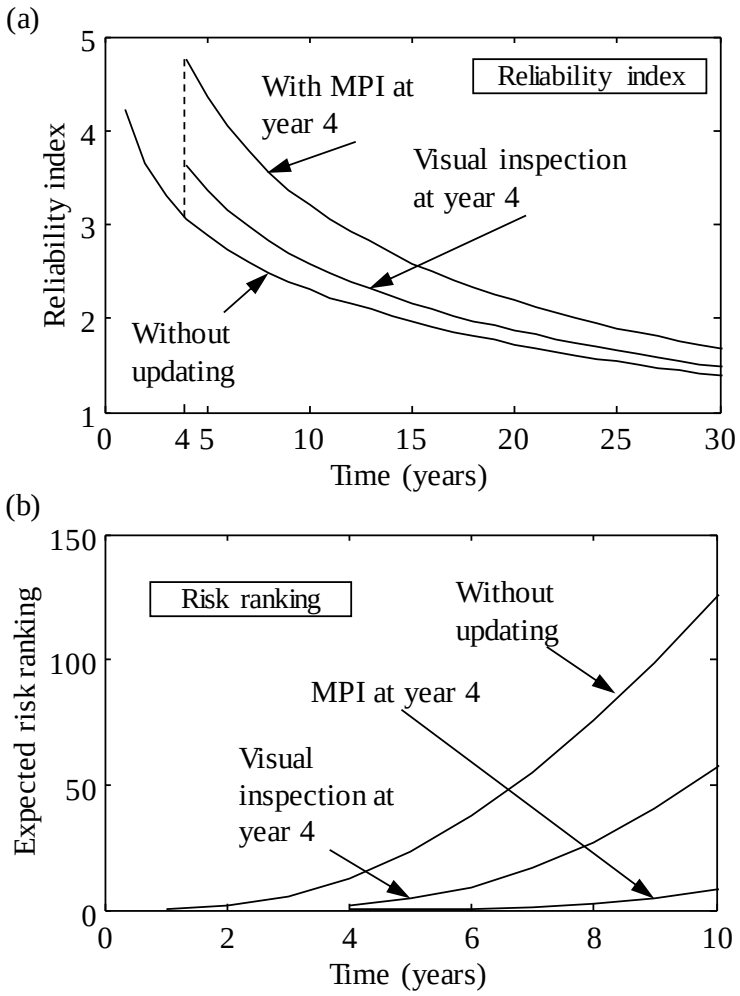

Figure 13.9 (a) Updated reliability and (b) updated risk ranking of an inspected fatigue-sensitive detail using two different inspection methods without detecting a fatigue crack at year 4

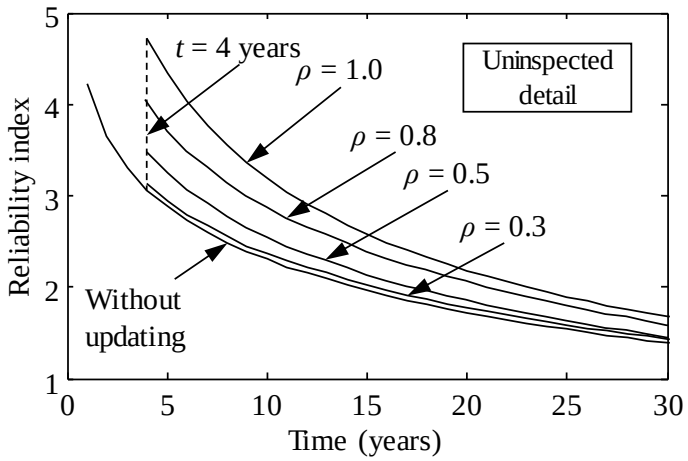

Figure 13.10 Updated reliability of uninspected detail considering different correlation coefficients with no crack detected at year 4 by using MPI method

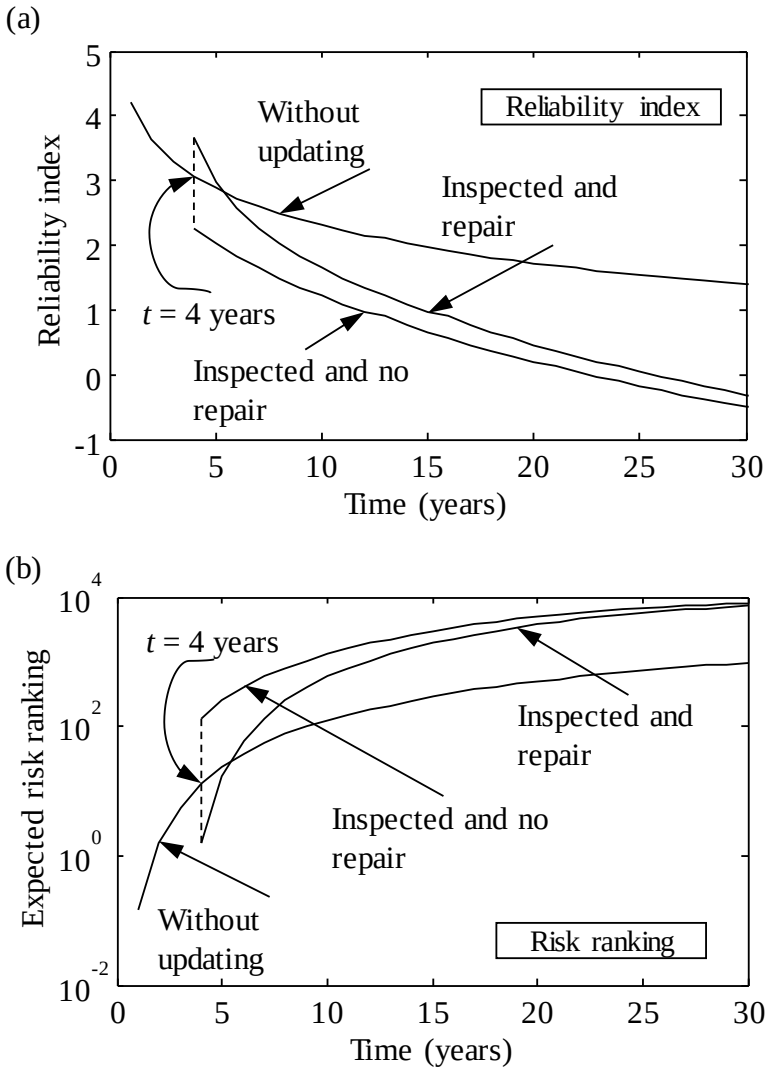

Figure 13.11 (a) Updated reliability and (b) updated risk ranking of an inspected detail under fatigue damage with crack detected at year 4 by using MPI method

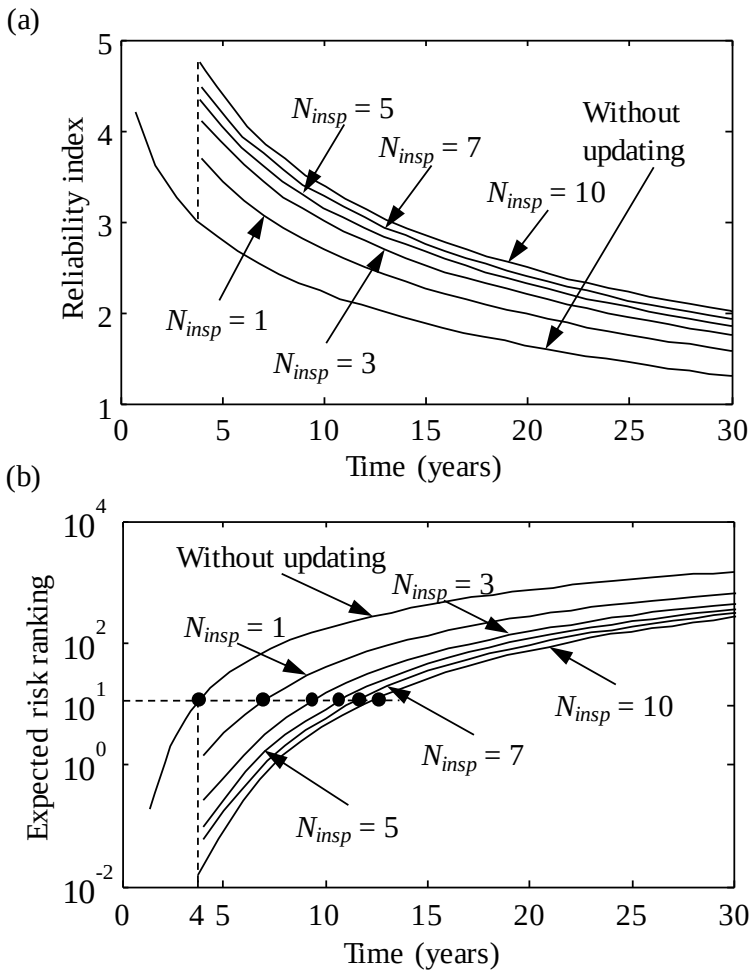

Figure 13.12 (a) Update reliability and (b) updated risk ranking of uninspected detail under different number of inspected details with no crack detected at year 4 by using MPI method

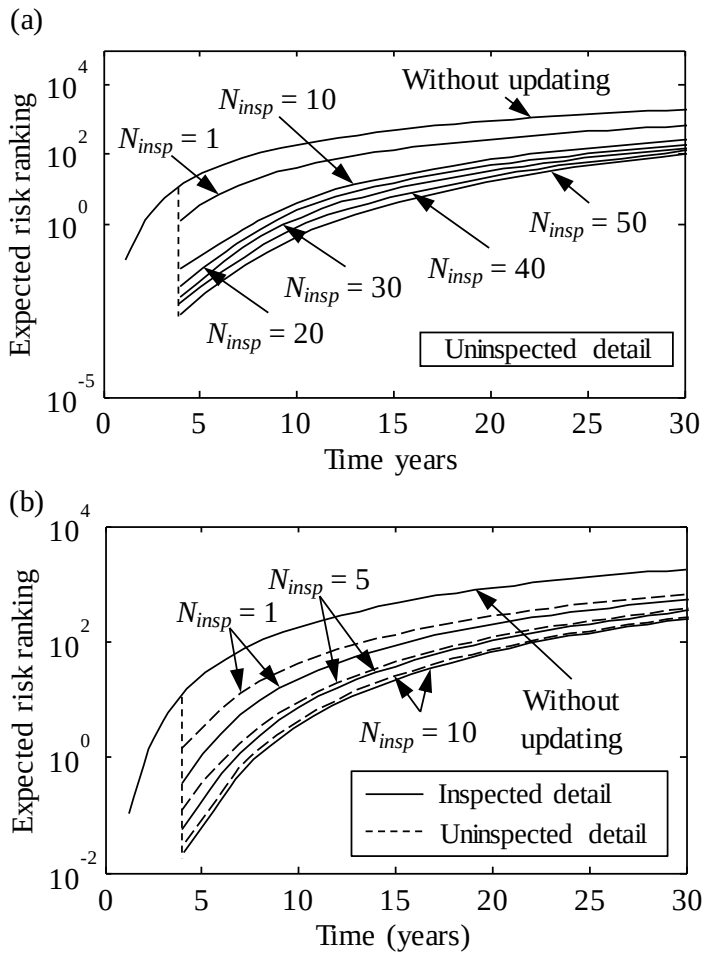

Figure 13.13 (a) Update risk ranking of an uninspected detail considering different numbers of inspected details with no crack detected at year 4 and (b) update risk ranking of inspected and uninspected details considering different numbers of inspected details with no crack detected at year 4 by using MPI method

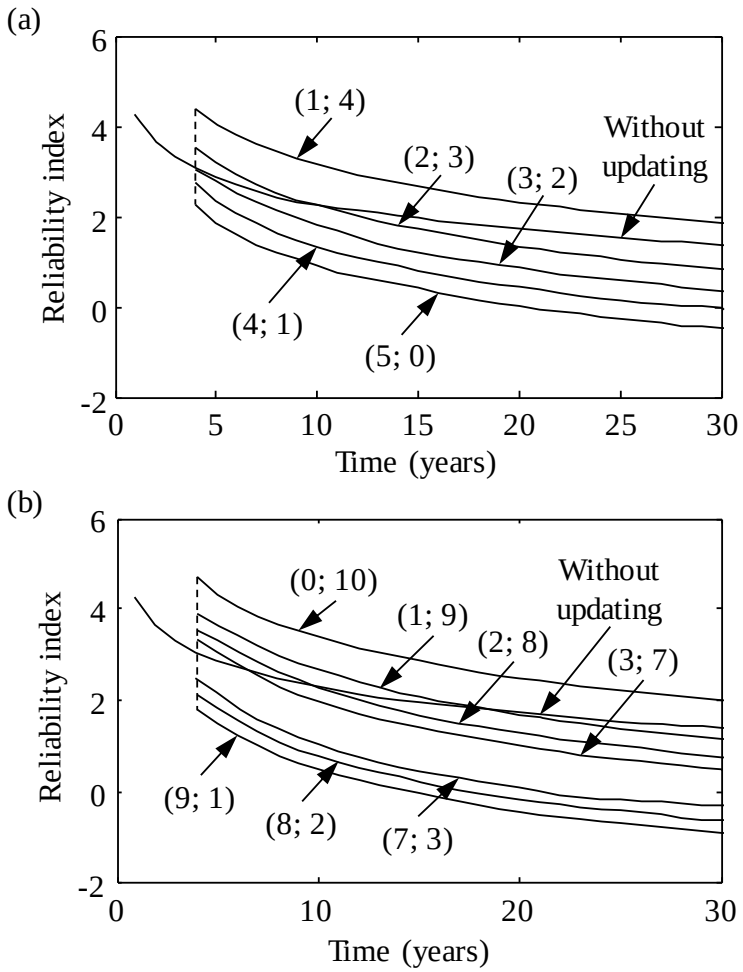

Figure 13.14 Time-variant reliability index of an uninspected fatigue-sensitive detail based on the results of the inspections of (a) five fatigue-sensitive details at year 4 and (b) ten fatigue-sensitive details at year 4 by using MPI method ((*s*; *r*): *s* = number of inspected details showing fatigue damage and *r* = number of inspected details which do not show fatigue damage)

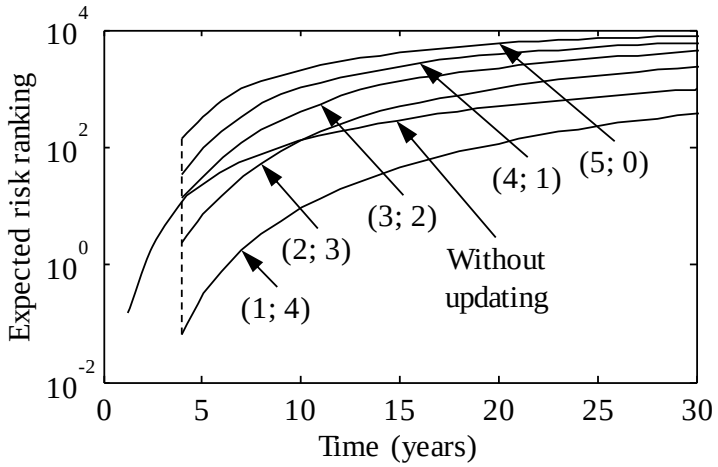

Figure 13.15 Time-variant expected risk ranking of an uninspected fatigue-sensitive detail based on the results of the inspections of five fatigue-sensitive details at year 4 by using MPI method

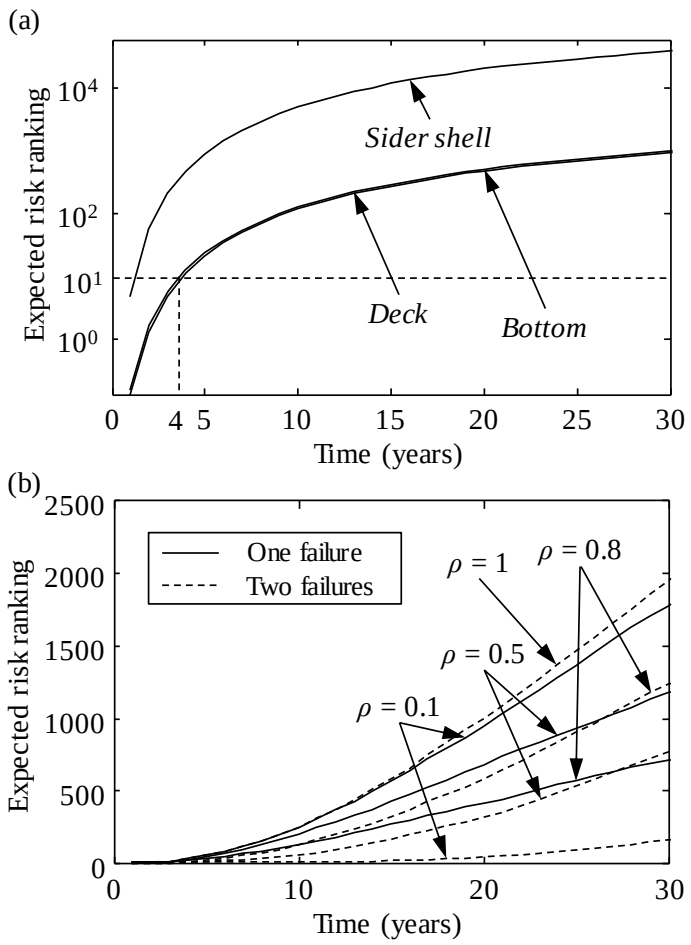

Figure 13.16 (a) Expected risk ranking for different fatigue critical details and (b) expected risk ranking of two deck fatigue-sensitive details given the failure of one or two details

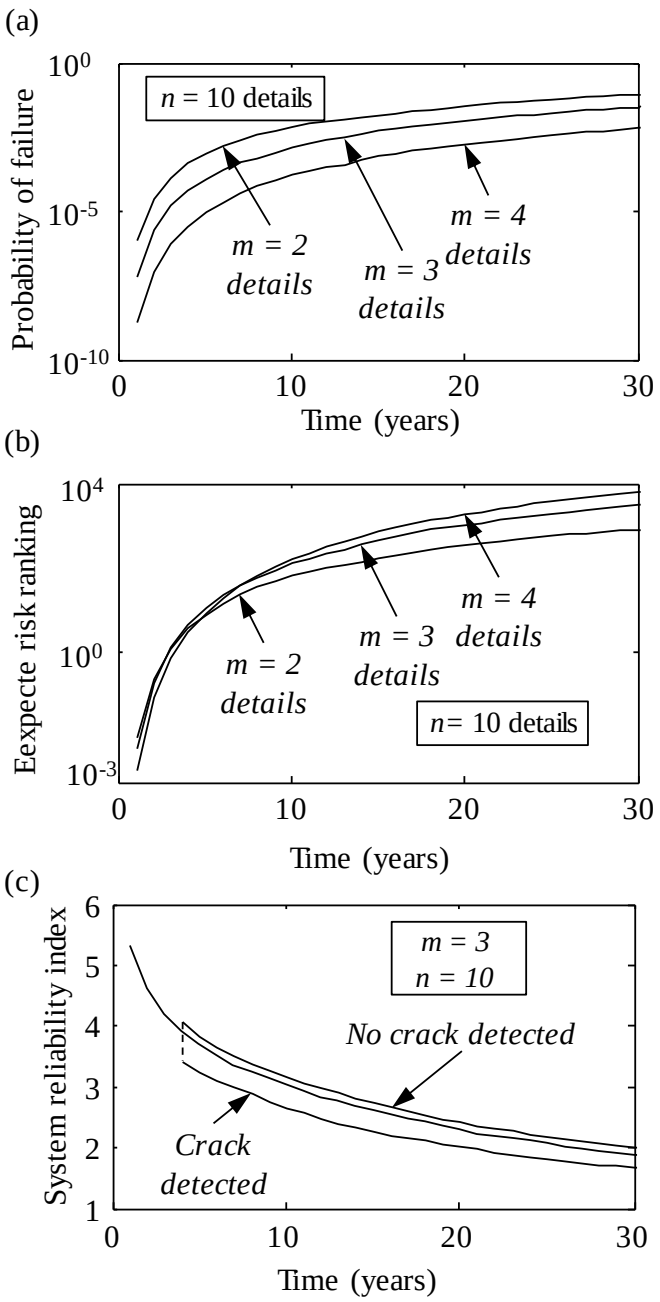

Figure 13.17 System with 10 fatigue-sensitive details (a) probability of system failure when m = 2, 3, and 4; (b) expected risk ranking when m = 2, 3, and 4; (c) updated system reliability index considering inspection results at 4 years

CHAPTER 14

SUMMARY, CONCLUSIONS, AND SUGGESTIONS FOR FUTURE WORK

14.1. SUMMARY

This study developed a framework for life-cycle management and decision making of structural systems under structural deteriorations and extreme events incorporating risk and sustainability. Specifically, this study covered the following tasks within the life-cycle management: assessing and predicting structural performance, updating structural performance using information from inspection, optimizing the management actions, and decision making on structural systems under structural deteriorations and extreme events.

A framework for assessing the time-variant sustainability and resilience of bridges under climate change and multiple hazards considering effects of deterioration and aging has been proposed. Sustainability was quantified in terms of social, environmental, and economic metrics. Uncertainties associated with the occurrence of hazard, structural performance, and consequences evaluation were considered. Additionally, seismic performance of highway bridges under MS only and MSAS sequence were computed separately and compared with each other. Time-variant functionality, indirect loss, and resilience of the bridge under due to MSAS were also computed.

The sustainability of bridge networks was computed and quantified accounting for the probabilities of occurrence of a set of seismic scenarios that reflect the earthquake

activity of the region. It was found that seismic risk and sustainability highly depended on the damage states of the links and the bridges within the network.

The environmental impacts and resilience of conventional and base-isolated buildings under seismic hazard were also investigated. Uncertainties associated with structural and non-structural performances and consequences were incorporated within the assessment process.

A probabilistic framework was proposed for the healthcare - bridge network systems performance considering spatial seismic hazard, vulnerability of bridges and links, and damage condition of a hospital at component and system levels. The effects of correlation among the seismic intensities at different locations are investigated. Additionally, the correlations associated with damage of the investigated structures are also incorporated within the probabilistic assessment process. The conditional seismic performance of the hospital given the damage conditions of the bridge network and the effect of bridge retrofit actions are also investigated.

In order to mitigate seismic damage to economy, society, and environment, a sustainability - inform approach for pre-earthquake retrofit optimization of bridge networks was proposed. The approach integrated the time-variant probabilistic sustainability with multi-objective optimization techniques to get the optimum retrofit planning to assist the decision maker. The total retrofit cost and maximum expected value of economic loss were considered as conflicting objectives. This study proposed a holistic and quantitative approach for the seismic retrofit optimization of bridge networks considering the utility associated with the retrofit cost and benefit of mitigation.

Risk and sustainability assessments of ship collision were investigated. The decision maker's attitude was incorporated within the decision making process by employing the utility theory. Repair loss, fatigue damage accumulation, total travel time, and CO_2 emissions were considered as performance criteria for ship routing decision making and were carefully investigated. Both the attitude of the decision maker and weighting factors employed in the multi-attribute utility assessment have significant effects on the multi-attribute utility value obtained for a route.

The risk- informed life-cycle management of aging ship structures under corrosion and fatigue was investigated. Time effects and uncertainties associated with both corrosion and fatigue were considered. The process of finding optimum inspection and repair planning was formulated as a bi-objective optimization problem, where the total maintenance cost and the maximum annual risk during the investigated time interval were considered as conflicting objectives.

In order to reduce uncertainty in structural performance assessment, a probabilistic framework for risk updating of ship structures under fatigue damage incorporating inspection information was proposed. The uncertainties and correlations among the random variables involved in fatigue damage assessment and inspection were incorporated within the framework. The results of inspection were utilized for reliability and risk updating associated with inspected and uninspected fatigue-sensitive details at both component and system levels.

14.2. CONCLUSIONS

The following conclusions are drawn from the performance assessment of highway bridges and bridge networks under multiple hazards:

- Quantifying sustainability of highway bridges and bridge networks under seismic hazard in terms of economic, social, and environmental metrics. The expected total loss depends on the social and environmental consequences.
- As structural deterioration can induce severe reduction in structural capacity, the seismic risk and sustainability of bridges and bridge networks located in regions prone to high-corrosion should be carefully investigated in a life-cycle context. Furthermore, the time elapsed since the bridge was built has a impact on the metrics of sustainability as the effects of the deterioration are increasing with time.
- The effects of aftershocks have an influence on the seismic repair loss and residual functionality of a bridge after a seismic event. The uncertainties associated with repair loss increase when aftershocks are considered. Consequently, it is of vital importance to consider the effects of aftershocks on bridge seismic performance. The resilience and economic loss are affected by the aftershocks.
- Total life-cycle hazard loss is sensitive to changes in time from the last earthquake, discount rate of money, and remaining service life. The life-cycle loss is more sensitive to the parameters associated with the time-dependent hazard model than to the aging effects.
- Given various hazard occurrence models and discount rates, the total hazard loss associated with earthquake and flood under an investigated time interval is

different and the contribution of the hazards changes. Therefore, different hazards (e.g., earthquake, flood) can dominate the total loss of structural systems under hazards in a life-cycle context.

- It is important to consider the correlation among ground motion intensities in the seismic risk assessment of spatially distributed highway bridge networks. The correlation has a larger effect on the variations of the seismic risk and sustainability than on the expected values.

Based on the sustainability and resilience assessment of buildings under seismic hazard, the following conclusions are drawn:

- Seismic performance improvement associated with base-isolated buildings is significant compared with that of the conventional buildings. Based on the results of seismic performance of conventional and base-isolated buildings, the base isolation can reduce the seismic repair loss, downtime, fatalities, and environmental impacts.
- The methodology estimated the environmental impacts and repair loss as well as downtime and fatalities. The downtime loss is sensitive to the repair scheme (i.e., quick-track and slow-track). The downtime loss for the conventional building under 1995 Kobe earthquake using slow-track is almost 2.3 times of that associated with quick-track.
- The base-isolated building can reduce the damage loss of non-structural components. Under 1940 El Centro earthquake, the repair loss associated with

non-structural components of the base-isolated building is reduced to 40.5% of that associated with conventional building.

- The two performance indicators (i.e., sustainability and resilience) should be both investigated for the conventional and base-isolated buildings under seismic hazard and integrated for a more comprehensive performance-based assessment content. There is a need to expand upon the seismic resilience to include the sustainability metrics.

Based on the seismic performance assessment of interdependent healthcare – bridge network systems, following conclusions are obtained:

- The correlation among the random damage indices has an effect on the probabilities of links being in different damage states and extra travel time. Without considering the correlation effect, the probabilities of link being in none and major damage states would be underestimated. For example, the probability of the link 2 being in major damage state associated with uncorrelated case is approximate 51% of that associated with fully correlated.
- Regarding the system level performance assessment, the extra travel and waiting time decrease when the correlation coefficients (e.g., correlations among the ground motion intensities and seismic damage indices) are accounted for. Additionally, the correlation among the ground motion intensities has a larger effect on the extra travel time than that among the damage indices.

- The effects of retrofit and seismic strengthening associated with bridges and hospital are significant. Bridge retrofit actions could result in an improvement of the performance of healthcare – bridge network systems. Given the specific bridge retrofit actions and correlation coefficients, the extra travel time of the injured persons associated with the case when bridges are retrofitted is nearly 24 % of the case when bridges are not retrofitted.

The following conclusions are drawn from the pre-earthquake retrofit optimization of bridge networks in a life-cycle context:

- This approach provided the opportunity to observe the optimum solutions with different trade-offs and select the one which fits best the decision maker's needs (e.g., structural performance in terms of risk). Each of the Pareto optimal solutions corresponds to an optimum retrofit plan indicating sequence and timing of bridges within a bridge network. These depend on the budget limit and annual loss that the decision maker can tolerate.
- The cost-benefit evaluation and optimization of retrofit actions can produce the retrofit planning considering the utility associated with both the cost and benefit. The cost and benefit should be considered together to determine the effectiveness of an alternative.
- The time interval under investigation and risk attitude of the decision maker have impacts on the optimal solutions resulting from the proposed framework. A longer time interval yielded a higher utility associated with benefit than that corresponding to a shorter time interval.

The following conclusions are based on the ship performance assessment under collision and routing decision making using utility theory.

- The collision risk and sustainability are dependent on the damage condition of the ship. It is important to consider the decision maker's risk attitude in the collision risk and sustainability assessment.
- The ship routing decision making is related with four performance criteria: repair loss, fatigue damage accumulation, total travel time, and CO_2 emissions. MAUT is utilized to combine all single-attribute utilities into a uniform metric that reflects the overall utility associated with a specific ship route.
- Both the attitude of the decision maker and weighting factors employed in the MAUT have effects on the utility value obtained for a route. The proposed methodology may be used to assist decision making regarding traffic control and risk mitigation activities, and to ultimately improve the traffic safety of maritime transportation

Based on the system-level risk assessment and intervention optimization of ship structures under corrosion and fatigue, the following conclusions are drawn:

- Corrosion and fatigue have an impact on the risk of ships. In this study, the effect of corrosion is larger than that associated with fatigue cracking, while fatigue cracking acts as the main factor for risk assessment close to the end of the service life.

- The risk associated with structural failure increases with time due to corrosion and fatigue. Several inspection actions are needed for a ship structure to meet the risk-based performance requirement. The risk associated with ship failure can be reduced significantly by optimum inspection and repair planning.
- Optimum inspection plans are obtained based on the proposed bi-objective optimization approach. Each of the Pareto optimal solutions corresponds to an optimum inspection and repair plan of an aging ship structure.

The following conclusions are based on the risk-based updating of fatigue-sensitive details incorporating inspection information.

- The inspection methods and associated expected detectable crack sizes have effects on reliability and risk updating. Given no fatigue crack detected, the inspection interval of uninspected fatigue-sensitive details increases if correlations are considered. Neglecting correlation can affect the reliability and risk ranking of fatigue-sensitive details.
- It should be noted that the inspection priority among fatigue-sensitive details considering risk ranking is sensitive to consequence evaluation. Given the system reliability and risk thresholds, the inspection priority and planning can be obtained and updated using inspection information.
- The information associated with inspection can be used to update the deterioration models and to reduce uncertainty. Bayesian approach can be adopted to update

the reliability and risk ranking associated with inspected and uninspected fatigue-sensitive details at both component and system levels.

14.3. SUGGESTIONS FOR FUTURE WORK

The suggestions for future work related to Part I are presented as follows:

- First of all, information from historic data and/or input from experts should be incorporated within the assessment and prediction of bridge and link performance under extreme events, evaluation of retrofit actions on bridge seismic performance, and treatment of uncertainties both in performance and consequences associated with the three metrics of sustainability. Additionally, further studies are needed to investigate the effects of multiple maintenance actions (both preventive and essential) on the structural performances and incorporate these maintenance actions within the intervention optimization procedure.
- Future work is needed to develop more advanced and complicated finite element models to capture seismic performance of structural systems under multiple aftershock sequences. Different seismic demand parameters (e.g., seismic energy dissipation) and ground motion intensities could be investigated using a sufficient sample of ground motion inputs.
- Further efforts are needed to focus on optimal design of high-performance and environmentally friendly bridges and buildings using optimization approach, which can facilitate the reduction of economic losses associated with natural hazards, improve safety and energy efficiency, and subsequently reduce the environmental

impacts within a life-cycle context. For example, the renewable energy sources, such as wind and solar energy, will be considered within the design procedure of structural systems to meet the energy demand and mitigate greenhouse gas emissions.

- The probabilistic approach for resilience and sustainability assessment of single bridges, buildings, bridge networks, and interdependent structural systems could be enhanced and applied to other lifeline systems at community scale. Additionally, other hazard effects, such as extreme wind and tsunami, should also be investigated and incorporated within the assessment and management framework. The research will encompass several other concepts, including: assessing the system-level sustainability and resilience and modeling the correlation between the networks.

For Part II associated with ship structures, the suggestions for future work are summarized as follows:

- Future research is needed to include nonlinear fracture mechanics in the damage assessment of fatigue-sensitive details. Additionally, effects of multiple fatigue cracks on the structural capacity should be taken into account for the risk assessment of fatigue-sensitive structures. A combined effect of both corrosion and fatigue needs to be considered in the future work.
- In future studies, the information from structural health monitoring should be incorporated within the management process to update the structural performance

and to reduce uncertainties, ultimately leading to updated optimal management planning.

- Future research is needed for the implementation of detailed dynamic analysis of wave load on ship performance, such as whipping and springing. The effects associated with shear and torsion could also be considered within the ship performance assessment process.

Overall, these are the suggestions for the future work associated with civil infrastructure systems and ship structures.

REFERENCES

ABS. (2010). *Guide for fatigue assessment of off shore structures*. American Bureau of Shipping, Houston.

Achour, N., Miyajima, M., Kitaura, M., and Price, A. (2011). Earthquake-induced structural and nonstructural damage in hospital. *Earthquake Spectra*, 37(3), 617-634.

Adachi, T., and Ellingwood, B.R. (2009). Serviceability assessment of a municipal water system under spatially correlated seismic intensities. *Computer-Aided Civil and Infrastructure Engineering*, 24, 237-248.

Adams, W.M. (2006). "The future of sustainability: re-thinking environment and development in the twenty-first century." *Report of the International Union for Conservation of Nature (IUCN) Renowned Thinkers Meeting*, The World Conservation Union, Gland, Switzerland.

Akiyama, M., Frangopol, D.M., and Koshimura, S. (2013). Reliability of bridges under Tsunami hazard: emphasis on the 2011 Tohoku-Oki Earthquake. *Earthquake Spectra*, 29(S1), S295-S317.

Akiyama, M., Frangopol, D.M., and Matsuzaki, H. (2011). Life-cycle reliability of RC bridge piers under seismic and airborne chloride hazards. *Earthquake Engineering & Structural Dynamics*, 40 (15), 1671-1687.

Akiyama, M., Frangopol, D.M., and Suzuki, M. (2012). Integration of the effects of airborne chlorides into reliability-based durability design of R/C structures in a marine environment. *Structure and Infrastructure Engineering*, 8(2), 125-134.

Akpan, U.O., Koko, T.S., Ayyub, B., Dunbar, T.E. (2002). Risk assessment of aging ship hull structures in the presence of corrosion and fatigue. *Marine Structures*, 15, 211-231.

Alcorn, A. (2003). Embodied energy and CO_2 coefficients for New Zealand building materials. *Centre for Building Performance Research Report*, Centre for Building Performance Research, Victoria University of Wellington, Wellington, New Zealand.

Almufti, I., and Willford, M. (2013). *Resilience-based earthquake design initiative (REDi™) for the next generation of buildings*. Arup, San Francisco, CA.

Altiok, T., Almaz, O.A., and Ghafoori, A. (2012). Modeling and analysis of the vessel traffic in the Delaware and Bay Area: Risk assessment and mitigation, *Report No. 204-RU6532*, New Jersey Department of Transportation, Office of Maritime Resources.

American Bureau of Shipping (ABS 2003). Guide for fatigue assessment of offshore structures. *American Bureau of Shipping*, BS Plaza 16855 Northchase Drive, Houston, TX.

Anderson, J., Shiers, D., and Sinclair, M. (2002). *Green guide to housing specification: an environmental profiling system for building materials and components*. 3rd ed. Oxford, Blackwell.

Anderson, J., Wesnousky, S.G., and Stirling, M.W. (1996). Earthquake size as a function of slip rate. *Bulletin of the Seismological Society of America*, 86(3), 683–690.

Ang, A. H-S. (2010). Significance of uncertainty in the calculation of risk and reliability: Emphasis on decisions for protection against natural hazards, *International Symposium on Reliability Engineering and Risk Management* (ISRERM2010), September 23–26, Shanghai, China.

Ang, A.H-S, and De Leon, D. (1997). Determination of optimal target reliabilities for design and upgrading of structures. *Structural Safety*, 19(1), 91-103.

Ang, A.H-S, and De Leon, D. (2005). Modeling and analysis of uncertainties for risk-informed decisions in infrastructures engineering. *Structure and Infrastructure Engineering*, 1(1), 19-31.

Ang, A. H-S, and Tang, W.H. (2007). *Probability concepts in engineering: Emphasis on applications to civil and environmental engineering*, 2nd edition, Wiley and Sons, NY.

Aslani, H., and Miranda, E. (2005). Fragility assessment of slab-column connections in existing non-ductile reinforced concrete buildings. *Journal of Earthquake Engineering*, 9(6), 777-804.

Association of Bay Area Governments (ABAG) (1997), The Bay area is in earthquake country. Association of Bay Area Governments, Oakland, CA.

ATC (1985). *ATC-13 Earthquake damage evaluation data for California*. Redwood City, CA.

Aviram, A., Mackie, K., and Stojadinovic, B. (2008). Guidelines for Nonlinear Analysis of Bridge Structures in California. *Technical Report, Pacific Earthquake Engineering Research Center*, University of California, Berkeley, CA.

Ayala-Uraga, E., and Moan, T. (2002). System reliability issues of offshore structures considering fatigue failure and updating based on inspection. *In proceedings of 1st International ASRANet Colloquium*, July 8-10, 2002, Glasgow, Scotland.

Ayyub, B.M., Assakkaf, I.A., and Atua, K.I. (2000). Reliability-Based Load and Resistance Factor Design (LRFD) of Hull Girders for Surface Ships. *Naval Engineers Journal*, 112(4), 279-296.

Ayyub, B.M., Assakkaf, I.A., Kihl, D.P., and Siev, M.W. (2002). Reliability-based design guidelines for fatigue of ship structures. *Naval Engineers Journal*, 114(2), 113-138.

Bai, Y. (2003). *Marine Structural Design*, Elsevier Science.

Banerjee, S., and Prasad, G. (2012). Seismic risk of a reinforced concrete bridge in the presence of flood-induced scour. *Structures Congress*, ASCE, Chicago.

Banerjee, S., and Shinozuka, M. (2008). Mechanistic quantification of RC bridge damage states under earthquake through fragility analysis. *Probabilistic Engineering Mechanics*, 23(1), 12-22.

Basöz, N., and Mander, J. (1999). Enhancement of the highway transportation lifeline module in HAZUS. *National Institute of Building Sciences* (NIBS), Washington, D.C.

Bazzurro, P., and Luco, N. (2005). Accounting for uncertainty and correlation in earthquake loss estimation. *Proceedings of 9th International Conference on Structural Safety and Reliability*, Rome, Italy, 2687–2694.

Beck, J.L., Kiremidjian, A., Wilkie, S., Mason, A., Salmo, T., Goltz, J., Olson, R., Workman, J., Irfanoglu, A., and Porter, K.A. (1999). *Decision Support Tools for Earthquake Recovery of Business*, Final Report for CUREe-Kajima Phase III Project, Consortium of Universities for Research in Earthquake Engineering, Richmond, CA.

Berg, D., Tammer, M., and Kaminski, M.L. (2014). Updating fatigue reliability of uninspectable joints using structurally correlated inspection data. *Proceedings of the Twenty-fourth (2014) International Ocean and Polar Engineering Conference Busan*, Korea, June 15-20, 423-432.

Biello, D. (2010). The BP spill's growing toll on the sea life of the Gulf. *Yale Environment 360*, Yale School of Forestry & Environmental Studies.

Bird, J.F., and Bommer, J.J. (2004). Earthquake losses due to ground failure. *Engineering Geology*, 75, 147-179.

Bocchini, P. (2013). Computational procedure for the assisted resilience-oriented disaster management of transportation systems. *In Safety, Reliability, Risk and Life-Cycle Performance of Structures and Infrastructures*, Deodatis, G., Ellingwood, B.R., Frangopol, D.M. eds., CRC Press, 581-588.

Bocchini, P., and Frangopol, D.M. (2011). A stochastic computational framework for the joint transportation network fragility analysis and traffic flow distribution under extreme events. *Probabilistic Engineering Mechanics*, 26, 182-193.

Bocchini, P., and Frangopol, D. M. (2012). Restoration of bridge networks after an earthquake: Multi-criteria intervention optimization. *Earthquake Spectra*, 28, 426–455.

Bocchini, P., Frangopol, D.M., Ummenhofer, T., and Zinke, T. (2014). Resilience and sustainability of civil infrastructure: Toward a unified approach. *Journal of Infrastructure Systems*, 20(2), 04014004, 1-16.

Bonowitz, D. (2011). Resilience criteria for seismic evaluation of existing buildings. *A 2008 Special Projects Initiative Report*, Structural Engineers Association of Northern California.

Boore, D.M., Joyner, W.B., and Fumal, T.E. (1997). Equations for estimating horizontal response spectra and peak acceleration from western North American earthquakes: A summary of recent work. *Seismological Research Letters*, 68(1), 128–153.

Brown, A.J., and Chen, D. (2002). Probability method for predicting ship collision damage, *Ocean Engineering*, 6(1), 54-65.

Brundtland, H. (1987). Our common future. *Oxford University Press*, New York, NY.

Bruneau, M., and Reinhorn, A. (2007). Exploring the concept of seismic resilience for acute care facilities. *Earthquake Spectra*, 23(1), 41–62.

Bruno, S., and Valente, C. (2002) Comparative response analysis of conventional and innovative seismic protection strategies. *Earthquake Engineering and Structural Dynamics*, 31(5), 1067-1092.

BS 7910 (2013). Guide to methods for assessing the acceptability of flaws in metallic structures. British Standard Institute.

Bucher, C., Frangopol, D.M. (2006). Optimization of lifetime maintenance strategies for deteriorating structures considering probabilities of violating safety, condition, and cost thresholds. *Probabilistic Engineering Mechanics*, 21(1), 1–8.

Buckle, I., Friedland, I., J. Mander, G. Martin, R. Nutt, and Power, M. (2006). *Seismic retrofitting manual for highway structures: part 1-bridges*, Federal Highway Administration, Office of Research, Development and Technology, Turner-Fairbank Highway Research Center, McLean, VA.

Campbell, K.W., and Bozorgnia, Y. (2008). NGA ground motion model for the geometric mean horizontal component of PGA, PGV, PGD and 5% damped linear elastic response spectra for periods ranging from 0.01 to 10 s. *Earthquake Spectra*, 24, 139–171.

Campbell, K.W. and Seligson, H.A. (2003). Quantitative method for developing hazard-consistent earthquake scenarios. *Proceedings of the 6th U.S. Conference and Workshop on Lifeline Earthquake Engineering*, Long Beach, CA.

Caltrans (2006). *Seismic design criteria*, California DOT, Sacramento, CA.

Cha, E.J., and Ellingwood, B.R. (2013). Seismic risk mitigation of building structures: The role of risk aversion, *Structural Safety*, 44, 28-36.

Chang, L., Peng, F., Ouyang, Y., Elnashai, A., and Spencer, B. (2012). Bridge seismic retrofit program planning to maximize postearthquake transportation network capacity, *Journal of Infrastructure Systems*, 18(2), 75–88.

Chang, S.E., and Shinozuka, M. (2004). Measuring improvements in the disaster resilience of communities. *Earthquake Spectra*, 20(3), 739–755.

Chang, S.E., Shinozuka, M., and Moore, J.E. (2000). Probabilistic earthquake scenarios: extending risk analysis methodologies to spatially distributed systems. *Earthquake Spectra*, 16(3), 557–572.

Chau, C.K., Hui, W.K., Ng, W.Y., and Powell, G. (2012) Assessment of CO_2 emissions reduction in high-rise concrete office buildings using different material use options. *Resources, Conservation and Recycling*, 61, 22-34.

Chaudhuri, S., and Hutchinson, T. (2004). Distribution of peak horizontal floor acceleration for estimating nonstructural element vulnerability. *13th World Conference on Earthquake Engineering*, Vancouver, B.C., Canada.

Chen, N.Z., Wang, G., and Guedes Soares, C. (2011). Palmgren-Miner's rule and fracture mechanics-based inspection planning. *Engineering Fracture Mechanics*, 78, 3166-3182.

Chiou, B., Darragh, R., Gregor, N., and Silva, W. (2008). NGA project strong-motion database. *Earthquake Spectra*, 24(1), 23-44.

Choe, D., Gardoni, P., Rosowsky, D., and Haukaas, T. (2008). Probabilistic capacity models and seismic fragility estimates for RC columns subject to corrosion. *Reliability Engineering and System Safety*, 93(3), 383-393.

Choe, D., Gardoni, P., Rosowsky, D., and Haukaas, T. (2009). Seismic fragility estimates for reinforced concrete bridges subject to corrosion. *Structural Safety*, 31(4), 275–283.

Choi, E., DesRoches, R., and Nielson, B. (2004). Seismic fragility of typical bridges in moderate seismic zones. *Engineering Structures*, 26,187-199.

CIB. (2001). *Risk assessment and risk communication in civil engineering*. Rotterdam, The Netherlands: Council for Research and Innovation in Building and Construction; 2001 TG 32 Report 259.

Cimellaro, G.P., Reinhorn, A.M., and Bruneau, M. (2010). Framework for analytical quantification of disaster resilience. *Engineering Structures*, 32(11), 3639–3649.

Cimellaro, G.P., Reinhorn, A.M., and Bruneau, M. (2011). Performance-based metamodel for healthcare facilities. *Earthquake Engineering and Structural Dynamics*, 40, 1197-1217.

Comber, M., Poland, C., and Sinclair, M. (2012) Environmental impacts seismic assessment: Application of performance-based earthquake engineering methodologies to optimize environmental performance. *Structures Congress*, Chicago, IL, 910-921.

Comerio, M.C. (2006). Estimating downtime in loss modeling. *Earthquake Spectra*, 22(2), 349-365.

Constantinou, M.C., Whittaker, A., Kalpakidis, Y., Fenz, D., and Warn, G.P. (2007) Performance of seismic isolation hardware under service and seismic loading. *Technical Rep. No. MCEER-07-0012*, Multidisciplinary Center for Earthquake Engineering Research, Buffalo, NY.

Cornell, C.A., Jalayer, F., Hamburger, R.O., and Foutch, D.A. (2002). The probabilistic basis for the 2000 SAC/FEMA steel moment frame guidelines. *Journal of Structural Engineering*, 128(4), 526-533.

Cramer, E.H., and Friis-Hansen, P. (1994). Reliability-based optimization of multi-component welded structures. *Journal of Mechanics and Arctic Engineering*, 116, 233-238.

Decò, A., and Frangopol, D.M. (2011). Risk assessment of highway bridges under multiple hazards. *Journal of Risk Research*, 14(9), 1057-1089.

Decò, A., and Frangopol, D.M. (2013). Life-cycle risk assessment of spatially distributed aging bridges under seismic and traffic hazards. *Earthquake Spectra*, 29(1), 127-153.

Decò, A., and Frangopol, D.M. (2013). Risk-informed optimal routing of ships considering different damage scenarios and operational conditions. *Reliability Engineering and System Safety*, 19, 126-140.

Decò, A., Frangopol, D.M., and Bocchini, P. (2013). Probabilistic seismic resilience of bridge networks. *In Safety, Reliability, Risk and Life-Cycle Performance of Structures and Infrastructures*, Deodatis, G., Ellingwood, B.R., Frangopol, D.M. eds., CRC Press, 621-628.

Decò, A., Frangopol, D.M., and Okasha, N.M. (2011). Time-variant redundancy of ship structures. *Journal of Ship Research*, SNAME, 55(3), 208-219.

Dennemann, K.L. (2009). *Life-cycle cost-benefit analysis for bridge seismic retrofits*. Master Thesis, Houston, TX.

Dequidt, T. (2012). *Life cycle assessment of a Norwegian bridge*. Department of Civil and Transport Engineering, Norwegian University of Science and Technology, Master Thesis, Trondheim, Norway.

Det Norske Veritas (2010). Fatigue design of offshore steel structures. *Recommended Practice DNV-RP-C203*, April 2010.

Devine, E.A. (2009). *An overview of the recently-completed JHSS monohull and trimaran structural seaways loads test program*. Naval Surface Warfare Center, Carderock Division.

DNV (Det Norske Veritas) (2014). Fatigue assessment of ship structures. Classification Notes, No. 30.7, Høvik, Norway.

Dong, Y., and Frangopol, D.M. (2015a). Probabilistic ship collision risk and sustainability assessment considering risk attitudes. *Structural Safety*, 53, 75-84.

Dong, Y., and Frangopol, D.M. (2015b). Informed life-cycle optimum inspection and maintenance of ship structures considering corrosion and fatigue. *Ocean Engineering*, 101, 161-171.

Dong, Y., and Frangopol, D.M. (2015c). Risk and resilience assessment of bridges under mainshock and aftershocks incorporating uncertainties. *Engineering Structures*, 83, 198-208.

Dong, Y., and Frangopol, D.M. (2015d). Probabilistic assessment of an interdependent healthcare – bridge network system under seismic hazard. *Structure and Infrastructure Engineering* (under review).

Dong, Y., and Frangopol, D.M. (2016a). Incorporation of risk and updating in inspection of fatigue-sensitive details. *International Journal of Fatigue*, 82, 676-688.

Dong, Y., and Frangopol, D.M. (2016b). Performance-based seismic assessment of conventional and base-isolated steel buildings including environmental impact and resilience. *Earthquake Engineering and Structural Dynamics*, doi:10.1002/eqe.2682 (in press).

Dong, Y., and Frangopol, D.M. (2016c). Time-dependent multi-hazard life-cycle assessment of bridges considering climate change. *Journal of Performance of Constructed Facilities* (accepted).

Dong, Y., Frangopol, D.M., and Sabatino, S. (2016d). A decision support system for mission-based considering multiple performance criteria. *Reliability Engineering & System Safety* (under revision).

Dong, Y., Frangopol, D.M., and Sabatino, S. (2015). Optimizing bridge network retrofit planning based on cost-benefit evaluation and multi-attribute utility associated with sustainability. *Earthquake Spectra*, 31(4), 2255-2280.

Dong, Y., Frangopol, D.M., and Saydam, D. (2013). Time-variant sustainability assessment of seismically vulnerable bridges subjected to multiple hazards. *Earthquake Engineering and Structural Dynamics*, 42(10), 1451-1467.

Dong, Y., Frangopol, D.M., and Saydam, D. (2014a). Sustainability of highway bridge networks under seismic hazard. *Journal of Earthquake Engineering*, 18, 41-66.

Dong, Y., Frangopol, D.M., and Saydam, D. (2014b). Pre-earthquake probabilistic retrofit optimization of bridge networks based on sustainability. *Journal of Bridge Engineering*, 19(6), 04014018, 1-10.

Ditlevsen, O. (1979). Narrow reliability bounds for structure systems. *Journal of Structural Mechanics*, 7(4), 453-451.

Dueñas-Osorio, L., Craig, J.I., and Goodno, B.J. (2007). Seismic response of critical interdependent networks. *Earthquake Engineering and Structural Dynamics*, 36, 285-306.

Elkington, J. (2004) Enter the Triple Bottom Line, in Adrian Henriques and Julie Richardson(ed). *The triple bottom line: does it all add up?* Earthscan, Sterling, VA.

Ellingwood, B.R. (2007). Assessment and mitigation of risk from low-probability, high-consequence hazards. *International Forum on Engineering Decision Making*, Third IFED Forum, Shoal Bay, Australia.

Ellingwood, B.R., and Wen, Y.K. (2005). Risk-benefit-based design decisions for low-probability/high consequence earthquake events in Mid-America. *Progress in Structural Engineering and Materials*, 7, 56–70.

Engelhardt, M.D., Fry, G., Jones, S., Venti, M., and Holliday, S. (2000). Behavior and design of radius cut reduced beam section connections, *SAC/BD-00/17*, SAC, Joint Venture.

Esposito, S., and Iervolino, I. (2011). PGA and PGV spatial correlation models based on European multievent datasets. *Bulletin of the Seismological Society of America*, 101(5), 2532–2541.

Estes, A.C., and Frangopol, D.M. (1998). RELSYS: A computer program for structural system reliability analysis. *Structural Engineering and Mechanics*, 6(8), 901-919.

Etkin, D.S. (2004). Modeling oil spill response and damage costs. *Proceedings of the Fifth Biennial Freshwater Spills Symposium*, http://www.epa.gov/oem/docs/oil/fss/fss04/ etkin2_04.pdf.

Faltinsen, O.M. (1990). *Sea Loads on Ships and Offshore Structures*. Cambridge University Press, Cambridge, UK.

Federal Emergency Management Agency (FEMA) (2000). Planning for a sustainable future: the link between hazard mitigation and livability. *Publication No. 364*, Federal Emergency Management Agency, Washington, D.C.

FEMA (2000). *Prestandard and commentary for the seismic rehabilitation of buildings*. Report FEMA 356, Washington, D.C.

FEMA (2012). Next-generation methodology for seismic performance assessment of buildings. The Applied Technology Council for the Federal Emergency Management Agency, *Report No. FEMA P-58*, Washington, D.C.

FEMA (2014). State of the art report on performance predication and evaluation of steel moment-frame building, Federal Emergency Management Agency, *Report No. FEMA 355F*, Washington, D.C.

Fonseca, N., and Guedes Soares, C. (1998). Time domain analysis of large-amplitude vertical ship motions and wave loads. *Journal of Ship Research*, 22, 139-153.

Frangopol, D.M. (1995). Reliability-based optimum structural design. *Chapter 16 in Probabilistic Structural Mechanics Handbook* (Edited by C. Sundararajan), Chapman & Hall, New York, 352-387.

Frangopol, D.M. (1999). Life-cycle cost analysis for bridges. *Bridge Safety and Reliability*, Reston, VA, 210-236.

Frangopol, D.M. (2011) Life-cycle performance, management, and optimization of structural systems under uncertainty: accomplishments and challenges. *Structure and Infrastructure Engineering*, 7(6), 389-413.

Frangopol, D.M., and Bocchini, P. (2011). Resilience as optimization criterion for the rehabilitation of bridges belonging to a transportation network subject to earthquake. *In: SEI-ASCE 2011 Structures Congress*, Las Vegas, NV, 2044-2055.

Frangopol, D.M., Bocchini, P., Decò, A., Kim, S., Kwon, K., Okasha, N.M., and Saydam, D. (2012). Integrated life-cycle framework for maintenance, monitoring, and reliability of naval ship structures. *Naval Engineers Journal*, 124(1), 89-99.

Frangopol, D.M., and Soliman, M. (2016). Life-cycle structural systems: Recent achievements and future directions. *Structure and Infrastructure Engineering*, 12(1), 1-20.

FREE!ship (2006). *FREE!ship manual - Version 2.6*. Website: www.freeship.org.

Fujii, Y., and Tanaka, K. (1971). Traffic capacity. *Journal of Navigation*, 24(4), 543-552.

Gallivan, F., Ang-Olson, J., Papson, A., and Venner, M. (2010). Greenhouse gas mitigation measures for transportation construction, maintenance, and operations activities. *Project 25-25*, National Cooperative Highway Research Program, Washington, D.C.

Ghosh, J., and Padgett, P.E. (2010) Aging consideration in the development of time-dependent seismic fragility curve. *Journal of Structural Engineering*, 136(12), 1497-1511.

Gilton, C., Chi, B., and Uang, C.M. (2000). Cyclic response of RBS moment connections: weak-axis configuration and deep column effects. *SAC/BD-00/23*, SAC Joint Venture.

Goda, K., and Hong, H.P. (2008). Spatial correlation of peak ground motions and response spectra. *Bull. Seismol. Soc. Am.*, 98(1), 354–365.

Goyet, J., Straub, D., and Faber, M.H. (2002). Risk-based inspection planning of offshore installations. *Structural Engineering International*, 3, 200-208.

Graizer, V., and Kalkan, E. (2007). Ground motion attenuation model for peak horizontal acceleration from shallow *Crustal* Earthquakes. *Earthquake Spectra*, 23(3), 585-613.

Guedes Soares, C. (1992). Combination of primary load effects in ship structures. *Probabilistic Engineering Mechanics*, 7(2), 103-111.

Guedes Soares, C., and Garbatov, Y. (1999). Reliability of maintained ship hulls subjected to corrosion and fatigue under combined loading. *Journal of Constructional Steel Research*, 52, 93-115.

Guedes Soares, C., Garbatov, Y., and von Selle, H. (2003). Fatigue damage assessment of ship structural components based on the long-term distribution of local stresses, *Int Shipbuild Prog*, 50, 35–56.

Guedes Soares, C., and Moan, T. (1991). Model uncertainty in the long term distribution of wave induced bending moments for fatigue design of ship structures. *Marine Structures*, 4(4), 295-315.

Guedes Soares, C., and Schellin, T.E. (1998). Nonlinear effects on long-term distribution of wave-induced loads for tankers. *J Offshore Mech Arct Eng*, 120, 65 - 70.

Guedes Soares, C., and Teixeira, A.P. (2000). Structural reliability of two bulk carrier designs. *Marine Structures*, 13(2), 107-128.

Hanks, T.C., and Bakun, W.H. (2002). A bilinear source-scaling model for M-log observations of continental earthquakes. *Bull. Seism. Soc. Am.*, 92, 1841-1846.

Harvat, J.A. (2009). *Effect of corrosion on the seismic response of a single-bent, reinforced concrete bridge*. Master Thesis, Texas A&M University, TX.

HAZUS (2003). *Multi-hazard loss estimation methodology earthquake model*. Technical Manual. Department of Homeland Security Emergency Preparedness and Response Directorate FEMA Mitigation Division, Washington, D.C.

Holmes, W.T., and Burkett, L. (2006). Seismic vulnerability of hospitals based on historical performance in California. *Proceedings of the 8th U.S. National Conference on Earthquake Engineering*, San Francisco, CA.

Horvath, A. (2004). Construction materials and the environment. *Annu. Rev. Environ. Resour.*; 29, 181–204.

Hossain, K.A., and Gencturk, B. (2014) Life-cycle environmental impact assessment of reinforced concrete building subjected to natural hazards. *Journal of Architectural Engineering*, A4014001, 1-12.

Howard, R.A., and Matheson, J.E. (1989). *Readings on the principles and applications of decision analysis*, Menlo Park, CA, Strategic Decisions Group.

Hørte, T., Wang, G., and White, N. (2007). Calibration of the hull girder ultimate capacity criterion for double hull tankers. *In: Proceedings of the 10th international symposium on practical design of ships and other floating structures*. Houston, TX, American Bureau of Shipping, 553–64.

Huang, W., and Guedes Soares, G. (2013). Fatigue reliability assessment of complex welded structure subjected to multiple cracks. *Engineering Structures*, 56, 868-879.

Hughes, O.F. (1983). *Ship structural design: A rationally-based, computer-aided, optimization approach*. Wiley and Sons, New York.

Hussein, A.W., and Guedes Soares, C. (2009). Reliability and residual strength of double hull tankers designed according to the new IACS common structural rules. *Ocean Engineering*, 36(17-18), 1446-1459.

Hwang, H., Liu, J.B., and Chiu, Y.H. (2001). Seismic fragility analysis of highway bridges. Mid-America Earthquake Center, *Technical Report*, RR-4 Project.

IACS (2006). *Goal-based new ship construction standards*. *MSC 81/INF.6*, Maritime Safety Committee, International Association of Classification Societies (IACS), London, UK.

IACS (2008). *Common structural rules for double hull oil tankers*. International Association of Classification Societies (IACS), London, UK.

IMO (2002). *Guidelines for formal safety assessment for use in the IMO rule-making process*, London, UK.

IMO (2008). *Formal safety assessment FSA-crude oil tankers*. London, UK.

International Building Code (2015). 2015 International building code, ICC; 1 edition, Washington, D.C.

Jayram, N., and Baker, J.W. (2009). Correlation model for spatially distributed ground-motion intensities. *Earthquake Engineering and Structural Dynamic*, 38, 1687-1708.

Jayaram, N., and Baker, J.W. (2010). Efficient sampling and data reduction techniques for probabilistic seismic lifeline risk assessment. *Earthquake Engineering and Structural Dynamic*, 39, 1109-1131.

JCSS probabilistic model code (2000). *Part 3: material properties.* Aalborg: JCCS; 2000. <http://www.jcss.byg.dtu.dk/>.

Jensen, J.J., and Pedersen, P.T. (1978). Wave induced bending moment in ships - quadratic theory, *Trans Royal Inst Naval Architects* (RINA), 120, 151-161.

Jibson, R.W., Crone, A.J., Harp, E.L., Baum, R.L., Major, J.J., Pullinger, C.R., Escobar, C.D., Martinez, M., and Smith, M. (2004). Landslides triggered by the 13 January and 13 February 2001 earthquakes in El Salvador. *Geological Society of America*, 375, 69- 88.

Jiménez, A., Ríos-Insua, S., and Mateos, A. (2003). A decision support system for multiattribute utility evaluation based on imprecise assignments. *Decision Support Systems*, 36(1), 65–79.

Keeney, R.L., and Raiffa, H. (1993). *Decisions with multiple objectives: preferences and value tradeoffs*, Cambridge University Press.

Kendall, A., Keoleian, G.A., and Helfand, G.E. (2008). Integrated life-cycle assessment and life-cycle cost analysis model for concrete bridge deck applications. *Journal of Infrastructure Systems*, 14(3), 214-222.

Khan, I.A., and Parmentier, G. (2006). Ultimate strength and reliability analysis of a VLCC. *Proceedings of the 3rd International ASRANet Colloquium*, Glasgow, UK, 1-14.

Kim, S., and Shinozuka, M. (2004). Development of fragility curves of bridges retrofitted by column jacketing. *Probabilistic Engineering Mechanics*, 19(1-2), 105-112.

Kim, S., and Frangopol, D.M. (2011). Optimum inspection planning for minimizing fatigue damage detection delay of ship hull structures. *International Journal of Fatigue*, 33(3), 448-459

Kim, S., Frangopol, D.M., and Soliman, M. (2013). Generalized probabilistic framework for optimum inspection and maintenance planning. *Journal of Structural Engineering*, 139(3), 435-447.

Kim, Y.S., Spencer, B.F., and Elnashai, A.S. (2008). Seismic loss assessment and mitigation for critical urban infrastructure systems. *Report No. NSEL-007*, Newmark Structural Engineering Laboratory, Department of Civil and Environmental Engineering, University of Illinois at Urbana-Champaign, Urbana, IL.

Kiremidjian, A., Moore, J., Fan, Y. Y., Yazlali, O., Basoz, N., and Williams, M. (2007). Seismic risk assessment of transportation networks. *Journal of Earthquake Engineering*, 11, 371–382.

Krawinkler, H., and Van, N. (2005). Van Nuys hotel building testbed report: exercising seismic performance assessment. *PEER Report No. 2005/11*, Pacific Earthquake Engineering Research Center, University of California at Berkeley, CA.

Ku, A., Serratella, C., Spong, R., Basu, R., Wang, G., and Angevine, D. (2004). Structural reliability applications in developing risk-based inspection plans for a floating production installation. *In: Proc 23nd int conf on offshore mechanics and arctic engineering*, Vancouver, Canada.

Kukkanen, T., and Mikkola, T.P.J. (2004). Fatigue assessment by spectral approach for the ISSC comparative study of the hatch cover bearing pad. *Marine Structures*, 17(1), 75-90.

Kwon, K., and Frangopol, D.M. (2011). Bridge fatigue assessment and management using reliability-based crack growth and probability of detection models. *Probabilistic Engineering Mechanics*, 26(3), 471–480.

Kwon, K., and Frangopol, D.M. (2012). Fatigue life assessment and lifetime management of aluminum ships using life-cycle optimization. *Journal of Ship Research*, 56(2), 91-105.

Kyriakidis, P.C. (2005). Sequential spatial simulation using Latin hypercube sampling, In O. Leuangthong, and C. V. Deutsch (Eds.) *Geostatistics Banff 2004: Seventh International Geostatistics Congress, Quantitative Geology and Geostatistics*, Dordrecht, The Netherlands: Kluwer Academic Publishers, 14(1), 65-74.

Larsen, L., Rajkovich, N., Leighton, C., McCoy, K., Calhoun, K., Mallen, E., Bush, K., Enriquez, J., Pyke, C., McMahon, S., and Kwok, A. (2011). *Green building and climate resilience: Understanding impacts and preparing for changing conditions*, University of Michigan, U.S. Green Building Council.

Lassen, T. (2013). Risk based fatigue inspection planning – state of the art. *5th Fatigue Design Conference of Fatigue Design*, 489-499.

Lee, R.G., and Kiremidjian, A.S. (2007). *Uncertainty and correlation in seismic risk assessment of transportation systems*. Department of Civil and Environmental Engineering, Stanford University, Pacific Earthquake Engineering Research Center, Richmond, CA.

LEED (2008). *LEED for existing buildings: operations & maintenance*, U.S. Green Building Council.

Liel, A.B., and Deierlein, G.G. (2013). Cost-benefit evaluation of seismic risk mitigation alternatives for older concrete frame buildings. *Earthquake Spectra*, 29(4), 1391-1411.

Liu, C., Fan, Y., and Ordóñez, F. (2009). A two-stage stochastic programming model for transportation network protection. *Computers & Operations Research*, 36, 1582-1590.

Liu, M., and Frangopol, D.M. (2006). Optimizing bridge network maintenance management under uncertainty with conflicting criteria: Life-cycle maintenance, failure, and user costs. *Journal of Structural Engineering*, 131(11), 1835–1845.

Liu, Y., and Weyers, R.E. (1998). Modeling the time-to-corrosion cracking in chloride contaminated reinforced concrete structures. *ACI Materials Journal*, 95(6), 675-681.

Loh, C.H., Lee, C.H., and Yeh, C. (2003). Seismic risk assessment of transportation systems: evaluation immediately after earthquake. *Technologies and disaster response for lifeline systems, Technical Council on Lifeline Earthquake Engineering*, Monograph No. 25, ASCE.

Lua, J., and Hess, P.E. (2006). First-failure-based reliability assessment and sensitivity analysis of a naval vessel under hogging. *Journal of Ship Research*, SNAME, 50(2), 158-170.

Lukic, M., and Cremona, C. (2001a). Probabilistic assessment of welded joints versus fatigue and fracture. *Journal of Structural Engineering*, 127, 211-218.

Lukic, M., and Cremona, C. (2001b). Probabilistic optimization of welded joints maintenance versus fatigue and fracture. *Reliability Engineering and System Safety*, 72, 253-264.

Mackie, K., and Stojadinovic, B. (2001). Probabilistic seismic demand model for California highway bridges. *Journal of Bridge Engineering*, 6(6), 468-481.

Macduff, T. (1974). Probability of vessel collisions. *Ocean Industry*, 9(9), 144–148.

Maljaars, J., and Vrouwenvelder, A.C.W.M. (2014). Probabilistic fatigue life updating accounting for inspections of multiple critical locations. *International Journal of Fatigue*, 68, 24-37.

Mander, J.B. (1999). *Fragility curve development for assessing the seismic vulnerability of highway bridges*. Technical Report, University at Buffalo, State University of New York.

Mander, J.B., Priestley, M.N, and Park, R. (1998). Theoretical stress - strain behavior of confined concrete. *Journal of Structural Engineering*, 114(8), 1804-1826.

Mansour, A., Wirsching, P., White, G., and Ayyub, B. (1996). Probability based ship design: implementation of design guidelines. SSC-392, *Ship Struct Comm*, Washington, DC.

Mao, W., Li, Z., Ringsberg, J.W., and Rychlik, I. (2012). Application of a ship-routing fatigue model to case studies of 2800 TEU container vessels. *Proceeding of the Institution of Mechanical Engineers, Part M: Journal of Engineering for the Maritime Environment*, 222-234.

MathWorks. (2013). The MathWorks, Inc., Natick, MA.

McKay, M.D., Conover, W.J., and Beckman, R.J. (1979). A comparison of three methods for selecting values of output variables in the analysis of output from a computer code. *Technometrics*, 21(2), 239–45.

Min, H. (1994). International supplier selection: a multi-attribute utility approach, *International Journal of Physical Distribution & Logistics Management*, 24(5), 24–33.

Miroyannis, A. (2006). *Estimation of ship construction costs*. *Master thesis*. Department of Mechanical Engineering, Massachusetts Institute of Technology, Boston, MA

Mitrani-Reiser, J. (2007). Probabilistic loss estimation for performance-based earthquake engineering. *Ph.D Dissertation*. California Institute Technology, Pasadena, CA.

Moan, T. (2005). Reliability-based management of inspection, maintenance and repair of offshore structure. *Structure and Infrastructure Engineering*, 1(1), 33-62.

Moan, T., and Song, X. (2000). Implications of inspection updating on system fatigue reliability of offshore structures. *Journal of Offshore Mechanics and Arctic Engineering*, 122, 173-180.

Moan, T., Vardal, O., Hellevig, N., and Skjoldli, K. (1997). In-service observations of cracks in North Sea jackets- a study on initial crack depth and pod values. *Proceedings of 16th international Conference on Offshore Mechanics and Arctic Engineers*, Yokohama, ASME.

Montewka, J., Hinz, T., Kujala, P., and Matusiak, J. (2010). Probability modeling of vessel collisions. *Reliability Engineering and System Safety*, 95, 573-589.

Moretti, S., Trozzo, A., Terzic, V., Cimellaro, G.P., and Mahin, S. (2014). Utilizing base-isolation systems to increase earthquake resilience of healthcare and school building. *Proceeding of 4th Conference on Building Resilience, Building Resilience*, Salford Quays, UK.

Myrtle, R.C., Masri, S.E., Nigbor, R.L., and Caffrey, J.P. (2005). Classification and prioritization of essential systems in hospitals under extreme events. *Earthquake Spectra*, 21(3), 779-802.

National Academies (2012). *Disaster resilience: A national imperative*. Committee on Increasing National Resilience to Hazards and Disasters, National Academies Press, Washington, D.C.

NEES (2009). *NEES tips: Tools for isolation and protective systems*. 2009, (http://www.neng.usu.edu/cee/faculty/kryan/NEESTIPS/PBEE_study.html).

Newman, J.C., and Raju, J.S. (1981). An empirical stress-intensity factor equation for the surface crack. *Engineering Fracture Mechanics*, 15(1-2), 185-192.

Nguyen, K.T., Garbatov, Y., and Guedes Soares, C. (2013). Spectral fatigue damage assessment of tanker deck structural detail subjected to time-dependent corrosion. *International Journal of Fatigue*, 48, 147-155.

Niederreiter, H. (1992). *Random number generation and Quasi-Monte Carlo methods*. Society for Industrial and Applied Mathematics, Philadelphia, PA.

Ochsendorf, J.A. (2005). Sustainable engineering: The future of structural design. *Proceedings of the Structures Congress and the Forensic Engineering Symposium: Metropolis and Beyond*, New York, NY.

Okasha, N.M., and Frangopol, D.M. (2009). Lifetime-oriented multi-objective optimization of structural maintenance considering system reliability, redundancy and life-cycle cost using GA. *Structural Safety*, 31(6), 460-474.

Okasha, N.M., and Frangopol, D.M. (2010). Efficient method based on optimization and simulation for the probabilistic strength computation of the ship hull. *Journal of Ship Research*, 54(4), 1-13.

Okasha, N.M., Frangopol, D.M., Saydam, D., and Salvino, L.W. (2011). Reliability analysis and damage detection in high speed naval crafts based on structural health monitoring data. *Structural Health Monitoring*, 10(4), 361-379.

OpenSees (2012). Open system for earthquake engineering simulation. *Pacific Earthquake Engineering Research Center*, University of California, Berkeley.

Otto, S., Pedersen, P.T., Samuelides, M., and Sames, P.C. (2002). Elements of risk analysis for collision and grounding of a *RoRo* passenger ferry. *Marine Structure*, 15, 461-474.

Packman, P.F., Pearson, H.S., Owens, J.S., and Young, G. (1969). Definition of fatigue cracks through non-destructive testing. *Journal of Material*, 4(3), 666–700.

Padgett, J.E., Dennemann, K., and Ghosh, J. (2010) Risk-based seismic life-cycle cost-benefit analysis for bridge retrofit assessment. *Structural Safety*, 32(3), 165-173.

Padgett, J.E., Desroches, R., and Nilsson, E. (2010). Regional seismic risk assessment of bridge network in Charleston, South Carolina. *Journal of Earthquake Engineering*, 14, 918-833.

Padgett, J.E, Ghosh, J., and Dennemann, K. (2009). Sustainable infrastructure subjected to multiple threats. TCLEE 2009: *Lifeline Earthquake Engineering in a Multi-hazard Environment*, 703-713.

Park, J. (2004). Development and application of probabilistic decision support framework for seismic rehabilitation of structure systems. *Ph.D. Dissertation*, Civil and Environmental, Georgia Institute of Technology, Atlanta, GA.

Paik, J.K., and Frieze, P.A. (2001). Ship structural safety and reliability. *Progress in Structural Engineering and Materials*, 3(2), 198-210.

Paik, J.K., and Mansour, A.E. (1995). A simple formulation for prediction the ultimate strength of ships. *Journal of Marine Science and Technology*, 1, 52-65.

Paik, J.K., Thayamballi, A.K., Kim, S.K., and Yang, S.H. (1998). Ship hull ultimate strength reliability considering corrosion. *Journal of Ship Research*, 42(2), 154-165.

Paris, P., and Erdogan, F. (1963). A critical analysis of crack propagation laws. *Journal of Fluids Engineering*, 85(4), 528-533.

Paul, J.A., George, S.K., Yi, P., and Lin, L. (2006). Transient modelling in simulation of hospital operations for emergency response. *Prehospital and Disaster Medicine*, 21(4), 223-236.

PDSTRIP (2006). Program PDSTRIP: Public domain strip method - User Manual. Website: http://sourceforge.net/projects/pdstrip.

Pearce, A.R., and Vanegas, J.A. (2002). Defining sustainability for built environment systems: an operational framework. *International Journal of Environmental Technology and Management*, 2(1-3), 94-113.

Pedersen, P.T. (1995). Collision and grounding mechanics. *Proceedings of the WEGEMT Association – A European Association of Universities in Marine Technology and Related Sciences*, Copenhagen, Denmark, 125-157.

Pedersen, P.T., and Zhang, S. (1998). On impact mechanics in ship collision. *Marine Structures*, 11, 429-449.

Perotti, F., Domaneschi, M., and De Grandis, S. (2013). The numerical computation of seismic fragility of base-isolated nuclear power plants buildings. *Nuclear Engineering and Design*, 262, 189-200.

Porter, K.A., Kiremidjian, A.S., and Legrue, J.S. (2001). Assembly-based vulnerability of buildings and its use in performance evaluation. *Earthquake Spectra*, 17(2), 291-312.

Prpić-Oršić, J., and Faltinsen, O.M. (2012). Estimation of ship speed loss and associated CO_2 emissions in a seaway. *Ocean Engineering*, 44, 1-10.

Rabiei, M., and Modarres, M. (2013). A recursive Bayesian framework for structural health management using online monitoring and periodic inspections. *Reliab Eng Syst Safe*, 112, 154–64.

Rackwitz, R. (2002). Optimization and risk acceptability based on the Life Quality Index. *Structural Safety*, 24(2-4), 297-331.

Rasmus, F. (1998). Spectral fatigue damage calculation in the side shells of ships, with due account taken of the effect of alternating wet and dry areas. *Marine Structures*, 11, 319–343.

Resolute Weather (2014). Pierson–Moskowitz Sea Spectrum. ⟨http://www.eustis.army.mil/weather⟩ (accessed March 3, 2014).

Richardson, E.V., and Davis, S.M. (2001). *Evaluating scour at bridges*. Hydraulic Engineering Circular (HEC) No. 18. Washington, Department of Transportation.

Ricles, J.M., Mao, C., Lu, L.W., and Fisher, J.W. (2002). Development and evaluation of improved details for ductile welded unreinforced flange connections. *SAC/BD-00/24*, SAC Joint Venture.

Rigterink, D., Collette, M., and Singer, D. (2013). A method for comparing panel complexity to traditional material and production cost estimating techniques. *Ocean Engineering*, 70, 61-70.

Ryan, K.L., and Chopra, A.K. (2004). Estimation of seismic demands on isolators based on nonlinear analysis. *Journal of Structural Engineering*, 130(3), 392-402.

Salvesen, N., Tuck, E., and Faltisen, O. (1970). Ship motions and sea loads. *Transactions the Society of Naval Architects and Marine Engineering*, 78, 250-287.

Sayani, P.J. (2009) Relative performance comparison and loss estimation of seismically isolated and fixed-based buildings using PBEE approach. *Ph.D Dissertation*, Civil and Environmental Engineering, Utah State University, 2009.

Sayani, P.J., Erduran, E., and Ryan, K.L. (2011) Comparative response assessment of minimally compliant low-rise base isolated and conventional steel moment-resisting frame buildings. *Journal of Structural Engineering*, 137(10), 1118-1131.

Saydam, D., Bocchini, P., and Frangopol, D.M. (2013). Time-dependent risk associated with highway bridge networks. *Engineering Structures*, 54, 221-233.

Saydam, D., and Frangopol, D.M. (2013). Performance assessment of damaged ship hulls. *Ocean Engineering*, 68, 65-76.

Schneider, R., Thons, S., Rucker, W., and Straub, D. (2013). Effect of different inspection strategies on the reliability of Daniels systems subjected to fatigue. *Proceedings of the Eleventh International Conference on Structural Safety and Reliability ICOSSAR2013*, New York, NY, 2637-2644.

Seismological Society of America (SSA) (2010). Issue of the Bulletin of the Seismological Society of America (BSSA), E1 Cerrito, CA, United States. (http://www.seismosoc.org/society/press_releases/BSSA_100-1_Tipsheet.pdf).

Shinozuka, M., Feng, M.Q., Lee, J., and Naganuma, T. (2000). Statistical analysis of fragility curves. *Journal of Engineering Mechanics*, 126(12), 1224-1231.

Shinozuka, M., Murachi, Y., Dong, X., Zhou, Y., and Orlikowski, M.J. (2003). Effect of seismic retrofit of bridges on transportation networks. *Earthquake Engineering and Engineering Vibration*, 2(2), 169-179.

Shinozuka, M., Zhou, Y., Kim, S.H., Murachi, Y., Banerjee, S., Cho, S., and Chung, H. (2005). Social-economic effect of seismic retrofit implemented on bridges in Los Angeles highway network. *Report No. CA06-0145*, Department of Civil and Environmental Engineering, University of California, Irvine, CA.

Ship Structure Committee (SSC) (1995). *Ship maintenance project: Fatigue damage evaluation*. SSC-396-I, Ship Structure Committee, U.S. Coast Guard, Washington, D.C..

Ship Structure Committee (SSC 2000). *Risk-based life cycle management of ship structures*. SSC-416, 2000, Ship Structure Committee, U.S. Coast Guard, Washington, D.C.

Shiraki, N., Shinozuka, M., Moore, J.E., Chang, S.E., Kameda, H., and Tanaka, S. (2007). System risk curves: probabilistic performance scenarios for highway networks subject to earthquake damage. *Journal of Infrastructure Systems*, 213(1), 43–54.

Shirley, T.C., Tunnell, J.W., Moretzsohn, F., and Brenner, J. (2010). Biodiversity of the gulf of Mexico: Applications to the deep horizon oil spill. *Harte Research Institute for Gulf of Mexico Studies*, Texas A&M University, College Station, TX.

Shome, N., Cornell, C.A., Bazzurro, P., and Carballo, J.E. (1998). Earthquakes, records, and nonlinear responses. *Earthquake Spectra*, 14(3), 469-500.

Siddiqui, N.A., and Ahmad, S. (2001). Fatigue and fracture reliability of TLP tethers under random loading. *Marine Structures*, 14, 331-352.

Simon, J., Bracci, J., and Gardoni, P. (2010). Seismic response and fragility of deteriorated reinforced concrete bridges. *Journal of Structural Engineering*, 136(10), 1273-1281.

Slovic, P. (2000). The perception of risk, *Earthscan*, Virginia.

Smyth, A.W., Altay, G., Deodatis, G., Erdik, M., Franco, G., Gulkan, P., Kunreuther, H., Lus, H., Mete, E., Seeber, N., and Yuzugullu, O. (2004). Probabilistic benefit-cost analysis for earthquake damage mitigation: Evaluating measures for apartment houses in Turkey. *Earthquake Spectra*, 20(1), 171-203.

Spencer, P.C., Hendy, C.R., and Petty, R. (2012). Quantification of sustainability principles in bridge projects. *Proceedings of the ICE - Bridge Engineering*, 165(2), 81-89.

Sohn, J., Kim, T.J., Hewings, G.J.D., Lee, J.S., and Jang, S-G. (2003). Retrofit priority of transport network links under an earthquake. *Journal of Urban Planning and Development*, 129(4), 195-210.

Soliman, M., and Frangopol, D.M. (2014). Life-cycle management of fatigue sensitive structures integrating inspection information. *Journal of Infrastructure Systems*, 20(2), 04014001, 1-13.

Soliman, M., Frangopol, D.M., and Kim, S. (2013). Probabilistic optimum inspection planning of steel bridges with multiple fatigue sensitive details. *Engineering Structures*, 49, 996-1006.

Stein, S.M., Young, G.K., Trent, R.E., and Pearson, D.R. (1999). Prioritizing scour vulnerable bridges using risk. *Journal of Infrastructure Systems*, 5(3), 95-101.

Stewart, T.J. (1996). Robustness of additive value function methods in MCDM. *Journal of Multi-Criteria Decision Analysis*, 5(4), 301-309.

Tammer, M., and Kaminski, M.L. (2013). Fatigue oriented risk based inspection and structural health monitoring of FPSOs. *Proceedings of the Twenty-third International Offshore and Polar Engineering Anchorage*, Alaska, 438-449.

Tapia, C., Ghosh, J. and Padgett, J.E. (2011). Life cycle performance metrics for aging and seismically vulnerable bridges. *Proceedings of the 2011 Structures Congress*, ASCE, Las Vegas, Nevada.

Taylor, C.E., Werner, S.D., and Jakubowski, S. (2001). Walkthrough method for catastrophe decision making. *Natural Hazards Review*, 2(4), 193–202.

Taylor, A.C., and Fletcher, T.D. (2006). Triple-bottom-line assessment of urban storm water projects. *Water Science Technology*, 54(6-7), 459-466.

Teixeira, A.P., Parunov, J., and Guedes Soares, C. (2011). Assessment of ship structural safety. *In Marine Technology and Engineering*, London, UK, 1377-94.

Terzic, V., Mahin, S.A., and Comerio, M.C. (2014) Comparative life-cycle cost and performance analysis of structural systems. *Proceedings of the 10th National Conference in Earthquake Engineering, Earthquake Engineering Research Institute*, Anchorage, AK.

Thoft-Christensen, P., Jensen, F.M., Middleton, C.R., and Blackmore, A. (1997). *Revised rules for* concrete *bridges.* Thomas Telford, London, UK, 175-188.

Thompson, A.C., Whittaker, A.S., Fenves, G.L., and Mahin, S.A. (2007). Property modification factors for elastomeric seismic isolation bearings. *Proceedings of the 12th World Conference on Earthquake Engineering*, Auckand, NZ.

Tversky, A., and Kahneman, D. (1992). Advances in prospect theory: Cumulative representation of uncertainty. *Journal of Risk Uncertainty*, 5(4), 297-323.

United States Geological Survey (USGS) (2003). Earthquake Probabilities in the San Francisco Bay Region: 2002–2031. *Open File Report 03-214*. Menlo Park, CA.

UNISDR (United Nations Office for Disaster Risk Reduction) (2014). *Disaster resilience scorecard for cities, based on UNISDR's "Ten Essentials"*. Version 1.5, United

Nations Office for Disaster Reduction, 2014 (http://www.unisdr.org/2014/campaign cities/Resilience%20Scorecard%20V1.5.pdf)

U.S. Coast Guard (*USCG*). (2009). Accident statistics from 1999 to 2008. *COMDTPUB P16754.26*, U.S. Department of Homeland Security, U.S. Coast Guard Office of Auxiliary and Boating Safety.

U.S. Army Corps of Engineers (*USACE*). (2011). Delaware River main channel deepening project updated economic assessment of relevant market and industry trends. Philadelphia District, North Atlantic Division, U.S. Army Corps of Engineers.

Val, D.V., and Stewart, M.G. (2003). Life-cycle cost analysis of reinforced concrete structures in marine environments. *Structural Safety*, 25(4), 343-362.

Vaziri, P., Davidson, R., Apivatanagul, P., and Nozick, L. (2012). Identification of optimization-based probabilistic earthquakes scenarios for regional loss estimation. *Journal of Earthquake Engineering*, 16, 296-315.

Visser, W. (2002). POD/POS curves for non-destructive examination. *Offshore Technology Report OTO 2000/018*, UK, Health & Safety Executive.

Von Neumann, J., and Morgenstern, O. (1953). *Theory of games and economic behavior*, Princeton: Princeton University Press.

Vu, K. (2003). *Corrosion-induced cracking and spatial time-dependent reliability analysis of reinforced concrete structures*. PhD thesis, The University of Newcastle, New South Wales, Australia.

Vu, K., and Stewart, M.G. (2000). Structural reliability of concrete bridges including improved chloride-induced corrosion models. *Structural Safety*, 22(4), 313-333.

Wang, M., and Takada, T. (2005). Macrospatial correlation model of seismic ground motions. *Earthquake Spectra*. 21(4), 1137–1156.

Wang, Y. (2010). Spectral fatigue analysis of a ship structural detail – A practical case study. *International Journal of Fatigue*, 32, 310-317.

Werner, S.D., Taylor, C.E., Cho, S., Lavoie, J-P., Huyck, C., Eitzel, C., Chung, H. and Eguchi, R.T. (2006). *REDARS 2 methodology and software for seismic risk analysis of highway systems* (MCEER-06-SP08), Buffalo, NY.

Whittemore, D. (2010). Sustainable structures for the bridge engineer. *Structure*, Structural sustainability, discussion of sustainability and preservation as they pertain to structural engineering, National Council of Structural Engineers Associations (*NCSEA)*, Chicago, IL.

Wirsching, P.H., Ortiz, K., and Chen, Y.N. (1987). Fracture mechanics model in a reliability format. *In: Proc 6th int symp offshore mechanics and arctic engineering*. New York, NY.

World Health Organization (WHO) (2007). Risk Reduction in the Health Sector and Status of Progress. *Proceedings of Disaster Risk Reduction in the Healthcare Sector-Thematic Workshop*, World Health Organization (WHO), Geneva, Switzerland.

Xue, J., Pittaluga, A., and Cervetto, D. (1994). Fatigue damage calculation for oil tanker and container ship structure. *Marine Structures*, 7(6), 499-535.

Yan, H., Shen, Q., Fan, L., Wang, Y., and Zhang, L. (2010). Greenhouse gas emissions in building construction: A case study of One Peking in Hong Kong. *Build. Environ*, 45, 949–955.

Yavari, S., Chang, S., and Elwood, K.J. (2010). Modeling post-earthquake functionality of regional health care facilities. *Earthquake Spectra*, 26(3), 869-892.

Yi, P. (2005). *Real-time generic hospital capacity estimation under emergency situations*. State University of New York at Buffalo, Buffalo, NY.

Zhou, Y. (2006). *Probabilistic seismic risk assessment of highway transportation network*. Ph.D. dissertation, University of California, Irvine, CA.

Zhou, Y., Banerjee, S., and Shinozuka, M. (2010). Socio-economic effect of seismic retrofit of bridges for highway transportation networks: a pilot study. *Structure and Infrastructure Engineering*, 6, 145-157.

Zhu, B., and Frangopol, D.M. (2013). Risk-based approach for optimum maintenance of bridges under traffic and earthquake loads. *Journal of Structural Engineering*, 139(3), 422-434.

Zhu, B., and Frangopol, D.M. (2013). Reliability assessment of ship structures using Bayesian updating. *Engineering Structures*, 56, 1836-1847.

Zinke, T., Bocchini. P., Frangopol, D.M., and Ummenhofer, T. (2013). Combining resilience and sustainability in infrastructure projects. *Life-Cycle and Sustainability of Civil Infrastructure Systems*, Strauss, A., Frangopol, D. M., Bergmeister, K. eds., Taylor and Francis, 2450-2457.

APPENDIX A

LIST OF NOTATIONS

Notations of Chapter 2

A	=	cross section area of steel reinforcement
c_{ATC}	=	average total compensation per hour
c_{AW}	=	average *wage* per hour
c_{goods}	=	time value of the goods
c_{REB}	=	rebuilding cost per square meter
$c_{Run,car}$	=	average costs for running cars
$c_{Run,truck}$	=	average costs for running trucks
C	=	concrete cover (*mm*)
C_S	=	bridge seismic capacity
d_i	=	downtime associated with the damage state *i*
D	=	diameter of steel reinforcement
D_l	=	length of the detour
D_i	=	initial diameter of steel reinforcement
D_S	=	seismic demand
DS_i	=	damage state *i* of the bridge
Enp_{car}	=	environmental metric per unit distance for cars
Enp_{Truck}	=	environmental metric per unit distance for trucks
f'_{cy}	=	concrete compressive strength

FT_i	=	number of fatalities associated with the damage state *i*
FV	=	future monetary value
$ICAFB$	=	implied cost of averting a fatality
L	=	bridge length
O_{Car}	=	average vehicle occupancies for cars
O_{Truck}	=	average vehicle occupancies for trucks
PGA	=	peak ground acceleration
$P_{DSi\|PGA}$	=	conditional probability of being in damage state *i* under certain *PGA*
PV	=	present monetary value
r	=	annual discount rate of money
r_{corr}	=	corrosion rate
RCR_i	=	repair cost ratio for damage state *i*
S	=	average detour speed
S_d	=	median value of the demand of displacement ductility
T	=	average daily traffic ratio
T_i	=	time to corrosion initiation
T_{cr1}	=	time from corrosion initiation to corrosion cracking
THA	=	time-history analysis
w/c	=	water-cement ratio
W	=	bridge width
β_c	=	lognormal standard deviations of the capacity, respectively
β_d	=	standard deviation of the demand of displacement ductility
$\Phi(.)$	=	standard normal cumulative distribution function

Notations of Chapter 3

a and b	=	regression coefficients associated with seismic demand
ADE	=	average daily traffic remaining on the damaged link
ADT	=	average daily traffic to detour
c_{ATC}	=	average total compensation per hour
c_{AW}	=	average wage per hour
c_{goods}	=	time value of the goods transported in a cargo
c_{REB}	=	rebuilding cost per square meter
$c_{Run,car}$	=	average costs for running cars and trucks per unit length
$c_{Run,truck}$	=	average costs for running cars and trucks per unit length
$C_{Cons\|DS}$	=	conditional consequence given a damage state
D	=	length of the detour
DS	=	damage state
DR_{MSAS}	=	ductility demand ratio
$f(\boldsymbol{X})$	=	joint PDF of the considered random variables $\boldsymbol{X} = (x_1, x_2, \dots, x_k)$
FR_i	=	functionality ratio associated with damage state i
IM	=	ground motion intensity measure
l	=	route segment containing the bridge
L	=	bridge length
MSAS	=	mainshock and aftershock
O_{car}	=	average vehicle occupancies for cars
O_{truck}	=	average vehicle occupancies for trucks
$P_{DS\|H}$	=	conditional probability of damage arising from hazard H

PGA	=	peak ground acceleration
PGA_{AS}	=	PGA at the location of the bridge associated with the aftershock
PGA_{MS}	=	PGA at the location of the bridge associated with mainshock
$P_{S=DSi\|IM}$	=	conditional probability of a bridge being in damage state *i* under *IM*
Q	=	functionality of the bridge under the recovery function
RCR_i	=	repair cost ratio for a bridge in damage state *i*;
S	=	average detour speed
S_0	=	average speed on the intact link
S_D	=	average speed on the damaged link
SDOF	=	single degree of freedom
t_h	=	investigated time point.
t_o	=	occurrence time of the extreme event
T	=	average daily truck traffic ratio
W	=	bridge width
$\beta_{c,i}$	=	lognormal standard deviation of the capacity
β_d	=	lognormal standard deviation of the demand
β_m	=	lognormal standard deviation that represents the modelling uncertainty
μ_d	=	median value for the seismic demands
$\mu_{c,i}$	=	median value associated with seismic capacity of damage state *i*
$\delta(\boldsymbol{X})$	=	consequences
$\Phi(.)$	=	standard normal cumulative distribution function

Notations of Chapter 4

a_o, b_o, c_o, and d_o = regression coefficients

a_{dr} = depth to the point of rotation

$ADTD$ = average daily traffic to detour

$ADTE$ = average daily traffic remaining on the damaged link

A_f = side friction area of the pile

A_F = total area of fault segment

A_p = tip resistance area

Apr = annual precipitation

c_{ATC} = compensation per hour

c_{AW} = wage per hour

c_{goods} = time value of the goods transported in a cargo

c_{reb} = rebuilding cost per square meter

$c_{Run,car}$ = costs for running cars per unit length

$c_{Run,truck}$ = costs for running trucks per unit length

$C_{Cons|DS}$ = conditional consequence

C_D = drag coefficient

Cov = covariance between two random variables

d_r = damage ratio

D = diameter of the pier

D_l = length of the detour

Dra = drainage area

e = eccentricity of loading

E = expected value

f_u	=	ultimate side friction coefficient
g_1	=	performance functions associated with vertical limit states
g_2	=	performance functions associated with lateral limit state
IM	=	seismic intensity measure
K_p	=	passive earth pressure coefficient
l_l	=	route segment
L	=	bridge length
L_F	=	segment length
L_p	=	embedded length of pile
L_{REP}	=	annual repair loss
L_{RUN}	=	annual operation loss
L_{TL}	=	annual time loss
$L_T(t_k)$	=	expected annual hazard loss at time t_k
L_v	=	vertical load effect
m_i	=	median value of ground motion intensity associated with damage state i
m_{io}	=	median value of the ground motion intensity for damage state i
Mel	=	elevation
$N(t_{int})$	=	number of hazard events that occur during the time interval
O_{Car}	=	average vehicle occupancies for cars
O_{Truck}	=	average vehicle occupancies for trucks
p_{avg}	=	average pressure of flowing water
p_u	=	ultimate point pressure
P	=	conditional time-dependent probability of occurrence

$P_{DS\|H}$	=	conditional probability of a damage state given a hazard
Q	=	functionality of a bridge under recovery function
R	=	Reynolds number
RCR	=	repair cost ratio
R_{sf}	=	scaling factor
S	=	average detour speed
S_0	=	average speed on the intact link
S_D	=	average speed on the damaged link
t_0	=	investigated point in time
t_e	=	elapsed time
t_{int}	=	investigated time interval
t_{IL}	=	time interval until the bridge reaches full functionality
t_m	=	median recurrence interval
T	=	average daily truck traffic ratio
υ_w	=	water viscosity
V_f	=	velocity of flow
V_{sl}	=	slip rate associated with the investigated fault
V_w	=	velocity of water
W	=	bridge width
W_F	=	fault segment width
x_l	=	unbiased value of load effect
x_u	=	unbiased value of resistance
z	=	scour depth

$\dot{z}_i$ = initial rate of scour

$\hat{z}_{max}$ = maximum depth of scour

ξ = shape factor

δ = interface friction angle between the pile and the soil

γ = aging coefficients

γ_s = effective unit weight of soil

γ_w = density of water

ϕ' = internal friction angle of the soil;

η = shape factor

Notations of Chapter 5

$A(M,F)$ = magnitude and fault-type scaling function

b = correlation length

BDI_i = bridge damage index for the respective damage state i

d_{ij} = downtime associated with the damage states of each link

D_0 = parameter quantifying the intensity of bump on the attenuation curve

D_1 = parameter accounting for distances larger than R_1

F = a parameter characterizing faulting style

FT_{ij} = number of fatalities associated with the damage state i of bridge j

h = distance between two sites

IM = seismic intensity measure

LDI = link damage index

m = number of the bridges in the transportation network

m_i = median value of intensity measure of damage state *i*

m_{io} = median value of intensity of the original fragility curve

M = earthquake magnitude

n = number of the bridges located in the link

$P_{BDSij|IM}$ = conditional probability of the bridge *j* being at damage state *i*

$P_{DSi|IM}$ = conditional probabilities of being in damage state *i*

$P_{LDSij|IM}$ = conditional probability of the link *j* being in damage state *i*

R = source-to-site distance

R_0 = corner distance

R_1 = distance threshold after which faster attenuation takes place

VS_{30} = average shear-wave velocity in upper 30 m

Y = strong-motion parameter of interest

γ = aging coefficient

σ_{lnY} = total standard deviation of *lnY*

β_i = standard deviation of the logarithm of ground motion intensity

$\Phi(.)$ = standard normal cumulative distribution function

Notations of Chapter 6

cn = number of crews available for the repair action

C = collapse

C_C = rebuilding cost associated with the collapsed building

$C_{NStDr,}$ = repair cost associated with drift sensitive non-structural component being in damage state *j*

$C_{NStAc,k}$ = repair cost associated with acceleration sensitive non-structural component being in damage state *k*

$C_{StDr,i}$ = repair cost of a drift sensitive structural component being in state *i*

$L_{C|IM}$ = repair loss associated with the collapse of the building under a given *IM*

$L_{NC|IM}$ = repair loss associated with non-collapse of building under a given *IM*

m = number of assembly groups

n_{fa} = number of people under the fatality risk

n_j = number of component *j*

N = number of damage states associated with investigated component

NC = non-collapse

$P_{C|IM}$ = conditional probability of building collapse given IM

$PFA_{fai|DMi}$ = probability of fatality associated with building being in state *i* under *IM*

$P_{DMi|IM}$ = conditional probability of building being in state *i* under *IM*

$P_{j,DSi|IM}$ = probability of the building component *j* being in damage state *i* conditioned on the survival of structure under a given *IM*

$P_{StDr,DSi|IM}$ = conditional probability of being in a given damage state under *IM* associated with drift sensitive structural components

$P_{NStDr,DSj|IM}$ = conditional probability of being in a given damage state under *IM* associated with drift sensitive non-structural components

$P_{NStAc,DSk|IM}$ = conditional probability of being in a given damage state under *IM* associated with acceleration sensitive non-structural components

Q = functionality of the building

$RT_{C|IM}$ = repair time of the collapsed building under *IM*

$RT_{j,RT|DSi,IM}$ = repair time for the building component *j* at damage state *i* conditioned on the survival of the structure and repaired to initial condition under a given *IM*

$RT_{j,NC|IM}$ = total expected repair time for the building component *j* under a given *IM* conditioned on the survival of the structure

$RT_{NC|IM}$ = repair time of the not collapsed building under *IM*

$RT_{T|IM}$ = total expected repair time of building under given IM

t_o = occurrence time of the extreme event

$TC_{Cons|C}$ = conditional total consequence *Cons* given collapse *C* of the building

$TC_{Cons|NC}$ = conditional total consequence *Cons* given non-collapse *NC*

T_r = investigated time horizon

Tt_C = total repair time associated with the collapsed building

wh = workday hours

wr = workday ratio of calendar days

Notations of Chapter 7

A_i and B_i = constants associated with the hospital functionality level *i*

ADR_{ij} = daily number of injured persons that remain on *j*th link under state *i*

ADT_{ij} = daily number of injured persons that follow detour under damage state *i*

ATV = total number of injured persons transferred to a hospital

$BDDI_i$ = damage index associated with the damage state *i*

D_j = length of the extra detour of *j*th link (km)

h_{nor} = normalized height computed as floor height divided by building height

$HCDI_{NSC,i}$ = damage indices associated with state *i* of non-structural components

$HCDI_{SC,i}$ = damage indices associated with state i of structural components

HDI = hospital damage index

$HFL_{j|IM}$ = event that a hospital is in functionality level j given IM

l_j = length of link j (km)

LDI = link damage index

$LDS_{i|IM}$ = event that a link is in damage state i given IM

n_H = number of functionality levels of a hospital under investigation

n_l = number of links in a bridge network

n_{LD} = number of damage states associated with link damage

n_{NSD} = numbers of damage states associated with non-structural components

n_{SD} = numbers of damage states associated with structural components

$P_{DSki|IM}$ = probability of a bridge k being in a damage state i

$P_{HFi|IM}$ = probability of hospital being in functionality level i under IM

$P_{LDSj,i|IM}$ = probability of the jth link being in damage state i

$P_{NSCi|IM}$ = probability of the non-structural components being in damage state i

$P_{SCi|IM}$ = probability of the structural components being in damage state i

r_{NSC} = weighting factor associated with non-structural D_{NSC} damage index

r_{SC} = weighting factor associated with structural D_{SC} damage index

S = detour speed (km/h)

S_{0j} = traffic speed on intact link j (km/h)

$S_{Dj,i}$ = traffic speed on link j associated with damage state i (km/h)

$WT_0(ATV)$ = waiting time associated with the intact hospital under ATV

WT_i = waiting time associated with functionality level i given ATV

WT_L = waiting time associated with the normal hospital operation

WT_{Ui} = waiting time associated with functionality level i under λ_U

α_1 and α_2 = empirical constants

λ_L = pre-disaster average daily patient arrival number

λ_U = maximum daily arrival number

Notations of Chapter 8

$m_i(t)$ = median value associated with damage state i at time t without retrofit

$\gamma_{RET,i}$ = retrofit enhancement ratio associated with damage state i

Notations of Chapter 9

a, b, and c = constants in the generalized form for each sub-attribute's utility function

C_{max} = maximum retrofit cost

C_{Ret} = total expected retrofit cost

CB_{RET} = cost-benefit indicator

Eco_0 = expected values of the economic metric of sustainability without retrofit

Eco_R = expected values of the economic metric of sustainability with retrofit

Env_0 = expected values of environmental metric without retrofit

Env_R = expected values of environmental metric of sustainability with retrofit

Soc_0 = expected values of the social metric of sustainability without retrofit

Soc_R = expected values of the social metric of sustainability with retrofit

γ = risk attitude of the decision maker

u_{Eco} = utility functions for the economic attribute

u_{Env} = utility functions for the environmental attribute

u_{Soc} = utility functions for the social attribute

$u_{S,R}$ = multi-attribute utility value of expected sustainability with retrofit

$u_{S,0}$ = multi-attribute utility value of expected sustainability without retrofit

w_{Eco} = weighting factors corresponding to economic metric

w_{Env} = weighting factors corresponding to environmental metric

w_{Soc} = weighting factors corresponding to social metric

w_i^L = lower bound for the weight

w_i^U = upper bound for the weight

Notations of Chapter 10

B_1 = breadth of ship 1

B_2 = breadth of ship 2

c = width of the segment of waterway

c_{Env} = cost value of environmental metric per unit volume

c_{inj} = average comprehensive cost of injury

c_{time} = monetary value of time loss

c_{Rep} = unit repair cost

$C(Cons|DS)$ = conditional consequence

C_{DT} = time loss costs due to the unavailability of damaged ships

C_{Inj} = costs associated with injuries

C_{LL} = cost associated with fatalities

C_{OS} = environmental costs associated with oil spill

C_{Rep}	=	repair costs
C_T	=	total economic consequence associated with the ship collision
d_i	=	downtime associated with damage state *i*
dl	=	damage length of the ship
dp	=	damage penetration in the ship
DA	=	penetration area of the damaged ship
DT	=	downtime
E_{dt}	=	a factor considering epistemic uncertainties for downtime loss costs
E_{fat}	=	a factor that considers the epistemic uncertainties for fatalities costs
E_{inj}	=	a factor that considers the epistemic uncertainties for injuries costs
E_{os}	=	a factor that considers the epistemic uncertainties for oil spill costs
E_{Rep}	=	a factor accounting for the epistemic uncertainties repair costs
FT	=	number of fatalities
FV	=	future monetary value
$f_R(r)$	=	*PDF* of *R*
k_{RR}	=	a risk reduction factor
L	=	length of the route segment
L_c	=	average comprehensive cost of per human death
N	=	number of damage states considered
N_1	=	annual number of ship 1
N_2	=	annual number of ship 2
N_{inj}	=	average number of injury
O_{spi}	=	magnitude of oil spill associated with ship collision

P_C = causation probability that two ships do not undertake any evasive actions

P_I = probability that the routes of two ships intersect

P_G = geometrical collision probability

PDF = probability density function

$P(DS_i)$ = probability of a ship being in damage state i

$P(DS|H)$ = conditional probability of damage state given the extreme event H

$P(H)$ = annual rate of occurrence of the extreme event H

P_G = geometrical collision probability

P_T = annual probability of meeting within one route segment

PV = present monetary value

r = annual interest rate of money

R = risk

R_{Col} = probabilistic risk associated with ship collision

$u(r)$ = utility function associated with ship collision risk

$u(r_{col})$ = utility function associated with ship collision risk

V_1 = speed of ship 1

V_2 = speed of ship 2

x_{max} = maximum value associated with the parameter

θ = angle between the routes

ρ = attitude of the decision maker

Notations of Chapter 11

A = fatigue strength coefficient

cde = carbon dioxide emission per unit distance

C_b = ship block coefficient

C_{wv} = wave coefficient

$DISP$ = ship full load displacement

$f_{sw,CS}$ = a factor accounting for the variation of VBMs along the vessel length

f_{oi} = zero-up crossing frequency of the stress response

g = gravitational acceleration

$H_\sigma(w_e|\theta,H)$ = stress transfer function obtained by linear hydrodynamic analysis

$H_M(w_e|U,\theta)$ = RAO for the VBMs

H_s = significant wave height

I_{yy} = moment of inertia with respect to the horizontal axis of the section

k_i = scaling factor corresponding to the ith attribute

l = length of the route

L = ship length

m = fatigue strength exponent

m_2 = spectral moments of the stress process

$m_{0,M}$ = zeroth moment of the VBM response spectrum

M_{SW} = still water bending moment

M_w = wave-induced VBM response

M_{UR} = resisting bending moment associated with ultimate failure

p_i = probability of occurrence of sea state i

$P(SS)$ = probability of occurrence of sea state (SS)

$P(U,\theta|SS)$ = probability of ship operation cases

$P(f|SS, U, \theta)$ = conditional probability of ship section failure given the occurrence of a specific set of *SS*, *U*, and θ

RAOs = response amplitude operators

STF = ship type factor

$S_X(\omega)$ = spectral density functions of the output and input

T = service time of a ship structure

T_1 = wave mean period

U = forward ship speed

x = attribute value under investigation

x_{max} = maximum value of the attribute

x_R = model uncertainty associated with hull resistance determination

x_{SW} = model uncertainties associated with still water

x_W = model uncertainties associated with wave-induced bending moment

v_i = spectral width parameter

ω = circular frequency of excitation waves

WGT_{100} = weight of SWBS 100

z = vertical distance from the structural detail to the baseline

z_0 = vertical distance from the neutral axis to the baseline

ρ = attitude of the decision maker

θ = heading angle

σ_i = standard deviation of the stress process associated with sea state *i*

μ_M = mean associated with the random variable M_w

σ_M = standard deviation associated with the random variable M_w

λ = cycle counting correction factor

Γ = gamma function

Notations of Chapter 12

a = crack size

a_0 = initial crack size

$a_i(t)$ = fatigue crack at time t

a_l = limit size of fatigue crack size that can be detected

a_p = crack length associated with the plate

a_w = crack length associated with the web

A_D = total sectional area of deck

A_B = total sectional area of outer bottom

A'_B = total sectional area of inner bottom

A_S = total sectional area of sides

$b_{p,0}$ = plate breadth

B = ship breadth

c_{Cons} = construction cost per unit area

$c_{Insp,j}$ = inspection cost of component j

$c_{Rep,j}$ = repair cost for component j

C = fatigue coefficient

C_1 = annual corrosion rate

C_2 = a constant set to unity

C_b = ship block coefficient

C_{corr}	=	corrosion-enhanced crack growth parameter
$Cons$	=	monetary consequence associated with ship structural failure
C_{wv}	=	wave coefficient
$d(t)$	=	thickness loss
d_p	=	corrosion depth of the plate
ds_i	=	corrosion level of the component i
ds_p	=	fraction of thickness that is detected associated with probability p
d_w	=	corrosion depth of the web
D	=	hull depth
D_B	=	height of double bottom
$DISP$	=	ship full load displacement
$f_{sw,CS}$	=	a factor accounting for the variation of VBMs along the vessel length
g	=	neutral axis position above the base line
$h_{w,0}$	=	stiffener height
H	=	depth of non-collapse side of the hull section
I_Y	=	moment of inertia of hull cross-section about transverse axis
K_{axial}	=	stress concentration factor for the structural detail
L_j	=	length associated with component j
L	=	ship length
m	=	fatigue exponent
M_{SW}	=	still water bending moment
M_{UR}	=	resisting bending moment associated with ultimate failure
M_W	=	wave-induced bending moment

$n_{0,CR}$	=	number of components of corrosion loss larger than a critical value
$n_{0,FC}$	=	number of components associated with cracks larger than a_l
N_{avg}	=	average daily number of cycles
N_{Tot}	=	total number of the components inspected at a given time
P_f	=	conditional probability of ship cross-section failure
$P_{ED,CR}$	=	probability of detecting corroded component
$P_{ED,FC}$	=	probability of detecting crack sizes larger than the critical value
$P_{RE,CR}$	=	average probability of repair of corroded components
$P_{RE,FC}$	=	probability of repair at the inspection time t considering fatigue
$P_{RE,j}$	=	probability of repairing the component under inspection action
r	=	annual discount rate of money
t_0	=	corrosion initiation time
$t_{o,i}$	=	coating life for ship structure
$t_{insp,i}$	=	time of inspection i
$t_{p,0}$	=	plate thickness
$t_{w,0}$	=	stiffener thickness
T	=	investigated time interval
STF	=	ship type factor
VBM	=	vertical bending moment
W_j	=	width associated with component j
WGT_{100}	=	weight of Ship Work Breakdown Structure
x_R	=	model uncertainty associated with hull resistance determination
x_{SW}	=	model uncertainty associated with still water

x_W = model uncertainty associated with wave-induced bending moment

$Y(a)$ = geometric factor

$\delta(\mathbf{X})$ = consequences

α = annual ship operation rate

ΔK = stress range intensity factor

$\Delta\sigma$ = stress range

σ_{yB}, σ'_{yB}, σ_{yD}, and σ_{yS} = yield strengths of outer bottom, inner bottom, decks and side

σ_{uB}, σ'_{uB}, σ_{uD}, and σ_{uS} = ultimate strengths of outer bottom, inner bottom, decks, and side

λ_d = a parameter of the specific fatigue crack detection method

λ_s = a parameter that is associated with corrosion damage detection method

Notations of Chapter 13

a = crack size

a_{ci} = critical crack size

a_D = detectable crack size

$a_i(t)$ = crack size of fatigue-sensitive detail i at time t

a_{oi} = initial fatigue crack size associated with detail i

A = parameter associated with Weibull scale

B = parameter associated with Weibull shape

c_{Cons} = construction cost per unit area

C = fatigue coefficient

C_f = consequence of failure

C_{min}	=	minimum cost value
C_{max}	=	maximum cost value
$C_{Di,F}$	=	consequence of detail i failure while all other details survived
$E_{Di,F}$	=	event of failure of detail i
$E_{Di,S}$	=	event of survival of detail i
E_{SysF}	=	event associated with system failure
$g_i(\boldsymbol{X})$	=	performance function associated with fatigue-sensitive detail i
IE_j	=	inspection event j
$IR_{i,no}$	=	inspection event associated with no fatigue crack
$IR_{i,yes}$	=	inspection event associated with fatigue crack detected
L	=	length associated with structural detail under investigation
m	=	fatigue exponent
m_{ad}	=	number of adjacent details
M_i	=	limit state function associated with detail i
M_k	=	a stress magnification factor
n	=	number of fatigue-sensitive details
P	=	probability of occurrence of an adverse event
r_{cr}	=	ratio between repair and construction cost
$Rt_c(C)$	=	rating factor associated with consequence
Rt_{max}	=	maximum value associated with rating factor
Rt_{min}	=	minimum value associated with rating factor
t_{IE}	=	inspection time
v_{0i}	=	average zero-crossing rate of stress cycle

W	=	width associated with structural detail under investigation
$Y(a)$	=	geometrical correction factor
α_1, α_2, and α_3	=	parameters associated with rating functions
β	=	reliability index
ε_S	=	modeling uncertainty associated with stress modeling
ε_Y	=	modeling uncertainty associated with geometry function
λ_D	=	mean detectable crack size
Γ	=	Gamma function

VITA

You Dong was born in Rizhao, China, to Qingguo Dong and his wife, Zongyun Mu. He obtained his Degree in Bridge Engineering from Hunan University, Changsha, China in 2009. In the August of 2010, he joined the Ph.D. program at Lehigh University, Bethlehem, PA, working under the supervision of Prof. Dan M. Frangopol. During his Ph.D. work at Lehigh University, he was awarded the P.C. Rossin Fellowship of Lehigh University in 2014 and the International Civil Engineering Risk and Reliability Association (CERRA) Student Recognition Award in 2015.